



**HAL**  
open science

## **JRJC 2018. Book of proceedings**

Christina Agapopoulou, Mario Alcocer-Avila, Konie Al Khoury, Edgar Barlerin, Giovanni Bartolini, Guillaume Bourgatte, Martin Briday, Reina Camacho Toro, Camille Camen, Joao Coelho, et al.

► **To cite this version:**

Christina Agapopoulou, Mario Alcocer-Avila, Konie Al Khoury, Edgar Barlerin, Giovanni Bartolini, et al. (Dir.). JRJC 2018. Book of proceedings. 2019. hal-02271401

**HAL Id: hal-02271401**

**<https://hal.science/hal-02271401>**

Submitted on 4 Sep 2019

**HAL** is a multi-disciplinary open access archive for the deposit and dissemination of scientific research documents, whether they are published or not. The documents may come from teaching and research institutions in France or abroad, or from public or private research centers.

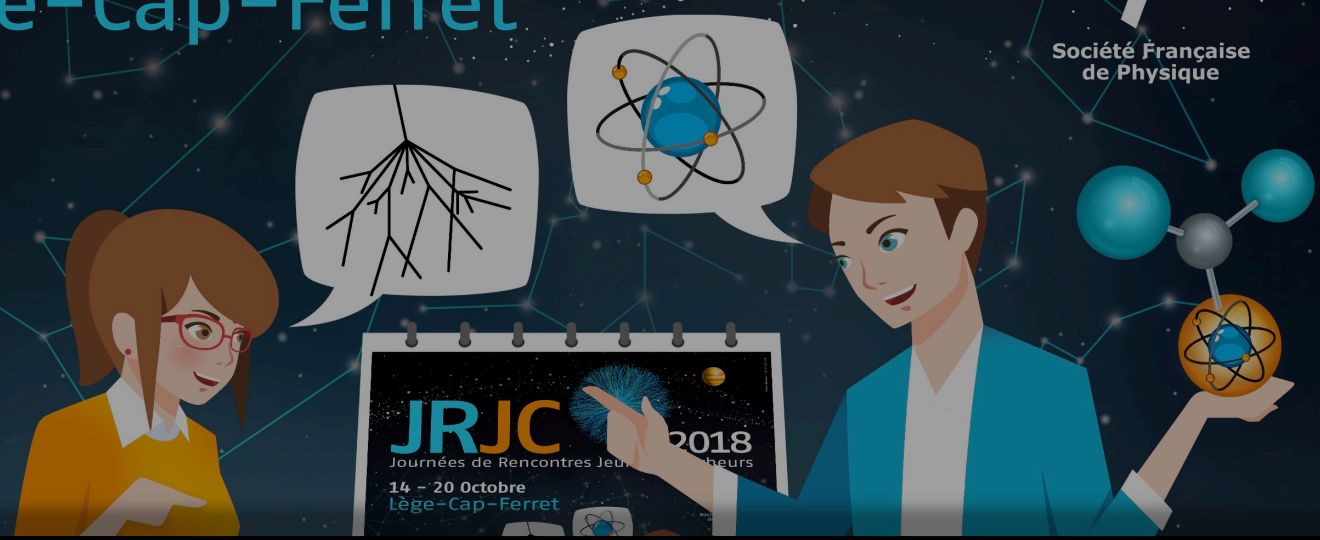
L'archive ouverte pluridisciplinaire **HAL**, est destinée au dépôt et à la diffusion de documents scientifiques de niveau recherche, publiés ou non, émanant des établissements d'enseignement et de recherche français ou étrangers, des laboratoires publics ou privés.

# JRJC

# 2018

## Journées de Rencontres Jeunes Chercheurs

### 14 - 20 Octobre Lège-Cap-Ferret



# BOOK of PROCEEDINGS

#### Secrétariat

Isabelle Cossin, LPNHE  
isabelle.cossin@lpnhe.in2p3.fr  
Tel: +33 (0)1 44 27 68 95

<http://jrjc2018.sciencesconf.org>

- Energie nucléaire
- Structure du noyau
- Astrophysique nucléaire
- Physique médicale
- Physique hadronique
- Cosmologie
- Instrumentation
- Modèle standard électrofaible
- Au-delà du modèle standard
- Neutrinos
- Astroparticules
- Physique des saveurs



<http://jrjc2018.sciencesconf.org>



## **Comité d'organisation :**

Pauline Ascher	(ENBG)
Fabrice Balli	(CEA Saclay)
Karim Benakli	(LPTHE)
Nicolas Chanon	(IPNL)
Emmanuel Chauveau	(CENBG)
Rachel Delorme	(IMNC)
Claudio Giganti	(LPNHE)
Julien Masbou	(SUBATECH)
Julien Piot	(Ganil)
Antonio Uras (*)	(IPNL)
Dimitris Varouchas	(LAL)

(\*) Editor of these proceedings

## **Secrétariat :**

Isabelle Cossin	(LPNHE)
-----------------	---------

# Table des matières

<b>I</b>	<b>Beyond Standard Model</b>	<b>9</b>
	<b>Loïc Valéry : <i>Introduction à la Physique au-delà du Modèle Standard</i></b>	<b>11</b>
1	Forces et lacunes du Modèle Standard . . . . .	11
2	La Supersymétrie . . . . .	12
3	Théories avec dimensions supplémentaires . . . . .	13
4	Quarks de type vecteurs . . . . .	14
5	Conclusion . . . . .	14
	<b>Camille Camen : <i>Recherche d'un second boson de Higgs de basse masse (<math>m_{\gamma\gamma} &lt; 110</math> GeV) se désintégrant en deux photons avec l'expérience CMS</i></b>	<b>17</b>
1	Introduction . . . . .	17
2	Contexte théorique . . . . .	17
3	Motivations . . . . .	17
4	Bruits de fond de l'analyse . . . . .	18
5	Stratégie d'analyse . . . . .	19
6	Résultats . . . . .	20
7	Conclusion . . . . .	20
	<b>Yufeng Wang : <i>Search for new resonances in diphoton events with the ATLAS detector</i></b>	<b>23</b>
1	Theoretical context . . . . .	23
2	Experiment . . . . .	23
3	Analysis . . . . .	24
4	Results . . . . .	25
5	Conclusion and futher plan . . . . .	25
<b>II</b>	<b>Hadronic Physics</b>	<b>27</b>
	<b>Laure Massacrier : <i>Introduction to hadronic physics</i></b>	<b>29</b>
1	Introduction . . . . .	29
2	Important features of QCD . . . . .	29
3	Experimental and theoretical tools . . . . .	30
4	Nucleon structure . . . . .	31
5	Quark Gluon Plasma and Cold Nuclear Matter effects . . . . .	31
	<b>Jan Maelger : <i>Introduction to the Curci-Ferrari Model : Results and Open Questions</i></b>	<b>33</b>
1	Introduction . . . . .	33
2	Heavy Quark Phase Diagram . . . . .	34
3	Conclusion . . . . .	36
<b>III</b>	<b>Medical Physics</b>	<b>39</b>
	<b>Mario E. Alcocer-Avila<sup>1</sup>, Michele A. Quinto<sup>2</sup>, Juan M. Monti<sup>2</sup>, Roberto D. Rivarola<sup>2</sup>, Christophe Champion<sup>1</sup> : <i>Proton track-structure simulation in biological media</i></b>	<b>41</b>
1	Introduction . . . . .	41
2	Materials and methods . . . . .	41
3	Results . . . . .	43
4	From protons to $\alpha$ particles : the role of TAT . . . . .	44

<b>Enzo FABIANI, Christophe DEROULERS : <i>A 1D model of tumor cell migration with polarization : numerical and analytical study</i></b>		<b>49</b>
1	Introduction . . . . .	49
2	Model . . . . .	50
3	Continuum limit . . . . .	51
4	Results and discussion . . . . .	51
5	Conclusion . . . . .	52
6	Acknowledgments . . . . .	52
<b>Erwan Olivier, Thanh-Hà Nguyen-Bui, Christophe Champion : <i>Modelling of heavy ion transport in matter with entropic moment methods</i></b>		<b>55</b>
1	Introduction . . . . .	55
2	The deterministic code $M_1$ . . . . .	55
3	Results . . . . .	56
4	Conclusion . . . . .	57
5	Acknowledgments . . . . .	57
<b>IV Standard Model</b>		<b>59</b>
<b>Reina Camacho Toro : <i>Introduction to the Standard Model session</i></b>		<b>61</b>
1	Introduction . . . . .	61
2	Results on Standard Model Physics . . . . .	61
3	Higgs boson measurements . . . . .	61
4	Conclusion . . . . .	63
<b>Konie Al Khoury : <i>A New Method to Estimate Systematic Uncertainties in the <math>VH(H \rightarrow b\bar{b})</math> Analysis with the ATLAS Detector</i></b>		<b>65</b>
1	Introduction . . . . .	65
2	$VH(H \rightarrow b\bar{b})$ Analysis . . . . .	65
3	BDT-Based Method to Model Systematic Uncertainties . . . . .	67
4	Result . . . . .	68
<b>Mykola Khandoga : <i>Data-driven correction of electromagnetic shower shapes in Monte-Carlo modelling of ATLAS calorimeter</i></b>		<b>69</b>
1	Introduction . . . . .	69
2	Shower shapes measurement and correction . . . . .	70
3	Résultats . . . . .	71
<b>Giovanni Bartolini : <i>Boosted Decision Trees and b-jet Trigger Calibration Studies for <math>t\bar{t}H(b\bar{b})</math> Fully Hadronic Analysis with the ATLAS Detector</i></b>		<b>75</b>
1	Introduction . . . . .	75
2	Two-steps multivariate analysis . . . . .	75
3	Combined calibration . . . . .	76
4	Conclusions . . . . .	78
<b>Merve Nazlim Agaras : <i>Measurement of the Higgs Top Yukawa coupling with the ATLAS detector at LHC</i></b>		<b>81</b>
1	Introduction . . . . .	81
2	Signal Region Definition and background estimates . . . . .	82
3	Systematic uncertainties . . . . .	83
4	Statistical Model and Results . . . . .	83
5	Possible improvements in Two Lepton Same Sign . . . . .	84
<b>Guillaume Bourgatte : <i>Observables de spin des leptons taus dans l'expérience CMS auprès du LHC</i></b>		<b>85</b>
1	Introduction . . . . .	85
2	Description du détecteur CMS . . . . .	85
3	Variables optimales . . . . .	86
4	Higgs CP . . . . .	88
5	Remerciements . . . . .	88

<b>V Instrumentation</b>	<b>89</b>
<b>Agapopoulou Christina : <i>A High-Granularity Timing Detector for the Phase-II upgrade of the ATLAS Detector System</i></b>	<b>91</b>
1 Introduction . . . . .	91
2 Detector Overview . . . . .	92
3 Sensors . . . . .	92
4 Front-End Electronics . . . . .	93
5 Conclusions . . . . .	94
<b>Edgar Barlerin : <i>Cross-sections measurements for hadrontherapy : conception of a large acceptance mass spectrometer</i></b>	<b>95</b>
1 Introduction . . . . .	95
2 Design and construction of FRACAS detectors . . . . .	97
3 Conclusion . . . . .	98
<b>Bing Liu : <i>Hadron selection using Boosted Decision Trees in the semi-digital hadronic calorimeter</i></b>	<b>99</b>
1 Introduction . . . . .	99
2 Particle identification using Boosted Decision Trees . . . . .	99
3 Hadron events selection and hadronic energy reconstruction . . . . .	100
4 Uncertainties estimation . . . . .	101
5 Conclusion . . . . .	101
<b>Mara Corbetta : <i>Studies on Gas Mixture and Gas Recirculation Effects on GEM Detectors Operation</i></b>	<b>103</b>
1 Introduction . . . . .	103
2 Gas-Related Studies . . . . .	103
3 Irradiation Campaign at GIF++ . . . . .	104
4 Conclusion . . . . .	106
<b>Khalil Latifa : <i>Caractérisation du système de lecture du CCD dans DAMIC</i></b>	<b>107</b>
1 Introduction . . . . .	107
2 Banc de test du DAMIC . . . . .	107
3 L'ADC dans DAMIC M . . . . .	108
4 Conclusion . . . . .	108
<b>VI Flavour Physics</b>	<b>109</b>
<b>João Coelho : <i>Introduction to the Flavour Physics Session</i></b>	<b>111</b>
<b>Dawid Gerstel : <i>Tests of Lepton Flavour Universality in semitauonic decays of b-hadrons at the LHCb experiment</i></b>	<b>113</b>
1 Introduction . . . . .	113
2 $R(D^*)$ with $\tau \rightarrow 3\pi\nu_\tau$ at LHCb . . . . .	114
3 Updating $R(D^*)$ with $\tau \rightarrow 3\pi\nu_\tau$ using 2015-2016 data at LHCb . . . . .	115
4 Conclusions and prospects . . . . .	116
<b>Boris Quintana : <i>Study of <math>B \rightarrow hh\gamma</math> decays with the LHCb experiment</i></b>	<b>117</b>
1 Introduction . . . . .	117
2 Data selection . . . . .	117
3 $B_{(s)}$ mass fit . . . . .	118
4 Study of the $h^+h^-$ resonances . . . . .	119
5 Conclusion and prospects . . . . .	119
<b>VII Cosmology</b>	<b>121</b>
<b>Florian Mondon : <i>Étude des biais cosmologiques induits par les variabilités nouvelles détectées sur les supernovas de type Ia</i></b>	<b>123</b>
1 Le modèle <i>The SUpernova Generator And Reconstructor</i> . . . . .	123
2 Résultats obtenus après ajustement de données spectroscopiques par le modèle de SED SUGAR . . . . .	124

3	Ajustement des courbes de lumière à partir du modèle de SED SUGAR . . . . .	124
<b>Martin BRIDAY : <i>Host galaxies environment influence study on Type Ia Supernovae</i></b>		<b>127</b>
1	Introduction . . . . .	127
2	Star age measurement methods . . . . .	128
3	Results . . . . .	129
4	Conclusion . . . . .	130
<b>Gabriel Moreau : <i>Backreaction of the infrared modes of scalar fields on de Sitter geometry</i></b>		<b>131</b>
1	Introduction . . . . .	131
2	Free scalar field in de Sitter spacetime and particle production . . . . .	132
3	Getting to the modified Friedman equation . . . . .	132
4	Analytic results for large $N$ . . . . .	133
5	Conclusion . . . . .	134
6	Acknowledgments . . . . .	134
<b>VIII Astrophysics</b>		<b>135</b>
<b>Arnaud Mares : <i>Étude des sources gamma HESS J1640.6-4633 et HESS J1641.0-4619</i></b>		<b>137</b>
1	Introduction . . . . .	137
2	Présentation de l'instrument et des sources . . . . .	137
3	Résultat . . . . .	138
4	Conclusion . . . . .	139
<b>Gabriel Emery : <i>Variability of Active Galactic Nuclei at Very High Energy with H.E.S.S.</i></b>		<b>141</b>
1	Introduction . . . . .	141
2	Very High Energy Astronomy . . . . .	141
3	Active Galactic Nuclei . . . . .	142
4	Target of Opportunity program and analysis . . . . .	143
5	Other activities . . . . .	143
6	Conclusion . . . . .	144
<b>Quentin Piel : <i>Gamma-Ray Burst detection at very high energy</i></b>		<b>147</b>
1	Gamma Ray Bursts . . . . .	147
2	The H.E.S.S. telescope array . . . . .	147
3	Cherenkov Telescope Array . . . . .	148
4	Conclusion . . . . .	150
<b>Marion Spir-Jacob : <i>Pulsars at very high energies</i></b>		<b>151</b>
1	Compact objets, final stages of stellar evolution . . . . .	151
2	Gamma-ray emitting pulsar models . . . . .	152
3	PIC simulations . . . . .	153
4	Pulsars in the VHE domain . . . . .	153
5	Perspectives for the future . . . . .	154
<b>Chloé Therreau : <i>Calibration of XENON1T for the search of new physics</i></b>		<b>155</b>
1	Introduction . . . . .	155
2	XENON1T experiment . . . . .	155
3	Calibration using a $^{83m}\text{Kr}$ source . . . . .	156
4	Search for neutrinoless double $\beta$ decay with XENON1T . . . . .	157
5	Conclusion . . . . .	158
<b>IX Neutrino Physics</b>		<b>161</b>
<b>Laura ZAMBELLI : <i>Introduction à la physique des neutrinos</i></b>		<b>163</b>
1	Du postulat aux découvertes . . . . .	163
2	Les anomalies et les oscillations . . . . .	163
3	Les questions actuelles . . . . .	163

**Axel PIN : *Study of the nature of neutrinos with the SuperNEMO experiment and the LiquidO project*** **165**

1	Introduction . . . . .	165
2	Double beta decays with SuperNEMO and LiquidO . . . . .	165
3	Results . . . . .	167
4	Conclusions . . . . .	168



Première partie

# Beyond Standard Model

session dirigée par Loïc VALÉRY



# Introduction à la Physique au-delà du Modèle Standard

Loïc Valéry

*Deutsches Elektronen-Synchrotron (DESY)  
Hambourg, Allemagne*



## Résumé

En dépit des nombreuses confirmations expérimentales, le Modèle Standard (MS) présente des lacunes quant à la description de certains phénomènes, à l'échelle cosmologique, mais également à l'échelle de la physique des particules élémentaires. Ce document tente de donner quelques indications sur ces lacunes et quelques possibles solutions à ces difficultés, trouvées dans le contexte d'extensions du Modèle Standard (*Beyond the Standard Model* (BSM))

## 1 Forces et lacunes du Modèle Standard

Le Modèle Standard a montré une très grande robustesse et un caractère prédictif très souvent confirmé par l'expérience. Par exemple, l'existence des bosons  $W$  et  $Z$  fut postulée avant leur découverte expérimentale en 1983 [1, 2] de même que pour le boson de Higgs. De plus, les sections efficaces de divers processus, tels que la production de paires top-antitop ou de bosons de jauge sont mesurées expérimentalement et sont compatibles avec les attentes du Modèle Standard [3, 4].

Néanmoins, plusieurs indications laissent à penser que le Modèle Standard pourrait n'être qu'une théorie effective aux énergies testées jusqu'alors.

### 1.1 Non-compréhension de la gravitation

La première limitation, théorique, concerne la **gravitation**. Cette interaction est la seule des quatre interactions fondamentales non-comprise dans le Modèle Standard. Elle demeure négligeable lorsque l'échelle d'énergie considérée est de l'ordre de l'échelle électrofaible ( $\approx 100$  GeV). Cependant, à l'échelle de Planck ( $\Lambda_p \approx 10^{19}$  GeV), elle doit être prise en compte : le Modèle Standard n'est donc pas une théorie valide à cette échelle d'énergie. La différence entre les deux échelles d'énergie (échelle de Planck et échelle électrofaible) constitue l'une des difficultés du Modèle Standard, appelée **problème de hiérarchie**.

### 1.2 La matière sombre

Diverses observations astrophysiques ont conduit à l'hypothèse de l'existence d'une grande quantité de matière non-baryonique, appelée **matière sombre**.

Ainsi la mesure des vitesses de rotation des galaxies et des amas de galaxies montrent que ces objets doivent avoir un contenu en matière bien supérieur à ce qui peut être déduit de la quantité de lumière émise.

Le "*bullet cluster*" est une autre observation très parlante de matière sombre. Il y a 150 millions d'années (vu depuis la Terre) cet amas de galaxies a traversé un autre amas plus gros, tous deux ayant leurs matières baryoniques essentiellement sous forme de gaz. Lors de la collision, les deux amas de gaz se sont freinés l'un l'autre tout en s'échauffant et émettant une grande quantité de rayons X. Par des mesures de lentille gravitationnelle, il a été démontré que ces amas avaient une autre composante de matière qui n'a pas été freinée et qui maintenant se trouve au devant de la composante visible des amas. L'explication la plus simple et la plus efficace est que ces deux amas de galaxies contenaient une composante importante de matière sombre.

À ces observations astrophysiques vient se rajouter une observation cosmologique. L'expérience Planck a mesuré le fond diffus cosmologique avec une très grande précision. L'interprétation de cette mesure conduit à une mesure de densité de matière sombre de 23%, quand celle de la matière ordinaire n'est que de 4.8%.

La nature exacte de la matière sombre n'est pas connue et il semble maintenant peu probable qu'elle puisse être expliquée par un ou plusieurs type de particules du MS. Dès lors, il est de la première importance que le Modèle Standard de la physique des particules puisse être étendu pour répondre à ces observations astrophysiques et cosmologiques.

### 1.3 Le problème de naturalité

La masse nue du boson de Higgs, notée  $m_0$  n'est pas la masse à laquelle ce dernier peut être détecté, notée  $m$ . Cette dernière est le résultat de la prise en compte de corrections radiatives. Par exemple, une boucle de fermions peut conduire à une correction donnée, au premier ordre par l'Équation 1 [5].

$$m^2 = m_0^2 - \frac{\lambda_f^2}{8\pi^2} \Lambda_c^2 + \dots \quad (1)$$

dans laquelle  $\lambda_f$  est le couplage de Yukawa du fermion  $f$  et  $\Lambda_c$  l'échelle d'énergie jusqu'à laquelle le Modèle Standard est supposé valide. Des termes quadratiques et d'ordres supérieurs apparaissent et conduisent naturellement à une masse attendue du boson de Higgs importante. Cependant, les contraintes expérimentales et la récente découverte du boson de Higgs montrent

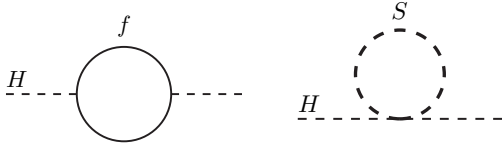


FIGURE 1: Corrections radiatives à la masse du boson de Higgs par la prise en compte de boucles fermioniques (gauche) et de scalaire (droite).

que cette masse doit être faible : les divergences quadratiques doivent être compensées par  $m_0$ . En réalité l'ajustement des variables  $m_0$  et  $\lambda$  doit être réalisé jusqu'à la 32<sup>ème</sup> décimale ! C'est le **problème de naturalité**.

À partir de cet état de fait, il existe plusieurs façons d'obtenir naturellement  $m \approx 100$  GeV :

- rajouter une nouvelle symétrie telle que la supersymétrie pour inclure de nouvelles boucles compensant les corrections divergentes du MS ;
- rajouter de nouvelles dimensions d'espace pour ramener  $\Lambda_P$  à des énergies proches de l'échelle électrofaible ;
- supposer que le boson de Higgs puisse être (au moins en partie) composite.  $\Lambda_c$  est alors égale à l'échelle de composité.

Généralement, il est considéré que l'introduction de ces nouvelles propriétés doit se faire à des énergies de l'ordre du TeV pour être le plus efficace possible.

D'autres exemples, tel que le nombre inexplicé de familles (générations) de fermions, l'addition *ad-hoc* du mécanisme *de Higgs* peuvent également constituer des faiblesses du MS.

## 2 La Supersymétrie

Les modèles supersymétriques s'appuient sur l'existence d'opérateurs associant à tout fermion du Modèle Standard un boson et *vice versa*, ce qui permet de résoudre le problème de naturalité. En effet, au deuxième ordre, la correction liée à une boucle de fermions (Figure 1 (gauche)) est donnée par :

$$m^2 = m_0^2 - \frac{\lambda_f^2}{8\pi^2} \Lambda_c^2 - \frac{3m_f^2}{8} \ln \left( \frac{\Lambda_c}{m_f} \right) \dots \quad (2)$$

et la contribution d'une boucle de scalaire (Figure 1 (droite)) est donnée par l'équation :

$$m^2 = m_0^2 + \frac{\lambda_s^2}{16\pi^2} \Lambda_c^2 - \frac{m_s^2}{8} \ln \left( \frac{\Lambda_c}{m_s} \right) \dots \quad (3)$$

Dans ces équations  $\lambda_f$  est le couplage de Yukawa du fermion  $f$  du fermion de masse  $m_f$ . De même, le couplage entre le scalaire  $s$  de masse  $m_s$  et le boson de Higgs est notée  $\lambda_s$ .

Il apparaît donc que les divergences quadratiques peuvent être supprimées si, à chaque fermion du Modèle Standard sont associés deux superpartenaires sca-

laire présentant les mêmes couplages que lui ( $\lambda_s = \lambda_f$ ), et étant de même masse. Seules des divergences logarithmiques subsistent, et demeurent faibles si les différences de masse entre les particules du Modèle Standard et leurs superpartenaires sont faibles (typiquement de l'ordre du TeV). Si la supersymétrie est exacte, les superpartenaires doivent avoir des masses identiques, mais cette hypothèse est contredite par les observations expérimentales : la supersymétrie est brisée. La brisure doit être *douce*, évitant l'introduction de nouveaux termes divergeant quadratiquement. Son mécanisme est à l'heure actuelle inconnu.

Les fermions du Modèle Standard et leurs superpartenaires scalaires sont compris dans un ensemble, appelé supermultiplet *chiral*. Ce dernier contient le spineur du fermion et les deux champs scalaires réels partenaires. Ces champs se mélangent et conduisent à un champ scalaire complexe, correspondant au superpartenaire, appelé *sfermion*. De la même façon, les bosons vecteurs peuvent être trouvés au sein de supermultiplets dits *vecteurs*, avec leur superpartenaire fermionique, appelé *jaugino*. Par exemple, le gluon de spin 1 se voit associé le gluino de spin  $\frac{1}{2}$ . Dans chacun de ces supermultiplets, les nombres de degrés de liberté fermionique et bosonique sont identiques ( $n_B = n_F = 2$ ).

Les contraintes expérimentales ont nécessité l'introduction d'un nouveau nombre quantique, multiplicatif, appelé parité  $R$ . En effet, le MSSM (Modèle Standard Supersymétrique Minimal) pourrait conduire à un temps de vie du proton bien plus faible que la contrainte expérimentale actuelle ( $> 10^{32}$  ans [6]), par le biais de la violation des nombres baryonique  $B$  et leptonique  $L$ . La conservation de la parité  $R$ , définie dans l'équation 4 (dans laquelle  $s$  est le spin de la particule) au cours des processus physiques permet de supprimer de tels effets.

$$R = (-1)^{3(B-L)+2s} \quad (4)$$

$R$  prend alors la valeur de  $+1$  pour les particules du Modèle Standard, et de  $-1$  pour les particules supersymétriques. La conservation de la parité  $R$  conduit à plusieurs conséquences phénoménologiques majeures quant aux modèles supersymétriques. Tout d'abord, la production célibataire de particules supersymétriques est impossible (la parité dans l'état initial étant de  $+1$ , il doit en être de même dans l'état final) et la désintégration à deux corps d'une particule supersymétrique doit comprendre une particule de parité  $R = -1$  et une particule du Modèle Standard. En conséquence, la particule supersymétrique la plus légère (appelée LSP pour *Lightest Supersymmetric Particle*) est stable, et fournit naturellement un bon candidat pour décrire la matière noire.

En dépit du fait que cette théorie résolve une partie des difficultés du Modèle Standard, certaines de ses incarnations peuvent être en contradiction avec les observations expérimentales. Par exemple, le MSSM peut permettre une violation de la symétrie  $CP$  plus importante que les contraintes expérimentales [7]. Aussi, des extensions supersymétriques, telles que les modèles hybrides  $N = 1/N = 2$  (où  $N$  est le nombre de géné-

rateurs de supersymétrie) ou les modèles avec symétrie continue  $R$  (généralisation continue de la parité  $R$ ) proposent une solution à ces difficultés.

La supersymétrie fait l'objet d'un grand nombre de recherches auprès des collisionneurs, tant elle peut conduire à une multitude d'états finals : grande multiplicité d'objets physiques (électrons, muons, photons, jets), ou bien souvent à une énergie transverse manquante<sup>1</sup> importante. L'ensemble des résultats des recherches réalisées dans l'expérience ATLAS est présenté sur la Figure 2.

Cette dernière classe les contraintes expérimentales selon le type de particules recherché. Par exemple la recherche de **superpartenaires des quarks de troisième génération** (*stop* et *sbottom*) conduit à des contraintes expérimentales qui excluent leur existence pour des masses situées entre légèrement en deçà du TeV pour la plupart des états finals considérés. Des **modèles simplifiés** permettent de réaliser une recherche inclusive et de faire varier l'ensemble de leurs paramètres. Dans ce cadre, les masses des gluinos sont contraintes à être supérieures au TeV.

### 3 Théories avec dimensions supplémentaires

Introduites par Kaluza [8] et Klein [9] en 1921 et 1926 respectivement, la notion de dimension supplémentaire a été complétée plus récemment par Randall et Sundrum [10] en 1999. Dans ces modèles, la différence entre l'échelle électrofaible et l'échelle de Planck (et donc, de la gravitation) peut être expliquée par l'existence de dimensions supplémentaires dans lesquelles la gravitation et ses bosons médiateurs, les *gravitons*, se propageraient. Dans ce cas, l'application du théorème de Gauss gravitationnel conduirait à une expression de la force d'interaction gravitationnelle de la forme :

$$F = G_g \frac{m_a m_b}{r_{AB}^{2+d}} \quad (5)$$

où  $r_{AB}$  est la distance entre les points  $A$  et  $B$  de masses respectives  $m_A$  et  $m_B$  et  $G_g$  est l'équivalent de la constante de gravitation universelle dans le cas de  $4 + d$  dimensions d'espace-temps.

Ces dimensions supplémentaires d'espace doivent toutefois être enroulées sur elles-mêmes (ou compactifiées) afin de conserver les observables prédites par les lois de Newton et notamment les orbites des planètes. Ainsi, l'équation 5 peut s'écrire :

$$F = G_g \frac{m_a m_b}{r_{AB}^2 R^d} \quad (6)$$

où  $R$  est le rayon de compactification de la dimension supplémentaire.

Ainsi, en identifiant l'équation 5 à l'expression classique de l'interaction gravitationnelle en quatre dimen-

sions, on tire que :

$$G_N = \frac{G_g}{R^d} \quad (7)$$

où  $G_N$  est la constante de gravitation universelle. En conséquence, l'interaction gravitationnelle ne serait pas plus faible que l'interaction électrofaible par essence, mais parce qu'elle se propagerait dans plus de quatre dimensions d'espace-temps, résolvant le problème de hiérarchie.

Ces dimensions peuvent se présenter sous différents types de géométries. À partir des considérations précédentes, la hiérarchie entre la gravitation et l'échelle électrofaible peut s'expliquer par des dimensions supplémentaires de grand rayon de compactification  $R$ , ou très nombreuses. Ces deux cas permettent de réduire la valeur de la constante  $G_N$  et correspondent aux théories dites ADD (Arkani, Dimopoulos, Dvali).

D'autres théories, cependant, considèrent une unique dimension supplémentaire de petite taille. *A priori*, dans une géométrie plane, cette configuration ne conduit pas à la résolution du problème de hiérarchie. Dans le modèle introduit en 1999 par Randall et Sundrum [10], la compactification de l'unique dimension spatiale supplémentaire est réalisée selon un orbifold de symétrie  $S^1/Z_2$  (Figure 3). Il y a dans ces modèles deux branes (hyper plans quadri-dimensionnels) localisées aux points fixes de l'orbifold et repérées dans la dimension supplémentaire par la coordonnée  $y : y = 0$  (appelée brane de Planck) et  $y = \pi R$  (brane du Modèle Standard) où  $R$  est le rayon du cercle défini par la symétrie  $S^1$ .

La métrique utilisée est alors définie par :

$$ds^2 = e^{-k|y|} dx^\mu dx^\nu \eta_{\mu\nu} + dy^2 \quad (8)$$

où  $k$  représente la courbure de l'espace-temps introduite par ce choix,  $\eta_{\mu\nu}$  la métrique de Minkowski classique, et  $e^{-k|y|}$  est le **facteur de courbure**.

Ainsi, sur la brane de Planck ( $y = 0$ ), l'échelle de Planck est de l'ordre de  $10^{19}$  GeV. Sur la brane du Modèle Standard, cette échelle est pondérée par le facteur de courbure  $e^{-k\pi R}$ .

Dans le modèle original [10], les particules du Modèle Standard étaient contraintes à rester dans la brane Modèle Standard, tandis que les gravitons pouvaient se propager dans les cinq dimensions d'espace-temps. Néanmoins, ce modèle conduit à des contributions trop importantes (en comparaison aux contraintes expérimentales) des processus de violation de la saveur par courant neutre (FCNC).

Pour pallier ces difficultés, une solution est de laisser les particules du Modèle Standard libres : elles peuvent être (à l'exception du boson de Higgs) entre les deux branes, permettant d'expliquer, entre autres, les hiérarchies de masses entre les différentes particules. De tels modèles conduisent également à l'apparition de nouvelles excitations des particules du Modèle Standard, appelées excitations de Kaluza Klein, le mode 0 correspondant à l'état de la particule dans les quatre di-

1. Correspondant à la quantité de mouvement nécessaire dans le plan transverse afin d'y obtenir un bilan total nul.

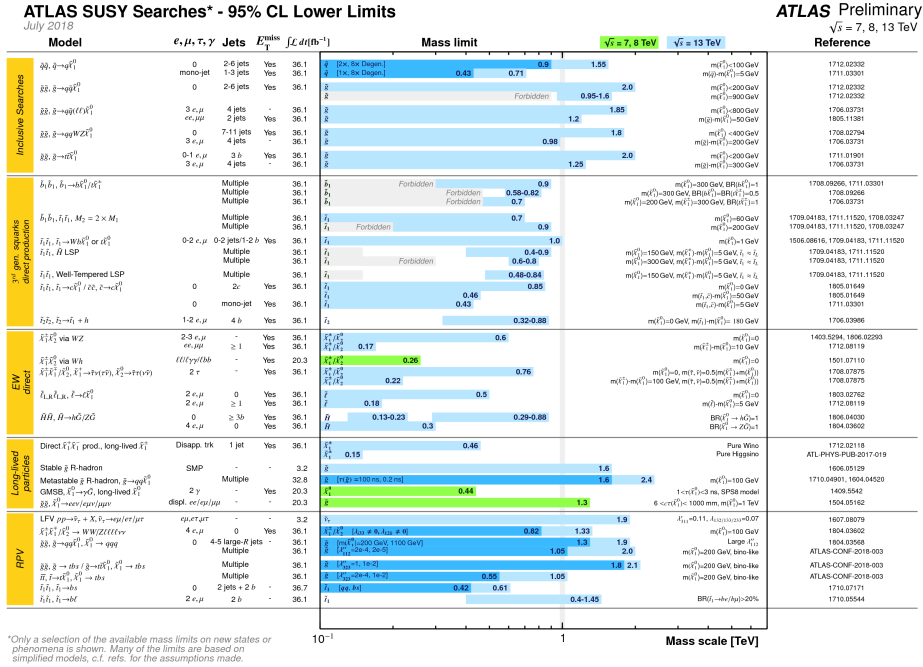


FIGURE 2: Résultats des recherches de supersymétrie par la collaboration ATLAS de 2010 à 2018 dans le contexte de différents modèles effectifs simplifiés.

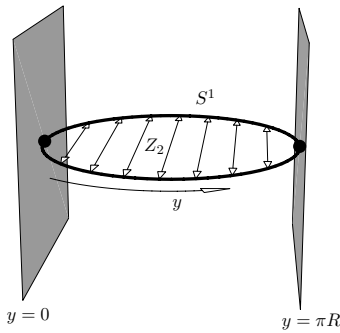


FIGURE 3: Schéma de la compactification utilisée pour la dimension d'espace supplémentaire dans le cadre des modèles de Randall-Sundrum (orbifold  $S^1/Z_2$ ), ainsi que les deux branes [13].

mensions d'espace temps, donc, celui du Modèle Standard. Au LHC, du fait de l'environnement hadronique, la production d'excitations du gluon, appelées gluons de Kaluza-Klein est fortement favorisée.

## 4 Quarks de type vecteurs

Les quarks de type vecteurs (ou VLQ d'après l'anglais *vector-like quarks*) [11] sont prédits par beaucoup de théories (extra-dimensions, boson de Higgs composite, grande unification, ...) et, à ce titre, sont activement recherchés au LHC. Comme leur nom l'indique, ils possèdent à la fois des courants gauche et droit. Le terme de couplage faible s'écrit donc  $\bar{u}\gamma^\mu dW^+$  au lieu de  $\bar{u}\gamma^\mu(1-\gamma^5)dW^+$  pour les quarks du MS. Il est important de noter que leurs termes de masse sont alors invariants sans l'aide d'un mécanisme de Brout-Englert-

Higgs.

Les VLQ peuvent avoir différentes représentations de  $SU(2)$  :

- singlets :  $t', b'$  ;
- doublets :  $\begin{pmatrix} X \\ t' \end{pmatrix}, \begin{pmatrix} t' \\ b' \end{pmatrix}, \begin{pmatrix} b' \\ Y' \end{pmatrix}$  ;
- triplets :  $\begin{pmatrix} X \\ t' \\ b' \end{pmatrix}, \begin{pmatrix} t' \\ b' \\ Y \end{pmatrix}$ .

Ainsi si l'on prend l'exemple de la particule  $t'$ , elle devra être recherchée en considérant plusieurs chaînes de désintégration possibles :  $t' \rightarrow Zu_i, t' \rightarrow Hu_i, t' \rightarrow W^+d_i$  et  $t' \rightarrow W^-X$ . À la manière des recherches de supersymétrie, il faut combiner plusieurs analyses pour être à même d'exclure l'ensemble de l'espace des paramètres [12].

## 5 Conclusion

Au cours de ce bref document, différentes solutions aux lacunes du Modèle Standard ont été présentées, mais il ne s'agit que d'une sélection limitée. Une revue plus approfondie est présentée dans la référence [13]. À l'heure actuelle, les expériences du LHC n'ont pas mis en évidence de Physique au-delà du Modèle Standard, mais de nombreux modèles et signatures expérimentales n'ont pas encore été couvertes : la Nouvelle Physique pourrait être observée dans les années à venir.

## References

[1] G. Arnison et al., Physics Letters B (1983) 122, Publication

- [2] G. Arnison et *al.*, Physics Letters B (1983) 126, **Publication**
- [3] CMS Collaboration, CMS Standard Model group results, **Website**
- [4] ATLAS Collaboration, ATLAS Standard Model group results, **Website**
- [5] Martin, Stephen P., *A Supersymmetry primer*, **arXiv:hep-ph/9709356**
- [6] Beringer, J. and others, *Review of Particle Physics (RPP)*, Phys. Rev. D (2012) 86, **Publication**
- [7] Gabbiani, F. and Gabrielli, E. and Masiero, A. and Silvestrini, L., *A Complete analysis of FCNC and CP constraints in general SUSY extensions of the standard model*, Nucl. Phys. B (1996) 477, **arXiv:hep-ph/9604387**
- [8] Kaluza, T., *On the Problem of Unity in Physics*, Sitzungsber.Preuss.Akad.Wiss.Berlin (Math.Phys.), 1921
- [9] Klein, O., *Quantum Theory and Five-Dimensional Theory of Relativity.*, Z.Phys., 1926, **Publication**
- [10] Randall, L. and Sundrum, R., *A Large mass hierarchy from a small extra dimension*, Phys. Rev. Letter (1999) 83, **arXiv:hep-ph/9905221**
- [11] J. A. Aguilar-Saavedra, R. Benbrik, S. Heinemeyer, M. Pérez-Victoria, *A handbook of vector-like quarks : mixing and single production*, Phys. Rev. D (2013) 88, **arXiv:hep-ph/1306.0572**
- [12] ATLAS Collaboration, ATLAS Vector-like quarks searches summary, **Website**
- [13] Pomarol, A., *Beyond the Standard Model*, **arXiv:hep-ph/1202.1391**



# Recherche d'un second boson de Higgs de basse masse ( $m_{\gamma\gamma} < 110$ GeV) se désintégrant en deux photons avec l'expérience CMS



Camille Camen

Institut de Physique Nucléaire de Lyon

## 1 Introduction

Le Modèle Standard (MS), qui décrit les constituants élémentaires de la matière ainsi que trois forces fondamentales, est une théorie qui a fait ses preuves notamment avec la découverte en 2012 au LHC (Large Hadron Collider) du boson de Higgs, particule centrale de la théorie. Prédit en 1964 par trois équipes de théoriciens (Higgs-Englert, Brout-Hagen et Guralnik-Kibble), le boson de Higgs a été imaginé pour répondre à la problématique suivante : comment donner une masse aux bosons vecteurs de l'interaction faible Z et W (l'interaction faible ayant une portée finie) sans briser l'invariance de jauge du MS. Avec l'ajout d'un doublet de champ scalaire complexe dans le MS et à travers le mécanisme de brisure spontanée de la symétrie électrofaible, des termes de masse sont générés pour les bosons Z et W, ainsi que pour les fermions via les couplages de Yukawa, et une nouvelle particule est prédite : le boson de Higgs. Néanmoins le MS reste une théorie incomplète puisque plusieurs zones d'ombre, comme la gravitation ou les masses non-nulles des neutrinos, sont encore présentes. Pour remédier aux divers problèmes du MS, des théories dites "au delà du MS" ont été imaginées, certaines prédisant des bosons de Higgs supplémentaires.

C'est dans le cadre de ces modèles que s'effectue la recherche d'un boson de Higgs supplémentaire à basse masse ( $< 110$  GeV) se désintégrant en deux photons. Le canal diphoton ( $\gamma\gamma$ ) a l'avantage d'être une signature claire au sein d'un collisionneur hadronique, et possède une section efficace non négligeable par rapport au canal  $ZZ$ , ainsi qu'une bonne résolution en masse invariante.

Je commencerai donc par présenter rapidement le contexte théorique, à savoir les modèles à deux doublets de Higgs (*Two Higgs Doublet Models : 2HDM*), puis je présenterai les motivations et les différentes étapes de l'analyse  $H \rightarrow \gamma\gamma$  à basse masse ainsi que les résultats.

## 2 Contexte théorique

### 2.1 Modèle à deux doublets de Higgs

Ces modèles reposent sur une extension simple du secteur scalaire du MS : un doublet de champ scalaire complexe est ajouté afin d'obtenir deux doublets scalaires  $SU(2)$   $\Phi_1$  et  $\Phi_2$ . Afin d'éviter les changements de saveur par courant neutre, les fermions d'une charge électrique donnée ne peuvent se coupler qu'à un seul des deux doublets, ce qui conduit à quatre types de

modèles, avec leur phénoménologie spécifique, comme illustré sur la Figure 1.

	Type I	Type II	Flipped (Type Y)	Lepton Specific (Type X)
Up-type quark	$\phi_2$	$\phi_2$	$\phi_2$	$\phi_2$
Down-type quark	$\phi_2$	$\phi_1$	$\phi_1$	$\phi_2$
Leptons	$\phi_2$	$\phi_1$	$\phi_2$	$\phi_1$

FIGURE 1: Table illustrant les différents couplages entre les fermions SM et les deux doublets scalaires  $\Phi_1$  et  $\Phi_2$  [2].

Dans le cadre des modèles 2HDM, la brisure de symétrie conduit à cinq états physiques : deux particules chargées  $H^\pm$  et trois particules neutres  $h$ ,  $H$  (CP pair) et  $A$  (CP impair). Ces modèles présentent en outre différentes hiérarchies de masse possibles. Dans le cadre de cette analyse, le quatrième cas illustré sur la Figure 2 est utilisé :  $h$  est identifié à la résonance légère de masse inférieure à 125 GeV recherchée, tandis que  $H$  est assimilé au boson de Higgs de masse 125 GeV découvert au LHC en 2012.

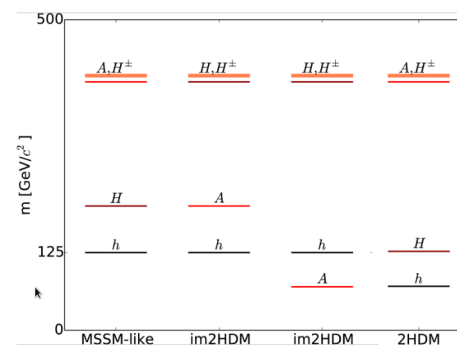


FIGURE 2: Exemple de différentes hiérarchies de masse possibles pour les 2HDM.

## 3 Motivations

### 3.1 Motivation historique

La première motivation est historique et provient des résultats combinés du LEP (DELPHI, L3, OPAL, et ALEPH) qui ont mis en évidence un léger excès d'événements à  $2.2 \sigma$  ( $\sigma$  représentant la déviation standard) pour une masse de 98 GeV environ pour le mode de production  $e^+e^- \rightarrow ZH$  dans les canaux  $b\bar{b}$  et  $\tau\bar{\tau}$ , comme

illustré sur la Figure 4 qui montre la probabilité que les données soient compatibles avec l'hypothèse bruit de fond seul ( $p$ -value).

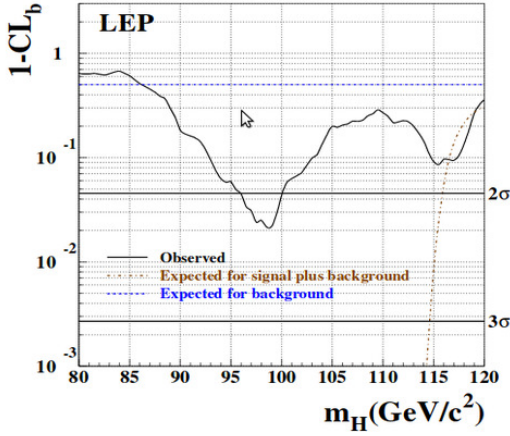


FIGURE 3:  $p$ -value en fonction de la masse hypothétique du boson de Higgs [1]

### 3.2 Faisabilité au LHC

La deuxième motivation concerne la force du signal. La Figure 5 illustre le produit de la section efficace et du taux de branchement  $h \rightarrow \gamma\gamma$  en fonction de  $\sin(\beta - \alpha)$  qui est l'un des huit paramètres des modèles 2HDM.<sup>1</sup>

Les points rouges sont les prédictions du modèle (lorsqu'on explore l'espace de phase des paramètres du 2HDM) passant toutes les contraintes théoriques et expérimentales (provenant du LEP et du Run 1 du LHC). La ligne en pointillés correspond à la sensibilité typique du LHC attendue pour une analyse de recherche  $h \rightarrow \gamma\gamma$ . On observe un certain nombre de prédictions au dessus de cette ligne, jusqu'à 100 fb, ce qui indique que les données du LHC peuvent être sensibles à des bosons additionnels, correspondant à des combinaisons des paramètres des 2HDM pour le modèle de type I. À l'inverse, pour les modèles de type II, les sections efficaces prédites sont trop faibles et invisibles pour le LHC.

### 3.3 Résultats de la recherche au Run 1 (8 TeV) du LHC

Les résultats du run 1 du LHC à une énergie de centre de masse de 8 TeV en 2012 constituent une motivation supplémentaire.

La Figure 5 présente les limites d'exclusion à 95% de degré de confiance (CL) observée et attendue sur le produit de la section efficace de production d'un second boson de Higgs par son taux de branchement en deux photons, pour des hypothèses de masse allant de 80 à

1.  $\beta$  est l'angle de rotation des doublets dans la base où un seul des deux acquiert une v.e.v. (*vacuum expectation value*) et  $\alpha$  est l'angle de mélange des états de CP pairs générant les états propres de masse.

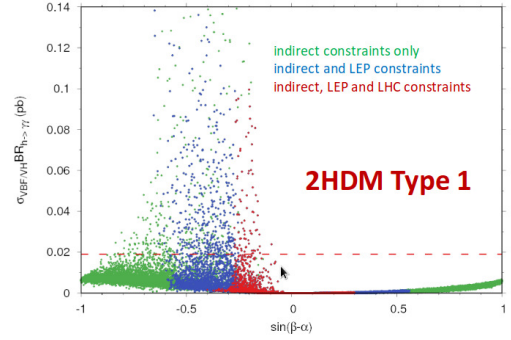


FIGURE 4: Produit de la section efficace et du taux de branchement  $h \rightarrow \gamma\gamma$  pour les modèles de type I [2] en fonction de  $\sin(\beta - \alpha)$ .

110 GeV. Les bandes jaune et verte représentent respectivement les incertitudes à  $\pm 1\sigma$  et  $\pm 2\sigma$  associées à la limite d'exclusion attendue. Les limites d'exclusion attendue (pointillée) et observée (pleine) sont compatibles, sauf autour de 97 GeV où une déviation d'environ  $2\sigma$  est observée.

Le pic à une masse de 90 GeV est dû à la désintégration du boson Z en deux leptons. Ces derniers peuvent être identifiés à tort comme des photons et constituent ainsi un bruit de fond notable.

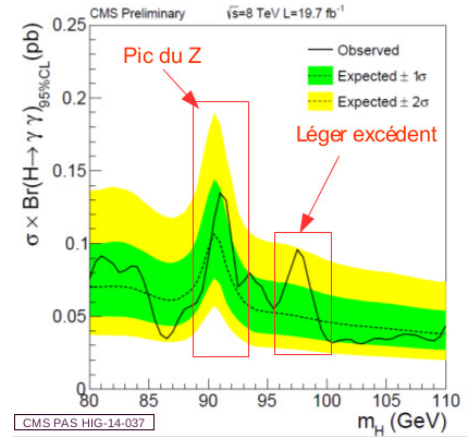


FIGURE 5: Limite supérieure à 95% CL sur la section efficace de production du boson de Higgs pour différentes hypothèses de masse [3].

## 4 Bruits de fond de l'analyse

Pour observer un signal dans le spectre de masse invariante diphoton, il faut pouvoir l'extraire du bruit de fond, et par conséquent bien identifier ce dernier. La source principale du bruit de fond est appelée "continuum diphoton". Il est formé de deux composantes : une composante **réductible** correspondant aux événements jet+jet ou jet+ $\gamma$  dans lesquels les jets contiennent des pions neutres se désintégrant en deux photons très énergétiques, et pouvant être reconstruits à tort comme un

photon prompt. Il existe également une composante **ir-réductible** constituée des processus de physique standard ayant pour état final deux photons prompts. Une deuxième source de bruit provient de la désintégration du boson  $Z$  en deux électrons (Section 2).

## 5 Stratégie d'analyse

L'analyse de recherche  $h \rightarrow \gamma\gamma$  est une succession complexe d'étapes dont le but est de rejeter au mieux les bruits de fond. La première étape consiste à passer les systèmes de déclenchement de l'analyse, qui sélectionnent des paires de photons satisfaisant différents critères : sélections en masse invariante, impulsion transverse, isolation et variables de forme de gerbe. Un critère de veto permet également de rejeter les photons pour lesquels on trouve un coup dans le détecteur à pixel (les conversions se produisent principalement après le détecteur à pixels.)

### 5.1 Reconstruction des événements

Le nombre d'événements de bruit de fond étant très grand devant le nombre d'événements de signal, il faut une excellente résolution en masse invariante pour pouvoir observer un pic de signal fin et de grande amplitude. La masse invariante de deux photons est donnée par :

$$m_{\gamma\gamma} = \sqrt{2E_1 E_2 (1 - \cos \theta)} \quad (1)$$

où  $E_{1,2}$  est l'énergie des deux photons et  $\theta$  l'angle entre les deux photons. Une bonne résolution sur la masse repose donc sur une bonne résolution en énergie des photons et une bonne résolution angulaire donnée par la position du vertex. L'énergie des photons est mesurée en regroupant les dépôts d'énergie au sein des cristaux du calorimètre électromagnétique, puis corrigée via une méthode de régression. La méthode du "vertex ID", arbre de décision boosté (BDT), est utilisée pour déterminer si le vertex d'interaction est correctement apparié à l'événement. Plus précisément, on considère que l'appariement est correct si le vertex considéré est à moins de 1 cm du vertex réel d'interaction. Enfin, un second BDT est utilisé afin d'estimer la probabilité que l'appariement du vertex soit correct.

### 5.2 Identification des photons

Après l'application de sélections plus strictes qu'au niveau du système de déclenchement, un nouveau BDT ("Photon ID") est utilisé pour discriminer les "faux" photons provenant de la désintégration des mésons au sein des jets et les photons prompts (issus de la désintégration d'un boson de Higgs). Cet algorithme se base sur les variables d'isolation, et de forme de gerbe pour trier les photons, en attribuant une note d'autant plus élevée que les photons se comportent comme du signal (Figure 6).

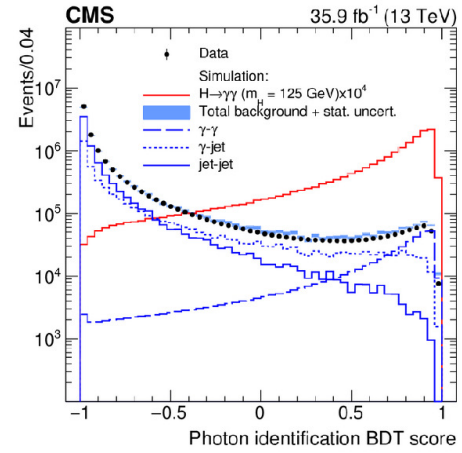


FIGURE 6: Distribution de la variable de sortie du BDT "Photon ID". À gauche les photons "bruit de fond" et à droite les photons "signal" [5].

### 5.3 Sélection et catégorisation des événements diphotons

Cette étape permet de discriminer les paires diphoton provenant du boson de Higgs, du bruit irréductible. Le "BDT diphoton" permet cela en classant les événements diphotons selon leur compatibilité avec le signal, en se basant sur les profils de différentes variables : la résolution en masse invariante par événement, les variables cinématiques, mais aussi la variable de sortie du Photon ID (Section 5.2). La Figure 7 présente la distribution de la note du BDT diphoton : les notes récoltées par le signal (en rouge) sont plus élevées que celles récoltées par le bruit de fond (en bleu). D'autre part, cette distribution est utilisée pour catégoriser les événements diphotons afin d'optimiser la sensibilité de l'analyse. Ainsi, la distribution est utilisée pour définir des catégories avec différents rapports signal/bruit. Le nombre et la définition exacte de ces catégories sont optimisés, et la catégorie avec le moins bon rapport signal/bruit est rejetée.

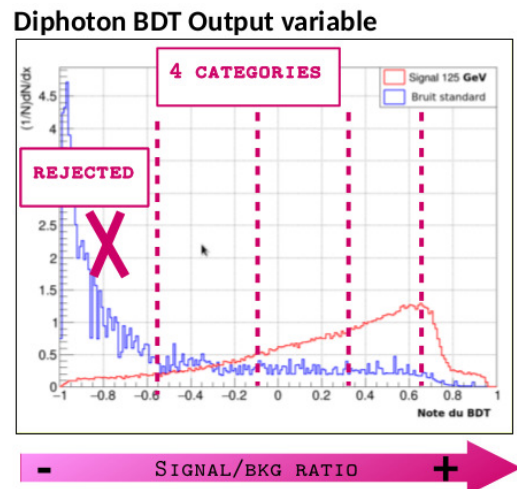


FIGURE 7: Distribution de la variable de sortie du BDT diphoton.

## 5.4 Modélisation du signal et du bruit de fond

Le modèle paramétrique du signal est extrait de la simulation d'échantillons  $H \rightarrow \gamma\gamma$  standards pour différentes masses du boson de Higgs. Le modèle de bruit de fond est extrait de la simulation avec des échantillons  $Z \rightarrow e^+e^-$  pour la composante Drell-Yan et des données pour le continuum diphoton.

## 6 Résultats

Finalement le signal est extrait du bruit de fond en ajustant la distribution en masse diphoton observée dans chaque catégorie d'analyse (Section 5.3). On procède à un ajustement du modèle signal + bruit de fond sur les données et on soustrait la composante de bruit de fond des données. La Figure 9 montre un léger excès à une masse de 95.3 GeV pour les données 2016 du LHC avec une énergie dans le référentiel du centre de masse de 13 TeV et une luminosité de  $35.9 \text{ fb}^{-1}$ .

La Figure 10(haut) présente les limites d'exclusion observée et attendue à 95% de niveau de confiance sur le produit de la section efficace de production d'un second boson de Higgs par son taux de branchement en deux photons, en fonction de sa masse. Les bandes jaune et verte représentent les incertitudes à  $\pm 1\sigma$  et  $\pm 2\sigma$  associées à la limite d'exclusion attendue. La limite observée est compatible avec la limite attendue, sauf à une masse de 95.3 GeV où une légère déviation est observée.

La Figure 10(bas) présente les  $p$ -values locales observée et attendue en fonction de la masse d'un second boson de Higgs pour les analyses de données à 8 TeV (run 1), 13 TeV (run 2), et leur combinaison. À 8 TeV un excès local d'environ  $2\sigma$  est observé pour une hypothèse de masse de 97.6 GeV. À 13 TeV un excès local est observé à  $2.9\sigma$  pour une hypothèse de masse de 95.3 GeV. Pour la combinaison 8 + 13 TeV, la signification locale est évaluée à  $2.8\sigma$ , soit une valeur globale de  $1.3\sigma$  pour une masse de 95.3 GeV.

## 7 Conclusion

La recherche d'une nouvelle résonance à basse masse se désintégrant en deux photons est basée sur des données collectées au LHC et représentant une luminosité intégrée de  $19.7 \text{ fb}^{-1}$  (8 TeV, 2012) et  $35.9 \text{ fb}^{-1}$  (13 TeV 2016). De nouvelles données collectées en 2017 vont permettre d'augmenter la statistique et la sensibilité de cette analyse pour contraindre les modèles et confirmer ou non le léger excès observé jusqu'à présent.

## Références

- [1] The LEP Collaboration, "Search for the Standard Model Higgs boson at LEP", Physics Letters B 565 61 à 75, 2003
- [2] Giacomo Cacciapaglia, Aldo Deandrea, Suzanne Gascon-Shotkin, Solène Le Corre, Morgan Le-

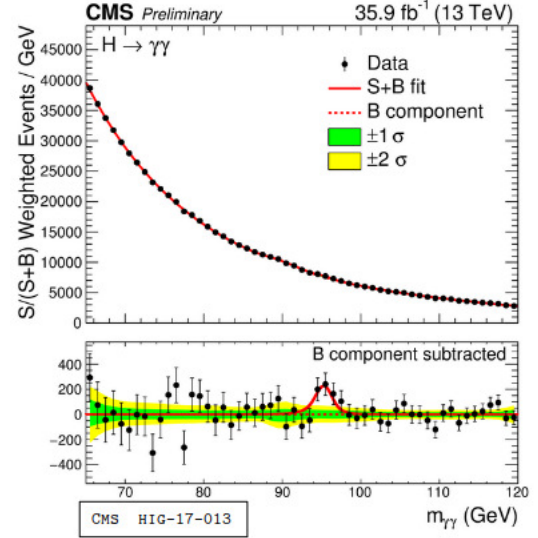


FIGURE 8: Distribution de la masse invariante diphoton pondérée pour chaque catégorie.[4]

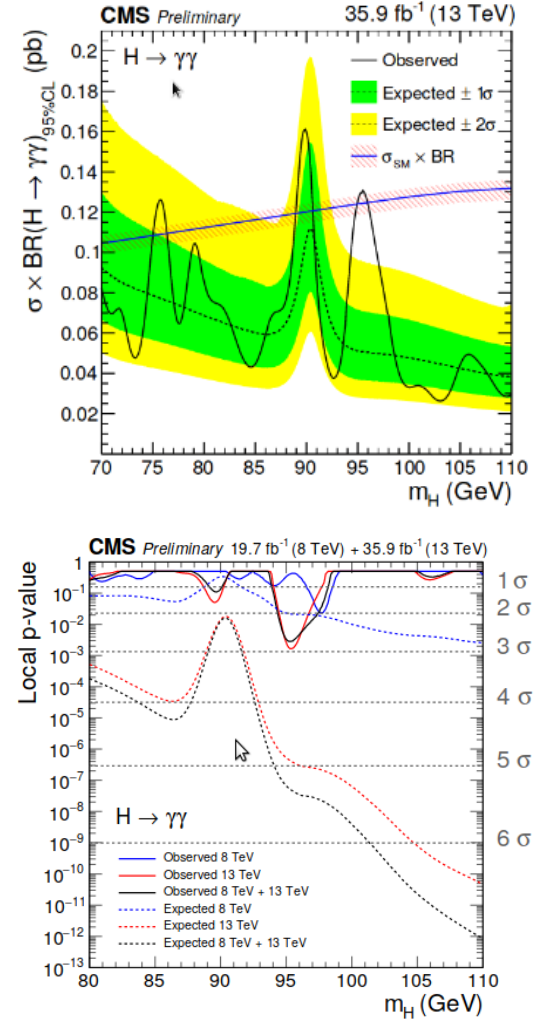


FIGURE 9: (Haut) Limite supérieure sur le produit de la section efficace du boson de Higgs et du taux de branchement et (Bas)  $p$ -values locales pour différentes hypothèses de masse [4]. Les  $p$ -values sont présentées pour les analyses à 8 et 13 TeV et leur combinaison.

thuilier, Junquan Tao, "Search for a lighter Higgs boson in Two Higgs Doublet Models", JHEP 1612 068, 2016

- [3] CMS Collaboration, "Search for new resonances in the diphoton final state in the mass range between 80 and 110 GeV in pp collisions at  $\sqrt{s}=8$  TeV", CMS PAS HIG-14-037, 2015
- [4] CMS Collaboration, "Search for new resonances in the diphoton final state in the mass range between 80 and 110 GeV in pp collisions at  $\sqrt{s}=8$  TeV", CMS HIG-17-013, arXiv :1811.08459, 2018
- [5] CMS Collaboration, Measurements of properties of the Higgs boson in the diphoton decay channel with the full 2016 data set, CMS-HIG-16-040, arXiv :1804.02716, 2017



# Search for new resonances in diphoton events with the ATLAS detector

Yufeng Wang

*Laboratoire de Physique Nucléaire et des Hautes Energies – Paris*



## Résumé

A search for new resonances decaying into two photons is performed, using  $80 \text{ fb}^{-1}$  of proton-proton ( $pp$ ) collision data at  $\sqrt{s} = 13 \text{ TeV}$  collected by the ATLAS detector in 2015, 2016 and 2017. Pairs of isolated photon candidates with invariant mass between 65 to 110 GeV are selected. No significant excess with respect to the Standard Model expectation is found and limits at 95% confidence level (CL) are set on narrow resonance fiducial cross-section times branching ratio, ranging from 30 to 101 fb depending on the diphoton invariant mass.

## 1 Theoretical context

Currently, as our best description of elementary particles and their interactions, the Standard Model is incomplete. Two-Higgs-doublet model (2HDM) is the simplest possible extension of the Standard Model with an enriched scalar sector. Introducing a second doublet of scalar fields in the Lagrangian results in five physical scalar (Higgs) fields after symmetry breaking : two CP-even bosons  $h$  and  $H$  with  $m_h < m_H$ , one CP-odd boson  $A$ , two charged bosons  $H^+$  and  $H^-$ . Considering  $H$  or  $h$  as the 125 GeV Higgs boson discovered in 2012, a new low-mass (or high-mass) resonance can be searched for. This is the motivation of the analysis.

The diphoton decay channel is chosen for this search in the low-mass region between 65 and 110 GeV. The branching ratio of  $\gamma\gamma$  final state is not large but the channel provides a clean experimental signature with an excellent mass resolution and a smoothly falling background.

## 2 Experiment

The Large Hadron Collider (LHC) is the world's largest and most powerful particle collider. It is located 100 meters underground beneath the France-Switzerland border near Geneva. The LHC is designed to provide  $pp$  collisions at a centre-of-mass energy of 14 TeV with peak luminosity of  $10^{34} \text{ cm}^{-2} \text{ s}^{-1}$ . Seven experiments use detectors to analyse the myriad of particles produced by collisions in the accelerator. A Toroidal LHC Apparatus (ATLAS) and Compact Muon Solenoid (CMS) are two general-purpose detectors, aiming to investigate the largest possible range of physics.

The ATLAS detector is composed of three sub-detectors : the Inner Detector (ID), the calorimeters and the Muon Spectrometer (MS). The basic function of the ID is to track the charged particles and to obtain detailed information about their type and momentum. The electromagnetic (EM) and hadronic calorimeters are designed to measure the energy of the particles. Electrons, positrons and photons deposit most of their energy through three layers of the EM calorimeter by developing electromagnetic showers. The EM calorimeter and the ID are the most relevant detectors for the reconstruction of photon candidates.

### 2.1 Photon reconstruction

Photons are reconstructed through their interaction with the material of the ATLAS detector. A photon candidate deposits its energy in a cluster of calorimeter cells. The cluster might be matched with tracks if the photon interacts with the material upstream of the calorimeter, and converts into electron pairs. In that case, the track (tracks) is (are) reconstructed with the ID, originating from a conversion vertex. Electromagnetic clusters (EM clusters) matched to tracks from a conversion vertex are reconstructed as converted photons, while clusters without matching tracks are unconverted photons.

### 2.2 Photon energy calibration

The energy of photon candidates is corrected by a dedicated energy calibration. The MC-based calibration is applied to calibrate the cluster energy to the original energy. Then the absolute energy scale is obtained by a data-driven method using  $Z \rightarrow ee$  events, correcting for data/MC difference. The calibration is done for electrons. Photons share the same parameters with additional photon-specific uncertainties applied.

### 2.3 Photon identification

After reconstruction, the photon candidates include a significant number of background candidates (i.e. fake photons) from jets. Most of the fake photons come from neutral particles ( $\pi^0$ ) decaying into photon pairs. Figures 1 and 2 show two event displays for a prompt and a fake photon candidate respectively. Compared to a fake photon, the prompt photon has narrower shower in the EM calorimeter, and less energy leakage in the hadron calorimeter.

In order to reject background candidates, a group of discriminating variables are used to distinguish photons from fakes. The leakage in the hadronic calorimeter and the cluster shape in the second layer of EM calorimeter are used for a set of loose-photon identification requirement, while variables defined from the cluster shape in the first layer are added for a tighter requirement.

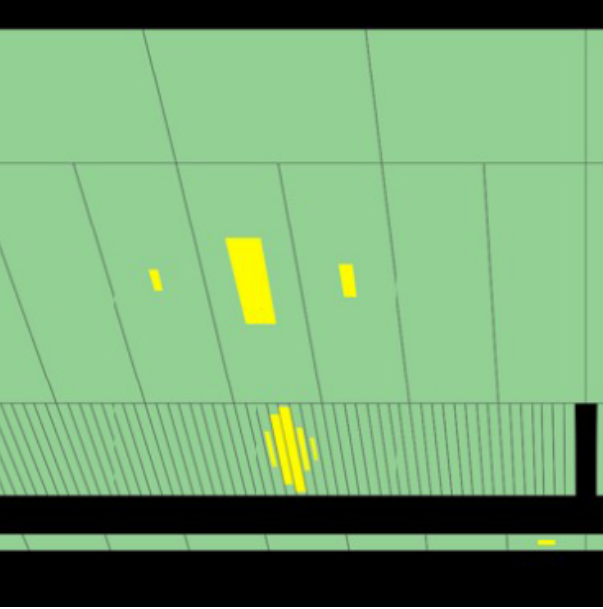


FIGURE 1: Event display of a prompt photon candidate in the calorimeter.

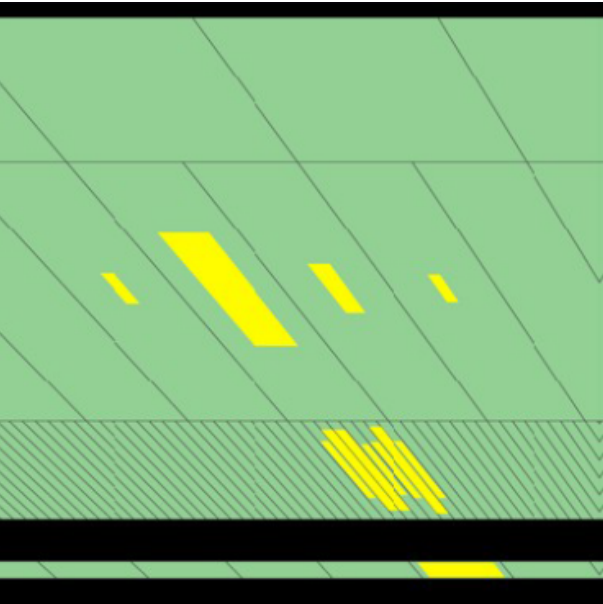


FIGURE 2: Event display of a fake photon candidate in the calorimeter.

## 2.4 Photon isolation

Compared with fake photons like jets with a large electromagnetic component, photons from hard pro-

cess (e.g. from resonance decays) are expected to be well isolated from hadronic activity. Requirements are applied on both track- and calorimeter-based isolation variables. The track-based variable is the scalar sum of transverse momenta of tracks in a cone around photon candidates. Only the tracks originating from the diphoton production vertex are used, and the tracks associated to converted photon candidates are excluded. The calorimeter-based variable is the sum of the transverse energy of clusters in a cone around photon candidates, while the contribution of the candidates themselves is subtracted, and the leakage of energy and effects of underlying event and pile-up are corrected for.

## 3 Analysis

This search is performed with data recorded at  $\sqrt{s} = 13$  TeV in 2015, 2016 and 2017, corresponding to a total integrated luminosity of  $80.4 \text{ fb}^{-1}$ . Results of a previous low-mass diphoton search performed during LHC Run-1 were obtained by ATLAS with  $20.3 \text{ fb}^{-1}$  data collected at 8 TeV. In a similar search, a small excess near 95 GeV with a local (global) significance of  $2.8\sigma$  ( $1.3\sigma$ ) was observed by CMS, combining data collected at 8 TeV and 13 TeV.

With signal and background models described by analytical functions, the search is performed by fitting the invariant mass of two photons in the range between 60 to 120 GeV, in order to set a limit in the 65-110 GeV range.

### 3.1 Event selection

In order to have a smoothly falling non-resonant background, one should consider the “turn-on” effect on the invariant mass distribution of the photon pairs introduced by the selection criteria applied on the photon transverse energy ( $E_T$ ). The trigger selection used for this analysis is defined by requiring two photon candidates with  $E_T > 20$  GeV. This set the peak of the turn-on below 60 GeV.

As for the kinematic selection, the photon candidates are required to fall within the pseudorapidity interval  $|\eta| < 2.37$ , excluding the transition region  $1.37 < |\eta| < 1.52$  between the barrel and end-cap region of calorimeters. After energy calibration, the two candidates with the highest transverse energies (i.e. the leading and sub-leading photons) are required to have  $E_T > 22$  GeV. A tight photon ID requirement is applied, as well as the isolation requirements applied on both the track- and calorimeter-based variables. Only events with invariant mass of photon pairs in the range between 60 to 120 GeV are considered.

In the search range [65, 110] GeV, the so-called Drell-Yan contribution has to be taken into account in the modelling of background. It comes from  $Z \rightarrow ee$  events with both electrons misidentified as photons, and forms a peak around the mass of  $Z$  boson. Events are split into three categories depending on how the two photon candidates are reconstructed, since the Drell-Yan con-

mination is more prominent when photons are identified as converted. Three categories are considered : two converted photons (CC), two unconverted photons (UU), one converted and one unconverted photon (UC). Roughly, number of events in the CC category takes up to 8-9% of the total.

### 3.2 Signal modelling

Two assumptions are made for this generic search while modelling the signal : new resonances are produced via gluon fusion, and are assumed to have a narrow decay width, which means that the shape of signal is dominated by the mass resolution of the detector. The signal is modelled by a Double-Sided Crystal Ball (DSCB) function, consisting of a Gaussian core and two power-law tails. Six parameters are extracted by fitting the invariant mass distributions in Monte Carlo samples, generated for a series of resonance mass hypotheses  $m_X$ . These parameters are then parameterised in each conversion category as a function of  $m_X$ . One example at  $m_X = 80$  GeV is shown in Figure 3. Good agreement is found between the signal model and the simulated invariant mass distribution of photon pairs.

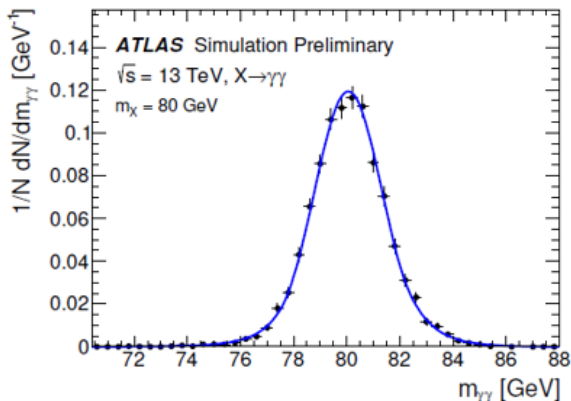


FIGURE 3: Simulated diphoton invariant mass distribution of a narrow-width signal particle  $X$  of mass 80 GeV (black markers) in the UU category, overlaid with the DSCB function resulting from the signal modelling (solid line).

### 3.3 Background modelling

The background shape is estimated separately in each conversion category. There are two main background components : the non-resonant continuum and the resonant Drell-Yan contribution. The non-resonant background comes from the QCD production of real photon pairs (“irreducible”), and photon-jet pairs or jet-jet pairs (“reducible”). The resonant background comes from Drell-Yan process when two electrons are misidentified as two photons. The Standard Model Higgs contamination is checked and proved to be negligible.

For the non-resonant background, a background template is build using simulated samples for the irredu-

cible component and a dedicated data-driven control region for the reducible photon-jet (jet-photon) component, while jet-jet component is neglected. The two components are then added together according to their respective fraction measured in data. The Drell-Yan background is estimated using a fit to the dielectron data sample. A Smirnov transformation derived from simulation is then used to correct the dielectron template, since the electrons faking photons tend to loose energy due to bremsstrahlung. The normalisation of the final resonant template is obtained from electron faking photon rates in data.

After the background template of each component is built, a set of analytical functions is used to describe the diphoton invariant mass spectrum shape. In order to check the quality of background modelling and to quantify the systematic uncertainties, the maximal “spurious signal” (in the range between 65 to 110 GeV) is extracted by a signal-plus-background fit to a background-only template. The analytical function with the smallest spurious signal value is chosen. For continuum background, the sum of a Landau distribution with an exponential function is selected for the UU and UC categories, while a fifth-order Bernstein polynomial function is selected for the CC category. The Drell-Yan background is described by a DSCB function. Figure 4 shows a background-only fit of data for the three conversion categories. Good agreement is found, and the Drell-Yan contribution is most prominent in the CC category as expected. No special structure can be seen in the residuals.

## 4 Results

The dominant systematic uncertainties comes from spurious signal, corresponding to the systematic uncertainty on the continuum background modelling. The results of the p-value scan is shown in Figure 5 and no significant excess with respect to the background-only hypothesis is observed. 95% CL upper limits are set on  $\sigma_{fid} \cdot B$  from 30 to 101 fb as a function of  $m_{\gamma\gamma}$ , as shown in Figure 6.

## 5 Conclusion and futher plan

No significant excesses above  $1\sigma$  are found in the search for a new resonance below the Higgs boson mass in the diphoton channel. However, the excess observed by the CMS group is not excluded by the current ATLAS search.

The analysis using the full 2015-2018 dataset and full mass range has started. It will be performed as well in the intermediate mass range [110, 200] GeV, the high-mass range above 200 GeV, and the very low mass range below 65 GeV. In addition, optimisations to reduce the systematics and to improve the background templates will be applied.

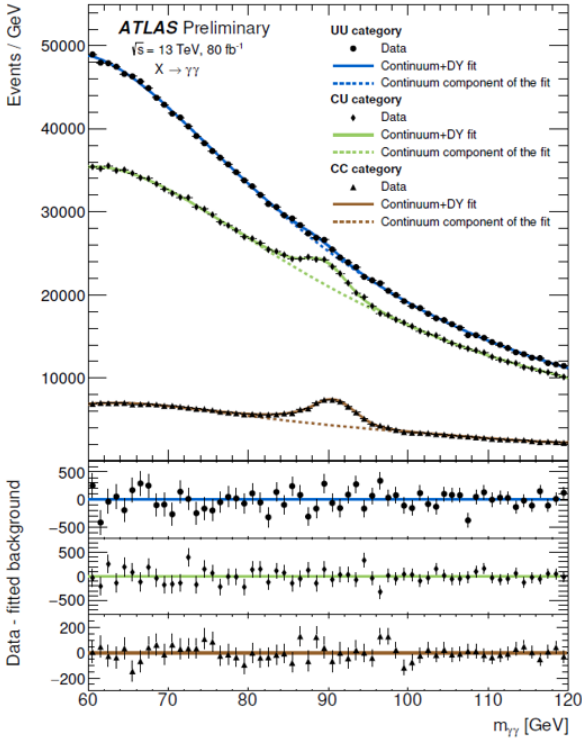


FIGURE 4: Background-only fit to the data (black markers) as a function of  $m_{\gamma\gamma}$  for three conversion categories. The solid lines show the sum of the Drell-Yan and the continuum background components, and the dashed lines show only the continuum components. Difference between the data and the total background component is shown in the lower pad separately for each category.

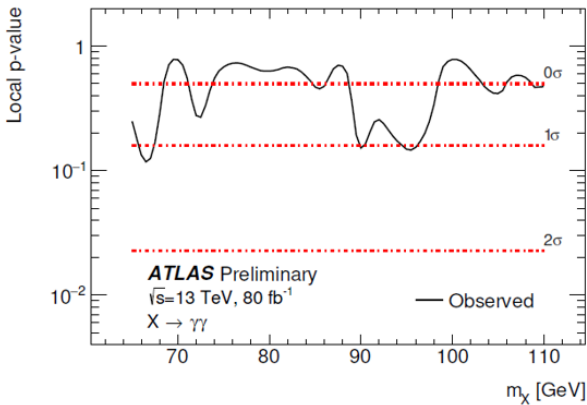


FIGURE 5: The compatibility, in terms of local p-value (solid line), with the background-only hypothesis as a function of the assumed signal mass  $m_X$ . The dotted-dashed line correspond to the standard deviation quantification  $\sigma$ .

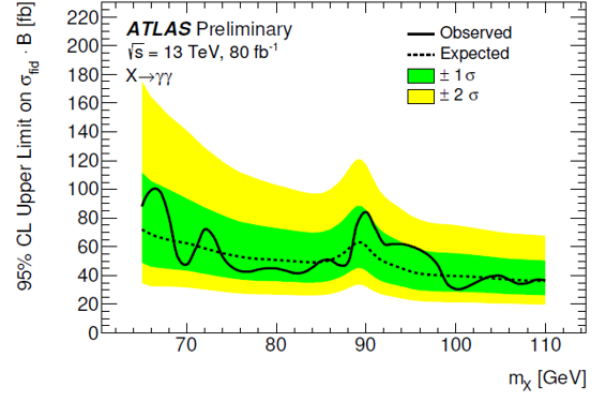


FIGURE 6: The upper limit on the fiducial cross-section times branching ratio ( $X \rightarrow \gamma\gamma$ ) as a function of  $m_X$ , where the solid (dashed) line corresponds to the observed (expected) limit, and the green (yellow) band corresponds to one (two) standard deviation from the expectation.

## Références

- [1] ATLAS Collaboration, Search for resonances in the 65 to 110 GeV diphoton invariant mass range using  $80 \text{ fb}^{-1}$  of pp collisions collected at  $\sqrt{s} = 13 \text{ TeV}$  with the ATLAS detector, ATLAS CONF Note, 2018
- [2] ATLAS Collaboration, Search for new phenomena in high-mass diphoton final states using  $37 \text{ fb}^{-1}$  of proton-proton collisions collected at  $\sqrt{s} = 13 \text{ TeV}$  with the ATLAS detector, Phys. Lett. B 775 (2017) 105
- [3] ATLAS Collaboration, Electron and photon energy calibration with the ATLAS detector using LHC Run 1 data, Eur. Phys. J. C 74 (2014) 3071
- [4] G. Cowan, K. Cranmer, E. Gross, and O. Vitells, Asymptotic formulae for likelihood-based tests of new physics, Eur. Phys. J. C71 (2011) 1554, [Erratum : Eur. Phys. J.C73,2501(2013)]
- [5] A. L. Read, Presentation of search results : The CL(s) technique, J. Phys. G28 (2002) 2693, [11(2002)]

Deuxième partie

# Hadronic Physics

session dirigée par Laure MASSACRIER



# Introduction to hadronic physics

Laure Massacrier

IPNO, Univ. Paris-Sud, CNRS/IN2P3,  
Université Paris-Saclay, Orsay, France



## Résumé

The hadronic physics field is devoted to the understanding of the strong interaction between quarks and gluons, which is governed by the theory of Quantum Chromodynamics. The hadronic physics session was composed of two student presentations covering experimental and theoretical aspects of the field. In this proceeding, we give a few key elements of introduction to hadronic physics to put those presentations into context. I will introduce several concepts related to the nucleon structure, the quark gluon plasma formation and cold nuclear matter effects.

## 1 Introduction

Hadronic physics studies the structure, the properties and the interactions of the hadrons in terms of quarks and gluons. The underlying theory is Quantum Chromodynamics (QCD), the theory of strong interaction between quarks and gluons. Using our understanding of QCD, we aim at describing a wide array of hadronic phenomena, ranging from terrestrial nuclear physics to the behaviour of matter in the early universe. A non exhaustive list of few open issues in the hadronic physics field is given below (see Ref [1] for an overview) :

- How does the nucleon spin and mass arise from its constituents?
- How do quarks and gluons evolve into hadrons via the dynamics of confinement?
- Can we determine precisely the parameters of QCD?
- What are the roles of quarks and gluons in nuclei and matter under extreme conditions?

Understanding the emergence of nucleons and nuclei from the properties and dynamics of quark and gluons in QCD is a fundamental goal of hadronic physics.

## 2 Important features of QCD

The strong interaction is the strongest of the four fundamental forces in nature and acts at subatomic distances. It is responsible for the binding of quarks and gluons inside the hadrons, and for the cohesion of protons and neutrons inside the atomic nuclei. The restriction of the strong force to subatomic distances is a consequence of two features called *Confinement* and *Asymptotic Freedom*. Therefore, any theory willing to describe the dynamics of quarks and gluons inside ha-

drons has to satisfy those two conditions. A theoretical description of the strong interaction by a quantum field theory, called QCD, was proposed by Fritzsche and Gell-Mann[2], in the 1970's. QCD can be introduced by analogy to Quantum ElectroDynamics (QED), the quantum field theory describing the electromagnetism interaction. In QED, the mediator of the electromagnetic interaction is the photon, which couples to electric charges. In QCD, the fundamental charge, which is the equivalent of the electrical charge in QED, is a quantum property called *color*. The introduction of this new quantum property was supported by several experimental observations. Indeed, for instance, in absence of color, the existence of baryons with spin 3/2, such as the  $\Delta^{++}$  baryon, would violate the Pauli exclusion principle, since  $\Delta^{++}$  is made of three up quarks with spins up. In QCD, each quark comes in one of the three colors (red, blue and green), while antiquarks are anti-colored. Colored spin-1 particles, the gluons, are the mediators of the strong interaction. They carry color charges themselves (unlike photons in QED). Gluons couple to color charges of quarks and also to colored gluons themselves. Those gluon self-interactions are believed to give rise to *color confinement*. Indeed, free quarks have never been observed in nature because their coupling is so strong that it is easier to create a new quark-antiquark pair than to isolate the quark. Therefore, quarks bind permanently into hadrons, which are color neutral objects. Hadrons consist either of three quarks (baryons) or a quark and an antiquark (mesons) such that their net color charge vanishes. Besides *confinement*, another remarkable property of QCD is *asymptotic freedom*. Experimentally, in high energy scattering processes of leptons with protons, it has been observed that the scattering occurs at pointlike and massless constituents, the quarks, rather than at homogeneous object with the size of the proton. At sufficiently high momentum transfers, quarks behave like quasi-free particles. From the theoretical point of view, the discovery of asymptotic freedom in the theory of strong interaction was performed by Gross, Politzer and Wilczek [3, 4] and was honored with a Nobel Price in 2004, thirty years after the original findings. Fig. 1 shows the world-average of  $\alpha_s$  measurements as a function of the energy (or momentum transfer) scale  $Q$ , where  $\alpha_s$  is the coupling strength of the strong interaction. At large momentum transfer  $Q$  (i.e short distance), the coupling constant becomes weak. It is the regime of asymptotic freedom where quarks behave like quasi-free particles. Perturbation theory can be applied in this energy domain. At

small momentum transfer ( $Q < 1$  GeV) and distances of the order of 1 fm (the typical size of hadrons), quarks are confined in the hadrons. Particles we observe in nature are therefore in the regime of non-perturbative QCD.

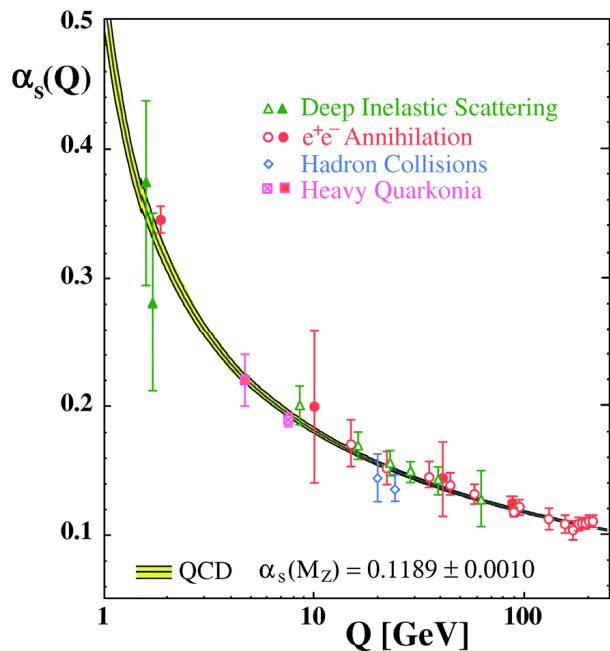


FIGURE 1: Summary of  $\alpha_s$  measurements as a function of the energy scale  $Q$  [5].

### 3 Experimental and theoretical tools

QCD has been extensively tested over the years thanks to a large variety of experimental tools (see Ref. [6]). Among the ones which have provided the most stringent tests of QCD, one can cite : Deep Inelastic Scattering (see Fig. 2a),  $e^+e^-$  annihilation (see Fig. 2b) and hadron-hadron collisions (see Fig. 2c). Thanks to the high statistics data available at  $e^+e^-$  colliders, it was possible to reach good precision on  $\alpha_s$  measurements (see Fig. 1). During  $e^+e^-$  annihilation, the produced virtual photon decays to leptons or quark pairs. The branching ratio into quarks is a counter of the number of colors available, while the detailed structure of the final state reflects the radiation of gluons. Therefore  $e^+e^-$  annihilation brought the first evidences for the existence of color (see [7, 8]) and the existence of gluon self-coupling with the observation of 4-jet events at the LEP collider [9]. In Deep Inelastic Scattering (DIS), leptons are used to probe the insides of hadrons. The highly energetic lepton has a very short wavelength and hence the ability to probe distances that are small as compared to the size of the target hadron. In the perturbative approximation, it is a high-energy virtual photon emitted from the lepton and absorbed by the target hadron which transfers energy to one of its constituent quarks. The constituent quark is knocked out of the

target hadron and hadronizes into observable particles (due to confinement), while the initial lepton is being deflected. DIS provided the first convincing evidence of the existence of quarks [10]. A third way to test QCD is with hard hadron-hadron collisions. The incoming hadrons provide beams of partons which possesses varying fractions of the momenta of their parent hadrons. Cross sections are dominated by gluon components, which are only indirectly accessible in DIS. Experiment at hadron colliders give less precise but still important tests of QCD.

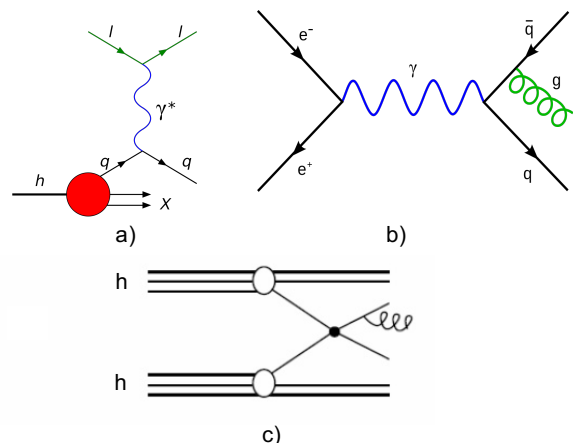


FIGURE 2: Feynman diagram for Deep Inelastic scattering (a),  $e^+e^-$  annihilation (b) and hadron-hadron collisions (c).

The QCD Lagrangian display in principle a complete description of the strong interaction. But in practice, it leads to equations hard to solve. In order to meet this challenge, several theoretical approaches have been developed. We briefly mention below few of them. In the high-energy (high-momentum transfer) regime, where quarks and gluons appear to be quasi-free, perturbative QCD can be applied. Although limited in scope, this approach has resulted in the most precise tests of QCD to date. Since the structure of hadrons has a non-perturbative nature, the QCD factorization theorem was introduced. Thanks to this theorem, cross sections of high energy processes involving a high momentum transfer can be separated into a process dependent perturbatively-calculable short-distance parton cross section, and universal long-distance functions. These universal long-distance functions (eg. parton distribution functions, fragmentation functions,...) can be measured with global fits to experiments.

Among the non-perturbative approaches to QCD, the most well established one is lattice QCD, which provides a framework for investigation of phenomena such as confinement and quark gluon plasma formation. Lattice QCD is a lattice gauge theory formulated on a grid of points in space and time (quarks are defined at lattice sites and gluon fields are the links connecting neighboring sites). If the lattice is taken infinitely large and its sites infinitesimally close, the continuum QCD is recovered. It is worth noting that numerical

lattice QCD calculations are computationally intensive and require the use of supercomputers. Finally, for specific problems, effective theories (eg. chiral perturbation theory) which use an effective Lagrangian equivalent to the QCD one, can be used. Jan Maelger presented a theoretical talk on the *Introduction to the Curci-Ferrari Model : Results and Open Questions*.

## 4 Nucleon structure

Thanks to Generalized Parton Distributions (GPDs), a multidimensional description of the nucleon structure is currently emerging. Form factors (FFs) were well known to provide information about the charge distribution inside the nucleon but no dynamical information, while Parton Distribution Functions (PDFs) allow for the access to quark longitudinal momentum but without information on their spatial location. It has however now been established that both FFs and PDFs are special cases of a more general class of distribution functions that merge spatial and dynamical information, the GPDs. GPDs are accessible through the analysis of hard exclusive processes, in which a target is probed by high-energy particles and is left almost intact apart from the production of one or two additional particles. Such processes, used for investigating GPDs, are Deeply virtual Compton Scattering (DVCS) and Deeply Virtual Meson Production (DVMP), where a photon or a meson is produced, respectively. Very recently, using the DVCS data collected with the CLAS detector at JLab and HERMES detector at DESY, the first nearly model-independent images of the proton started to appear. The result of this work is illustrated in Fig. 3, where the probabilities for the quark to be at various places inside the proton are shown at two different values of its longitudinal momentum  $x$ . As can be seen, when the longitudinal momentum of the quark decreases, the radius of the proton increases.

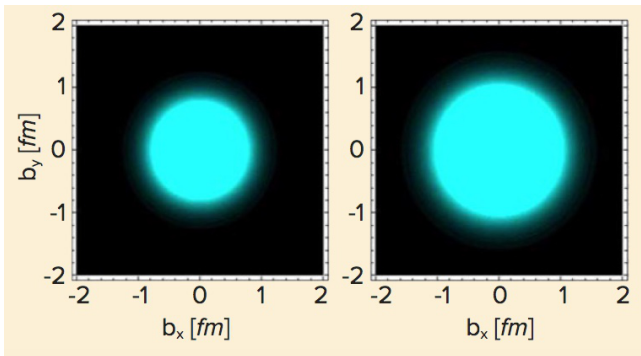


FIGURE 3: The first 3D views of the proton : the spatial charge densities of the protons in a plane ( $b_x, b_y$ ) positioned at two different values of the quarks longitudinal momentum  $x$  : 0.25 (left) and 0.09 (right) [11].

## 5 Quark Gluon Plasma and Cold Nuclear Matter effects

We have seen that in nature, under ordinary conditions, quarks and gluons cannot be observed as isolated particles and bind into hadrons. However, under extreme conditions, quarks and gluons can evolve freely during a short amount of time. This deconfined state of nuclear matter is called a Quark Gluon Plasma. Such conditions are realized either at high temperatures, like in the early universe shortly after the big bang, and/or at high matter density, such as it is believed to be the case in compact neutron stars. In order to recreate those extreme conditions in the laboratory, collisions of high-energy ultra-relativistic heavy-ions are performed. At the LHC collider, the ALICE experiment is devoted to the study of heavy-ion collisions. According to lattice QCD predictions, the phase transition towards deconfined nuclear matter occurs at temperature of about 170 MeV ( $\sim 10^5$  times the temperature inside the sun) and energy densities of about  $1 \text{ GeV}/\text{fm}^3$  (5 times the density of ordinary matter). Colliding different types of nuclei with different incident beam energies allows one to explore different regions of the phase diagram of nuclear matter (represented in Fig. 4). The nature of the phase transition and the existence of a critical point (ie the location on the phase diagram where the boundaries between phases disappears) are still open questions.

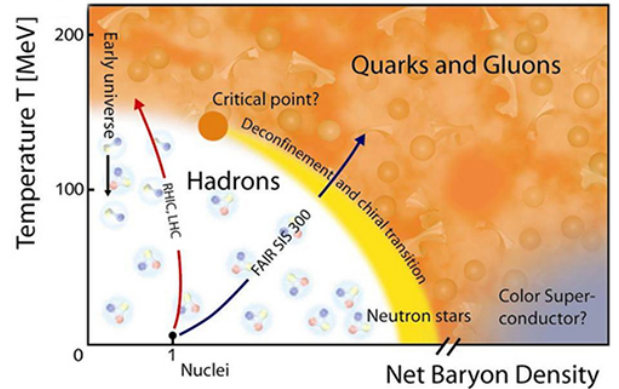


FIGURE 4: The QCD phase diagram, with a hadron phase of ordinary nuclear matter and a quark gluon plasma phase.

Experimentally, the QGP is not directly accessible to observation since it lasts only few fm/c at LHC energies. In order to demonstrate the formation of the QGP, observables modified by the presence of this hot medium are needed. A large variety of such observables exists (see [12] for an overview). We will briefly discuss one of those signatures : the suppression of quarkonia<sup>1</sup> in hot nuclear matter. Heavy quarks experience the full evolution of the heavy-ion collision since they are expected to be produced only during the initial stages of the collision in hard partonic interactions. It was

1. Quarkonia are  $c\bar{c}$  or  $b\bar{b}$  bound states

predicted that in a hot and dense deconfined medium, bound states of quarkonia are suppressed due to a screening effect induced by the high density of color charges present in the medium [13]. This screening would occur at different temperatures for the various quarkonia states, since they have different binding energies. Being able to measure the sequential suppression of quarkonia in nucleus-nucleus (AA) collisions could therefore provide information on the temperature of the formed medium<sup>2</sup>. In order to quantify the suppression of quarkonia in AA collisions, one needs to compare the quarkonia yield measured in such system to a reference value. Such reference is usually built from the quarkonia yield measured in proton-proton collisions, scaled by the number of binary nucleon-nucleon collisions. It is therefore important to have a good control of quarkonia production in elementary proton-proton collisions for the proper interpretation of the AA data. In addition to effects connected with the hot medium, Cold Nuclear Matter (CNM) effects can also influence the quarkonium yield in nuclear collisions. They can be more directly investigated by studying proton-nucleus collision, where the creation of a QGP is not expected to occur. Few examples of CNM effects relevant at LHC energies are given below. One of them is nuclear shadowing, i.e. the modification of the quark and gluon structure functions for nucleons inside nuclei [14, 15, 16]. This effect modifies the probability for a quark or a gluon to carry a given fraction  $x$  of the nucleon momentum. It affects the elementary production cross section for the creation of a  $q\bar{q}$  pair that will eventually form a quarkonium state. Another CNM effect is parton saturation, a coherent effect involving low- $x$  quarks and gluons and which modifies the initial state of the nucleus. It is described by the Colour Glass Condensate (CGC) effective theory [17]. Let us finally mention, the coherent energy-loss effect involving partons in the initial and final state, which can lead to a modification of the quarkonium yields [18]. Cold Nuclear Matter effects can be investigated with other probes than quarkonia, such as for instance Drell-Yan (DY) lepton pair production (see Fig. 5). The DY mechanism is especially interesting to probe initial-state energy loss mechanism since at leading order the final state is color neutral and therefore doesn't radiate gluons. Charles-Joseph Naïm made a presentation on the subject entitled *Initial-state energy loss in Cold QCD matter and the Drell-Yan process*.

## Références

- [1] Capstick S. et al., "Key issues in hadronic physics", arXiv :hep-ph/0012238.
- [2] H. Fritzsch et al., "Advantages of the Color Octet Gluon Picture", Phys. Lett. 47B (1973) 365-368.

<sup>2</sup>. For simplicity we didn't discuss the existence of other hot medium effects, such as charmonium regeneration at LHC energies, which can enhance the charmonium production yield.

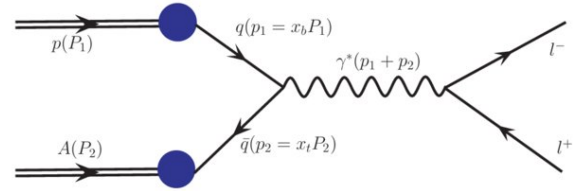


FIGURE 5: Feynman diagram for Drell-Yan lepton pair production at leading order in p-A collision.

- [3] D.J. Gross et al., "Ultraviolet Behavior of Nonabelian gauge Theories", Phys. Rev. Lett.30 (1973) 1343.
- [4] H.D. Politzer, "Reliable Perturbative Results for Strong Interactions", Phys. Rev. Lett. 30 (1973) 1346.
- [5] S. Bethke et al., "Experimental tests of asymptotic freedom", Prog. Part. Nucl. Phys. 58 (2007) 351-386.
- [6] T. Hansl-Kozanecka, "Experimental tests of QCD : Deep inelastic scattering,  $e^+e^-$  annihilation and hard hadron-hadron scattering", Conf. Proc. C910805 (1991) 105-153.
- [7] Halzen et al., "Quarks and Leptons", New York Wiley, copyright 0 1984, p. 229.
- [8] P. Soding et al., "Experimental evidence on QCD", Ann.Rev.Nucl.Part.Sci. 31 (1981) 231-293.
- [9] S. Bethke et al., "Four jet decays of the  $Z^0$  : Prospects of testing the triple gluon coupling", Z. Phys. C 49 (1991) 59.
- [10] E. M. Riordan, "The discovery of quarks", Science 256 (1992) 1287-1293.
- [11] A. Aprahamian et al., "The 2015 long range plan for Nuclear Science", [https://science.energy.gov/~media/np/nsac/pdf/2015LRP/2015\\_LRPNS\\_091815.pdf](https://science.energy.gov/~media/np/nsac/pdf/2015LRP/2015_LRPNS_091815.pdf).
- [12] Sarkar S. et al., "The Physics of the Quark-Gluon Plasma" , Lect.Notes Phys. 785 (2010) p. 1-369.
- [13] T. Matsui et al., " $J/\psi$  suppression by Quark Gluon Plasma formation", Phys. Lett. B178, 416 (1986).
- [14] K. J. Eskola et al., "EPS09 : A new Generation of NLO and LO Nuclear Parton Distribution Functions", JHEP 0904 (2009) 065.
- [15] K. Kovarik et al., "nCTEQ15 - Global analysis of nuclear parton distributions with uncertainties in the CTEQ framework", Phys. Rev. D93 no; 8, (2016) 085037.
- [16] K. J. Eskola et al., "EPPS16 : Nuclear parton distributions with LHC data", Eur. Phys. J. C77 no. , (2017) 163.
- [17] E. Iancu et al., "The Color Glass Condensate and high-energy scattering in QCD", arXiv :hep-ph/0303204 [hep-ph].
- [18] F. Arleo, "Heavy-quarkonium suppression in p-A collisions from parton energy loss in cold QCD matter", JHEP 1303 (2013) 122.

# Introduction to the Curci-Ferrari Model : Results and Open Questions

Jan Maelger

*CPHT, Ecole Polytechnique*

*APC, Univ. Paris Diderot*



## Résumé

After a brief review of the standard picture of infrared QCD, we motivate an alternative effective model, the so-called Curci-Ferrari Model, which is based on a minimal deformation of the Landau gauge Fadeev-Popov Lagrangian in the form of a phenomenological gluon mass term. We summarize some of the recent results of the CF Model, both in pure Yang-Mills theory as well as in the unquenched scenario. We mention some key aspects of its correlation functions, however we will mainly focus on the implications of the CF Model for the QCD phase diagram in the heavy quark regime.

## 1 Introduction

The theory of Quantum Chromodynamics (QCD) is the part of the Standard Model which describes the strong interactions. The fundamental particles of QCD are the six quarks, up, down, strange, charm, top and bottom, as well as the gluon, which is its mediating, force-carrying particle. Aside from spin 1/2 for the quarks and spin 1 for the gluons, each of the QCD particles exhibits a non-trivial color charge labelled by either red, green or blue. In field theory language, QCD is a non-abelian gauge theory with gauge group  $SU(3)$ , and the possible interaction vertices, three-gluon, four-gluon and quark-gluon, come with a proportionality factor which we call the coupling constant,  $g$ ,  $g^2$  or  $g$  respectively. It is important to note that the value of this coupling constant depends on the energy scale<sup>1</sup>  $E$  of the interaction,  $g(E)$ .

One of the most celebrated properties of QCD is asymptotic freedom, which means that for very large energy values, calculations are generally well-controlled perturbatively in a weak coupling expansion, if one accounts for non-converging asymptotic series and potentially necessary resummations. Upon decreasing the energy towards hadronic scales, perturbation theory formally breaks down and one enters the realm of non-perturbative methods, primarily Lattice QCD [1, 2, 3], or analytic ones, such as Dyson-Schwinger Equations (DSE) [4, 5] or the Functional Renormalization Group (FRG) [6, 7].

On the other hand, it has long been proven that the starting point for perturbation theory for covariant

gauges, the Fadeev-Popov (FP) procedure, while well-defined in the ultraviolet (UV), becomes increasingly invalid in the infrared (IR) due to non-complete gauge fixing and the presence of so-called Gribov copies [8]. The latter are the multiple intersections of the submanifold induced by a gauge fixing condition with individual gauge orbits, and the infinite number of copies renders the usual calculation of correlation functions via generating functionals and path integrals ill-defined. Thus, alternative IR QCD approaches have been pursued, in which one tries to control the Gribov ambiguity by one of two main strategies. Either by restricting the space of gauge configurations to be integrated over in the generating functional to a less problematic subregion, leading to the well-known (refined) Gribov-Zwanziger action (GZ) [9, 10], or by phenomenologically accounting for the IR effects of the Gribov copies in the form of a gluon mass term, leading to the Curci-Ferrari Model (CF). In both scenarios, one modifies the Fadeev-Popov (Landau<sup>2</sup>) gauge fixed action and proceeds to a perturbative analysis of the theory at hand.

The zero temperature Euclidean Lagrangian of the CF Model is given by :

$$\mathcal{L}_{\text{CF}} = \frac{1}{4}(F_{\mu\nu}^a)^2 + \bar{\psi}(\gamma_\mu \mathcal{D}_\mu + M)\psi + \mathcal{L}_{\text{FP}} + \frac{1}{2}m^2(A_\mu^a)^2,$$

where the FP term includes the usual ghost fields.

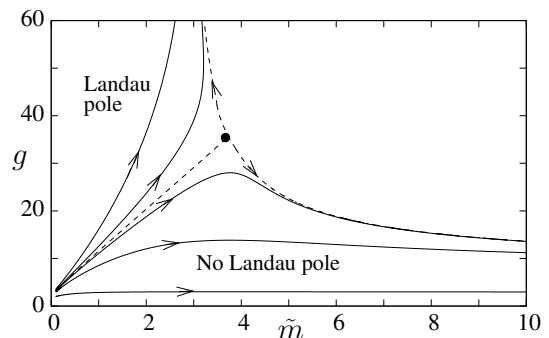


FIGURE 1: One loop Renormalization Group (RG) flow of the coupling  $g$  and rescaled gluon mass  $\tilde{m}$  in the CF Model. The scaling separatrix is denoted by the dashed line, connecting an ultraviolet fixed point in the origin with a gaussian IR fixed point. Not depicted are flows disconnected from the UV fixed point.

<sup>1</sup> In order to demonstrate self-consistency of the per-

<sup>2</sup> In principle for any covariant gauge  $\partial_\mu A_\mu = \omega$ , but here we only consider Landau gauge,  $\omega = 0$ .

<sup>1</sup> In Quantum Field Theory, energy  $E$ , mass  $M$  and temperature  $T$  all have the same units and can thus be used semi-interchangeably.

turbative treatment of the CF Model, a one loop RG flow diagram was computed in [11] for pure Yang-Mills theory (YM), see Fig. 4. As one can see, there are two qualitatively different regimes divided by a separatrix, denoting itself a scaling-type solution. Above the separatrix, which is the regime including the standard FP Lagrangian along the  $\tilde{m} \equiv \frac{m}{\mu} = 0$  axis, with  $\mu$  the momentum scale, the RG flow does exhibit a Landau pole. On the contrary, for suitable renormalization conditions in the UV, there exists flows below the separatrix, labelled IR safe, which do no longer suffer from a Landau pole. The corresponding flow of the coupling is bounded for all momenta. It is noteworthy that lattice Landau gauge-fixed simulations with decoupling-type behavior follow an IR-safe-like trajectory without a Landau pole. Despite the fact that the coupling constant  $g$  might become large along IR safe trajectories, it was shown that the true loop-expansion parameter is of the form  $\frac{\lambda}{1+\tilde{m}^2}$ , where  $\lambda = \frac{3g^2}{16\pi^2}$  [12]. For typical IR safe trajectories, this true expansion parameter never exceeds values of around 0.4, thus permitting perturbation theory at all momentum scales down to the deep IR.

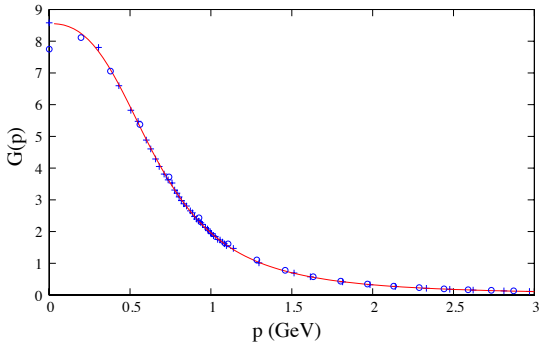


FIGURE 2: One loop gluon propagator within the CF Model (red) from [13] as a function of momentum against lattice YM simulations (dots [14], crosses [15]). The fitted value of  $m \approx 500$  MeV for the gluon mass is kept constant in all further computations of the CF Model.

The most natural quantities to start testing the validity of the CF Model are (two-point) correlation functions. For instance, the one loop results for the gluon propagator are depicted in Fig. 2 and compared with corresponding lattice counterparts from various groups. Both display the well-established decoupling behavior, meaning that the Landau gauge gluon propagator saturates in the IR and attains a finite value. The description of this non-trivial feature was the historical motivation for the CF Model. Further YM and QCD correlation functions, both in the vacuum as well as at finite temperature and chemical potential, have been computed perturbatively in the CF model in qualitative and quantitative agreement with lattice QCD findings [13, 16, 17, 18, 19].

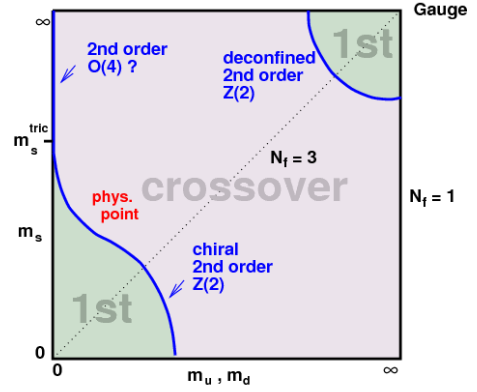


FIGURE 3: Columbia Plot : Pure YM point in the top right corner and two first order regions in the heavy and light quark corner. They are separated from the crossover region by critical second order lines.

## 2 Heavy Quark Phase Diagram

Confinement, i.e. the fact that experimentally quarks are confined into color singlet bound states, called hadrons, is a fundamental property of nature. Whether or not confinement is permitted by QCD itself has never been proven from first principles and remains to present one of the most studied open questions in physics. On the other hand, it is well-established that QCD allows for two phase transitions, one associated to chiral symmetry restoration and one to center symmetry breaking, which is related to deconfinement. Lattice QCD simulations indicate that for physical quark masses the two transitions happen at a similar temperature value and one therefore expects a non-trivial interplay between the two regimes. Consequently one tries to disentangle them and to first understand each one individually before attempting a more complicated scenario. Since chiral symmetry is dominant at small and suppressed at large quark masses, and vice versa for center symmetry, this is the motivation for the Columbia plot, shown in Fig. 3. It is a mere theoretical construct where one varies the quark masses as free parameters and depicts the resulting nature of the two corresponding chiral and center symmetry transitions. In so doing, one only accounts for the three lightest quarks in a partially isospin symmetric scenario where the mass of the up and down quark are taken to be degenerate.

In the following we focus on the physics of center symmetry breaking underlying the heavy quark regime, which is located in the top right corner of the Columbia plot. An appropriate order parameter at the YM point, i.e. for infinite quark masses, is the Polyakov loop  $\ell$ , defined as

$$\ell \equiv \frac{1}{3} \text{tr} \left\langle P \exp \left( ig \int_0^\beta d\tau A_0^a t^a \right) \right\rangle, \quad (1)$$

where  $P$  denotes path-ordering. Intact center symmetry implies  $\ell = 0$  and since the Polyakov loop is related to the free energy  $F_q$  of a static test charge in a heat bath

of gluons via  $\ell \sim e^{-\beta F_q}$ , one finds  $\ell = 0$  and  $F_q \rightarrow \infty$  in the center symmetric phase. Similar relations hold for the anti-Polyakov loop  $\bar{\ell}$  defined by anti-path ordering in (1) and which corresponds to a test anti-quark,  $\bar{\ell} \sim e^{-\beta F_{\bar{q}}}$ . For vanishing chemical potential one has explicit charge conjugation invariance and therefore  $\ell$  and  $\bar{\ell}$  coincide identically.

The inclusion of quarks explicitly breaks center symmetry, however for heavy quarks this breaking is soft and symmetry still holds approximately. Therefore, one is still allowed to associate  $\ell \approx 0$  with the center symmetric phase. However, this association becomes increasingly invalid as one descends from the YM point towards lighter quarks.

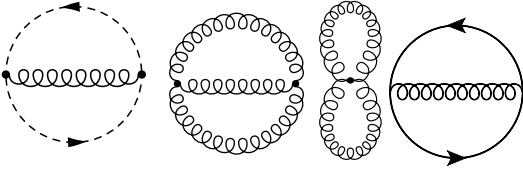


FIGURE 4: Feynman diagram representation of  $V_{\text{QCD}}^{(2)}$  and  $V_{\text{YM}}^{(2)}$  for the three leftmost diagrams.

At finite temperature, it is convenient to work in a choice of gauge with manifest center symmetry and which permits a non-trivial expansion point beyond simply pure Landau gauge. One such choice of gauge is the so-called Landau-DeWitt gauge [20], where one splits the gluon field  $A_\mu^a$  into a background  $\bar{A}_\mu^a$  and a fluctuating component  $a_\mu^a$ , such that  $A_\mu^a = \bar{A}_\mu^a + a_\mu^a$ . Then, for each temperature  $T$ , one chooses the background such that the expectation value of the fluctuating component,  $\langle a_\mu^a \rangle$ , vanishes in the limit of vanishing sources. In practice, this corresponds to locating the absolute minimum of the functional  $\tilde{\Gamma}[\bar{A}]$  defined as  $\tilde{\Gamma}[\bar{A}] \equiv \Gamma[\bar{A}, \langle a \rangle = 0]$ , where  $\Gamma[\bar{A}, \langle a \rangle]$  is the effective action for  $\langle a \rangle$  in the presence of  $\bar{A}$  [21]. Since any minimum has to respect the symmetries of the system at finite temperature, one can restrict the subspace of configurations  $\bar{A}$  to temporal and homogenous backgrounds

$$\bar{A}_\mu(\tau, \mathbf{x}) = \bar{A}_0 \delta_{\mu 0},$$

upon which the functional  $\tilde{\Gamma}[\bar{A}]$  reduces to an effective potential  $V(\bar{A}_0)$  for the constant matrix field  $\bar{A}_0$ . Furthermore, it is always possible to rotate this matrix  $\bar{A}_0$  into the Cartan subalgebra<sup>3</sup>:

$$\beta g \bar{A}_0 = r_3 \frac{\lambda_3}{2} + r_8 \frac{\lambda_8}{2},$$

where  $\lambda_3$  and  $\lambda_8$  are the diagonal Gell-Mann matrices.  $V(\bar{A}_0)$  is reduced to a mere function of 2 components  $V(r_3, r_8)$ . In order to have a real potential  $V$ , depending on the chemical potential  $\mu$ , there are distinct self-consistent choices for the parameters  $r_3$  and  $r_8$ . In par-

3. Here of  $\text{su}(3)$ , but in principle of any gauge algebra in question.

ticular, at  $\mu = 0$ , charge conjugation invariance implies that the global minimum lies on the  $r_3$ -axis, meaning that one can restrict to  $r_8 = 0$  identically. For imaginary  $\mu$ , both  $r_3$  and  $r_8$  are chosen to be real and for real  $\mu$ , we extend  $r_8$  to be purely imaginary.<sup>4</sup>

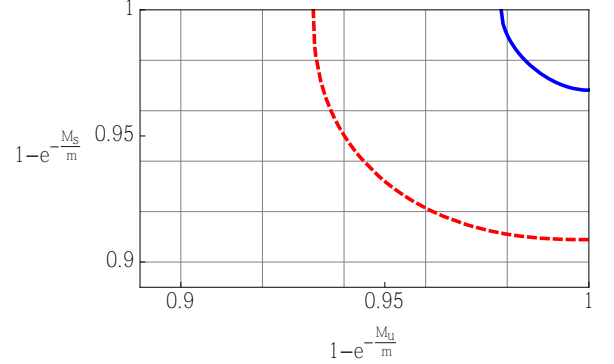


FIGURE 5: Second order critical lines in the top right corner of the Columbia plot, obtained from the CF Model, at one-loop order in red and two-loop order in blue.

The effective potential for the Polyakov loop has been computed to two-loop order in both YM [21] and QCD [22, 23]:  $V_{\text{QCD}}(r_3, r_8) = V_{\text{QCD}}^{(1)}(r_3, r_8) + V_{\text{QCD}}^{(2)}(r_3, r_8)$ , where

$$\begin{aligned} V_{\text{QCD}}^{(1)}(r_3, r_8) &= \frac{3}{2} \text{Tr Ln} (\bar{D}^2 + m^2) - \frac{1}{2} \text{Tr Ln} (\bar{D}^2) \\ &\quad - \text{Tr Ln} (\gamma_\mu \mathcal{D}_\mu + M + \mu \gamma_0) \end{aligned}$$

with  $\bar{D}_\mu = \partial_\mu - ig \delta_{\mu 0} \bar{A}^k T_{\text{adj}}^k$ . The two-loop contributions  $V_{\text{QCD}}^{(2)}(r_3, r_8)$  are shown diagrammatically in Fig. 4.

The subsequent results at vanishing chemical potential for the second order line in the Columbia plot at one- and two-loop order as well as the Polyakov loop at one-loop order can be seen in Fig. 5 and Fig. 6 respectively. Superficially, the second order lines look vastly different without any apparent convergence of the perturbative expansion at all. However, one has to remember that these critical lines are given in terms of bare quark masses. While at one-loop order there is a one-to-one correspondence between the renormalized and the bare quark mass, this is no longer true at two-loop order, where one deals with two renormalization factors of the form  $M_{\text{bare}} = Z_M M_{\text{ren.}} + C_M$ . The additive one,  $C_M$ , has to be included if the employed regulator explicitly breaks chiral symmetry, which is usually true for lattice QCD simulations, however it is not the case for analytic approaches. These renormalization factors make it a priori very difficult to not only compare CF one- and two-loop results, but also to compare findings amongst all approaches in general. It was argued in [25] that it is therefore more suitable to instead consider ratios of

4. At real  $\mu$ , there is another approach commonly used in the literature, where one takes both  $r_3$  and  $r_8$  real and neglects the imaginary part of the potential  $V$ . However, as argued in [23], this approach misses some of the essential physics.

	$\mu = 0$						$\mu = i\pi T/3$					
	$R_1$	$R_2$	$R_3$	$R_2/R_1$	$R_3/R_1$	$Y_3$	$R_1$	$R_2$	$R_3$	$R_2/R_1$	$R_3/R_1$	$Y_3$
Matrix [24]	8.04	8.85	9.33	1.10	1.16	1.59	5.00	5.90	6.40	1.18	1.28	1.56
GZ1 [25]	7.09	7.92	8.40	1.12	1.19	1.58	5.02	5.92	6.43	1.18	1.28	1.57
GZ2 [25]	9.45	10.25	10.72	1.08	1.13	1.58	7.51	8.34	8.82	1.11	1.17	1.58
CF 1-loop [22]	6.74	7.59	8.07	1.13	1.20	1.58	4.74	5.63	6.15	1.19	1.30	1.57
CF 2-loop [23]	7.53	8.40	8.90	1.12	1.18	1.57	5.47	6.41	6.94	1.17	1.27	1.57
Lattice [27]	7.23	7.92	8.33	1.10	1.15	1.59	5.56	6.25	6.66	1.12	1.20	1.59
DSE [28]	1.42	1.83	2.04	1.29	1.43	1.51	0.41	0.85	1.11	2.07	2.70	1.59

TABLE 1: Summary of the available results in the literature for the ratios of  $R_i$ 's and  $Y_3$ , for critical points in the  $\mu = 0$  case as well as for tricritical ones at  $\mu = i\pi T/3$ .

the quantities  $R_{N_f} \equiv \frac{M_c(N_f)}{T_c(N_f)}$  as well as, if  $C_M \neq 0$ , the difference ratio  $Y_3$ , defined by  $Y_{N_f} \equiv \frac{R_{N_f} - R_1}{R_2 - R_1}$ . These are scheme independent up to higher order corrections in the loop expansion. A selection of results in the literature in terms of these quantities for the second order critical line at  $\mu = 0$  in the Columbia plot can be found in the leftmost columns of Table 1.

For real and non-zero chemical potential  $\mu$ , one encounters the infamous sign problem due to a complex fermion determinant in the functional integral. The resulting lack of reliable importance sampling algorithms renders lattice QCD simulations void. To be able to nonetheless gain some insight into the real  $\mu$  regime, one instead studies the itself unphysical scenario of imaginary  $\mu$  and then extrapolates or analytically continues the findings. The QCD phase structure at imaginary

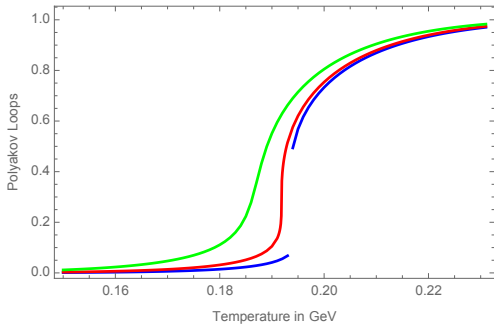


FIGURE 6: The Polyakov loop at one-loop order for different quark masses. The critical mass is  $M_c \approx 1.55$  GeV and yields the critical transition in red, whereas the first order jump in blue corresponds to  $M \approx 1.1M_c$  and the smooth crossover in green to  $M \approx 0.85M_c$ .

chemical potential is spearheaded by the Roberge-Weiss symmetry [29]. For some particular value of the quark mass,  $M_{\text{tric}}(N_f)$ , and at exactly  $\mu = i\pi T/3$ , it exhibits a tricritical point where two second order  $Z_2$ -symmetric points have merged with a first order transition line [26]. As before, these tricritical values found by different approaches in the literature are best compared amongst each other in context of the quantities of Table 1, cf. the rightmost columns. The overall good agreement, both for vanishing and imaginary chemical potential,

highlights that the dynamics of heavy quark QCD is well-described by perturbation theory in the CF Model. Moreover, the vicinity of the tricritical point follows a

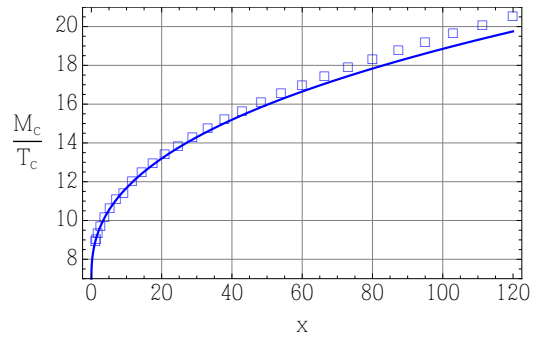


FIGURE 7: The blue curve shows the scaling behavior in Eq.(2) at imaginary  $\mu$  analytically continued in  $x$  to the case of real  $\mu$ , compared to our results (open squares) obtained directly at real  $\mu$ , both at  $N_f = 3$ .

mean field scaling behavior [26, 28] of the form :

$$\frac{M_c(\mu_i)}{T_c(\mu_i)} = \frac{M_{\text{tric.}}}{T_{\text{tric.}}} + K \left[ \underbrace{\left( \frac{\pi}{3} \right)^2 - \left( \frac{\mu_i}{T_c} \right)^2}_{=x} \right]^{\frac{2}{5}}, \quad (2)$$

where  $x$  measures the distance away from tricriticality. Its extrapolation to real chemical potential is shown in Fig. 7. As can be seen, this extrapolation describes the physics rather well up to very large  $x$  values. This not only indicates the accuracy of the mean field scaling description and it being well-captured by the CF Model, but also illustrates the physical merit of an analysis in the unphysical imaginary  $\mu$  regime.

### 3 Conclusion

A perturbative analysis within the CF Model already at one-loop level is capable of describing the dynamics underlying the physics of center symmetry breaking in the heavy quark regime. It is in qualitative agreement with lattice QCD findings. Additionally, a quantitative improvement is obtained upon including two-loop corrections, implying a robust perturbative expansion.

## Acknowledgements

All results shown have been obtained in collaboration with my PhD supervisors Urko Reinosa and Julien Serreau, both of whom I want to thank for their countless support related to this work and beyond.

## Références

- [1] C. Ratti, Rept. Prog. Phys. **81** (2018) no.8, 084301.
- [2] R. Gupta, hep-lat/9807028.
- [3] O. Philipsen, Eur. Phys. J. ST **152** (2007) 29.
- [4] C. D. Roberts and A. G. Williams, Prog. Part. Nucl. Phys. **33** (1994) 477.
- [5] C. S. Fischer, Prog. Part. Nucl. Phys. **105** (2019) 1.
- [6] B. Delamotte, Lect. Notes Phys. **852** (2012) 49.
- [7] J. M. Pawłowski, Annals Phys. **322** (2007) 2831.
- [8] I. M. Singer, Commun. Math. Phys. **60** (1978) 7.
- [9] N. Vandersickel and D. Zwanziger, Phys. Rept. **520** (2012) 175.
- [10] D. Dudal, J. A. Gracey, S. P. Sorella, N. Vandersickel and H. Verschelde, Phys. Rev. D **78** (2008) 065047.
- [11] J. Serreau and M. Tissier, Phys. Lett. B **712** (2012) 97.
- [12] U. Reinosa, J. Serreau, M. Tissier and N. Wschebor, Phys. Rev. D **96** (2017) no.1, 014005.
- [13] M. Tissier and N. Wschebor, Phys. Rev. D **84** (2011) 045018.
- [14] I. L. Bogolubsky, E. M. Ilgenfritz, M. Müller-Preussker and A. Sternbeck, Phys. Lett. B **676** (2009) 69.
- [15] D. Dudal, O. Oliveira and N. Vandersickel, Phys. Rev. D **81** (2010) 074505.
- [16] M. Peláez, M. Tissier and N. Wschebor, Phys. Rev. D **88** (2013) 125003.
- [17] U. Reinosa, J. Serreau, M. Tissier and N. Wschebor, Phys. Rev. D **89** (2014) no.10, 105016.
- [18] M. Peláez, M. Tissier and N. Wschebor, Phys. Rev. D **90** (2014) 065031.
- [19] M. Peláez, M. Tissier and N. Wschebor, Phys. Rev. D **92** (2015) no.4, 045012.
- [20] J. Braun, H. Gies and J. M. Pawłowski, Phys. Lett. B **684** (2010) 262.
- [21] U. Reinosa, J. Serreau, M. Tissier and N. Wschebor, Phys. Rev. D **93** (2016) no.10, 105002.
- [22] U. Reinosa, J. Serreau and M. Tissier, Phys. Rev. D **92** (2015) 025021.
- [23] J. Maelger, U. Reinosa and J. Serreau, Phys. Rev. D **97** (2018) no.7, 074027.
- [24] K. Kashiwa, R. D. Pisarski and V. V. Skokov, Phys. Rev. D **85** (2012) 114029.
- [25] J. Maelger, U. Reinosa and J. Serreau, Phys. Rev. D **98** (2018) no.9, 094020.
- [26] P. de Forcrand and O. Philipsen, Phys. Rev. Lett. **105** (2010) 152001.
- [27] M. Fromm, J. Langelage, S. Lottini and O. Philipsen, JHEP **1201** (2012) 042.
- [28] C. S. Fischer, J. Luecker and J. M. Pawłowski, Phys. Rev. D **91** (2015) no.1, 014024.
- [29] A. Roberge and N. Weiss, Nucl. Phys. B **275** (1986) 734.



Troisième partie  
Medical Physics

session dirigée par Rachel DELORME



# Proton track-structure simulation in biological media

**Mario E. Alcocer-Avila<sup>1</sup>, Michele A. Quinto<sup>2</sup>, Juan M. Monti<sup>2</sup>,  
Roberto D. Rivarola<sup>2</sup>, Christophe Champion<sup>1</sup>**

<sup>1</sup>*CELIA, Centre Lasers Intenses et Applications, Université de Bordeaux – CNRS – CEA,  
F-33400 Talence, France*

<sup>2</sup>*Instituto de Física Rosario, CONICET – Universidad Nacional de Rosario, S2000 EKF  
Rosario, Argentina*

## Résumé

The stopping power of protons in water and DNA has been computed for incident energies ranging from 10 keV to 100 MeV with the *TILDA-V* Monte Carlo track-structure code. In water, the results obtained are in good agreement with the available experimental data. On the other hand, our calculations also show that within this energy range, the stopping power of protons in DNA is always greater than in water, a result that cannot be reproduced only by applying a density rescaling factor. We conclude that an accurate description of the charged-particle transport in living matter has to take into account a realistic modeling of the biological medium.

## 1 Introduction

The radiation effects in living matter is a topic of active research. Among the existing techniques to model the radiation transport, the numerical codes based on the Monte Carlo method (MC) are of primary importance.

In this context, let us note that the MC codes can be divided into two categories : condensed-history (CH, also known as “general-purpose”) and track-structure codes (TS). The principle of CH codes is to group a large number of interactions in a step by applying multiple scattering theories [1]. This allows to reduce the computing time, which is the main drawback of MC codes. While CH codes can be accurate enough when dealing with macroscopic volumes and are in fact widely used in radiation dosimetry, it has been shown that they are not appropriate for radiation transport simulations involving very small geometries, i.e. when the target diameter is smaller than the incident radiation track length [2]. Under these conditions, TS codes are the only reliable tool to correctly determine the energy deposition in the target, since they track the primary and secondary particles event-by-event. Several TS codes have been successfully developed in the last decades to describe the interaction of charged particles with matter and predict the radiation-induced energy deposits at the nanoscale level in the medium of interest. A comprehensive review can be found in the works by Nikjoo *et al.* [1, 3].

The purpose of this paper is to summarize the main features of the *TILDA-V* TS code [4] and to report stopping power values computed for protons in water

and DNA. Additionally, we discuss how similar calculations with  $\alpha$  particles could help to elucidate the therapeutic potential of several  $\alpha$ -emitting radionuclides currently considered as promising candidates for targeted alpha therapy (TAT).

## 2 Materials and methods

We present in this section the main aspects of the *TILDA-V* code as well as a summary of the theoretical and semi-empirical models used to describe the various interactions induced by incident protons and secondary electrons in the medium under consideration (water and DNA).

### 2.1 The *TILDA-V* code

*TILDA-V* is a homemade Monte Carlo TS code designed to simulate the transport of protons of 10 keV-100 MeV in water and DNA [4]. *TILDA-V* is based on a set of *ab initio* multiple differential and total cross sections (TCS) mainly calculated within the quantum mechanical framework. These cross sections are the only necessary input data for modeling the different physical processes and then computing macroscopic quantities such as the proton stopping power. In the most recent version of the code, the interactions taken into account are : ionization, excitation, electron capture and elastic scattering by protons ( $H^+$ ); ionization, excitation, electron loss and elastic scattering by neutral hydrogen ( $H^0$ ); ionization, excitation and elastic scattering by the secondary electrons.

Figure 1 provides a flowchart depicting the basic steps followed in a simulation with *TILDA-V*. Once the user has specified all necessary parameters for the simulation (charge of the ion, number of primary particles, density and molar mass of the target, physical models, etc.) and the code starts to run, the next step consists in loading the cross section database. Then a first random sampling is performed in order to compute the distance traveled by the projectile before interacting with the target. A second random sampling determines the type of interaction taking place at that point. The code then computes the total energy transfer to the medium and determines whether or not a charge exchange has occurred. Naturally, the latter is only relevant for the electron capture and electron loss processes. For the inelastic interactions able to induce electron emission from the target/projectile, additional

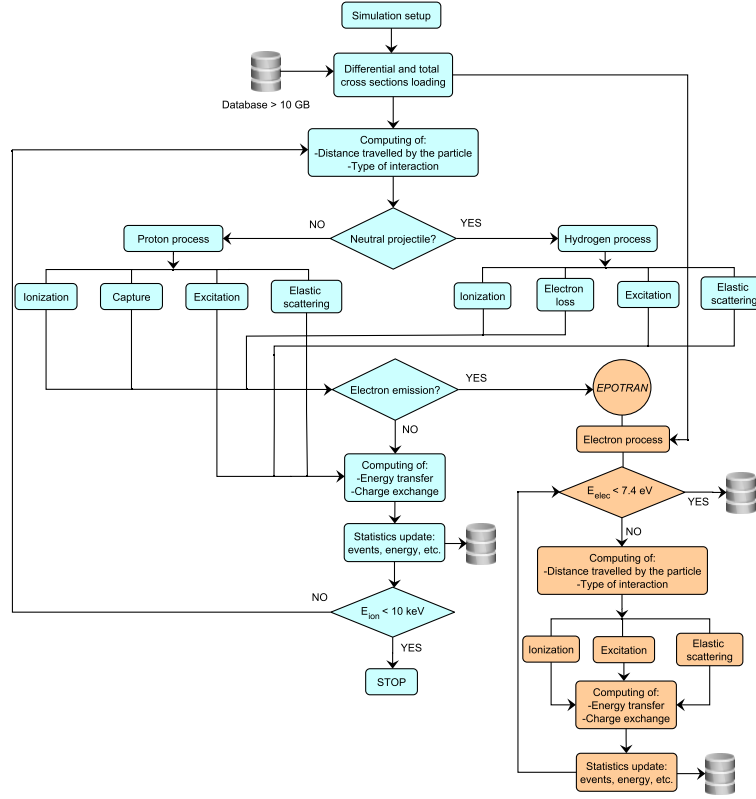


FIGURE 1: Simplified flowchart describing the functioning of the *TILDA-V* code.

random samplings using singly and doubly differential cross sections are carried out to obtain the ejected electron energy and angle. The tracking of the secondary particles is based on routines initially developed for the *EPOTRAN* TS code [5] and which are now fully implemented into *TILDA-V*. After each collision, the statistics of the simulation is updated. A simulation stops when the energy of the primary particles falls below the cutoff of 10 keV. For the secondary electrons the tracking cutoff is fixed to 7.4 eV. In both cases, the remaining energy is deposited locally.

## 2.2 The physical models

It is worth noting that in *TILDA-V* all targets are considered in vapor state. For water, the binding energies are computed employing the MO-SCF-LCAO (molecular orbital self-consistent field-linear combination of atomic orbitals) approach reported by Moccia [6], who described the water molecule by means of single-center wave functions, all centered on the oxygen atom and expressed in terms of Slater-type functions.

The description of DNA follows the *ab initio* approach of Ref. [7] to express the molecular wave function of each DNA component at the RHF/3-21G level with the GAUSSIAN09 software [8]. In this framework, each target is described via  $N$  molecular subshell wave functions with  $N = 35, 29, 39, 33$  and 48 molecular orbitals (MOs) for adenine, cytosine, guanine, thymine and sugar-phosphate backbone unit, respectively. In each case, the molecular subshell wave function is expressed

as a linear combination of atomic wave functions corresponding to the different atomic components. For each MO, the effective number of electrons relative to the atomic component was derived from a standard Mulliken population analysis and their sum for each occupied MO is very close to 2 [9]. Besides, the computed ionization energies of the occupied MOs of the biological targets investigated here were scaled so that their calculated Koopmans ionization energy, i.e. the ionization energy of their highest occupied molecular orbital (HOMO), coincides with experimental values available in the literature. More details are given in Ref. [7]. In all simulations performed in this work, we have considered hydrated DNA with a density of  $1.29 \text{ g cm}^{-3}$ . In this case, a typical nucleotide is described by the following fractions : 0.58 for adenine and thymine, 0.42 for cytosine and guanine, 2 for the sugar-phosphate group and 18 for water. The rationale behind these quantities can be found in Ref. [4].

The main theoretical framework to calculate the inelastic cross sections used in *TILDA-V* is the perturbative method known as continuum distorted wave-eikonal initial state approximation (CDW-EIS). The method has been successfully applied to investigate the ionization and electron capture processes in ion-molecule collisions [10, 11, 12].

On the other hand, the excitation and electron loss processes are essentially based on a semi-empirical approach developed by Miller and Green [13]. For proton excitation, we used the set of parameters suggested by Dingfelder *et al.* [14]. The excitation by  $\text{H}^0$  follows the

Particle	Process	Model
Proton	Ionization	<i>Prior</i> CDW-EIS [10]
	Capture	<i>Prior</i> CDW-EIS [11]
	Excitation	Miller and Green [4, 13, 14]
	Elastic scattering	Classical description [16]
Hydrogen	Ionization	<i>Prior</i> CDW-EIS [12]
	Excitation	Miller and Green [4, 13, 15]
	Electron loss	Miller and Green [4, 13]
	Elastic scattering	Classical description [17]
Electron	Ionization	DWBA [18]
	Excitation	Olivero [19]
	Elastic scattering	Partial wave formalism [20]

TABLE 1: Set of models used in *TILDA-V* for the present calculations. CDW-EIS : Continuum distorted wave-eikonal initial state approximation ; DWBA : Distorted-wave Born approximation.

approach of Uehara *et al.* [15] who assumed that for  $H^0$  one of the fitting parameters in the Miller and Green model is changed to 3/4 of the proton value.

Finally, the proton-induced elastic scattering cross sections are computed from the classical mechanical theory [16]. For  $H^0$ , we applied the cross section ratio proposed by Endo *et al.* [17].

For the secondary electrons, the ionization process is treated within the distorted-wave Born approximation [18]. The cross sections for excitation by electron impact are obtained with the semi-empirical method of Olivero *et al.* [19]. Regarding the elastic scattering process for electrons, the cross sections calculations are performed in the partial-wave formalism [20].

Table 1 provides a summary of the interactions and models considered for each type of projectile. For more details, the reader is referred to the references mentioned above.

Figure 2 shows the inelastic TCS for protons and neutral hydrogen atoms impinging on the water (panel a) and DNA (panel b) targets.

### 3 Results

Figure 3 presents the total electronic stopping power (SP) for protons in water and DNA, as provided by *TILDA-V*. The SP was obtained by simulating  $10^6$  projectiles (both  $H^+$  and  $H^0$ ) in stationary mode for each incident energy. In this mode, each primary particle is followed until it experiences an interaction with the medium. A sum over the energy loss and the distance traveled by each particle is carried out and the SP in keV/ $\mu\text{m}$  is computed for each type of projectile as

$$SP = \frac{E_{\text{tot}}}{L}, \quad (1)$$

where  $E_{\text{tot}}$  is the total energy lost by the projectiles and  $L$  is the track length. The total SP is obtained by adding the contributions of  $H^+$  and  $H^0$ , that is

$$SP = f_{H^+}(SP)_{H^+} + f_{H^0}(SP)_{H^0}, \quad (2)$$

where  $(SP)_{H^+}$  and  $(SP)_{H^0}$  refer to the electronic stopping power for the charged and neutral beams, respec-

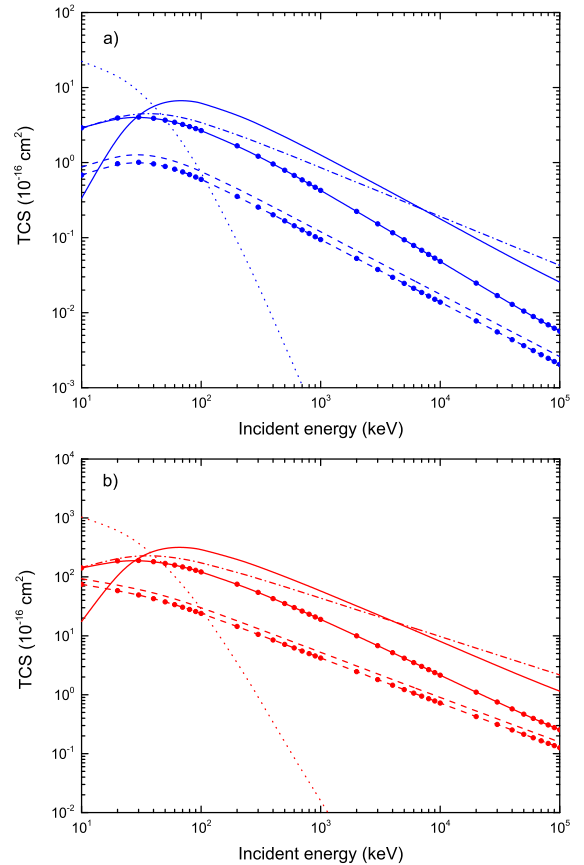


FIGURE 2: Inelastic TCS for  $H^+$  and  $H^0$  in water (panel a) and hydrated DNA (panel b). In both cases the TCS for ionization by  $H^+$  (solid line), ionization by  $H^0$  (solid line with circles), excitation by  $H^+$  (dashed line), excitation by  $H^0$  (dashed line with circles), electron capture (dotted line) and electron loss (dash-dotted line) are shown.

tively. The factors  $f_{H^+}$  and  $f_{H^0}$  are the corresponding equilibrium charge fractions which can be written as [29]

$$f_{H^+} = \frac{\sigma_L}{\sigma_L + \sigma_C} \quad (3)$$

and

$$f_{H^0} = \frac{\sigma_C}{\sigma_L + \sigma_C}, \quad (4)$$

where  $\sigma_L$  and  $\sigma_C$  denote the TCS for electron loss and electron capture, respectively.

As observed in Figure 3, our results for water have been compared with the available experimental data both for water vapor and liquid water. A good agreement is observed between our SP values for water and the corresponding experimental data for incident proton energies  $E_{\text{inc}} > 30$  keV. However, for  $E_{\text{inc}} < 30$  keV our results underestimate the experimental values, a behavior that can be attributed to the limitations of the *prior* CDW-EIS approach.

Since for DNA there is currently no available experimental data, we have plotted in Figure 3 the values computed by Abril *et al.* [27] and Tan *et al.* [28]. Both research groups considered dry DNA with a density of  $1.35 \text{ g cm}^{-3}$  and performed their calculations within

the dielectric formalism, but using different extension schemes. It can be observed that there are important differences between our results and their predictions for  $E_{\text{inc}} < 200$  keV. According to our calculations, the maximum stopping power for water ( $97.5 \text{ keV}/\mu\text{m}$ ) and DNA ( $110 \text{ keV}/\mu\text{m}$ ) is obtained for  $E_{\text{inc}} = 70$  keV, with a difference of about 13% between both media.

## 4 From protons to $\alpha$ particles : the role of TAT

The extension of *TILDA-V* to include the interactions of  $\alpha$  particles is under way. Once this work is completed, studies on radiation microdosimetry will be carried out with the purpose of describing the energy deposition in cells following the irradiation with  $\alpha$  particles. Such a description is of importance to assess the therapeutic potential of several  $\alpha$ -emitting radionuclides that are being considered for targeted alpha therapy (TAT).

TAT is a promising therapeutic approach to treat cancer in which  $\alpha$ -emitting radionuclides are combined with a targeting agent in order to reach and selectively irradiate the tumoral tissue. The targeting vector is normally a monoclonal antibody, a peptide or small molecules. The effectiveness of TAT is based on the ability of  $\alpha$  particles to deliver a very localized radiation dose, since they have a short range in matter (50–100  $\mu\text{m}$ ) and a high linear energy transfer (LET) ( $\sim 100 \text{ keV}/\mu\text{m}$ ), leaving behind them a densely ionizing track

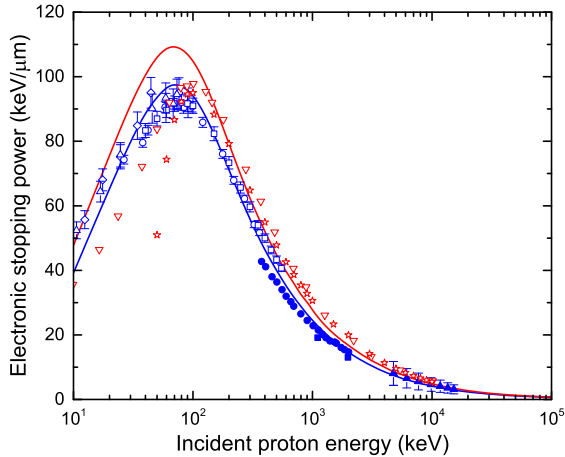


FIGURE 3: Total electronic stopping power for protons in water (solid blue line) and DNA (solid red line). Experimental data for water vapor are shown in open blue symbols and are taken from : Reynolds et al. [21] (squares), Phillips [22] (triangles), Mitterschiffthaler and Bauer [23] (circles) and Baek et al. [24] (diamonds). Measurements for liquid water are shown in solid blue symbols and are taken from : Shimizu et al. [25] (circles) and Siiskonen et al. [26] (triangles). For DNA, the calculations performed by Abril et al. [27] (open inverted red triangles) and Tan et al. [28] (open red stars) are shown for comparison.

Radionuclide	Properties	Potential applications
$^{223}\text{Ra}$	Half-life of 11.4 days. Total energy/decay $\sim 28$ MeV. Bone-seeker radionuclide [35].	Castration-resistant prostate cancer with symptomatic bone metastases but no visceral disease [36].
$^{211}\text{At}$	Half-life of 7.2 hours. $\sim 99\%$ of all energy emitted as $\alpha$ particles [37]. One $\alpha$ particle per decay of $\sim 7.5$ MeV.	Ovarian cancer, brain tumors, breast cancer [38, 39, 40].
$^{212}\text{Pb}/^{212}\text{Bi}$	$^{212}\text{Pb}$ (half-life 10.6 h) is a $\beta^-$ emitter used as an <i>in vivo</i> generator of the $\alpha$ emitter $^{212}\text{Bi}$ (half-life 60.6 min) [41]. One $\alpha$ particle per decay of $\sim 8.8$ MeV.	Ovarian cancer with peritoneal metastases [42].
$^{225}\text{Ac}$	Half-life of $\sim 10$ days. 4 $\alpha$ particles per decay with a total energy of 28 MeV.	Castration-resistant prostate cancer [43] and leukemia [44].
$^{213}\text{Bi}$	Half-life of 46 min. One $\alpha$ particle per decay of $\sim 8.4$ MeV [45].	Ovarian and prostate cancer, brain tumors, neuroendocrine tumors, among other cancers [46].

TABLE 2: Some promising  $\alpha$ -emitting radionuclides for TAT.

structure [30, 31]. Therefore, they can effectively destroy malignant cells without compromising the surrounding healthy tissue. Cell death can occur after only a few hits, although it has been shown that mammalian cells could survive single high-LET particle traversals in the cell nucleus [32, 33]. The short range of  $\alpha$  particles make TAT an ideal technique to fight micrometastases and residual disease [34].

However, only a few  $\alpha$  emitters are currently being considered for TAT because of constraints related to the half-life and production costs of the radionuclides, among other factors. Table 2 shows the properties and potential applications of some interesting  $\alpha$  emitters for TAT.

## Conclusion

The stopping power for protons of 10 keV–100 MeV in water and DNA has been computed with the Monte Carlo track-structure code *TILDA-V*. Important differences between the stopping power of both media have been underlined. This seems to support the idea that in this context the use of water as a surrogate for living matter, even applying density rescaling procedures, is not appropriate to describe the biological reality.

The validity of our approach has been confirmed by comparing our results with available experimental and theoretical data in the literature.

## Acknowledgments

We thank the CNRS for its financial support through its competitive funding programs for interdisciplinary research.

## Références

- [1] Nikjoo H, Uehara S, Emfietzoglou D, Cucinotta FA (2006) Track-structure codes in radiation research. *Radiat Meas* 41 :1052–1074. doi : 10.1016/j.radmeas.2006.02.001
- [2] Lazarakis P, Incerti S, Ivanchenko V, Kyriakou I, Emfietzoglou D, Corde S, Rosenfeld AB, Lerch M, Tehei M, Guatelli S (2018) Investigation of track structure and condensed history physics models for applications in radiation dosimetry on a micro and nano scale in Geant4. *Biomed Phys Eng Express* 4 :024001. doi : 10.1088/2057-1976/aaa6aa
- [3] Nikjoo H, Emfietzoglou D, Liamsuwan T, Taleei R, Liljequist D, Uehara S (2016) Radiation track, DNA damage and response-a review. *Rep Prog Phys* 79 :116601. doi : 10.1088/0034-4885/79/11/116601
- [4] Quinto MA, Monti JM, Weck PF, Fojón OA, Hanssen J, Rivarola RD, Senot P, Champion C (2017) Monte Carlo simulation of proton track structure in biological matter. *Eur Phys J D* 71 :130. doi : 10.1140/epjd/e2017-70709-6
- [5] Champion C, Le Loirec C, Stosic B (2012) EPO-TRAN : A full-differential Monte Carlo code for electron and positron transport in liquid and gaseous water. *Int J Radiat Biol* 88 :54–61. doi : 10.3109/09553002.2011.641451
- [6] Moccia R (1964) One-Center Basis Set SCF MO's. III. H<sub>2</sub>O, H<sub>2</sub>S, and HCl. *J Chem Phys* 40 :2186–2192. doi : 10.1063/1.1725491
- [7] Galassi ME, Champion C, Weck PF, Rivarola RD, Fojón O, Hanssen J (2012) Quantum-mechanical predictions of DNA and RNA ionization by energetic proton beams. *Phys Med Biol* 57 :2081–2099. doi : 10.1088/0031-9155/57/7/2081
- [8] M. J. Frisch, G. Trucks, H. B Schlegel, G. E Scuseria, M. Robb, J. Cheeseman, G. Scalmani, V. Barone, B. Mennucci, G. A. H. Petersson, H. Nakatsuji, M. Caricato, X. Li, H. P Hratchian, A. F Izmaylov, J. Bloino, G. Zheng, J. Sonnenberg, M. Hada, D. Fox, Gaussian 09 (revision A02), Gaussian Inc. Wallingford CT.
- [9] Mulliken RS (1955) Electronic Population Analysis on LCAO-MO Molecular Wave Functions. I. *J Chem Phys* 23 :1833–1840. doi : 10.1063/1.1740588
- [10] Monti JM, Tachino CA, Hanssen J, Fojón OA, Galassi ME, Champion C, Rivarola RD (2014) Distorted wave calculations for electron loss process induced by bare ion impact on biological targets. *Appl Radiat Isot* 83 :105–108. doi : 10.1016/j.apradiso.2012.12.016
- [11] Quinto MA, Montenegro PR, Monti JM, Fojón OA, Rivarola RD (2018) Electron capture by swift ions from molecules of biological interest. *J Phys B At Mol Opt Phys* 51 :165201. doi : 10.1088/1361-6455/aad152
- [12] M. A. Quinto, J. M. Monti, C. Champion, R. D. Rivarola, Neutral-hydrogen versus proton induced ionization in water vapor, *Journal of Physics B Atomic Molecular Physics* (In press).
- [13] Miller JH, Green AES (1973) Proton Energy Degradation in Water Vapor. *Radiat Res* 54 :343. doi : 10.2307/3573730
- [14] Dingfelder M, Inokuti M, Paretzke HG (2000) Inelastic-collision cross sections of liquid water for interactions of energetic protons. *Radiat Phys Chem* 59 :255–275
- [15] Uehara S, Toburen LH, Wilson WE, Goodhead DT, Nikjoo H (2000) Calculations of electronic stopping cross sections for low-energy protons in water. *Radiat Phys Chem* 59 :1–11. doi : 10.1016/S0969-806X(00)00190-0
- [16] Champion C, Incerti S, Tran HN, El Bitar Z (2012) Electron and proton elastic scattering in water vapour. *Nucl Instrum Methods Phys Res Sect B Beam Interact Mater At* 273 :98–101. doi : 10.1016/j.nimb.2011.07.049
- [17] Endo S, Yoshida E, Nikjoo H, Uehara S, Hoshi M, Ishikawa M, Shizuma K (2002) A Monte Carlo track structure code for low energy protons. *Nucl Instrum Methods Phys Res Sect B Beam Interact Mater At* 194 :123–131 . doi : 10.1016/S0168-583X(02)00497-4
- [18] Champion C, Cappello CD, Houamer S, Mansouri A (2006) Single ionization of the water molecule by electron impact : Angular distributions at low incident energy. *Phys Rev A* 73 :012717. doi : 10.1103/PhysRevA.73.012717
- [19] Olivero JJ, Stagat RW, Green AES (1972) Electron deposition in water vapor, with atmospheric applications. *J Geophys Res* 77 :4797–4811. doi : 10.1029/JA077i025p04797
- [20] Aouchiche H, Champion C, Oubaziz D (2008) Electron and positron elastic scattering in gaseous and liquid water : A comparative study. *Radiat Phys Chem* 77 :107–114. doi : 10.1016/j.radphyschem.2007.09.004
- [21] Reynolds HK, Dunbar DNF, Wenzel WA, Whaling W (1953) The Stopping Cross Section of Gases for Protons, 30-600 keV. *Phys Rev* 92 :742–748. doi : 10.1103/PhysRev.92.742
- [22] Phillips JA (1953) The Energy Loss of Low Energy Protons in Some Gases. *Phys Rev* 90 :532–537. doi : 10.1103/PhysRev.90.532
- [23] Mitterschiffthaler C, Bauer P (1990) Stopping cross section of water vapor for hydrogen ions. *Nucl Instrum Methods Phys Res Sect B Beam Interact Mater At* 48 :58–60. doi : 10.1016/0168-583X(90)90073-4

- [24] Baek WY, Grosswendt B, Willems G (2006) Ionization ranges of protons in water vapour in the energy range 1-100 keV. *Radiat Prot Dosimetry* 122 :32–35. doi : 10.1093/rpd/ncl514
- [25] Shimizu M, Hayakawa T, Kaneda M, Tsuchida H, Itoh A (2010) Stopping cross-sections of liquid water for 0.3-2.0 MeV protons. *Vacuum* 84 :1002–1004. doi : 10.1016/j.vacuum.2009.11.019
- [26] Siiskonen T, Kettunen H, Peräjärvi K, Javanainen A, Rossi M, Trzaska WH, Turunen J, Virtanen A (2011) Energy loss measurement of protons in liquid water. *Phys Med Biol* 56 :2367–2374. doi : 10.1088/0031-9155/56/8/003
- [27] Abril I, Garcia-Molina R, Denton CD, Kyriakou I, Emfietzoglou D (2011) Energy loss of hydrogen- and helium-ion beams in DNA : calculations based on a realistic energy-loss function of the target. *Radiat Res* 175 :247–255
- [28] Tan Z, Xia Y, Zhao M, Liu X (2006) Proton stopping power in a group of bioorganic compounds over the energy range of 0.05-10 MeV. *Nucl Instrum Methods Phys Res Sect B Beam Interact Mater At* 248 :1–6. doi : 10.1016/j.nimb.2006.04.073
- [29] Rivarola RD, Galassi ME, Fainstein PD, Champion C (2013) Computation of Distorted Wave Cross Sections for High-Energy Inelastic Collisions of Heavy Ions with Water Molecules. In : *Advances in Quantum Chemistry*. Elsevier, pp 231–267
- [30] Kim Y-S, Brechbiel MW (2012) An overview of targeted alpha therapy. *Tumor Biol* 33 :573–590. doi : 10.1007/s13277-011-0286-y
- [31] Elgqvist J, Frost S, Pouget J-P, Albertsson P (2014) The Potential and Hurdles of Targeted Alpha Therapy - Clinical Trials and Beyond. *Front Oncol* 3. doi : 10.3389/fonc.2013.00324
- [32] Miller RC, Randers-Pehrson G, Geard CR, Hall EJ, Brenner DJ (1999) The oncogenic transforming potential of the passage of single particles through mammalian cell nuclei. *Proc Natl Acad Sci* 96 :19–22. doi : 10.1073/pnas.96.1.19
- [33] Fournier C, Zahnreich S, Kraft D, Friedrich T, Voss K-O, Durante M, Ritter S (2012) The Fate of a Normal Human Cell Traversed by a Single Charged Particle. *Sci Rep* 2. doi : 10.1038/srep00643
- [34] Yong K, Brechbiel M (2015) Application of  $^{212}\text{Pb}$  for Targeted  $\alpha$ -particle Therapy (TAT) : Pre-clinical and Mechanistic Understanding through to Clinical Translation. *AIMS Med Sci* 2 :228–245. doi : 10.3934/medsci.2015.3.228
- [35] Vaidyanathan G, R. Zalutsky M (2011) Applications of  $^{211}\text{At}$  and  $^{223}\text{Ra}$  in Targeted Alpha-Particle Radiotherapy. *Curr Radiopharm* 4 :283–294. doi : 10.2174/1874471011104040283
- [36] Vogelzang NJ (2017) Radium-223 dichloride for the treatment of castration-resistant prostate cancer with symptomatic bone metastases. *Expert Rev Clin Pharmacol* 10 :809–819. doi : 10.1080/17512433.2017.1345624
- [37] Larsen RH, Murud KM, Akabani G, Hoff P (1999)  $^{211}\text{At}$ - and  $^{131}\text{I}$ -Labeled Bisphosphonates with High In Vivo Stability and Bone Accumulation. *J Nucl Med* 40 :1197–1203
- [38] Andersson H, Cederkrantz E, Back T, Divgi C, Elgqvist J, Himmelman J, Horvath G, Jacobsson L, Jensen H, Lindegren S, Palm S, Hultborn R (2009) Intraperitoneal  $\alpha$ -Particle Radioimmunotherapy of Ovarian Cancer Patients : Pharmacokinetics and Dosimetry of  $^{211}\text{At}$ -MX35 F(ab')<sub>2</sub>-A Phase I Study. *J Nucl Med* 50 :1153–1160. doi : 10.2967/jnumed.109.062604
- [39] Zalutsky MR, Reardon DA, Akabani G, Coleman RE, Friedman AH, Friedman HS, McLendon RE, Wong TZ, Bigner DD (2007) Clinical Experience with  $\alpha$ -Particle Emitting  $^{211}\text{At}$  : Treatment of Recurrent Brain Tumor Patients with  $^{211}\text{At}$ -Labeled Chimeric Antitumescin Monoclonal Antibody 81C6. *J Nucl Med* 49 :30–38. doi : 10.2967/jnumed.107.046938
- [40] Robinson MK, Shaller C, Garmestani K, Plascjak PS, Hodge KM, Yuan Q-A, Marks JD, Waldmann TA, Brechbiel MW, Adams GP (2008) Effective Treatment of Established Human Breast Tumor Xenografts in Immunodeficient Mice with a Single Dose of the  $\alpha$ -Emitting Radioisotope Astatine-211 Conjugated to Anti-HER2/neu Diabodies. *Clin Cancer Res* 14 :875–882. doi : 10.1158/1078-0432.CCR-07-1250
- [41] Weström S, Generalov R, Bønsdorff TB, Larsen RH (2017) Preparation of  $^{212}\text{Pb}$ -labeled monoclonal antibody using a novel  $^{224}\text{Ra}$ -based generator solution. *Nucl Med Biol* 51 :1–9. doi : 10.1016/j.nucmedbio.2017.04.005
- [42] Meredith RF, Torgue J, Azure MT, Shen S, Saddekni S, Banaga E, Carlise R, Bunch P, Yoder D, Alvarez R (2014) Pharmacokinetics and Imaging of  $^{212}\text{Pb}$ -TCMC-Trastuzumab After Intraperitoneal Administration in Ovarian Cancer Patients. *Cancer Biother Radiopharm* 29 :12–17. doi : 10.1089/cbr.2013.1531
- [43] Kratochwil C, Bruchertseifer F, Rathke H, Hohenfellner M, Giesel FL, Haberkorn U, Morgenstern A (2018) Targeted  $\alpha$ -Therapy of Metastatic Castration-Resistant Prostate Cancer with  $^{225}\text{Ac}$ -PSMA-617 : Swimmer-Plot Analysis Suggests Efficacy Regarding Duration of Tumor Control. *J Nucl Med* 59 :795–802. doi : 10.2967/jnumed.117.203539
- [44] Jurcic JG, Levy MY, Park JH, Ravandi F, Perl AE, Pagel JM, Smith BD, Estey EH, Kantarjian H, Cicic D, Scheinberg DA (2016) Phase I Trial of Targeted Alpha-Particle Therapy with Actinium-225 ( $^{225}\text{Ac}$ )-Lintuzumab and Low-Dose Cytarabine (LDAC) in Patients Age 60 or Older with Untreated Acute Myeloid Leukemia (AML). *Blood* 128 :4050
- [45] Morgenstern A, Bruchertseifer F, Apostolidis C (2012) Bismuth-213 and actinium-225-generator performance and evolving therapeutic applications

of two generator-derived alpha-emitting radioisotopes. *Curr Radiopharm* 5 :221–227

- [46] Dekempeneer Y, Keyaerts M, Krasniqi A, Puttemans J, Muyldermans S, Lahoutte T, D’huyvetter M, Devoogdt N (2016) Targeted alpha therapy using short-lived alpha-particles and the promise of nanobodies as targeting vehicle. *Expert Opin Biol Ther* 16 :1035–1047. doi : 10.1080/14712598.2016.1185412



# A 1D model of tumor cell migration with polarization : numerical and analytical study

Enzo FABIANI, Christophe DEROULERS

Université Paris Diderot, Paris



## Résumé

Poor medical prognosis leads us to take up the challenge of understanding the tumor growth mechanisms, helping the surgeon to delimit the infiltration of the disease and improving his exeresis, prescribed in 14 out of 16 brain tumor types. It is believed that the recurrences of some tumors after surgery are due to remnant infiltrated and undetectable tumor cells away from the tumor mass. Thus, to improve treatments, it may be useful to have good predictions of the spatial distribution of infiltrated cells, which relies on a faithful model of collective motion of cells in crowded environments. Here, we build a one-dimensional stochastic model, discrete in space and time, of migrating tumor cells which takes the biological phenomena of polarization and depolarization into account. Cells interact locally by exclusion (they can't penetrate each other). Our model has only three parameters, describing the behavior of individual cells. Then we study it by direct Monte Carlo simulations. We derive analytically an approximate continuum limit, which takes the form of a deterministic (nonlinear) partial differential equation for the cell density, allowing for quick predictions without relying on lengthy computer simulations. We successfully compare the two approaches, at least in the case of weak interactions between cells. We predict that, for some values of the parameters, aggregates of cells should form, even in absence of attraction or adhesion, as a consequence of emergent collective effects.

## 1 Introduction

Among the 74,000 brain tumors diagnosed in the US every year, 23,700 are malignant, which means, in the present state of treatments efficiency, that the survival rate after 5 years is at best of 1 out of 2 [1]. The World Health Organization has classified [2] all known brain tumors in different grades of malignancy, from the low grades (I and II), at a less advanced mutation state, to the high grades (III and IV), at a more advanced one. However, even tumors of grade II are observed to transform inevitably into higher grade tumors, more aggressive and growing faster [2]. Brain tumor diagnosis relies mainly on radiological examination (CT scan, MRI) with confirmation by histology (biopsies). The common therapeutic strategies, depending on the tumor type, are exeresis (surgery), prescribed in 14 out of 16 brain tumor types [3], chemotherapy, radiotherapy, and a multimodal combination. Nevertheless, in

the case of the so-called *diffuse* or *infiltrating* gliomas (gliomas are a type of brain tumor which is thought to be originating in glial cells), isolated tumor cells may be found several centimeters away from the region where their concentration is maximal. These disseminated cells can't be detected even by the most powerful MRI devices, let alone by routine clinical MRI devices. Of course, they can't also be seen by the surgeon's eyes. Thus, after surgery, except if the tumor is removed with very wide margins with respect to what appears as a signal abnormality on MRIs, living tumor cells remain in the brain. Usually, the margins of tumor resection are limited by the risk of impairing the patient's life if part of his/her functional brain tissue is removed. The remaining tumor cells are the cause of recurrences, *i.e.* regrowth of tumors away from the initial tumor, which finally lead to the patient's death. This dissemination of tumor cells is probably due to the migration of cells, which is easily observed in *in vitro* experiments and has some evidence *in vivo* [4, 5].

Therefore, understanding the migration and being able to predict the position of cells at different times during tumor development may be quite helpful to improve the treatments, *e.g.* by guiding the surgery or the adjuvant radiotherapy. Building a mathematical model of this migration is the purpose of the present work, which, for simplicity, will neglect other key biological phenomena involved in tumor growth, such as proliferation and apoptosis seen in Figure 1. Previous models for the migration of cells have been proposed [7], but they considered cells as objects with a fixed, sphere-like shape. In contrast, here we take into account the variation of shape of the cells during migration, along with the persistence of the direction of migration (instead of a continuously changing direction of motion), due to the phenomenon of cell polarization. The variation of the shape of cells should play an important role in crowded environments either in healthy or tumoral brain tissue, because they impose steric constraints on the movement of cells.

Indeed, during cell motion, the typical RhoGTPases proteins—made of RhoA, Rac1 and Cdc42—maintain cell polarity by acting on the cytoskeleton dynamics [8, 9]. In polarized cells, at the front, Rac1 and Cdc42 activate the formation of cell protrusions, and at the back, RhoA activates cell contraction. These simultaneous protrusion and contraction yield the movement of the cell. More generally, cells can be in two states : compact, with little or no mobility, and extended (polarized), with maximal speed [15].

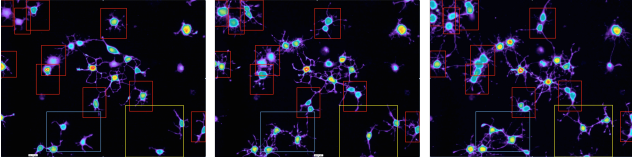


FIGURE 1: Fluorescence microscopy image of a cell culture of mice Oligodendrocyte Precursor Cells (OPC) *in vitro* at  $t=0h$ ,  $t=12h$ , and  $t=24h$  (from the left to the right). Real height of the whole image is  $708\mu m$ . The red squares show the proliferation processes, and the yellow squares show the formation of the protuberances (*lamellipodium*, *filopodia*) of the cell in the migration process. Source : Olivier SEKSEK (2017), IMNC - UMR8165 (CNRS).

Our model for cell migration with polarization and depolarization is formulated as a cellular automaton. The first studies on cellular automata were introduced by S. Ulam and J. von Neumann in the 1940s [10, 11] and have later been popularized with J. Conway's *Game of Life* [12]. Such a model is a stochastic process and can be described as a discrete time-depending system of cells (or boxes) in a fixed numbers of states, evolving by iterations according to trivial rules. The simplicity of the rules has many advantages and makes these models powerful tools to study collective effects in large assemblies of individuals (like a population of tumor cells) : it allows for an easy formulation of the model, for very quick computer simulations, and for easy analytical approximations in the continuum limit [13] (establishing equations for the whole population seen as a kind of fluid). And, even with simple rules, complex phenomena can arise because of the number of constituents.

## 2 Model

In our case, tumor cells are the fundamental entities of the cellular automaton (we do not take into account intracellular dynamics or changes of genetic expression, for instance). The rules reflect the individual behavior of the cells (polarization, motion, depolarization) and their interaction with the nearest neighbors (cells can't penetrate each other).

Space is discretized as a 1D ring of  $L$  boxes/sites. Each site is occupied by a number of cells denoted with  $S(i, t)$  at time  $t$  on site  $i$ . The total number of cells,  $N$ , is constant during time evolution. Each cell is in one of the three following states : compact, extended (+), or extended (-). A compact cell is motionless and is counted as 1 on the only site it occupies. A polarized cell occupies two nearest-neighbor sites and is counted as  $1/2$  on each of the two sites it occupies. We choose a real number  $E$  between 0 and 1 to interpolate between the situation of penetrating cells (when  $E = 0$ ) and a cellular automaton with exclusion (when  $E = 1$ ; two cells cannot occupy the same site, therefore one site is occupied by zero cell, or one compact cell, or one half

of a polarized cell). A typical configuration for  $E = 1$  is shown in Figure 2.

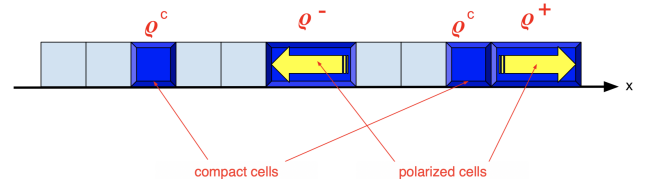


FIGURE 2: A typical configuration of our 1D cellular automaton. Only part of the finite ring is displayed.

Time is also discrete and the evolution of the automaton takes place asynchronously according to the random shuffle scheme [14] : before each time step, the order in which each of the  $N$  cells will have an opportunity to evolve is drawn uniformly at random among the  $N!$  permutations. Then each cell is examined at its turn.

The automaton involves three real parameters  $t_{c \rightarrow e}$ ,  $t_{e \rightarrow c}$ , and  $t_D$ , fixed between 0 and 1. An extended ("e", either "+" or "-") cell retracts into a compact ("c") cell with probability  $t_{e \rightarrow c}$ . Reciprocally, a compact cell can become extended with a probability  $t_{c \rightarrow e}$ . Finally, a polarized cell has the probability  $t_D$  to try to jump in the polarity migration direction.

In more details : if the cell is compact (and sitting on site number, say,  $i$ ), a random number  $u$  is uniformly drawn between 0 and 1 and, if  $u < t_{c \rightarrow e}/2$ , the cell attempts to polarize as a "+" cell (and therefore occupy sites  $i$  and  $i + 1$ ). If  $t_{c \rightarrow e}/2 \leq u < t_{c \rightarrow e}$ , the cell attempts to polarize as a "-" cell (and therefore occupy sites  $i$  and  $i - 1$ ). Otherwise, the cell does not evolve. An "attempt" to polarize means that the actual polarization takes place with probability 1 if the site where the cell should extend ( $i + 1$  or  $i - 1$ ) is empty, and with probability  $1 - E$  if this site is full (this is achieved by drawing at random another number  $u'$  uniformly between 0 and 1).

If the cell instead is polarized, a random number  $u$  is uniformly drawn between 0 and 1. If  $u < t_{e \rightarrow c}$ , the cell depolarizes, changing its state to "compact". If the cell was polarized in the direction + (resp. -) and occupied sites  $i$  and  $i + 1$  (resp.  $i - 1$ ), it frees the site  $i + 1$  (resp.  $i - 1$ ) and occupies only site  $i$  after this move.

If  $t_{e \rightarrow c} \leq u < t_{e \rightarrow c} + t_D$ , the cell attempts to move by one site in its direction of polarization. For instance, if the cell is in the state "+" and occupied sites  $i$  and  $i + 1$ , it attempts to move to sites  $i + 1$  and  $i + 2$ . An "attempt" to move means that the actual movement takes place with probability 1 if site  $i + 2$  is empty, and with probability  $1 - E$  if this site is full. Otherwise, the cell does not evolve.

We used two kinds of initial conditions. In the first one, the positions of the  $N$  cells are drawn uniformly at random.

In the second kind of initial conditions, all cells are in the compact state and put on  $N$  contiguous sites at the center of the system : at (initial) time 0,  $S(i, 0) = 1$  if  $|i| \leq N/2$ , and 0 otherwise. Since the evolution of the

cellular automaton is a stochastic process,  $S(i, t)$  is a random variable, and we average it over  $N_s = 100,000$  statistically independent simulations to drastically reduce fluctuations. The resulting density profile, displayed on Figure 3, reminds one of a diffusion process.

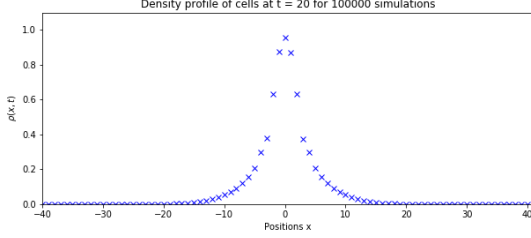


FIGURE 3: The density profile at time  $t = 20$  (average of  $\rho(x, t)$  of  $S(x, 20)$  over  $N_s = 100,000$  simulations, plotted as a function of the site number  $x$ ), from an initial set of 7 compact cells in the middle of the 1D-chain, with  $t_{c \rightarrow e} = t_{e \rightarrow c} = 0.3$ , and  $E = 1$ .

In the next Section, we compute the so-called continuum limit [13] of our cellular automaton. This technique yields approximate, yet deterministic (and analytic) predictions for the cell density, without many repetitions of direct Monte Carlo simulations.

### 3 Continuum limit

To begin with, let's write approximate master equations for our stochastic process [13]. We define  $\rho_i^c(t)$  as the probability to find a compact cell on a site  $i$  at a time  $t$ , and  $\rho_{i+1/2}^+(t)$  (respectively  $\rho_{i-1/2}^-(t)$ ) the probability to find a polarized (+) (respectively polarized (-)) cell on the sites  $i$  and  $i + 1$  (respectively  $i$  and  $i - 1$ ) at a time  $t$ .

We use three approximations. (A1) Time is made continuous, and the probabilities  $t_{c \rightarrow e}$ ,  $t_{e \rightarrow c}$  and  $t_D$  are changed (with an abuse of notation) into transition rates (for instance, the probability of a jump during the infinitely short duration  $dt$  is taken to be  $t_D dt$ ). (A2) We assume that the processes of movement and depolarization happen in parallel (they are not mutually exclusive). (A3) We neglect correlations between the occupancies of nearest-neighbor sites (mean field approximation).

This leads to :

$$\begin{aligned} \partial_t \rho_{i+\frac{1}{2}}^+(t) = & \left[ \frac{t_{c \rightarrow e}}{2} \rho_i^c(t) + t_D \rho_{i-\frac{1}{2}}^+(t) \right] \times \\ & \left( 1 - E \left[ \rho_{i+1}^c(t) + \rho_{i+\frac{3}{2}}^+(t) + \rho_{i+\frac{3}{2}}^-(t) \right] \right) \\ - t_D \rho_{i+\frac{1}{2}}^+(t) & \left( 1 - E \left[ \rho_{i+2}^c(t) + \rho_{i+\frac{5}{2}}^+(t) + \rho_{i+\frac{5}{2}}^-(t) \right] \right) \\ & - t_{e \rightarrow c} \rho_{i+\frac{1}{2}}^+(t) \end{aligned} \quad (1)$$

$$\begin{aligned} \partial_t \rho_{i+\frac{1}{2}}^-(t) = & \left[ \frac{t_{c \rightarrow e}}{2} \rho_{i+1}^c(t) + t_D \rho_{i+\frac{3}{2}}^-(t) \right] \times \\ & \left( 1 - E \left[ \rho_i^c(t) + \rho_{i-\frac{1}{2}}^+(t) + \rho_{i-\frac{1}{2}}^-(t) \right] \right) \\ - t_D \rho_{i+\frac{1}{2}}^-(t) & \left( 1 - E \left[ \rho_{i+2}^c(t) + \rho_{i+\frac{5}{2}}^+(t) + \rho_{i+\frac{5}{2}}^-(t) \right] \right) \\ & - t_{e \rightarrow c} \rho_{i+\frac{1}{2}}^-(t) \end{aligned} \quad (2)$$

$$\begin{aligned} \partial_t \rho_i^c(t) = & t_{e \rightarrow c} \left[ \rho_{i+\frac{1}{2}}^+(t) + \rho_{i-\frac{1}{2}}^-(t) \right] - \frac{t_{c \rightarrow e}}{2} \rho_i^c(t) \times \\ & \left( 2 - E \left[ \rho_{i+1}^c(t) + \rho_{i-1}^c(t) + \rho_{i+\frac{3}{2}}^+(t) + \rho_{i+\frac{3}{2}}^-(t) \right. \right. \\ & \left. \left. + \rho_{i-\frac{3}{2}}^+(t) + \rho_{i-\frac{3}{2}}^-(t) \right] \right). \end{aligned} \quad (3)$$

Now we perform two additional approximations, to go to the continuum limit where we treat the population of cells as a kind of fluid. First, we assume that, at each time  $t$ , there are three differentiable functions of position  $x$ ,  $x \mapsto \tilde{\rho}^s(x, t)$  for  $s = c, +$ , or  $-$ , which interpolate the corresponding densities  $\rho_i^s(t)$  over non-integer values of  $i$ . Neglecting derivatives with respect to  $x$  of order 4 and more, we find from the master equations three partial differential equations for the  $\tilde{\rho}^c$ 's. Second, it turns out that the ratios  $\tilde{\rho}^+/\tilde{\rho}^-$  and  $\tilde{\rho}^+/\tilde{\rho}^c$ , at a given position  $x$ , reach a stationary value within a few time steps, while the total cell density  $\tilde{\rho}^{\text{tot}}(x, t)$ , defined as  $\tilde{\rho}^+ + \tilde{\rho}^- + \tilde{\rho}^c$ , evolves over longer time scales. Interested in the slow dynamics only, we approximate the two ratios by their stationary values, which fixes two out of the three densities. Finally, we proved that  $\tilde{\rho}^{\text{tot}}$  follows a nonlinear diffusion equation :

$$\partial_t \tilde{\rho}^{\text{tot}} = \partial_x \left( D_{\text{eff}} [\tilde{\rho}^{\text{tot}}(x, t)] \partial_x \tilde{\rho}^{\text{tot}}(x, t) \right) \quad (4)$$

where  $D_{\text{eff}}$  is the effective diffusivity of our continuous model.

### 4 Results and discussion

**Comparison to simulations.** To simplify and remove one parameter in our study, we restrict ourselves to the situation where  $t_D = 1 - t_{e \rightarrow c}$ . In the limit where  $E \rightarrow 0$  or  $\rho \rightarrow 0$  (vanishing interaction between cells), the effective diffusivity  $D_{\text{eff}}$  reads :

$$D_{\text{eff}} = \frac{1}{2} \frac{t_{c \rightarrow e} (2 - t_{e \rightarrow c}) (1 - t_{e \rightarrow c})}{t_{e \rightarrow c} + t_{c \rightarrow e}} \quad (5)$$

Let us compare this result to direct simulations of the automaton. We choose a low density  $\rho$  and low transition rates ( $t_{c \rightarrow e}, t_{e \rightarrow c} < 10\%$ ) to make sure that (A1-3) are valid. From the average Mean Square Displacement (MSD)  $\langle (x(t) - x(0))^2 \rangle$  of cells obtained in the simulation, we deduce an estimate of  $D_{\text{eff}}$  through  $2D_{\text{eff}}t = \langle x^2(t) \rangle$  [16], which is in very good agreement with (5) (see Figure 4).

**Possible aggregation.** In a diffusion process, the dif-

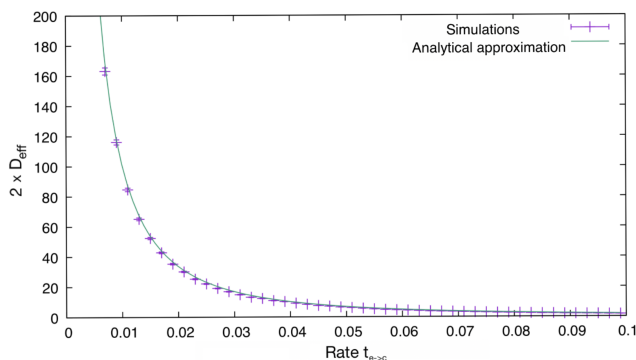


FIGURE 4: Diffusivity with vanishing interactions for a fixed rate  $t_{c \rightarrow e} = 0.01$ .

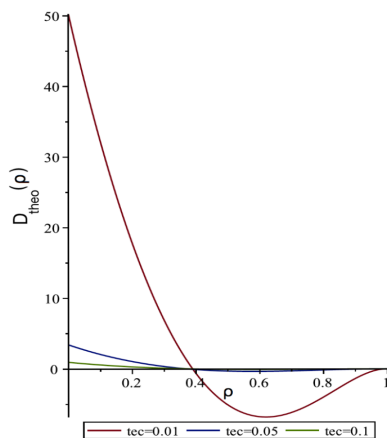


FIGURE 5: Approximate effective diffusivity  $D_{\text{eff}}$  as a function of cell density  $\rho$  for  $t_{c \rightarrow e} = 0.01$  and three values of  $t_{e \rightarrow c}$ . For  $t_{e \rightarrow c} = t_{c \rightarrow e} = 0.01$  when  $\rho \gtrsim 0.4$ ,  $D_{\text{eff}}$  takes negative values.

fusivity  $D$  is positive and particles tend to move away from their initial positions [16]. Finding negative values for  $D$  is a probable indication that formation of clusters of cells, instead of diffusion, takes place [17]. Here, far from the limit of vanishing interactions ( $E = 1$ , finite  $\rho$ ), our expression for  $D_{\text{eff}}$  can take negative values, as shown in Figure 5. In such a case, the cell population shouldn't remain uniformly distributed and cells should build aggregates. We are currently testing this prediction. However, the approximations leading to the continuum equation (4) will likely break down, and predicting analytically the collective behavior of the cells is be a challenge.

## 5 Conclusion

We introduced a stochastic model, discrete in space and time, for the motion of tumor cells, which takes the polarization and depolarization of cells, and the steric constraints they impose, into account. We derived analytically an approximate nonlinear diffusion equation for the density of cells, which can be used to predict directly the distribution of cells (at least in the case of low cell densities) without averaging over many expli-

cit Monte Carlo simulations. In absence of interactions between cells, we found a good agreement between this approximation and results from direct Monte Carlo simulations. We predict that cells should form aggregates for some values of the parameters of their motion and medium cell densities. We are now checking this prediction and working on an extension of our model to two-dimensional space.

## 6 Acknowledgments

EF thanks Olivier SEKSEK for providing the images of Fig. 1 and his work on OPC *in vitro* culture. EF's PhD thesis is financially supported by the CNRS/IN2P3. CD acknowledges financial support from the French Région Île-de-France through the DIM "Problématiques transversales aux systèmes complexes", grant number ISC-2014-PME-003.

## Références

- [1] Q. T. OSTROM, H. GITTLEMAN, J. XU, C. KROMER, Y. WOLINSKY, C. KRUCHKO, & J. S. BARNHOLTZ-SLOAN (2016). CBTRUS statistical report : primary brain and other central nervous system tumors diagnosed in the United States in 2009–2013. *Neuro-oncology*, 18(suppl 5), v1-v75.
- [2] N. LOUIS, A. PERRY, G. REIFENBERGER, A. VON DEIMLING, D. FIGARELLA -BRANGER, W. K. CAVENEE, H. OHGAKI, O. D. WIESTLER, P. KLEIHUES, & D. W. ELLISON (2016). The 2016 World Health Organization Classification of Tumors of the Central Nervous System : a summary. *Acta Neuropathologica*, 131(6) :803–820.
- [3] S. R. CHANDANA, S. MOVVA, M. ARORA, & T. SINGH (2008). Primary brain tumors in adults. *American family physician*, 77(10) :1423–1230.
- [4] P. FRIEDL & K. WOLF (2003). Tumour-cell invasion and migration : diversity and escape mechanisms. *Nature Reviews Cancer*, 3(5) :362–374.
- [5] A. F. CHAMBERS, A. C. GROOM & I. C. MACDONALD (2002). Dissemination and growth of cancer cells in metastatic sites. *Nature Reviews Cancer*, 2(8) :563–572.
- [6] P. SHARMA, K. SHEETS, S. ELANKUMARAN, & A. S. NAIN (2013). The mechanistic influence of aligned nanofibers on cell shape, migration and blebbing dynamics of glioma cells. *Integrative Biology*, 5(8) :1036–1044.
- [7] M. AUBERT, M. BADOUAL, S. FÉREOL, C. CHRISTOV, & B. GRAMMATICOS (2006). A cellular automaton model for the migration of glioma cells. *Physical Biology*, 3(2) :93.
- [8] O. PERTZ, L. HODGSON, R. KLEMKE, & K. HAHN (2006). Spatiotemporal dynamics of RhoA activity in migrating cells. *Nature*, 440 :1069–72.
- [9] K. ROTTNER, A. HALL, & J.V. SMALL (1999). Interplay between Rac and Rho in the control

- of substrate contact dynamics. *Current Biology*, 9(12) :640–648.
- [10] J. VON NEUMANN (1948). The general and logical theory of automata. *Cerebral Mechanisms in Behavior : The Hixon Symposium*, John Wiley & Sons, New York. 1–41.
- [11] J. VON NEUMANN (1966). Theory of self-reproducing automata. *University of Illinois Press*
- [12] M. GARDNER, Mathematical Games : the fantastic combinations of John Conway’s new solitaire game “ life ” (1970). *Scientific American*, 223, 120–123.
- [13] C. GARDINER (2009). Stochastic Methods. *Springer*.
- [14] C. APPERT-ROLLAND, J. CIVIDINI, & H. J. HILHORST (2011). Frozen shuffle update for a deterministic totally asymmetric simple exclusion process with open boundaries. *J. Stat. Mech.* 2011(10) :P10013.
- [15] A. M. JIMENEZ VALENCIA, P.-H. WU, O. N. YOGURTCU, P. RAO, J. DIGIACOMO, I. GODET, L. HE, M.-H. LEE, D. GILKES, S. X. SUN, & D. WIRTZ (2015). Collective cancer cell invasion induced by coordinated contractile stresses. *Oncotarget*, 6(41) :43438–43451.
- [16] F. SCHWABL (2006). Statistical Mechanics, Second Edition. *Springer*, 412–414.
- [17] P. ARGYRAKIS09, A. A. CHUMAK, M. MARAGAKIS, N. TSAKARIS (2009). Negative diffusion coefficient in a two-dimensional lattice-gas system with attractive nearest-neighbor interactions. *Physical Review B*, 80 :104203.



# Modelling of heavy ion transport in matter with entropic moment methods

**Erwan Olivier, Thanh-Hà Nguyen-Bui, Christophe Champion**  
*CELIA, Centre Lasers Intenses et Applications, Université de Bordeaux – CNRS – CEA,  
F-33405 Talence, France*

## Résumé

In this paper, we describe a method that allows fast and accurate simulations of the transport of protons in water. After an overview of the system of transport equations and the entropic closure relation, we present some results in terms of stopping power and dose deposited in water.

## 1 Introduction

In various cases, studying the behaviour of particle beams requires an accurate knowledge of the particle propagation through the medium of interest. Thus, many features can be calculated such as the deposited dose profiles. In principle, such calculations can be performed by solving the linear Boltzmann transport equation which generally describes the evolution across space and time of the distribution function in phase space for N-body system, under binary collisions. The transport of a system of particles is described by this equation, which is numerically too costly to be solved in short time. Up to now, alternative methods like pencil beam codes or fast Monte Carlo simulations are fast but low-accurate for the first one, and limited by the amount of needed statistics for the second one. In order to reduce the calculation time for simulations and preserve the solution accuracy, we use the moments method.

## 2 The deterministic code $M_1$

### 2.1 Boltzmann transport equation

The transport of particles in matter is governed by the Boltzmann equation. Let us briefly present some assumptions made to build the model. The interested reader will find more details in Refs. [1, 2].

- no collisions occur between transported particles;
- the transported particles have no effect on the background medium;
- the particles of the medium are assumed to be fixed;
- the flux of injected particles is assumed to be constant, the transport model can be assumed to be steady;
- collision features are entirely given by the cross section.

Moreover, we assume that the medium is cold, which is the case in several applications such as hadrontherapy.

Thus, these hypotheses allow us to consider the collisionless Boltzmann equation and to linearize it, leading to the linearized Boltzmann transport equation (LBTE). This so-called LBTE is presented hereafter.

For  $n$  different kinds of particles, we have to solve a system of  $n$  coupled transport equations :

$$\mathbf{\Omega} \cdot \nabla_x \psi_i + \sigma_{i,T} \psi_i = \rho \sum_{p=[i,j]} \int d\epsilon \int_{S^2} \sigma_{p,i}(\epsilon \rightarrow \epsilon', \mathbf{\Omega} \rightarrow \mathbf{\Omega}') \times \psi^i(\mathbf{r}, \epsilon, \mathbf{\Omega}) d\mathbf{\Omega} \quad (1)$$

with  $i$  and  $j$  the species (protons  $H^+$ , neutrals  $H^0$ ) of particles,  $\mathbf{r}$  the position vector,  $\epsilon$  the particle energy,  $\mathbf{\Omega}$  the flight direction,  $\psi$  the angular flux,  $\sigma_T$  the total cross section for each species and  $\sigma(\epsilon, \mathbf{\Omega})$  the differential cross section.

### 2.2 $M_1$ model

The  $M_1$  model aims at solving the LBTE, while allowing fast calculations needed for specific applications like Treatment Planning System (TPS) in radiotherapy. It was designed to model radiation transport, first for fires, then in plasmas and has been adapted for the relativistic electron transport ([3, 4]). More recently, its ability to simulate efficiently the transport of energetic particles has been demonstrated in the context of radiotherapy ([2, 5, 6]).

So,  $M_1$  allows the modelling of any species and process, the main requirement being the knowledge of cross sections for interactions involving the chosen particles. For our simulations, the inelastic processes (responsible for the slowing-down of particles) taken into account are :

- for protons : ionization [7], excitation [8] and electron capture [9];
- for neutrals : ionization [10, 11], excitation [12] and electron loss [13].

Let us note that the neutral population comes from the electron capture induced by proton beams. Similarly, the neutral beam becomes charged after the electron loss (*stripping*) process. These two populations are coupled but it is possible to run simulations only with one of them.

Then, averaging the transport equations over angles leads to moment equations. In general, we calculate the  $m$ -th moment by averaging  $m$  times over angle  $\mathbf{\Omega}$ . Such a moment is defined by :

$$\psi^m(\mathbf{x}, \epsilon) = 2\pi \int_{S^2} \underbrace{\boldsymbol{\Omega} \otimes \boldsymbol{\Omega} \cdots \otimes \boldsymbol{\Omega}}_{m \text{ times}} \psi(\mathbf{x}, \epsilon) d\boldsymbol{\Omega} \quad (2)$$

$\boldsymbol{\Omega}$  is the direction of flight, often written in spherical coordinates :  $\boldsymbol{\Omega} = (\mu, \sqrt{1-\mu^2} \cos \phi, \sqrt{1-\mu^2} \sin \phi)^T$ , where  $\mu = \cos \theta \in [-1, 1]$ ,  $\phi \in [0, 2\pi]$ . Moments do not depend on the azimuthal angle  $\phi$ , since the scattering center is assumed to be invariant under rotation around the initial direction of the incoming particle. Hence, one can write moments only involving the cosine of scattering angle  $\theta$  as follows :

$$\psi^m(\mathbf{x}, \epsilon) = 2\pi \int_{-1}^1 \mu^m \psi(\mathbf{x}, \epsilon, \mu) d\mu \quad (3)$$

Subsequently, all macroscopic quantities (number of particles, stopping power, dose) can be derived from moments.

The first three moments of the distribution function are :

$$\psi^0(\mathbf{x}, \epsilon) = \int_{S^2} \psi(\mathbf{x}, \epsilon, \boldsymbol{\Omega}) d\boldsymbol{\Omega} \quad (4)$$

$$\psi^1(\mathbf{x}, \epsilon) = \int_{S^2} \boldsymbol{\Omega} \cdot \psi(\mathbf{x}, \epsilon, \boldsymbol{\Omega}) d\boldsymbol{\Omega} \quad (5)$$

$$\psi^2(\mathbf{x}, \epsilon) = \int_{S^2} (\boldsymbol{\Omega} \otimes \boldsymbol{\Omega}) \psi(\mathbf{x}, \epsilon, \boldsymbol{\Omega}) d\boldsymbol{\Omega} \quad (6)$$

This approach leads to averaged equations with less degrees of freedom. Thus, both calculation time and computational memory are reduced, while keeping a good accuracy. Moreover, the closure relation involves Boltzmann's H-theorem whereby the entropy has to be maximized [14]. Thus, the closure of the system is linked to a strong physical principle.

### 2.3 Stopping power and deposited dose

The derivation of the closure relation is a constrained optimization problem. The solution is a Maxwellian distribution function :

$$\psi_{ME} = a_0 e^{-\boldsymbol{\Omega} \cdot \mathbf{a}_1}$$

with  $a_0 \geq 0$  et  $\mathbf{a}_1 \in \mathbb{R}^3$  (Lagrange's multipliers)

Finally, all the moments can be explicitly expressed by introducing an anisotropy factor, acting as an input parameter for our simulations.

We substitute now the exact integral operator described above by a Fokker-Planck operator, reflecting the continuous slowing-down approximation (CSDA), as shown by Pomraning ([15]). In this case, the transport equation reads :

$$\nabla_x \psi^{m+1} = \rho \frac{\partial}{\partial \epsilon} [S(\epsilon) \psi^m] + \rho L [T(\epsilon) \psi^m] \quad (7)$$

where  $\psi$  is the fluence of particles,  $S$  and  $T$  are respectively the stopping power of the medium for the particles and the angular dispersion coefficient of the beam, defined by :

$$S(\epsilon) = 2\pi \int_{\epsilon_{min}}^{\epsilon} \int_{-1}^1 \epsilon' \sigma(\epsilon, \epsilon', \mu) d\mu d\epsilon' \quad (8)$$

$$T(\epsilon) = 2\pi \int_0^{\epsilon} \int_{-1}^1 (1-\mu) \sigma(\epsilon, \epsilon', \mu) d\mu d\epsilon' \quad (9)$$

$S$  denotes the amount of kinetic energy loss by the particles while they travel through the medium and directly modulates the depth of energy deposition.  $T$  quantifies the straggling, due to successive deflections. These quantities can be calculated from the doubly differential cross sections  $\sigma(\epsilon, \epsilon', \mu)$ . Doubly-, singly-differential and total cross sections are calculated analytically in the framework of quantum mechanics, leading to a database of cross sections for inelastic processes involving  $H^+$  and  $H^0$ . Analytical calculations have been performed using a continuous-distorted wave model with eikonal initial state (CDW-EIS) [16].

Besides, the linear operator called  $L[f]$  (Laplace-Beltrami operator) describes the angular scattering of the particles. It is given by :

$$L[f] = \frac{\partial}{\partial \mu} (1-\mu^2) \frac{\partial f}{\partial \mu} + \frac{1}{(1-\mu^2)} \frac{\partial^2 f}{\partial \phi^2} \quad (10)$$

where  $\mu = \cos \theta$ ,  $\theta$  and  $\phi$  being the polar and azimuthal angles of the flight vector.

Consequently, it is possible with our model to solve efficiently the LBTE. By taking into account the above-cited theoretical cross sections, we have performed the calculations of  $S$  and  $T$ , then resolved the LBTE on a regular mesh and finally, calculated the deposited dose profile, since the deposited dose reads :

$$D = 2\pi \int_0^{\infty} \int_{-1}^1 \rho S(\epsilon) \psi^0(\mathbf{x}, \epsilon, \mu) d\epsilon d\mu \quad (11)$$

## 3 Results

We first calculated the electronic stopping power of protons in water by using the Eq. 8 where the cross sections were taken from the above-cited database [16]. The results obtained are reported in Figure 1 and compared with the PSTAR simulation as tabulated in the NIST database [17].

For proton energies above 3 MeV, the stopping power is in very good agreement with the NIST data. For low energies, *i.e.* in the range 10 keV–1 MeV, a deviation appears between NIST and the Eq. 8. This is expected because the underlying cross sections are different, reflecting important divergences between the models used. Indeed, for these energies, the NIST stopping power results from a panel of several datasets taken from literature. Consequently, data must be considered more like an average over some models and experiments, while  $M_1$  uses data from one specific model. Thus  $M_1$  results are sensitive to assumptions made in the CDW-EIS model and could differ where low energies are concerned, according to data used. Neverthe-

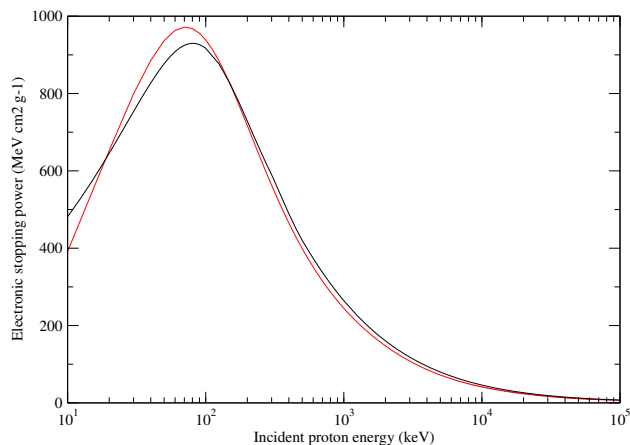


FIGURE 1: Electronic stopping power (expressed in  $\text{MeV cm}^2 \text{g}^{-1}$ ) analytically calculated by using cross sections provided by the CDW-EIS model (red line) and from the PSTAR database (black).

less, for high energies –typically greater than 10 MeV in some applications such as hadrontherapy–, the stopping power can be used for dose calculation.

In Figures 2 and 3, we report the deposited dose for 1D cases for 5 MeV and 90 MeV proton beams propagating in water, respectively.

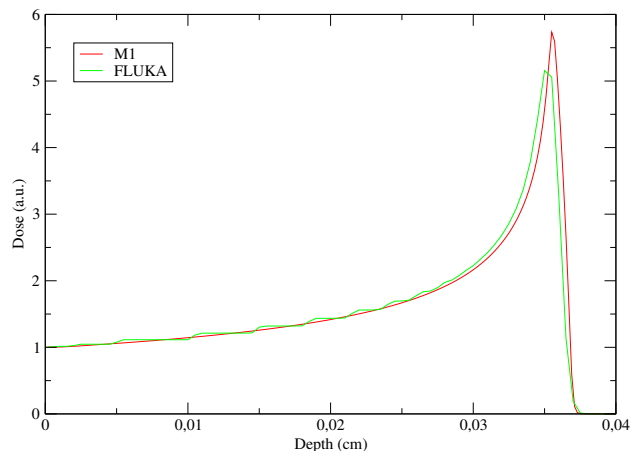


FIGURE 2: Deposited dose for 5 MeV protons in water. Results are normalized to the entrance value.

The calculated dose profiles are compared with the FLUKA results [18, 19]. According to the results presented, the code provides quite good results for 1D simulations. The Bragg peak occurs at a depth in accordance with Monte Carlo reference, *i.e.*  $35 \mu\text{m}$  and 6.4 cm for protons of 5 MeV (Figure 2) and 90 MeV (Figure 3), respectively. Comments made above for low energies are still valid, since the calculation of the dose is based on the stopping power.  $M_1$  gives accurate results with a very short computation time (around 1s). In view of the foregoing, this is a real benefit, since the same calculations performed with FLUKA have required 8 min, and it is reasonable to expect the same order of magnitude for 2D and 3D simulations.

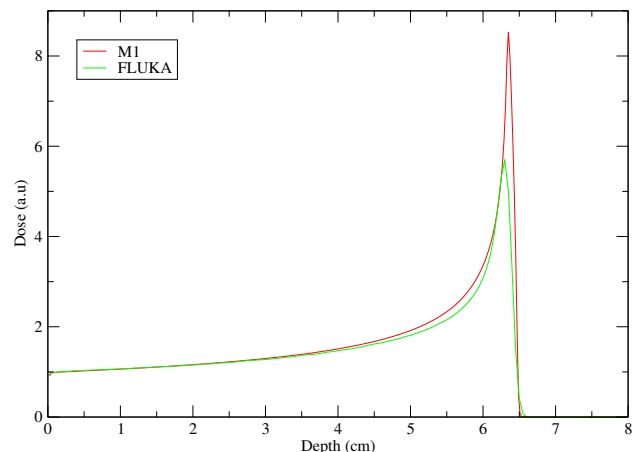


FIGURE 3: Deposited dose for 90 MeV protons in water. Results are normalized to the entrance value.

## 4 Conclusion

$M_1$  relies on an entropic moment method. It consists of averaging the linearized Boltzmann transport equation over angles in order to reduce the number of freedom degrees. The system of transport equations is closed using the physical principle of entropy through the Boltzmann H-theorem. The CSDA involves the calculation of the stopping power, which we have performed analytically thanks to *ab initio* differential cross sections of the CDW-EIS quantum model. We obtain a narrow Bragg peak and at the good depth, in accordance with Monte Carlo simulations.

## 5 Acknowledgments

This work was carried out by the financial support of the Agence Nationale de la Recherche (ANR-SHINE). We address special thanks to Bruno Dubroca for his scientific support and his advice. We are very grateful to Juan M. Monti, Michele A. Quinto and Roberto D. Rivarola for providing us the CDW-EIS data and would also like to thank Mario E. Alcocer-Avila for fruitful comparisons between  $M_1$  results and his own results provided by the *TILDA-V* Monte Carlo code.

## Références

- [1] T. Pichard, Ph.D. thesis, University of Bordeaux, France, 2016
- [2] J. Caron, J.-L. Feugeas, B. Dubroca, G. Kantor, C. Dejean, G. Birindelli, T. Pichard, P. Nicolai, E. d’Humières, M. Frank, V. Tikhonchuk, *Physica Medica* **31**, 912 (2015)
- [3] M. Touati, J.-L. Feugeas, P. Nicolai, J.J. Santos, L. Gremillet, V.T. Tikhonchuk, *New J. Phys.* **16**, 073014 (2014)
- [4] D. Del Sorbo, J.-L. Feugeas, P. Nicolai, M. Olazabal-Loumé, B. Dubroca, S. Guisset, M.

- Touati, V.T. Tikhonchuk, *Physics of Plasmas* **22**, 8 082706 (2015)
- [5] M. Frank, B. Dubroca, *Progress in Industrial Mathematics at ECMI 2008*, 407 (2010)
- [6] G. Birindelli, J.-L. Feugeas, J. Caron, B. Dubroca, G. Kantor, J. Page, T. Pichard, V. Tikhonchuk, P. Nicolaï, *Physica Medica* **45**, 305 (2017)
- [7] M.A. Quinto, J.M. Monti, P.D. Montenegro, O.A. Fojón, C. Champion, R.D. Rivarola, *Eur. Phys. J. D* **71**, 35 (2017)
- [8] J.H. Miller, A.E.S. Green, *Radiat. Res.* **54**, 343 (1973)
- [9] M.A. Quinto, P.R. Montenegro, J.M. Monti, O.A. Fojón, R.D. Rivarola, *J. Phys. B : At. Mol. Opt. Phys.*, **51**, 165201 (2018)
- [10] A.E. Martínez, G.R. Deco, R.D. Rivarola, P.D. Fainstein, *Nucl. Instrum. Methods B* **43**, 24 (1989)
- [11] P.N. Abufager, A.E. Martínez, R.D. Rivarola, P.D. Fainstein, *J. Phys. B* **37**, 817 (2004)
- [12] S. Uehara, L.H. Toburen, W.E. Wilson, D.T. Goodhead, H. Nikjoo, *Radiat. Phys. Chem.* **59**, 1 (2000)
- [13] J.H. Miller, A.E.S. Green, *Radiat. Res.* **54**, 343 (1973)
- [14] G.N. Minerbo, *J. Quant. Spectrosc. Radiat. Transfer* **20**, 541 (1978)
- [15] G.C. Pomraning, *Math. Models Methods Appl. Sci.* **2**, 21 (1992)
- [16] M.A. Quinto, J.M. Monti, P.F. Weck, O.A. Fojón, J. Hanssen, R.D. Rivarola, P. Senot, C. Champion, *Eur. Phys. Jour. D* **71**, 130 (2017)
- [17] Stopping-Power & Range Tables for Electrons, Protons, and Helium Ions; NIST Standard Reference Database 124
- [18] A. Ferrari, P.R. Sala, A. Fassò, J. Ranft, CERN-2005-10 (2005), INFN/TC\_05/11, SLAC-R-773
- [19] T.T. Böhlen, F. Cerutti, M.P.W. Chin, A. Fassò, A. Ferrari, P.G. Ortega, A. Mairani, P.R. Sala, G. Smirnov, V. Vlachoudis, *Nuclear Data Sheets* **120**, 211 (2014)

Quatrième partie

**Standard Model**

session dirigée par Reina CAMACHO TORO



## Introduction to the Standard Model session

Reina Camacho Toro

*LPNHE-CNRS, Paris*

### Résumé

The Standard Model (SM) of particle physics is a relativistic quantum field theory that attempts to describe the known fundamental particles and their interactions, except the gravitation. The SM has been studied at collider experiments for decades, and repeatedly held up to precision tests since its initial formulation in 1970s and the Large Hadron Collider (LHC) at CERN is its latest testbed. This proceeding aims to serve as an introduction to the different student contributions to the Standard Model session at the JRJC 2018, which are in general focused on the Brout- Englert- Higgs sector and the improvement of the description of Monte Carlo models. The data collected to date, the detector and physics performance, and measurements of Standard Model processes are reviewed briefly before summarizing the latest results in the Brout- Englert- Higgs sector, where substantial progress has been made since the discovery.

### 1 Introduction

The LHC at CERN provides proton-proton (pp) collisions at the center-of-mass energy of 13 TeV since 2015. Two huge multi-purpose experiments, ATLAS [1] and CMS [2] operate at the LHC. In total, the ATLAS and CMS detectors each accumulated large amount of data corresponding to an integrated luminosity of more than  $150 \text{ fb}^{-1}$  at 13 TeV,  $23 \text{ fb}^{-1}$  at 8 TeV and  $5 \text{ fb}^{-1}$  at 7 TeV pp-collisions with very high data acquisition efficiency ( $> 90\%$ ). The status of the detectors is excellent, with close to 100% of readout channels available across all sub-detectors. The peak luminosity delivered by LHC was  $2.14 \times 10^{34} \text{ cm}^{-2} \text{ s}^{-1}$ , greater than the design value of  $1 \times 10^{34} \text{ cm}^{-2} \text{ s}^{-1}$ .

A detailed understanding of the detector performance is essential for the production of high quality results. In particular, as the mean number of interactions per crossing (pile-up) has continuously increased in the last few years, extensive work has been done to reduce its impact on the reconstruction performance of basic objects such as leptons, photons, hadronic jets, jets from b-quarks (known as *b*-tagged jets), imbalance of momentum transverse to the direction of the beams (also known as missing energy), etc. In this sense, we invite you to look at the studies on *b*-tagging calibration for ATLAS by Giovanni Bartolini, on data-driven corrections of electromagnetic shower shapes with ATLAS by Mykola Khandoga, on  $\tau$ -lepton identification

at the trigger level by Cristina Martin and on electron energy calibration for ATLAS by Hicham Atmani.

### 2 Results on Standard Model Physics

A detailed understanding of the SM processes is essential for the ATLAS physics program. On one side they allow to probe the SM theory but they are also fundamental in the search program for new physics contributions beyond the SM. Precision measurements can both help constrain - or observe - new physics processes, e.g. enhancements of extremely rare production processes or processes involving anomalous couplings and they also represent a key ingredient for the description of the backgrounds and Monte Carlo models in the new physics searches, which are pushing into increasingly intricate event signatures. An overview of such cross-section measurements is shown in Fig. 1 for ATLAS and CMS.

Two specific results were presented at the JRJC 2018 : the use of  $Z \rightarrow e^+e^-$  events to derive data-driven corrections of electromagnetic shower shapes with ATLAS by Mykola Khandoga and the study of the  $\tau$ -leptons polarisation coming the decay of a  $Z$  boson by Guillaume Bourgatte. The first one demonstrates that accurate predictions from different Monte Carlo generators are needed to face the challenge of the precision of LHC data. The second one demonstrates the importance of measuring SM processes in a precise way since they might be backgrounds of other processes and searches.  $Z \rightarrow \tau\tau$  is the main background for the Higgs bosons disintegrating into pair of  $\tau$ -leptons. For more SM results, the interested reader is referred to the ATLAS and CMS public results web page [3, 4].

### 3 Higgs boson measurements

A new boson with a mass of 125 GeV was discovered by the ATLAS [7] and CMS [8] collaborations six years ago. This discovery was a great success of the SM as, so far, all measured properties of this particle are found to be compatible with the predictions for the SM Higgs boson. A search for the SM Higgs boson at the LHC is a complicated task because the expected production cross section is  $O(10)$  pb while the rate of background processes are much higher.

There are four main mechanisms of the SM Higgs boson production at the LHC energies : gluon fusion

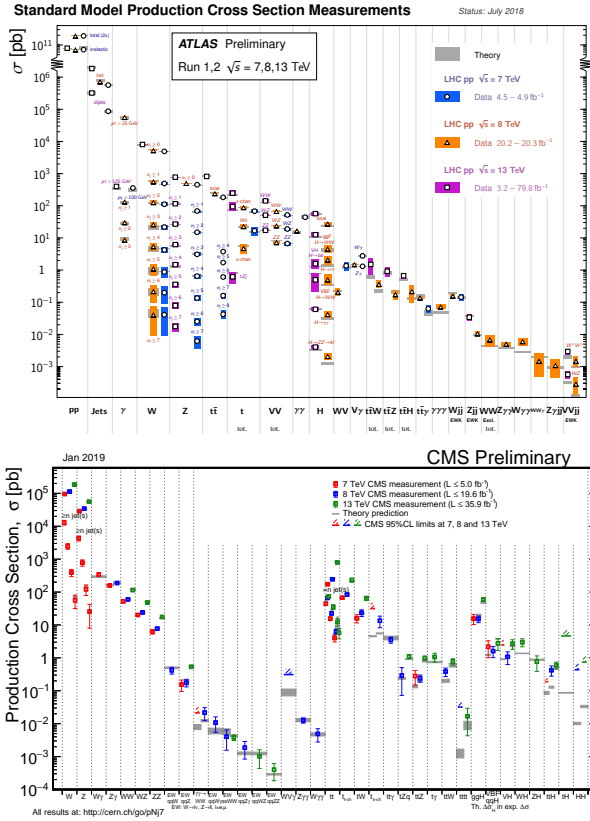


FIGURE 1: Summary of several Standard Model total production cross section measurements, corrected for leptonic branching fractions, compared to the corresponding theoretical expectations from ATLAS (top) and CMS (bottom).

(ggF) via heavy-quark (mostly top) triangular loop, vector-boson fusion (VBF) where the Higgs boson is accompanied by two jets going at small polar angles, associated production with one vector boson ( $Vh$ , where  $V$  stands for  $W$  or  $Z$ ) and top-antitop fusion, known as  $t\bar{t}h$ . The first and the last mechanisms as well as the second and the third ones have common couplings ( $t\bar{t}h$  and  $VVh$ , respectively). At 13 TeV the ggF mechanism dominates while rates via VBF ( $Vh, t\bar{t}h$ ) mechanisms are ten (a few dozen) times smaller, respectively.

The expected branching ratios (BR) of the experimentally favorable decay modes are shown in Fig. 2. Despite of 57% probability, the  $h \rightarrow b\bar{b}$  channel is very difficult experimentally due to a huge background and it is very difficult to see it via the ggF mechanism. However, one can try to extract the signal in the associated production of the  $h$  with a vector boson or a pair of top quarks. The  $h \rightarrow WW^* \rightarrow l\nu l\nu$  channel is easier to observe even if the branching ratio is only around 1%. However, it does not allow to reconstruct a Higgs boson mass. The cleanest decay channels where this is possible are the  $h \rightarrow ZZ^* \rightarrow 4l$  ( $BR = 1.3 \times 10^{-4}$ ) and the  $h \rightarrow \gamma\gamma$  ( $BR = 2.3 \times 10^{-3}$ ). In the last case a signal is searched above large background. The easiest experimental way to access the  $h \rightarrow \tau\tau$  channel is in the VBF production mode or using boosted  $\tau$ -leptons. Therefore

the easiness to observe the Higgs in a particular decay channel is an interplay between the production and decay modes, based on the background level. The first channels to be observed were  $h \rightarrow \gamma\gamma$ ,  $h \rightarrow WW$  and  $h \rightarrow ZZ$  and now we are doing precision measurements with the amount of data collected in these channels, like mass and differential cross-section measurements. The results obtained for the mentioned individual channels are combined to extract a Higgs boson signal strength at 13 TeV in different production mechanisms and in different decay modes and the global signal strength measured in the ATLAS (CMS) experiment is found to be  $1.13 \pm 0.09$  ( $1.17 \pm 0.10$ ), in agreement with the SM prediction [10, 9].

The  $h \rightarrow \tau\tau$  was observed later, independently by each experiment, using the data collected until 2016,  $36 \text{ fb}^{-1}$  [11, 12]. Events are categorized to improve signal significance: the VBF and boosted- $\tau$  categories play a major role. The observed (expected) signal significance in the ATLAS experiment in the  $\tau\tau$  channel is  $4.4\sigma$  ( $4.1\sigma$ ). It rises to  $6.4\sigma$  ( $5.4\sigma$ ) if one combines 13 TeV results with those obtained earlier at 7-8 TeV. The observed (expected) signal significance in the CMS experiment is  $4.9\sigma$  ( $4.7\sigma$ ). It increases to  $5.9\sigma$  ( $5.9\sigma$ ) if one combines results at 13 TeV with those obtained earlier at 7 and 8 TeV. The signal strength was found to be compatible with the SM.

The  $h \rightarrow b\bar{b}$  was observed last summer in the  $Vh$  production mode [13, 14]. Multivariate analyses are performed to discriminate the signal from the background. A statistic of  $80 \text{ fb}^{-1}$  is used for these analyses in both experiments. The observed (expected) signal significance in the ATLAS experiment in the  $Vh$  production mode is  $4.9\sigma$  ( $4.4\sigma$ ). It increases to  $5.4\sigma$  ( $5.5\sigma$ ) if one combines 13 TeV results with earlier measurements at 7 and 8 TeV. The observed (expected) signal significance in the CMS experiment in the same production mode is  $4.8\sigma$  ( $4.9\sigma$ ). It increases to  $5.6\sigma$  ( $5.5\sigma$ ) if one combines results for all possible production modes. For more information about this analysis in ATLAS we invite you to consult Konie Al Khoury's contribution.

Finally the  $t\bar{t}h$  production mode was also observed quite recently [15, 16]. It is studied using a variety of multi-lepton final states as well as the  $b\bar{b}$  and  $\gamma\gamma$  ones. A multivariate technique to discriminate the signal from a background is used by both experiments. The measured signal strength is  $1.32 \pm 0.28$  in the ATLAS experiment which corresponds to observed (expected) signal significance  $5.8\sigma$  ( $4.9\sigma$ ). It increases to  $6.3\sigma$  ( $5.1\sigma$ ) if one combines 13 TeV results (based on  $36\text{-}80 \text{ fb}^{-1}$  datasets) with older 7 and 8 TeV ones. The observed (expected) signal significance in the CMS experiment is  $5.2\sigma$  ( $4.2\sigma$ ) in the combined data taken at 13 TeV ( $36 \text{ fb}^{-1}$ ) and at 7 and 8 TeV. The value of signal strength is measured to be  $1.26 \pm 0.31$ . During JRJC 2018 three contributions related with  $t\bar{t}h$  production mode were presented: Cristina Martin discussed the search for  $h \rightarrow \tau\tau$  produced in the  $t\bar{t}h$  mode, Merve Nazlim Agaras discussed the multilepton final states and Giovanni Bartolini presented the full hadronic final state with  $h \rightarrow b\bar{b}$ .

For more Higgs results, the interested reader is refer-

red to the ATLAS and CMS Higgs public results web page [5, 6]

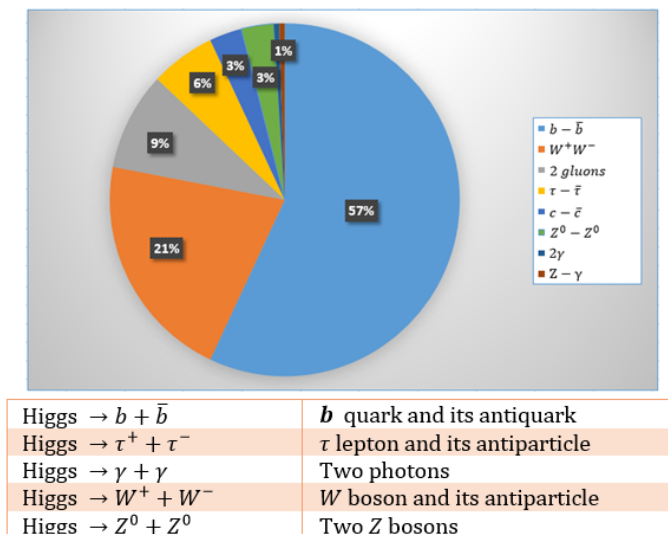


FIGURE 2: The various Higgs decay modes. The pie chart shows the relative occurrence of each decay mode.

## 4 Conclusion

In the last years many measurements of Standard Model processes have been made, accessing simple and complex final states, probing perturbative QCD, searching for Higgs couplings and starting precise measurements of its properties at 13 TeV. The SM has proven to be very successful so far from the experimental point of view, but we know it is incomplete and therefore it is important to increase the number and the precision of the measurements performed. The new generation of scientists are playing a key role in this sector. We hope the reader enjoy the work presented by the students in this session of the JRJC 2018.

## Références

- [1] ATLAS Collaboration, "The ATLAS experiment at the CERN Large Hadron Collider", JINST 3 (2008) S08003
- [2] CMS Collaboration, "The CMS experiment at the CERN LHC", JINST 3 (2008) S08004
- [3] ATLAS SM public results, AtlasPublic/StandardModelPublicResults
- [4] CMS SM public results, CMSPublic/PhysicsResultsSMP
- [5] ATLAS SM public results, AtlasPublic/HiggsPublicResults
- [6] CMS SM public results, CMSPublic/PhysicsResultsHIG
- [7] ATLAS Collaboration, Phys. Lett. B716 (2012) 1
- [8] CMS Collaboration, Phys. Lett. B716 (2012) 30

- [9] CMS Collaboration 2018 Preprint CMS-PAS-HIG-17-031
- [10] ATLAS Collaboration 2018 Preprint ATLAS-CONF-2018-043
- [11] ATLAS Collaboration 2018 Preprint ATLAS-CONF-2018-021
- [12] CMS Collaboration 2018 Phys. Lett. B779 283
- [13] ATLAS Collaboration 2018 Phys. Lett. B786 59
- [14] CMS Collaboration 2018 Phys. Rev. Lett. 121 121801
- [15] ATLAS Collaboration 2018 Phys. Lett. B784 173
- [16] CMS Collaboration 2018 Phys. Rev. Lett. 120 231801



# A New Method to Estimate Systematic Uncertainties in the $VH(H \rightarrow b\bar{b})$ Analysis with the ATLAS Detector

Konie Al Khoury  
Université Paris sud, Orsay



## Résumé

The Standard Model (SM) Higgs boson decaying to a pair of  $b$  quarks was recently observed by the ATLAS and CMS detectors using data collected during Run2 proton-proton collisions at a centre-of-mass energy of 13 TeV [1, 2]. This decay mode is interesting because it dominates the Higgs decay width and it allows a direct measurement of the coupling between the Higgs boson and  $b$  quarks. In addition, the Higgs boson produced in association with a vector boson ( $W$  or  $Z$  boson) was also observed [1]. The best sensitivity in the  $H \rightarrow b\bar{b}$  associated vector boson search is obtained when the vector boson decays to leptons since the leptons have a clean signature in the detector. However this channel represents a challenge for the analysis because of the large multijet and electroweak backgrounds contamination. Monte Carlo generators are used to model the backgrounds, therefore systematic uncertainties are assigned to these predictions. A new method using Machine Learning for background modeling uncertainties is under study. It consists of using a Boosted Decision Tree (BDT) trained to separate between events generated with two different Monte-Carlo generators of the same process to parametrize the difference. The benefit of this method is that it uses one variable (the BDT output) to represent the full phase space.

## 1 Introduction

The SM describes two types of elementary particles : the fermions and the bosons. The fermions are the building blocks of matter in the universe and they correspond to 6 quarks (up, down, charm, strange, top and beauty) and 6 leptons (electron, muon, tau and their corresponding neutrinos) and its antiparticles. These fermions interact through three forces called the electromagnetic, weak and strong interactions. The mediators of these forces are called bosons : photons for the electromagnetic force,  $Z$  and  $W$  bosons for the weak force and gluons for the strong force. The SM predicts the presence of another boson called the Higgs boson,  $H$ , observed in 2012 by both ATLAS [3] and CMS [4] experiments, that is the experimental manifestation of the Higgs field and fundamental particles gain mass through their interaction with the Higgs field. The Higgs boson production can be produced at the LHC (Large Hadron Collider) at CERN by colliding two proton beams at high energy : the quarks and gluons contained in the collided proton interact and as a conse-

quence the Higgs boson is produced. Four main production mechanisms are achievable at the LHC, as shown in Figure 1. They are the gluon-gluon fusion (ggF), vector boson fusion (VBF), Higgs radiation also known as associate production with a vector boson (VH) and associated production with a pair of top quarks (ttH). The Higgs boson can either decay to bosons or fermions as shown in Figure 2. The decay mode with the largest branching ratio is the Higgs decaying to  $b$  quarks ( $H \rightarrow b\bar{b}$ ) with a branching ratio of 58%. The analysis of this channel is very challenging because of multijet and electroweak backgrounds. In order to suppress the multijet background, the Hbb channel is chosen to be studied when the Higgs is produced alongside a vector boson decaying leptonically, noted VHbb. This means that the vector boson can either be a  $W$  boson that decays into a charged lepton and its neutrino or a  $Z$  boson that decays either to a neutrino and its antiparticle or decays to a charged lepton and its antiparticle. This allows to divide the  $VH(H \rightarrow b\bar{b})$  analysis into three channels of study : the 0-lepton, 1-lepton and 2-lepton channels, where the name of the channel refers to the number of charged leptons in the final state.

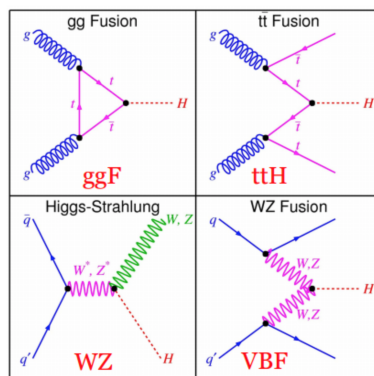


FIGURE 1: The four main production modes of the Higgs boson at the LHC.

## 2 $VH(H \rightarrow b\bar{b})$ Analysis

### 2.1 Event Selection

The analysis is done by categorizing the events into three channels of decay based on the lepton and jet multiplicity [1]. Only events with exactly 2  $b$ -tagged jets are selected using a  $b$ -tagging algorithm [5]. This algorithm uses the fact that  $b$ -hadrons have a time of flight

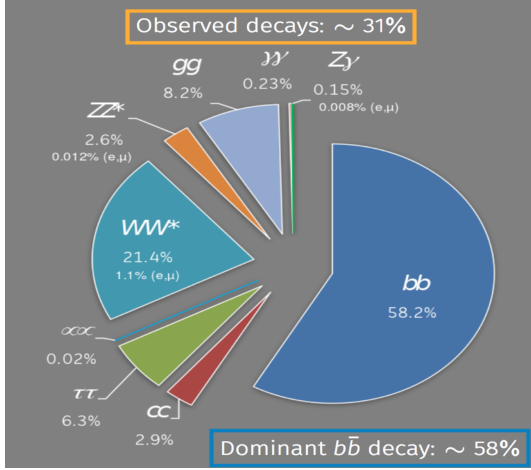


FIGURE 2: Branching ratios of the decay modes of the Higgs boson with a mass of 125 GeV.

before decaying, which allows to reconstruct the decay vertices. Only jets with transverse momentum ( $p_T$ ) greater than 20 GeV are selected. The leading (highest  $p_T$ ) b-tagged jet transverse momentum should be greater than 45 GeV. Because of large background contamination, cuts are applied on the collected events to eliminate background events with the intention of only keeping signal events. The main background events come from  $t\bar{t}$  events since each of the top quarks decays into a  $b$  quark and a  $W$  boson, Diboson ( $VZ$ ) events where a  $Z$  boson is created instead of the Higgs boson and then decays to two  $b$  quarks,  $V$ +jets events where a vector boson can be created alongside a gluon decaying to a pair of  $b$  quarks. The cuts to be applied depend on the channel of interest. In the 0-lepton channel ( $Z \rightarrow \nu\nu$ ), the transverse momentum of the vector boson  $p_T^V$  identifies with the missing transverse energy  $E_T^{\text{miss}}$ . The  $E_T^{\text{miss}}$  is reconstructed to account for neutrinos and other particles that did not interact inside the detector. In this channel  $E_T^{\text{miss}}$  should be greater than 150 GeV and some additional anti-QCD cuts are applied. In the 1-lepton channel ( $W \rightarrow l\nu$ ),  $p_T^V$  should be greater than 150 GeV. In this channel the  $W$  boson can either decay to an electron or a muon and their corresponding neutrinos. In the electron channel, the transverse momentum of the electron should be greater than 27 GeV and the  $E_T^{\text{miss}}$  should be greater than 30 GeV. In the muon decay channel, the transverse momentum of the muon should be greater than 25 GeV. In the 2-lepton channel ( $Z \rightarrow ll$ ), the analysis divides events with  $75 \text{ GeV} < p_T^V < 150 \text{ GeV}$  from events with  $p_T^V$  greater than 150 GeV. In this channel, the transverse momentum of the leading lepton should be greater than 27 GeV, the subleading lepton should be greater than 7 GeV and the invariant mass of the lepton pair should be compatible with the  $Z$  boson mass:  $81 \text{ GeV} < m_{ll} < 101 \text{ GeV}$ .

## 2.2 MultiVariate Analysis

The Analysis uses a MVA (MultiVariate Analysis) BDT (Boosted Decision Trees) technique to improve

the sensitivity. The BDT is trained on Monte-Carlo (MC) signal and all background sources of events, to separate between the expected signal and background using kinematics variables. The BDT is then applied to the collected data and its output is assigned to each event depending how signal-like or background-like it is. The training is done separately in the different analysis categories and channels. The three most important variables in the training are  $p_T^V$ , the invariant mass of the two  $b$  quark system ( $m_{bb}$ ) and the angular distance between the two b-jets  $\Delta R_{bb}$ . As shown in Figure 3, a binned likelihood fit is performed to extract the significance from the BDT output distribution. Since MC simulated samples are used to model the backgrounds, then background modelling systematics must be taken into account in the analysis when measuring the significance. Statistical and systematic uncertainties (MC background modelling, jet energy scale,  $b$ -tagging efficiencies, luminosity uncertainties, ...) determine the uncertainty of the measurement of the signal strength.

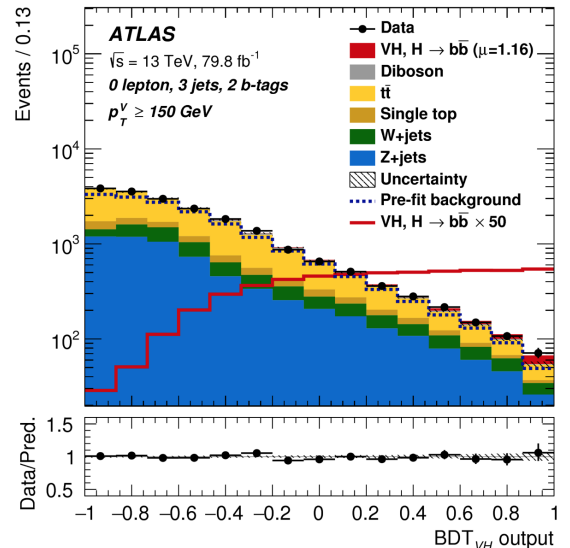


FIGURE 3: The  $BDT_{VH}$  output distribution post the fit in the 0-lepton channel, 2 b-tags, 3 jets category.

## 2.3 Observation with Run-2 Data

The Observation by the ATLAS experiment of the  $H \rightarrow b\bar{b}$  decay mode and of the  $VH$  production was achieved in July 2018. It was done using data collected during 2015-2017 with an integrated luminosity of  $79.8 \text{ fb}^{-1}$  of 13 TeV data. The results of the MVA were checked with what is called the cut-based analysis that uses additional cuts on  $\Delta R_{bb}$  as function of  $p_T^V$  and on the transverse mass of the vector boson  $m_T^W$  to restrain the signal region. Then a fit on  $m_{bb}$  is performed since it is the most important variable. The results are also checked with a diboson analysis noted  $VZ$   $Z \rightarrow b\bar{b}$  where exactly the same MVA is done, using a specially trained BDT to discriminate  $VZ$  events from backgrounds. For  $VH(H \rightarrow b\bar{b})$ , an excess of the signal over the expected background after combining the 3 channels was

observed to be  $4.9\sigma$ . The signal strength  $\mu$ , defined as the ratio of number of events to the SM prediction, was measured to be  $1.16 \pm 0.26$ . The  $H \rightarrow b\bar{b}$  decay mode was observed with a significance of  $5.4\sigma$  and the signal strength was observed to be  $\mu = 1.01 \pm 0.2$  by combining VH with the  $t\bar{t}H$  and VBF production modes. And the VH production mode was observed with a significance of  $5.3\sigma$  after combining with the  $\gamma\gamma$  and 4l channels and the signal strength was measured to be  $\mu = 1.13 \pm 0.24$ .

### 3 BDT-Based Method to Model Systematic Uncertainties

#### 3.1 Background Modeling Uncertainties

MC generated samples are used to estimate the background contributions in the analysis. Therefore systematic uncertainties need to be assigned to these predictions. The usual method consists of comparing events from the "nominal" generator that is used in the analysis to another "alternative" generator that differs either by the Matrix Element (ME) or the Parton Shower (PS) and do a bin-by-bin comparison of the  $BDT_{VH}$  distribution between the two generators. In the case of the  $VH(H \rightarrow b\bar{b})$  analysis this approach is not doable because it requires sufficient statistics in the alternative MC samples to be able to well represent the variation of the nominal generator. The lack of statistics in the alternative samples is due to the low acceptance of background events after  $VH(H \rightarrow b\bar{b})$  analysis selection. Producing MC samples with more statistics is not easily possible since it requires a lot of CPU and disk space. To compensate for that, the difference between nominal and alternative samples can be represented with weights. They are calculated by taking the most important variables and fitting the ratio of the alternative and nominal distributions. The weighting function is then applied to the nominal sample so that it looks like the alternative sample. The weighting functions are calculated at truth-particle level, where enough statistics are available, and propagated to events at reconstructed level. The weights are calculated for each of the background generators and each of the categories separately.

#### 3.2 Current $t\bar{t}$ Background Systematic Uncertainties in the 1-lepton Channel

In the 1-lepton channel almost half of the background events come from  $t\bar{t}$  process. The MC generator used by the analysis to model this background is Powheg-Pythia8 (Powheg [6] is used for the hard scatter generation (ME) and the showering (PS) is done with Pythia8 [7]). The alternative generator used to estimate the variation is aMCAtNLoPythia8 (difference in ME). As described above, the weights are derived from the most important kinematic variables. In the case of  $t\bar{t}$ ,

the systematic uncertainties are derived for  $m_{bb}$  and  $p_T^V$ . The weights derived from  $m_{bb}$  and  $p_T^V$  are then applied to the nominal generator. This method of estimating uncertainties is reliable, but a new method is proposed to look at the full phase space and use more than two variables in computing systematics.

#### 3.3 New BDT-Based Method

The study focuses on the  $t\bar{t}$  background in the 1-lepton channel. The systematics are derived from a BDT constructed with 11 kinematic variables trained separately in the 2 jets and 3 jets categories and separately on 2  $b$ -jets and  $bc$  jets events. The advantage of this method is that it does not focus on two variables, but rather takes into account the correlations between all kinematic variables. The training is performed to separate between the PowhegPythia8 events and the aMCAtNLoPythia8 events (MC generators differ with the ME). Another BDT is trained to separate between PowhegPythia8 and PowhegHerwig7 (which has a different PS) events. The training is done using events at truth-particle level. The BDT output is a value between -1 (100% background) and 1 (100% signal) assigned to each event. The ratio of the BDT output distribution between the nominal and the alternative generators is fitted. The fitted ratio can be used as a weight on nominal events. An example of the BDT distributions and the fit is showed in Figure 4.

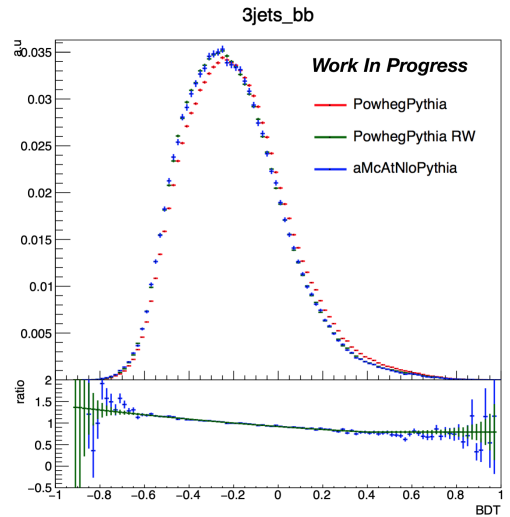


FIGURE 4: BDT distribution, in the 3jet  $bb$  category, of the PowhegPythia8, aMCAtNLOPythia8 and the BDT-reweighted PowhegPythia8 generated events in the upper pad. The lower pad shows the ratio between the two generators in blue and the function used to fit the ratio in green.

#### 3.4 Performance of the New Method

A first test of the method is to apply the weights on the nominal sample at truth-level as used in the training and compare it to the alternative sample. The re-

weighting is applied on all the kinematic variables, and an example of the  $p_T^V$  distribution of the 3jets, bb category is shown in Figure 5. By using the reweighting method, the reweighted nominal generator should be comparable to the alternative one : it allows to morph one generator into the other. The method of reweighting works well since the reweighted nominal events look similar to the alternative ones.

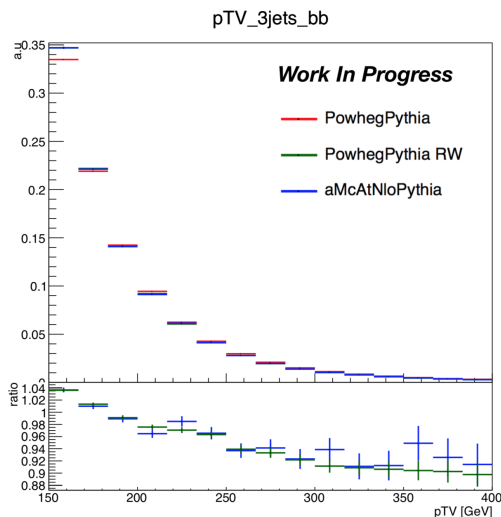


FIGURE 5:  $p_T^V$  distribution showing the behavior of the reweighted nominal events compared to the alternative generated events in the 3jet bb category at truth-level. The lower pad shows the ratio of the alternative to the nominal generator in blue and the reweighted-nominal to the nominal generator ratio in green.

### 3.5 Weights Applied to Reconstructed Events and Final Fit

The analysis uses events that pass ATLAS full simulation and reconstructed by the same reconstruction algorithm as the collision data. After that, events are selected passing the cuts of the analysis described in Section 2.1 for each channel. Statistical and systematic uncertainties are applied on the MC background prediction. As mentioned before, the reason that these events are not used to derive the systematics is the lack of statistics of the MC samples of the alternative generators caused by the low acceptance of the  $VH(H \rightarrow b\bar{b})$  analysis. As a solution the training of the BDT is done using events at truth-level and then the BDT is applied to reconstructed events where the truth information is still saved for each event. For  $t\bar{t}$  events two new systematics uncertainties, noted as Sys\_Herwig (derived from the difference between Pythia and Herwig) and Sys\_amcat (derived from the difference between Powheg and aMCAtNLo), are introduced to replace the current systematic uncertainties TTbarPTV (uncertainty derived from  $p_T^V$  distribution) and TTbarMBB (uncertainty derived from  $m_{bb}$  distribution).

## 4 Result

A fit of the Asimov data allows to evaluate the contribution of the new systematic uncertainties to the uncertainty on the signal strength. Results are shown in Table 1. The impact of the  $t\bar{t}$  model on the significance is slightly reduced with the new systematics (BDT-based systematics), however the total uncertainties did not change with respect to the current uncertainties (TTbarMBB and TTbarPTV). The behavior of the new systematics seems reasonable. This indicates that using BDTs to describe modeling systematics is a reliable method. The results shown for  $t\bar{t}$  modeling in the 1-lepton channel are promising and the method will be tested in other channels and for other background processes.

	Current Systematics	New Systematics
Total	0.44	0.44
DataStat	0.27	0.27
FullSyst	0.35	0.35
Jets MET	0.06	0.06
BTag	0.13	0.16
Leptons	0.01	0.01
Luminosity	0.02	0.02
Model ttbar	0.07	0.05
MC stat	0.12	0.12

TABLE 1: Impact of the systematic uncertainties on the uncertainty of the signal strength.

## Références

- [1] M. Aaboud *et al.* [ATLAS Collaboration], Phys. Lett. B **786** (2018) 59 doi :10.1016/j.physletb.2018.09.013 [arXiv :1808.08238 [hep-ex]].
- [2] A. M. Sirunyan *et al.* [CMS Collaboration], Phys. Rev. Lett. **121** (2018) no.12, 121801 doi :10.1103/PhysRevLett.121.121801 [arXiv :1808.08242 [hep-ex]].
- [3] G. Aad *et al.* [ATLAS Collaboration], Phys. Lett. B **716** (2012) 1 doi :10.1016/j.physletb.2012.08.020 [arXiv :1207.7214 [hep-ex]].
- [4] S. Chatrchyan *et al.* [CMS Collaboration], Phys. Lett. B **716** (2012) 30 doi :10.1016/j.physletb.2012.08.021 [arXiv :1207.7235 [hep-ex]].
- [5] M. Aaboud *et al.* [ATLAS Collaboration], JHEP **1808**, 089 (2018) doi :10.1007/JHEP08(2018)089 [arXiv :1805.01845 [hep-ex]].
- [6] S. Frixione, P. Nason and G. Ridolfi, JHEP **0709**, 126 (2007) doi :10.1088/1126-6708/2007/09/126 [arXiv :0707.3088 [hep-ph]].
- [7] T. Sjostrand, S. Mrenna and P. Z. Skands, Comput. Phys. Commun. **178**, 852 (2008) doi :10.1016/j.cpc.2008.01.036 [arXiv :0710.3820 [hep-ph]].

# Data-driven correction of electromagnetic shower shapes in Monte-Carlo modelling of ATLAS calorimeter

Mykola Khandoga  
Universite Paris-Sud / CEA Saclay



## Résumé

The electromagnetic calorimeter is one of the key elements of the ATLAS detector at the Large Hadron Collider at CERN. In order to properly reconstruct the physical processes happening after the collision it is crucial to identify the origin of the measured particles and, in particular, to separate the signal electrons, coming from prompt decays, from the background. Electron identification is performed by means of multi-variate (MVA) analysis algorithm, which in turn strongly relies on a number of electromagnetic shower shape characteristics.

The Monte-Carlo model provides inaccurate energy distribution in the calorimeter cluster cells. Correcting the shower shapes allows to improve the electron identification and decrease the associated systematic uncertainty.

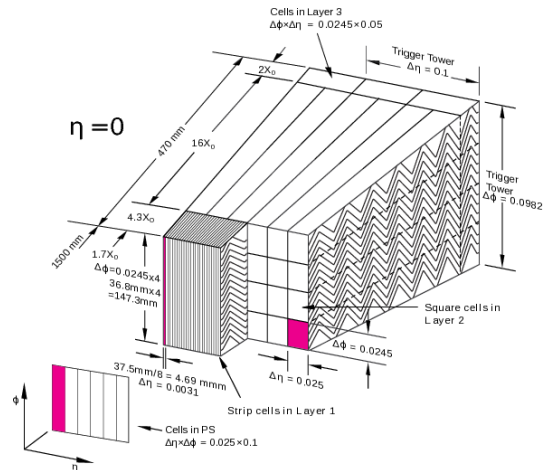


FIGURE 1: Layout of the ATLAS electromagnetic calorimeter.

## 1 Introduction

The ATLAS calorimeter is a very important part of the detector and consists of electromagnetic and hadronic part. It is designed to provide precision measurements of electrons, photons and jets energy as well as the missing transverse energy. Aside from energy measurements information from the calorimeter is also used for particle identification (ID). Particle ID, in turn, is crucial for most of the physics analysis in ATLAS. Hereafter we use the ATLAS coordinate system where  $z$  axis is directed along the beam,  $\phi$  is the azimuthal angle along the beam pipe, pseudorapidity  $\eta = -\ln[\tan(\theta/2)]$ , where  $\theta$  is the polar angle. Transverse momentum and energy are defined as  $p_T = p \sin\theta$ ,  $E_T = E \sin\theta$  respectively.

The ATLAS electromagnetic calorimeter [1] consists of three layers and a pre-sampler. The first layer has very high granularity in  $\eta$  dimension. The second layer has high granularity in both  $\eta$  and  $\phi$  dimensions and also absorbs most of the energy of electrons and photons. Such a fine structure of the detector not only allows to perform a precise measurement of particle energy but also to observe the development of the electromagnetic shower in all three dimensions.

A number of variables called shower shapes are used to describe shower development in different layers of the calorimeter and then are used as an input for particle identification MVA algorithm.

The current study primarily concentrates on the variables obtained from the second layer of the calorime-

ter, considering their importance for the MVA :

- Lateral shower width  $W_{\eta^2} = \frac{\sqrt{\sum(E_i \eta_i^2) - (\sum(E_i \eta_i))^2 / \sum(E_i)}}{\sum(E_i)}$  calculated within a window of  $3 \times 5$  cells ( $\eta \times \phi$ ) centered at the electron cluster position.
- $R_\phi$  - ratio of the energy in  $3 \times 3$  cells over the energy in  $3 \times 7$  cells centered at the electron cluster position.
- $R_\eta$  - ratio of the energy in  $3 \times 7$  cells over the energy in  $7 \times 7$  cells centered at the electron cluster position.

Figure 2 shows how  $R_\eta$  distribution is different in jets, signal electrons and background electrons. Background electrons denote non-prompt electrons which are not originated from primary vertex.

The shower shapes-based approach has proven to be a reliable source of information but also revealed a number of discrepancies between the data and Monte Carlo (MC) modeling. This, in turn, leads to discrepancies in particle ID which are later corrected using highly  $\eta$ - and  $p_T$ -dependent scale factors. The actual origin of the discrepancy is not clear.

Correction of the shower shapes aims to get the scale factors closer to unity, reducing the corresponding systematic uncertainties and improving the precision of the measurements with electrons in the final states. The MC samples were derived using Powheg [3] for the matrix element and Pythia8 [4] for the showering. The events are simulated using a GEANT4-based [5] full

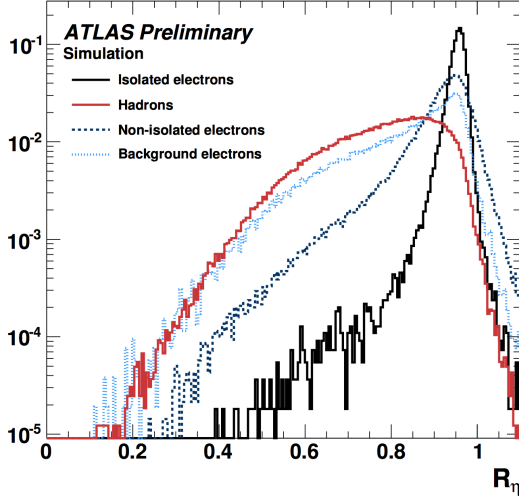


FIGURE 2: Distribution of  $R_\eta$  in simulation for electrons and jets

detector simulation [6].

## 2 Shower shapes measurement and correction

### 2.1 Event selection

For this study we have considered electrons from the  $Z \rightarrow ee$  decay. A set of recommended single electron triggers was used. Each event was required to have 2 electrons at least one of which has  $p_T > 25\text{GeV}$ . In order to suppress the background both electrons had to pass gradient isolation. A  $Z$  candidate invariant mass cut was applied with a window of  $80-120\text{GeV}$ . To avoid identification bias from triggering the tag and probe approach was used with only probe electrons taken into consideration Ref. [2]. The electron cluster in the second calorimeter layer was required to contain information from 77 calorimeter cells. Datasets of  $10^7$  events in data (2017 proton-proton collisions) and  $7 \times 10^6$  events in MC (Powheg+Pythia8) were used.

### 2.2 Data/MC discrepancies

Our consideration begins with the energy deposit of an electron in the second layer of the calorimeter. A window of 7 cells in  $\eta$  and 11 cells in  $\phi$  is centered around the cell with the highest energy. Shower shapes were considered in 14  $\eta$  bins in the range between  $|\eta| = (0, 2.4)$  in order to investigate how the discrepancy depends on  $\eta$ .

The  $\eta$ -dependent shower shapes in data are wider than the MC and show a larger discrepancy in the end-cap ( $|\eta| = (1.52, 2.4)$ ). For  $\phi$  dimension the situation is the opposite: MC is wider than the data and the barrel ( $|\eta| = (0, 1.52)$ ) shows larger discrepancy. Figure 4 contain examples of shower shapes in different eta bins.

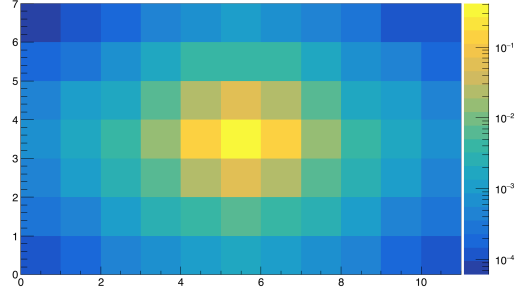


FIGURE 3: Energy profile of a window of  $7 \times 11$  cells in the 2nd calorimeter layer (logarithmic scale)

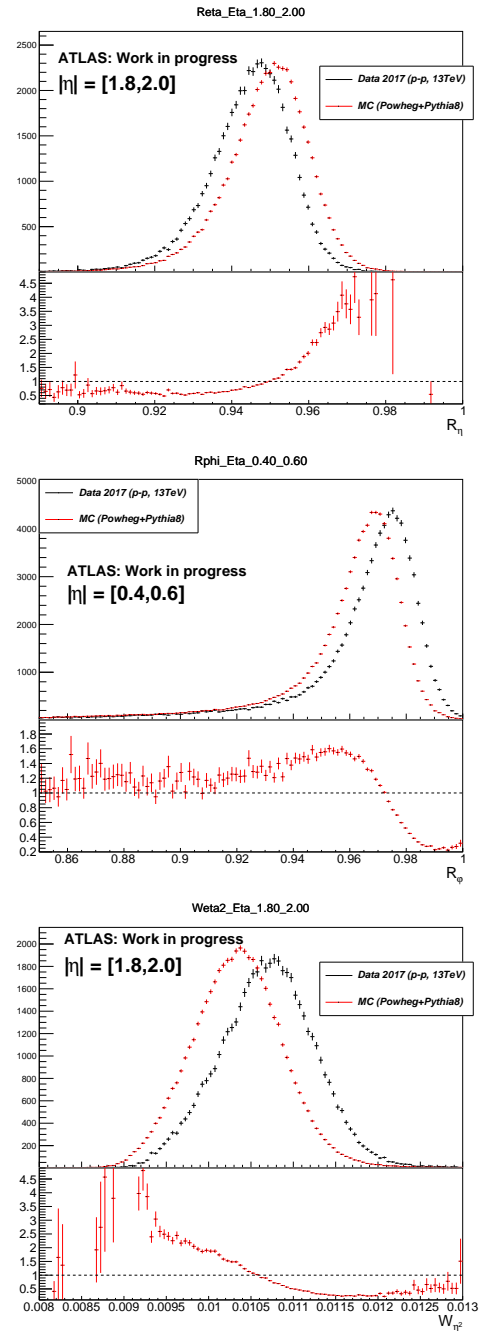


FIGURE 4:  $R_\eta$  in  $|\eta| = (1.8, 2.0)$  (top),  $R_\phi$  in  $|\eta| = (0.4, 0.6)$  (middle) and  $W_{\eta 2}$  in  $|\eta| = (1.8, 2.0)$  (bottom)

## 2.3 The correction procedure

### The correction matrix

The correction procedure is based on the redistribution of energy between the cluster cells in MC so that the distribution becomes consistent with the data. For every  $\eta$  bin a correction matrix is derived in the following way :

$$M_i^{Correction} = \frac{E_i^{Data}}{\Sigma E^{Data}} - \frac{E_i^{MC}}{\Sigma E^{MC}}$$

$$\Sigma_i M_i^{Correction} = 0, i = 1..77.$$

$E_i^{Data}$ ,  $E_i^{MC}$  - matrix elements of the averaged energy profiles. The correction is then applied to the electron cluster cells on event-by-event basis :

$$E_i^{Reweighted} = E_i^{Non-reweighted} (1 + M_i^{Correction}).$$

This redistributes the energy among the cells keeping the total energy exactly the same.

### Bremsstrahlung tails

The magnetic field directed along the  $\phi$  dimension leads to a significant asymmetry in energy deposits for electrons and positrons (figure 5). Considering the

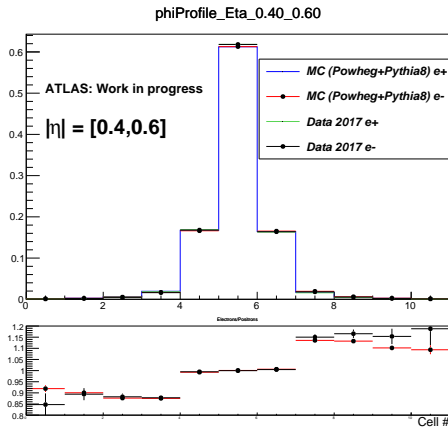


FIGURE 5: Energy profile in  $\phi$  for  $e^+$  and  $e^-$ .

fact that the reweighting is intended to correct for the data/MC discrepancies themselves and not for the bremsstrahlung effect it makes sense to develop the bremsstrahlung-free correction function based on  $e^+$  and  $e^-$  correction matrices. The principle is schematically explained on figure 6.

Good agreement of data and MC description of  $e^+$  and  $e^-$  asymmetry gives a hint that the material mis-modelling cannot be the main source of the data/MC disagreement.

## 3 Résultats

Figures 7, 8, 9 show the effect of the correction. The shower shapes in MC become very close to the data,

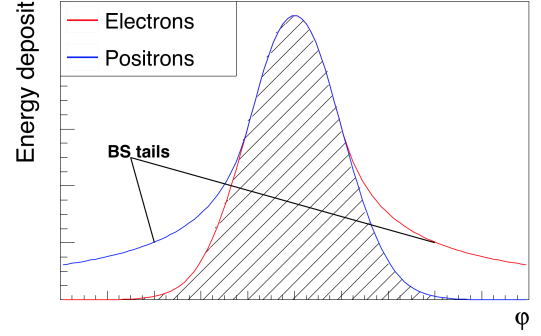


FIGURE 6: Schematic energy profile in  $\phi$  dimension. Bremsstrahlung tails subtraction based on  $e^+$  and  $e^-$  energy profiles.

correcting a significant discrepancy.

Figures 10, 11, 12 contain shower shapes vs  $p_T$  integrated over  $\eta$ . They demonstrate that the correction does not depend on the  $p_T$  which allows to expect the decreased systematic uncertainties for  $p_T$  regions distant from 40 – 50GeV.

Finally, figure 13 shows the effect of the correction on electron ID efficiency. We can see a visible improvement, notably in the endcap region. Nevertheless the barrel region shows little improvement. It can be explained by the fact that electron ID MVA relies on many variables while only a number of them were corrected during current study.

The proposed method is getting integrated into ATLAS Athena framework as an option and is planned to be used as a baseline for the data taking period that will start in 2021, known as Run 3.

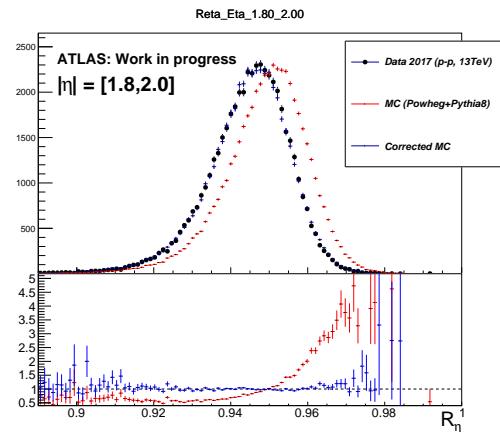


FIGURE 7: Reweighted  $R_\eta$  in  $|\eta| = (1.8, 2.0)$ .

## Références

- [1] ATLAS Collaboration, The ATLAS Experiment at the CERN Large Hadron Collider, JINST 3 (2008) S08003.
- [2] ATLAS Collaboration, Electron reconstruction and identification efficiency measurements with the AT-

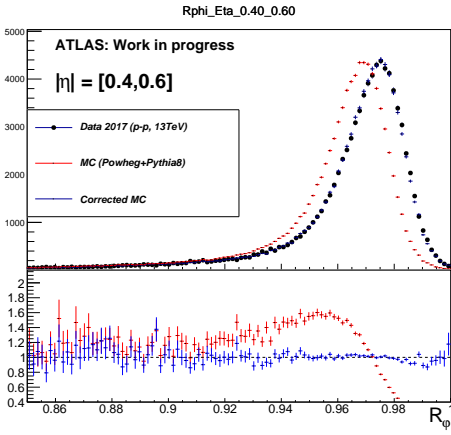
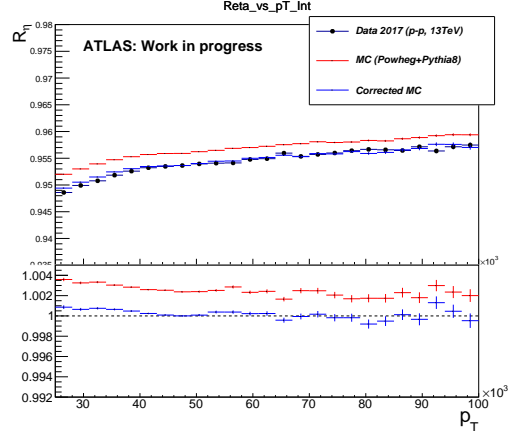
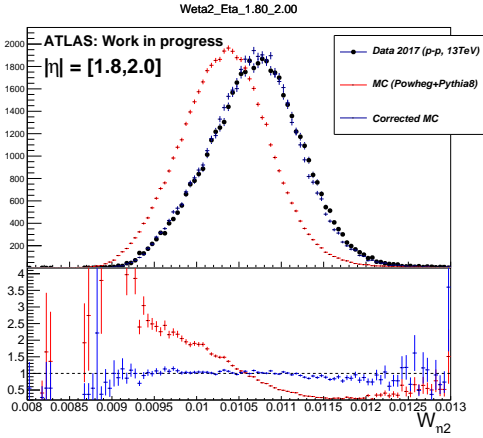
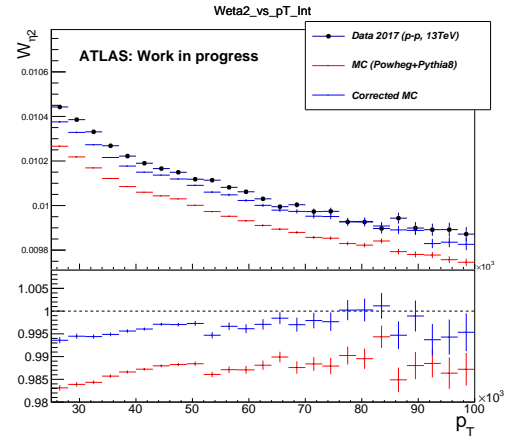
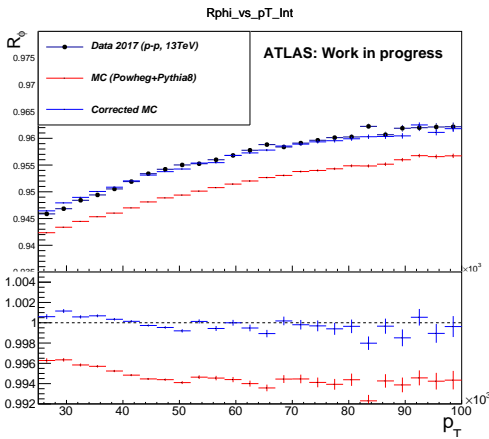
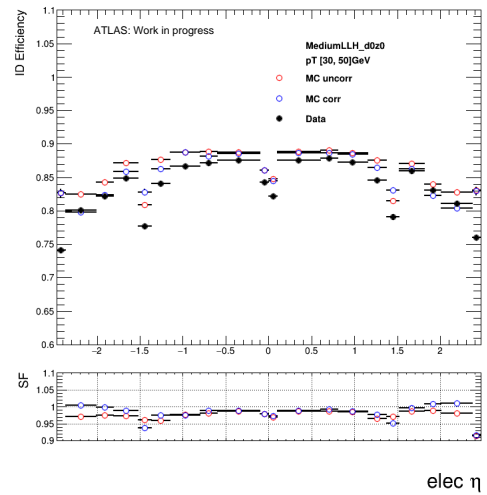
FIGURE 8: Reweighted  $R_\phi$  in  $|\eta| = (0.4, 0.6)$ .FIGURE 11: Reweighted  $R_\eta$  vs  $p_T$  integrated over  $\eta$ .FIGURE 9: Reweighted  $W_{\eta_2}$  in  $|\eta| = (1.8, 2.0)$ .FIGURE 12: Reweighted  $W_{\eta_2}$  vs  $p_T$  integrated over  $\eta$ .FIGURE 10: Reweighted  $R_\phi$  vs  $p_T$  integrated over  $\eta$ .

FIGURE 13: Electron identification efficiency as a function of the electron pseudo-rapidity

- LAS detector using the 2011 LHC proton-proton collision data, *Eur. Phys. J. C* 74 (2014) 2941.
- [3] S. Frixione, P. Nason and C. Oleari, Matching NLO QCD computations with Parton Shower simulations : the POWHEG method, *JHEP* 11 (2007) 070, arXiv : 0709.2092 [hep-ph].
- [4] T. Sjostrand, S. Mrenna and P. Z. Skands, A Brief Introduction to PYTHIA 8.1, *Comput. Phys. Commun.* 178 (2008) 852, arXiv : 0710.3820 [hep-ph].
- [5] S. Agostinelli et al., GEANT4 : A simulation toolkit, *Nucl. Instrum. Meth. A* 506 (2003) 250.
- [6] ATLAS Collaboration, The ATLAS Simulation Infrastructure, *Eur. Phys. J. C* 70 (2010) 823, arXiv : 1005.4568 [physics.ins-det].



# Boosted Decision Trees and $b$ -jet Trigger Calibration Studies for $t\bar{t}H(b\bar{b})$ Fully Hadronic Analysis with the ATLAS Detector

Giovanni Bartolini

Aix Marseille Univ, CNRS/IN2P3, CPPM, Marseille, France



## Résumé

This presentation concerns two expected improvements to the Run 1 analysis on the associated production of top quarks pair and Higgs boson  $t\bar{t}H(H \rightarrow b\bar{b})$  fully hadronic channel performed within the ATLAS collaboration. First, a two steps multivariate analysis, with Boosted Decision Trees, is implemented to optimize signal versus background separation. Second, due the large presence of heavy flavored jets in this final state, and the possible improvement coming from using the identification of  $b$ -jet ( $b$ -tagging) at trigger level, a combined calibration of the  $b$ -tagging algorithms at trigger and reconstruction level is presented.

## 1 Introduction

Since the discovery of the Higgs boson, the main focus is now shifted to the precise measure of its properties : any deviation from the Standard Model (SM) predictions can be interpreted as a hint of new physics beyond the SM (BSM). Anomalies on the Yukawa coupling,  $Y_t$ , between the Higgs boson and the quark top, the heaviest elementary particle, are predicted in many BSM models and a precise measure of the top anti-top pair and Higgs boson associated production ( $t\bar{t}H$ ) cross section is the only accessible way to directly measure  $Y_t$ . The observation of this process was recently published by the ATLAS collaboration [1] using a combination of Run 1 and Run 2 data and combining together the main decay channels of the Higgs boson :  $\gamma\gamma$ ,  $ZZ$ ,  $WW$ ,  $\tau\tau$  and  $b\bar{b}$ .

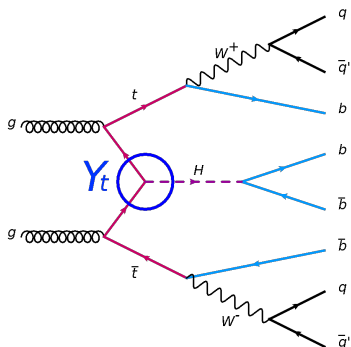


FIGURE 1:  $t\bar{t}H(H \rightarrow b\bar{b})$  fully hadronic process with eight quarks, four of which  $b$ -quarks, in the final state. The blue ring is highlighting the vertex where the top-Higgs Yukawa coupling  $Y_t$  intervenes.

Among the different  $t\bar{t}H$  final states, the fully hadronic channel has the largest branching ratio ( $\sim 33\%$ ) and it's characterized by the Higgs boson decaying into a  $b\bar{b}$  pair and by both  $W$  bosons from the top quarks decay that disintegrate into light quarks, as shown in Fig. 1, leading to a striking experimental signature composed by eight quarks (reconstructed as jets), four of which are  $b$ -quarks, and no leptons, thus it suffers from an overwhelming QCD multi-jet background, together with the irreducible  $t\bar{t} + b\bar{b}$  background.

A first analysis for this channel was already performed using Run 1 data [2], with a result for the signal strength of  $\mu_{t\bar{t}H} = 1.6 \pm 2.6$  that brought 10% improvement on the significance of the combination with the others  $t\bar{t}H(H \rightarrow b\bar{b})$  channels, that are single-lepton and di-lepton channels and targets different decays of the  $W$  bosons. The analysis strategy for this channel consists in four steps : events selection and categorization as a function of the number of jets and  $b$ -jets, QCD multi-jet background estimations with a data-driven method, multivariate analysis of the selected events to improve signal versus background separation, and final fit.

## 2 Two-steps multivariate analysis

To better separate the signal from the background, a multivariate analysis is performed on the selected events. The Run 1 version of the analysis used a Boosted Decision Trees (BDT) technique using global kinematic variables to classify the events. For the Run 2 this is replaced with a two-steps approach, summarized in Fig. 2 and composed by an event reconstruction step followed by a classification step, both of them using BDT.

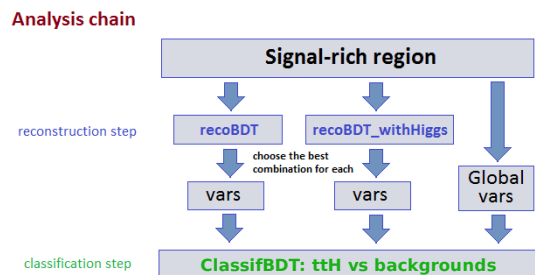


FIGURE 2: Two-steps multivariate analysis chain.

## 2.1 Reconstruction Step

The aim of this first step is to perform a full event reconstruction of the  $t\bar{t}H$  candidate event, by finding the best association between the jets reconstructed in the detectors and the final state partons. The large number of jets lead to a large numbers of possible associations, ranging from a minimum of 36 and easily reaching the order of thousands depending on the jets and  $b$ -tagged jets multiplicities. In this step two different BDTs are used : a first BDT, called *reco\_BDT*, is trained to reconstruct only the  $t\bar{t}$  system and has no bias in the Higgs candidate mass; the second one, called *reco\_BDTwithHiggs*, is trained to reconstruct the full  $t\bar{t}H$  system with the highest possible reconstruction efficiency. These two BDTs use as inputs the invariant masses and angular correlations between jets and they are trained using  $t\bar{t}H$  simulated events where all possible association are computed. Truth-level information from the simulation is used to find the correct matching between quarks and jets, when available. For each event in which this truth-matching is possible, the correct quark-jet association is used as signal for the BDT training, while all other possible combinations are treated as background. Events where the truth-matching is not available for every final state parton are not used for the training. Two of the variables used in the training are shown in Fig 3.

In events where a full truth-matching is available, the Higgs boson candidate is properly reconstructed 57% and 75% of times and the full event is properly assigned 41% and 53% by *reco\_BDT* and *reco\_BDTwithHiggs* respectively. These two BDTs are then applied to all selected events : Fig. 4 shows the invariant mass of the reconstructed Higgs boson candidates.

## 2.2 Classification Step

The aim of the second step of the chain is instead the proper signal versus background discrimination. The information from the reconstruction step is combined with global event kinematic variables to train a *classification BDT*. A combined optimizations against the two main backgrounds (QCD multi-jet and  $t\bar{t}$ ) is under study : the optimization against the multi-jet background, performed thanks to a data-driven technique (a new version of  $TRF_{MJ}$ , still under development), shows promising results and it presents some discriminating power also against the  $t\bar{t}$  background. The optimization of the choice of variables used for the classification BDT is performed separately in each of the four signal region, that are defined by jets and  $b$ -jets multiplicities as combination of 8 and  $\geq 9$  jets and 3 and  $\geq 4$   $b$ -jets. The figure of merit used for the optimization is the area under the ROC curve (AUC), where the ROC curve is defined by background rejection as a function of signal efficiency. The optimization method takes from a preselected set of variables the one with the highest separating power and then it adds recursively the variable that brings the largest improvement on the AUC, until the improvement from adding a new

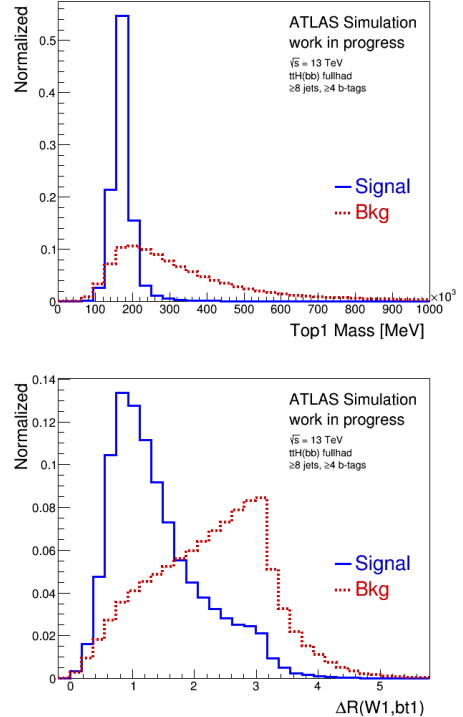


FIGURE 3: Two of the variables used by the reconstruction BDTs : invariant mass of the  $p_T$ -leading top (top-left),  $\Delta R$  between the  $b$  and the  $W$  boson from the  $p_T$ -leading top decay (top-right), difference between the invariant mass of the  $t\bar{t}$  system and the sum of the invariant mass of the tops (bottom-left), and minimum  $\Delta R$  between the  $b$ -jet and the light jets form the  $p_T$ -leading top decay (bottom-right). The blue histograms form the  $p_T$ -leading top decay (bottom-right). The light histograms show the distribution for the signal (correct jet-quark association), while in red are shown the distributions for the combinatorial background.

variable is less than 1%. Fig 5 shows the distribution of the classification BDT for each signal region.

## 3 Combined calibration

Trigger-level  $b$ -tagging has improved considerably with respect to Run 1 and it is now close in performance to offline algorithms, as shown in Fig 6.

The fully hadronic  $t\bar{t}H$  analysis will benefit from the increase in signal efficiency of a factor  $\sim 3$  from using  $b$ -jet triggers instead of multi-jet ones, the latter ones used in the Run 1 analysis. To use this kind of triggers, a calibration of the performances of the online  $b$ -tagging algorithms is needed. Data-to-simulation scale factors (SFs) are used to calibrate online algorithms. Generally  $b$ -tagging is used both at trigger and reconstruction level, therefore a calibration of the combined performance of the online plus offline  $b$ -tagging is performed, thanks to a geometrical matching ( $\Delta R = \sqrt{\Delta\eta^2 + \Delta\phi^2} < 0.2$ ) between trigger level jet objects and reconstruction level ones. The used tagger is the MV2 [4], in its online and offline versions, and this calibration was performed using data collected in 2016.

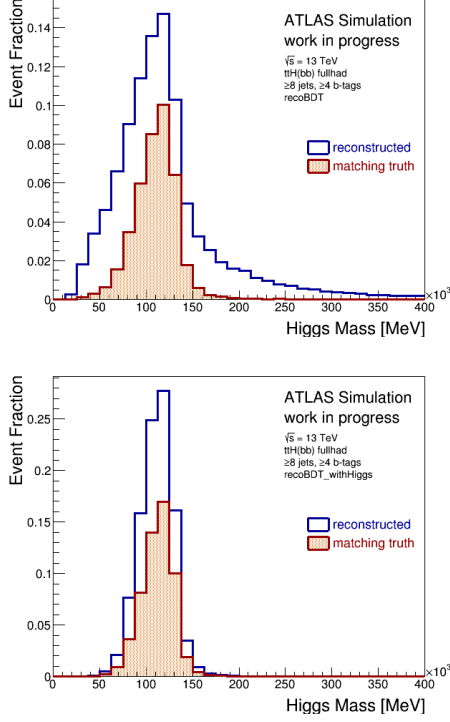


FIGURE 4: Invariant masses of the Higgs candidate as reconstructed by the reco\_BDT (on the left) and by the reco\_BDTwithHiggs (on the right). The red histograms show the mass distributions for the events in which the reconstructed object matches completely the truth object.

### 3.1 Calibration method

The calibration is evaluated in a highly pure  $t\bar{t}$  sample. At trigger level events are required to have at least one lepton and two jets with the online  $b$ -tagging algorithm evaluated. Then events are required to have exactly two jets with transverse momentum ( $p_T$ )  $> 35$  GeV and exactly two leptons with  $p_T > 28$  GeV opposite charge and different flavours, in order to target di-leptonic events and to reduce the level of the backgrounds.

Events are also required to have the matching between online and offline jet objects available for both jets. The  $b$ -tagging efficiency is then extracted thanks to a binned probability density function (p.d.f.) based likelihood [3] method, where the p.d.f. express the probability for a jet to have a given combination of values for  $p_T$  and  $b$ -tagging algorithm output value given its. The p.d.f. for  $b$ -jets is fitted from data, while the p.d.f. for light jets and also the flavour composition of the sample is extracted from simulation.

### 3.2 Results

The combined SFs are evaluated by measuring the efficiency of the online  $b$ -tagging in events where both jets are  $b$ -tagged by the offline algorithm. The results of the combined SFs, shown in Fig. 8, are close to 1 and with very small uncertainties: they range from a maximum of 3% to  $\sim 1\%$  in the central  $p_T$  region

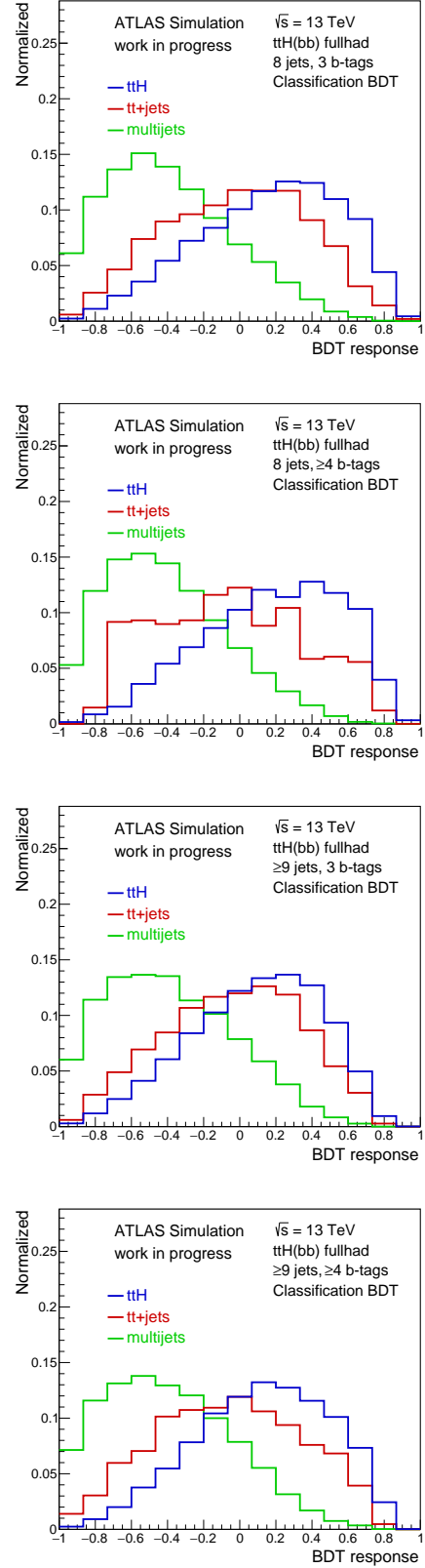


FIGURE 5: Classification BDT distributions for the signal (blue) and the two main backgrounds ( $t\bar{t}$  in red and multi-jet in green) in the four signal regions.

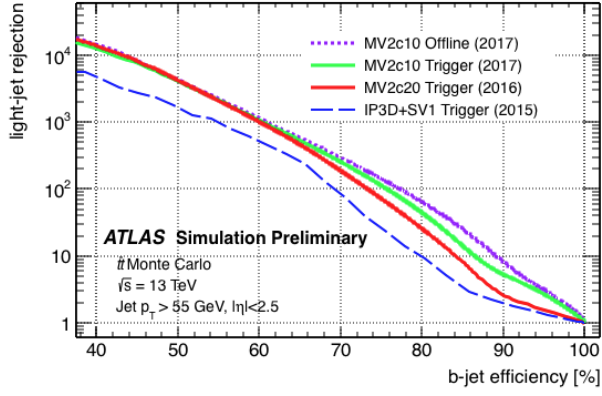


FIGURE 6: Comparison of the online  $b$ -tagging algorithm for different years with the offline algorithm (in purple).

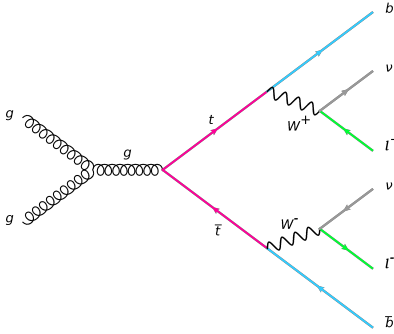


FIGURE 7: One of the major feynman diagram of  $t\bar{t}$  production with dileptonic decay.

and they are dominated by the statistical ones, while the major source of systematic uncertainties is the  $t\bar{t}$  modeling.

Investigations on the stability of the results with respect to jet  $\eta$ , pile-up and data period was studied and no relevant dependency was found.

## 4 Conclusions

My work is located in the framework of the analysis of the  $t\bar{t}H(H \rightarrow b\bar{b})$  fully hadronic channel, that is the  $t\bar{t}H$  final state with the largest BR but that is also overwhelmed by QCD multi-jet background. The presented work is divided in two main contributions : implementation of a two step multivariate analysis aimed at signal versus background separation and calibration of trigger level  $b$ -tagging. These two improvements, still in development, will be applied on the analysis of the full Run 2  $pp$  collision data at  $\sqrt{s} = 13$  TeV.

The multivariate analysis involves a reconstruction step with two BDTs trained to reconstruct either the  $t\bar{t}$  only system either the full  $t\bar{t}H$  system, with an efficiency for this second case of 53% in events with full truth-matching available, followed by a classification step with a BDT optimized to discriminate the  $t\bar{t}H$  signal from the QCD multi-jet background, that shows however some discrimination power also against the  $t\bar{t}$  background.

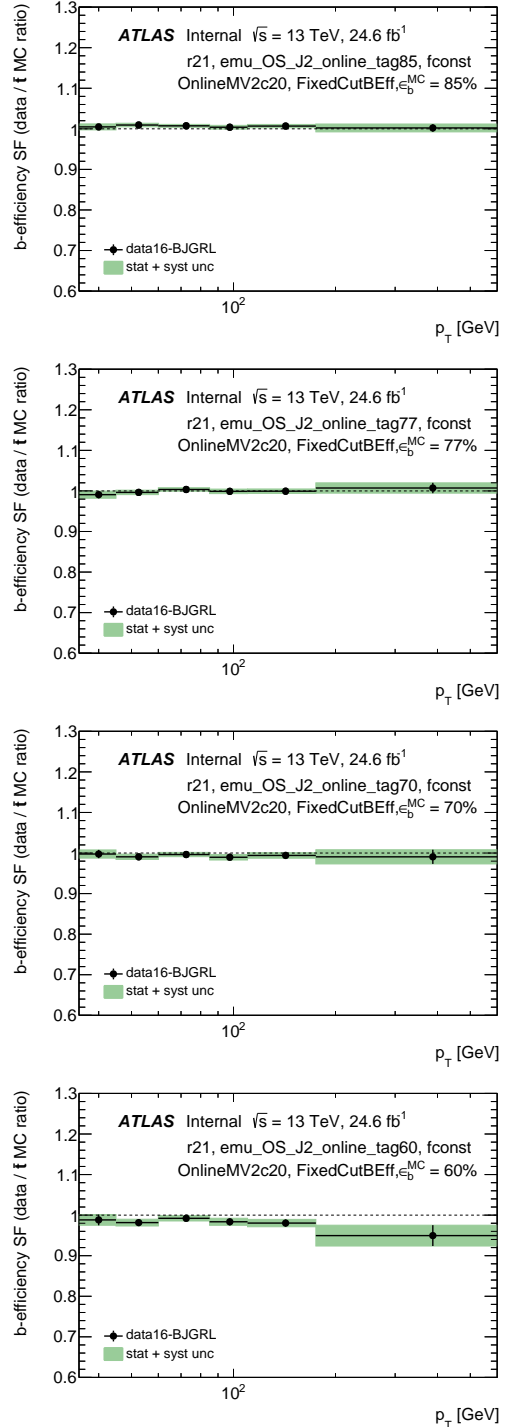


FIGURE 8: Results of the combined scale factors for diagonal combinations of online and offline  $b$ -tagging working points.

The trigger level  $b$ -tagging efficiency is calibrated in combination with the offline  $b$ -tagging thanks to a geometrical matching between trigger-level and reconstruction-level jet objects. A p.d.f. based likelihood method is used to extract the  $b$ -tagging efficiency and to produce data to MC scale factors.

## Références

- [1] Observation of Higgs boson production in association with a top quark pair at the LHC with the ATLAS detector, *ATLAS Collaboration*, CERN-EP-2018-138, Phys. Lett. B 784 (2018) 173, [arXiv:1806.00425 \[hep-ex\]](#).
- [2] Search for the Standard Model Higgs boson decaying into  $b\bar{b}$  produced in association with top quarks decaying hadronically in  $pp$  collisions at  $\sqrt{s} = 8$  TeV with the ATLAS detector, *ATLAS Collaboration*, CERN-EP-2016-058, JHEP 05 (2016) 160, [arXiv:1604.03812 \[hep-ex\]](#).
- [3] Measurements of  $b$ -jet tagging efficiency with the ATLAS detector using  $t\bar{t}$  events at  $\sqrt{s} = 13$  TeV, *ATLAS Collaboration*, CERN-EP-2018-047, JHEP 08 (2018) 89, [arXiv:1805.01845 \[hep-ex\]](#).
- [4] Optimisation and performance studies of the ATLAS  $b$ -tagging algorithms for the 2017-18 LHC run, *ATLAS Collaboration*, ATL-PHYS-PUB-2017-013.



# Measurement of the Higgs Top Yukawa coupling with the ATLAS detector at LHC

Merve Nazlim Agaras  
*Université Clermont Auvergne*



## Résumé

After the discovery of a Higgs boson ( $H$ ) in 2012, the measurements of its properties plays a very important role at the Large Hadron Collider (LHC). The determination of the associated production of the Higgs boson and a top quark pair ( $t\bar{t}H$  production) is of particular importance as it offers a tree-level access to measuring the Higgs-top Yukawa coupling. With a predicted numerical value close to unity, this coupling plays a crucial role in the stability of the Higgs potential at high energy scales and can also be a probe for physics beyond the Standard Model through the deviations from the SM predictions. The  $t\bar{t}H$  production analysis at ATLAS exploits several Higgs decay channels, together with different top quark decay modes. In this study, the general overview of the search for  $t\bar{t}H$  production in multilepton final states analysis at ATLAS is presented focusing mainly on the fitting procedure of the signal strength with two lepton same sign and a preliminary study of the Matrix Element Method that aims to improve the discrimination between the signal and the background in a specific decay channel. Both the ATLAS and the CMS collaboration have studied the  $t\bar{t}H$  production in proton-proton collisions at Run 1 of the LHC with an integrated luminosity of  $25 \text{ fb}^{-1}$  and center of mass  $\sqrt{s} = 7 - 8 \text{ TeV}$  with analyses sensitive to  $H \rightarrow WW^*$  and  $H \rightarrow \tau\tau$ . They observed a signal strength  $\mu_{t\bar{t}H}$ , defined as the measured  $t\bar{t}H$  yield divided by the prediction from the  $\mu_{t\bar{t}H} = 1.8^{+0.8}_{-0.8}$  and  $\mu_{t\bar{t}H} = 2.8^{+1.0}_{-1.0}$ , respectively [3][2]. The combined measurement of Run 1  $t\bar{t}H$  searches at ATLAS and CMS is  $\mu_{t\bar{t}H} = \sigma/\sigma_{\text{SM}}$ , of  $2.3^{+0.7}_{-0.6}$  with an observed (expected) significance of 4.4 (2.0) standard deviations from the over the SM background hypothesis [4]. Evidence for  $t\bar{t}H$  production was reported by ATLAS using  $36.1 \text{ fb}^{-1}$  of data collected during 2015 and 2016, with an observed (expected) significance of  $4.2\sigma$  ( $3.8\sigma$ ). The best-fit result of the ratio  $\mu_{t\bar{t}H}$  of the  $t\bar{t}H$  production rate to the SM expectation was found to be  $1.2 \pm 0.2$  (stat)  $^{+0.3}_{-0.2}$  (syst) and a  $t\bar{t}H$  production cross-section at  $\sqrt{s} = 13 \text{ TeV}$  of  $790^{+230}_{-210} \text{ fb}$ , both consistent with the SM expectation. The multilepton channel was the most sensitive in that analysis with an observed (expected) significance of  $4.1\sigma$  ( $2.8\sigma$ ).

## 1 Introduction

When studying the multi-lepton  $t\bar{t}H$  channel in the ATLAS experiment, the events are categorized in seven

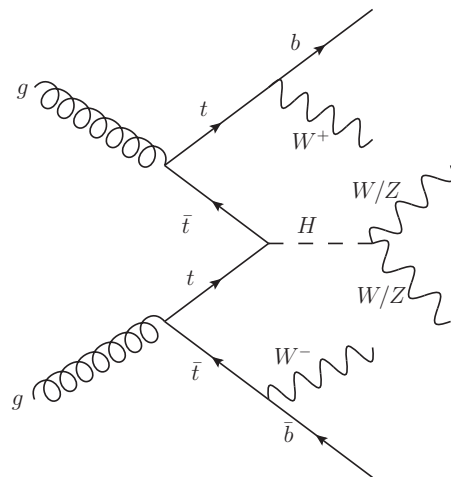


FIGURE 1: Examples of tree-level Feynman diagrams for the production of the Higgs boson in association with a pair of top quarks. Higgs boson decays to  $WW/ZZ$  (left) or  $\tau\tau$  (right) are shown.

orthogonal channels by multiplicities of light leptons ( $l=e, \mu$ ) and hadronically decaying tau leptons ( $\tau_{had}$ ). The leptonically decaying tau leptons ( $\tau_{lep}$ ) are not distinguishable from light leptons in the reconstruction. The seven channels, summarised in Figure 2.

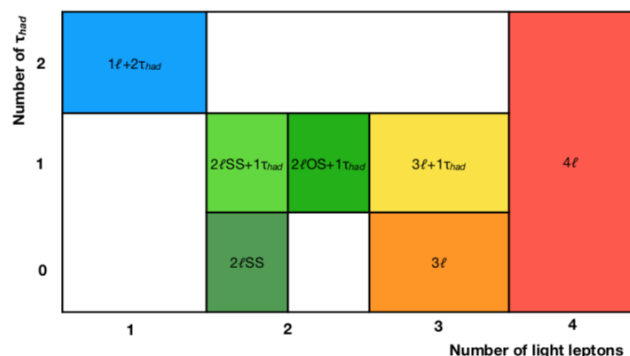


FIGURE 2: The classification of the seven analysis channels by  $\tau_{had}$  and light lepton multiplicities.

In this proceeding, the results of a search for  $t\bar{t}H$  production using  $36.1 \text{ fb}^{-1}$  of data collected during 2015 and 2016 is presented focusing on two lepton same-sign channel. Figure 1 illustrates the dominant  $t\bar{t}H$  process in two lepton same-sign channel. Several improvements regarding the fake estimates are ongoing and are expected to be included in the next version of the analysis,

using full Run-2 data (taken between 2015 and 2018).

## 2 Signal Region Definition and background estimates

In the two lepton same sign channel, events are required to have been selected by dilepton triggers ( $ee$ ,  $e\mu$ ,  $\mu\mu$ ). At the offline level, the two light leptons are required to have the same charge and to pass the tight lepton requirements including isolation working point, to be identified using a dedicated Multivariate Analysis (MVA). Both leptons are required to have transverse momentum  $p_T > 20$  GeV. There must be no  $\tau_{had}$  candidates in the event. Events must have  $\geq 4$  jets, of which  $\geq 1$  must be  $b$ -tagged. Events with at least three  $b$ -tagged jets (MV2c10 tagger with average efficiency of 70%) are removed. The leptons are classified using isolation requirements and other properties.

Background processes in signal regions can be categorized as irreducible backgrounds and reducible backgrounds. Irreducible backgrounds are events with the same number of prompt leptons as the  $t\bar{t}H$  signal, which includes  $t\bar{t}Z/W$ ,  $VV$  and rare processes ( $t\bar{t}WW$ ,  $tH$ ,  $tZ$ ,  $WtZ$ ,  $VVV$ ,  $t\bar{t}t\bar{t}$  and  $t\bar{t}$ ). Their estimation relies on good modeling of these processes in the Monte Carlo (MC) simulations. Reducible backgrounds contain at least one electron which charge was misidentified or one fake/non-prompt lepton (later call fake lepton). These reducible backgrounds mainly comes from  $t\bar{t}$  production. Various data-driven methods have been developed to estimate them instead of using MC simulations.

By construction, charge flip events are present only in two lepton channel and dominantly comes from  $t\bar{t}$ . These events pollute  $ee$  and  $e\mu$  signal regions where the actual event MVA is trained because of one electron having hard bremsstrahlung plus asymmetric conversion ( $e^\pm \rightarrow e^\pm \gamma^* \rightarrow e^\pm e^+ e^-$ ) or wrongly measured track curve. Muon charge flip is negligible. A dedicated event MVA discriminant is used in order to reduce electron charge flip by a factor 17 for a 95% electron efficiency is now used. The probability of electron charge flip is measured from a sample of  $Z$  events where  $Z \rightarrow e^+ e^-$  events ( $e^+ e^+$ ,  $e^- e^-$  in case of charge flip). A Likelihood based method is developed to measure charge flip rates,  $\epsilon_{mis\ id}$ , as a function of electron  $p_T$  and  $|\eta|$ . These rates are used to predict the number of charge flip events in the signal region. On the other hand, the non-prompt light lepton background in the two lepton channel has two origins of leptons from semi-leptonic heavy-flavour decays and photon conversions. Monte Carlo simulation is not reliable to estimate the fake lepton estimate and therefore a data-driven method, called the matrix method is used to estimate the number of non-prompt leptons in the pre-MVA region (the region where the event MVA trained) by splitting the events in four orthogonal categories :

- $TT_i$  : event with both leptons passing tight selection (Tot. events :  $N^{TT}$ ).

- $T\bar{T}_i$  : event with leading lepton passing tight selection and subleading lepton ( $p_T$ ) failing tight selection (Tot. events :  $N^{T\bar{T}}$ ).
- $\bar{T}T_i$  : event with leading lepton failing tight selection and subleading lepton ( $p_T$ ) passing tight selection (Tot. events :  $N^{\bar{T}T}$ ).
- $\bar{T}\bar{T}_i$  : event with both leptons failing tight selection (Tot. events :  $N^{\bar{T}\bar{T}}$ ).

where the tight selection includes isolation, non-prompt lepton Boosted Decision Trees (BDT), ID, charge-misassignment veto, transverse impact parameter and longitudinal impact parameter cut and anti-tight is the leptons fail the tight selection. The final number of fakes in the signal region  $N_{TT}^f$ , i.e. the total number of  $TT$  events with at least one fake lepton, can be obtained from the definition :

$$N_{TT}^f = w_{TT} N^{TT} + w_{T\bar{T}} N^{T\bar{T}} + w_{\bar{T}T} N^{\bar{T}T} + w_{\bar{T}\bar{T}} N^{\bar{T}\bar{T}} \quad (1)$$

The  $w$  weights are functions of the measured prompt and non-prompt lepton efficiencies. The non-prompt lepton estimates were validated in a region identical to the two lepton same sign signal region except for being orthogonal in the  $N_{jets}$  requirement (low multiplicity number of jets = 2, 3) (Figure 3)

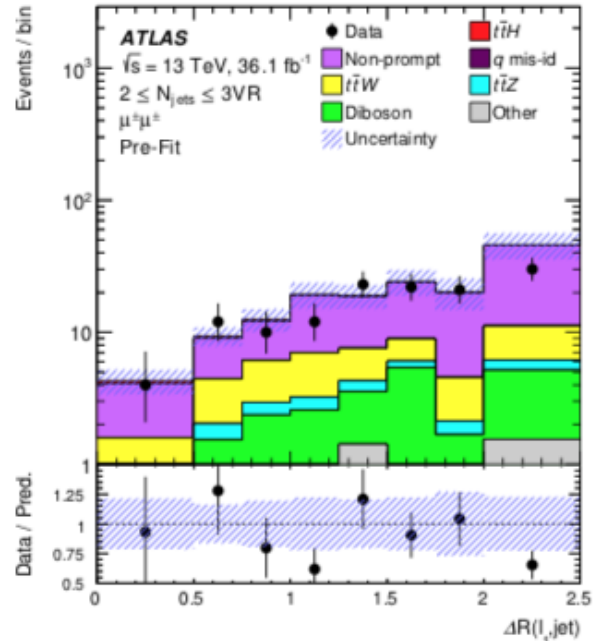


FIGURE 3: Comparison of data and prediction of the angular distance between the subleading lepton and the closest jet in the  $\mu\mu$  channel.

To further reject events with fake/non-prompt leptons and charged flip electrons as well as  $t\bar{t}W$ , two BDT scores ( $BDTG_{t\bar{t}bar}$  and  $BDTG_{t\bar{t}V}$ ) are trained in the two lepton channel. Nine input variables are used including number of jets, invariant mass of the two same-sign lepton, missing transverse energy (MET), sub-leading lepton  $p_T$ , maximum between leading and

subleading electron, distance between sub-leading lepton and its closest jet, distance between leading lepton and its closest jet, leptonic flavour, number of  $b$ -jets. The final discriminant is defined as :

$$BDTG = (BDTG_{t\bar{t}} + BDTG_{tV})/2 \quad (2)$$

### 3 Systematic uncertainties

In Table 1 all sources of systematic uncertainties are summarised. Three groups of systematic uncertainties are considered. They are included in the fit of data events to expectation in discriminant distributions through the so-called nuisance parameters (NPs) allowing for changes in the normalisation and the shape of these discriminant distributions. The NPs can therefore be of type normalisation-only (N), shape-only (S) or combined shape and normalisation (SN). The normalisation of an uncertainty has an impact on the total event yield of a signal or background sample. An uncertainty which is affecting the shape of a discriminating distribution is taken into account by the corresponding variation of input histograms in the fit.

TABLE 1: Summary of the effects of the most important groups of systematic uncertainties on  $\mu$ . Due to rounding effects and small correlations between the different sources of uncertainty, the total systematic uncertainty is different from the sum in quadrature of the individual sources.

Uncertainty Source	$\Delta\mu$
ttH modeling (cross section)	+0.20 -0.09
Jet energy scale and resolution	+0.18 -0.15
Non-prompt light-lepton estimates	+0.15 -0.13
Jet flavor tagging and Tauhad identification	+0.11 -0.09
ttW modeling	+0.10 -0.09
ttZ modeling	+0.08 -0.07
Other background modeling	+0.08 -0.07
Luminosity	+0.08 -0.06
ttH modeling (acceptance)	+0.08 -0.04
Fake Tauhad estimates	+0.07 -0.07
Other experimental uncertainties	+0.05 -0.04
Simulation sample size	+0.04 -0.04
Charge misassignment	+0.01 -0.01
Total systematic uncertainty	+0.39 -0.30

### 4 Statistical Model and Results

A maximum-likelihood fit is performed on all twelve categories simultaneously to extract the signal strength,  $\mu$ . If the SM Higgs boson signal is present then  $\mu = 1$ , but if it is absent then  $\mu = 0$ . The statistical analysis of the data uses a binned likelihood function  $\mathcal{L}(\mu, \vec{\theta})$ , which is constructed from a product of Poisson probability terms, to estimate  $\mu$ , which scales the ttH production cross section. The Higgs boson branching fractions and the single top-Higgs boson associated production cross section are fixed to their SM values.

The impact of each systematic uncertainty on the final result is assessed by performing the fit with the parameter fixed to its fitted value varied up or down by its fitted uncertainty, with all the other parameters allowed to vary and calculating the  $\mu$  to the baseline fit. The ranking obtained for those nuisance parameters with the largest contribution to the uncertainty in the signal strength is shown in Figure 5. The post-fit distributions of the discriminating variable in the two lepton same sign channel is shown in Figure 7.

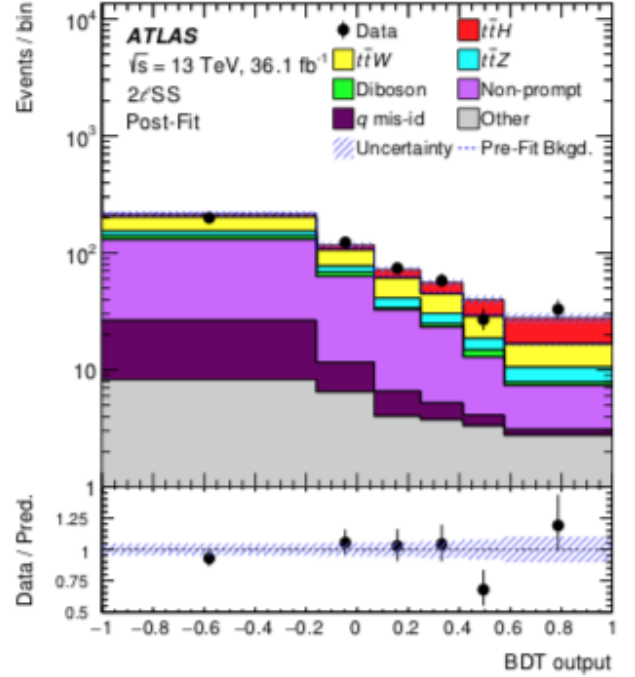


FIGURE 4: Distribution of the discriminant variable observed in data (points with error bars) and expected (histograms) in the two lepton same sign channel.

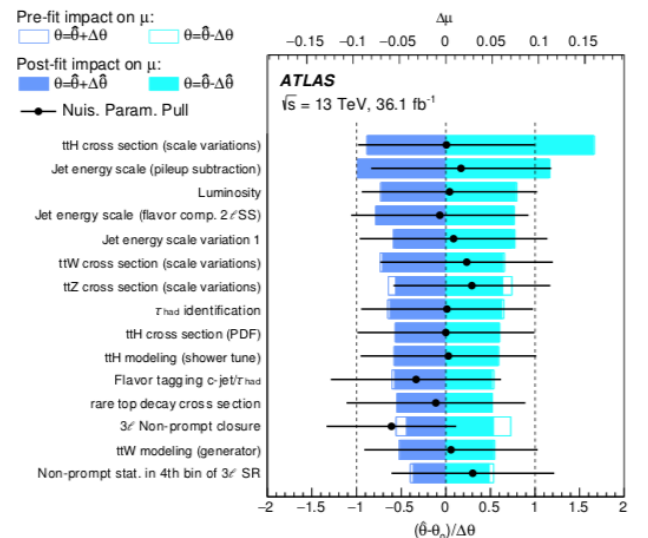


FIGURE 5: Impact of systematic uncertainties on the fitted signal-strength parameter for combination.

The observed (expected) best-fit value of  $\mu_{t\bar{t}H}$ , combining all channels, is  $1.6^{+0.3}_{-0.3}$  (stat)  $^{+0.4}_{-0.3}$  (syst)  $=1.6^{+0.5}_{-0.4}$  ( $1.00^{+0.3}_{-0.3}$  (stat)  $^{+0.3}_{-0.3}$  (syst)  $=1.00^{+0.4}_{-0.4}$ ). The best-fit value of  $\mu_{t\bar{t}H}$  for each individual final state category and the combination of all channels are shown in Figures 6.

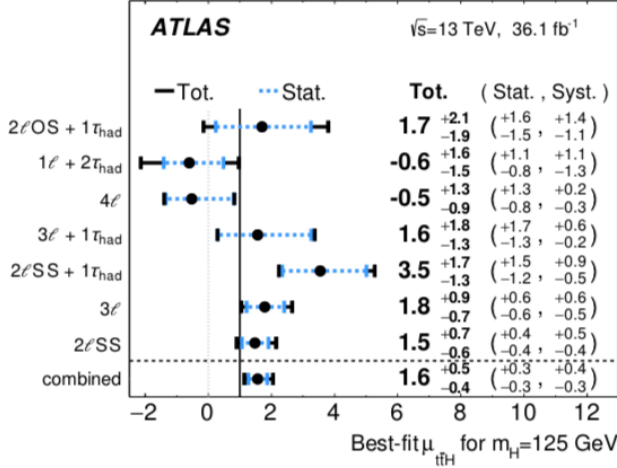


FIGURE 6: The observed best-fit values of the signal strength  $\mu$  and their uncertainties by final-state category and combined. The individual  $\mu$  values for the channels are obtained from a simultaneous fit with the signal-strength parameter for each channel floating independently.

## 5 Possible improvements in Two Lepton Same Sign

The Matrix Element Method (MEM) provides a way to calculate the likelihood that an event originates from a given production mechanism. Of particular interest to this analysis is discriminating between  $t\bar{t}H$  and  $t\bar{t}+jets$ . The MEM is thus used to calculate the two likelihoods  $L_S$  and  $L_B$ :

- $L_S$ : signal likelihood, likelihood of the event having been produced via a  $t\bar{t}H$  Feynman diagram
- $L_B$ : background likelihood, likelihood of the event having been produced via a  $t\bar{t} + b\bar{b}$  Feynman diagram

These likelihoods are defined as follows:

$$L_i = \sum \int \frac{f_1(x_1, Q^2) f_2(x_2, Q^2)}{|\vec{q}_1||\vec{q}_2|} |\mathcal{M}_i(\mathbf{y})|^2 T(\mathbf{x}; \mathbf{y}) d\Phi_n(\mathbf{y}) \quad (3)$$

The likelihood is a sum over different possible initial states (quarks or gluons) and over multiple jet-parton assignments. It contains a product of parton distribution functions  $f_1 f_2$ , which are probability distribution functions for a certain parton with momentum  $\vec{q}_j$  to carry energy fraction  $x_j$  of the proton in a collision at energy  $Q$  (for the two initial states  $j = 1, 2$ ). The matrix element (ME)  $\mathcal{M}_i$  is calculated for a phase space

configuration  $\mathbf{Y}$  at parton level, where the index  $i$  refers to either signal or background Feynman diagrams evaluated at leading order. The transfer function  $T$  is a probability distribution for a given jet measured on reconstruction level  $\mathbf{X}$  to be originating from a parton level configuration  $\mathbf{Y}$ . As only the reconstruction level information  $\mathbf{X}$  is available, all unknown parameters are integrated out via the phase space factor  $d\Phi_n$ .

The combination of signal and background likelihoods, which are evaluated on both data and MC, results in a powerful discrimination variable:

$$MEM_{D1} = \log_{10}(L_S) - \log_{10}(L_B) \quad (4)$$

MEM can be used to improve the signal-background discrimination in two lepton same sign channel. Preliminary studies are shown in Figure ?? for  $t\bar{t}H$  vs  $t\bar{t}+jets$  processes in six number of jet region. Currently, with all run2 dataset, the studies are on going for the 2 same sign lepton with one  $\tau$ -lepton channel. The improvements are expected to be applied in the next version of the analysis.

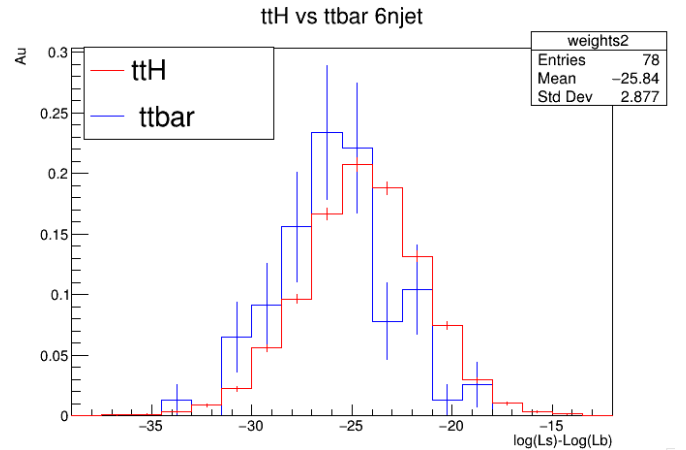


FIGURE 7: MEM results for  $t\bar{t}H$  vs  $t\bar{t}+jets$  processes in six number of jet region.

## Références

- [1] Phys. Rev. D 97, 072003 (2018), Evidence for the associated production of the Higgs boson and a top quark pair with the ATLAS detector
- [2] Search for the associated production of a Higgs boson with a top quark pair in final states with a  $\tau$  lepton at  $\sqrt{s} = 13$  TeV
- [3] Measurements of the Higgs boson production and decay rates and coupling strengths using pp collision data at  $\sqrt{s} = 7$  and 8 TeV in the ATLAS experiment
- [4] Measurements of the Higgs boson production and decay rates and constraints on its couplings from a combined ATLAS and CMS analysis of the LHC pp collision data at  $\sqrt{s} = 7$  and 8 TeV

# Observables de spin des leptons taus dans l'expérience CMS auprès du LHC

Guillaume Bourgatte  
IPHC, Strasbourg



## Résumé

À partir de grandeurs physiques cinématiques dans les désintégrations du boson Z en paires de leptons taus, on peut construire une variable  $\omega$  qui contient toutes les informations sur la polarisation des taus. Cette dernière permet de remonter à un paramètre important du modèle standard qu'est l'angle de mélange électrofaible dit de Weinberg  $\theta_W$  et d'obtenir une meilleure précision sur ce dernier. L'étude des observables de spin des leptons  $\tau$  permet d'étudier les corrélations longitudinales de spins des désintégrations en question. Ces événements étant le bruit de fond principal du boson de Higgs se désintégrant en paire de leptons taus, l'étude du boson Z permet d'étudier les propriétés CP du boson de Higgs en utilisant cette fois-ci les corrélations transverses de spins.

## 1 Introduction

L'interaction faible du modèle standard viole la symétrie dite de parité (inversion des coordonnées spatiales) ce qui entraîne des couplages différents selon si la particule est de chiralité gauche ou droite. Les bosons  $W^\pm$  interagissent uniquement avec les particules gauches ce qui mène à une violation de parité maximale. Le boson Z quant à lui se couple avec des intensités différentes. La chiralité, propriété intrinsèque d'une particule, ne pouvant être observée, on utilise l'hélicité pour accéder à cette dernière. L'hélicité d'une particule est la projection de son spin sur son vecteur impulsion :

$$\frac{\vec{s} \cdot \vec{p}}{|\vec{p}|}$$

Si  $h=+1$  alors la particule est de chiralité droite et si  $h=-1$  la particule est de type gauche.

Un paramètre important du modèle standard est l'angle de mélange électrofaible  $\theta_W$ , aussi appelé angle de Weinberg, qui relie les masses des bosons W et Z et entraîne une différence dans le couplage faible neutre aux fermions de chiralité droite et gauche. On peut obtenir  $\theta_W$  en mesurant la polarisation longitudinale des paires de  $\tau$  provenant d'une désintégration d'un boson Z. Les leptons  $\tau$ , contrairement aux  $\mu$  et  $e$ , vont se désintégrer à 65% en hadrons qui vont eux même se désintégrer. Ces  $\tau_h$  sont appelés taus hadroniques. Ceci est particulièrement intéressant car l'étude des distributions angulaires des produits de désintégration permet d'obtenir la polarisation.

À cause de la violation de la parité dans les interactions électrofaibles, les fermions provenant de la désintégration du boson Z ont une polarisation P moyenne non nulle. Cette dernière décrit l'asymétrie entre le nombre de particules N de chaque hélicité :

$$P = \frac{N(h = +1) - N(h = -1)}{N(h = +1) + N(h = -1)} \simeq -2 + 8\sin^2\theta_W$$

La polarisation est très fortement liée à l'angle de mélange  $\theta_W$  vu qu'elle dépend des couplages entre les leptons  $\tau$  et le boson Z. Sa mesure permet donc d'accéder à l'angle  $\theta_W$ .

Ceci a déjà été effectué avec des leptons  $\tau$  au Large Electron Positron collider (LEP) [1] avec des collisions  $e^+e^-$  à une énergie dans le centre de masse proche de la masse du boson Z puis par l'expérience ATLAS au LHC à une énergie de 8 TeV [2]. Actuellement le LHC opère à une énergie dans le centre de masse de 13 TeV. Le but est donc d'obtenir une meilleure précision que les mesures précédentes grâce à une plus grande quantité de données disponible et à l'amélioration de la méthode.

## 2 Description du détecteur CMS

Le Large Hadron Collider (LHC) est le plus grand accélérateur de particules au monde avec 27 km de circonférence et se situe à la frontière franco-suisse. L'expérience Compact Muon Solenoid (CMS) (cf. Fig. 1) est située sur le LHC :

1. Au centre de celle-ci est placé un trajectographe en silicium qui permet de retracer le passage des particules et de mesurer leurs impulsions.
2. Un calorimètre électromagnétique permet de récolter l'énergie déposée principalement par les électrons et photons tandis qu'un calorimètre hadronique récupère l'énergie des hadrons (protons ou pions par exemple).
3. En son sein règne un champ magnétique de 3.8 Teslas, soit 100 000 fois celui de la Terre, qui dévie les particules chargées grâce au solénoïde supraconducteur le plus grand et le plus puissant jamais construit.
4. Enfin une chambre à muons permet de détecter la présence de ces derniers qui sont très pénétrants.

Les collisions produisant une énorme quantité de données (40 millions d'événements par seconde), un

tri s'impose à l'aide d'un système de déclenchement. Le premier niveau (L1) est de type hardware et utilise l'information des calorimètres et du détecteur à muons pour sélectionner les événements les plus intéressants toutes les 4  $\mu\text{s}$  ce qui permet de réduire à cent mille événements par seconde le taux d'enregistrement des événements. Le second niveau dit de haut niveau (HLT) est de type software et utilise toute l'information des sous-détecteurs. Il réduit le taux d'événements à deux ou trois mille par seconde.

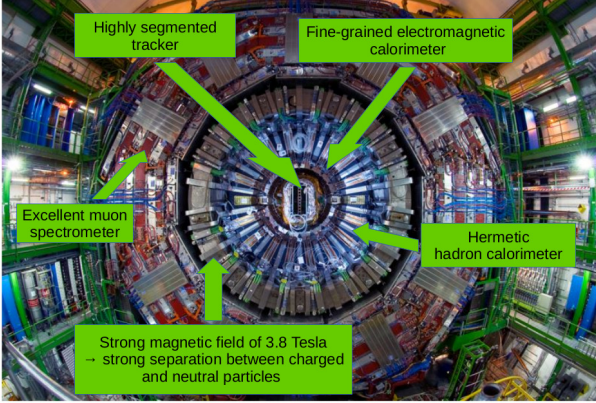


FIGURE 1: Image de la coupe transverse de l'expérience CMS.

Les jets de particules formés par les désintégrations des hadrons sont utilisés comme graines pour la reconstruction des  $\tau_h$ . Ceci est fait en exploitant la sous-structure des jets en utilisant l'algorithme hadrons-plus-strips (HPS) [3]. Les pions neutres sont reconstruits comme des bandes calorimétriques de tailles dynamiques à partir des candidats  $e$  et  $\gamma$  reconstruits contenus dans le jet servant de graine (cf. Fig 2). La taille de la bande varie suivant l'impulsion transverse ( $p_T$ ) des  $e$  et  $\gamma$ . Le mode de désintégration du  $\tau_h$  est obtenu en combinant les hadrons chargés avec les bandes. Comme ils ne portent pas de charges de couleur, les  $\tau$  à haut  $p_T$  sont supposés être isolés des autres activités hadroniques de l'événement comme le sont les  $e$  et  $\mu$  à haut  $p_T$  (cf. Fig 3). De plus, à cause du temps de vie fini du  $\tau$ , ses produits de désintégrations chargés sont légèrement déplacés par rapport au vertex primaire. Pour distinguer les désintégrations des  $\tau_h$  des jets originaires de l'hadronisation des quarks et gluons, un discriminant multivarié d'identification des  $\tau_h$  est utilisé. Il combine l'information de l'activité hadronique du détecteur dans les environs du candidat  $\tau_h$  avec le temps de vie reconstruit à partir des traces des produits de désintégrations chargés.

### 3 Variables optimales

Dans le canal  $\tau \rightarrow \pi\nu_\tau$ , suivant le spin du lepton  $\tau$ , seuls deux configurations sont possibles (cf. Fig. 4). On peut donc construire un angle  $\theta_\pi^*$  qui, suivant sa valeur, permettra de connaître le spin du  $\tau$  et donc son hélicité.

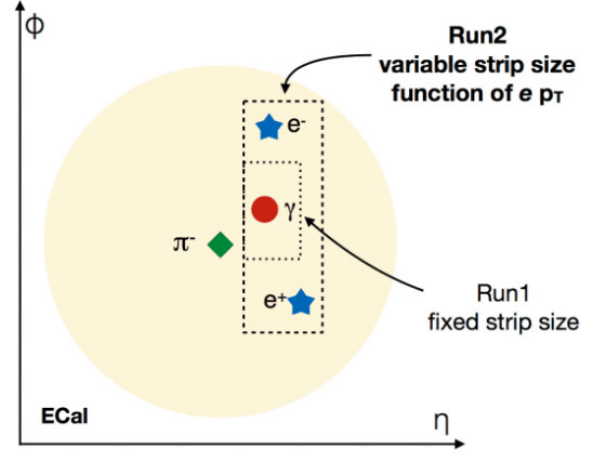


FIGURE 2: Schématisation de la reconstruction des pions neutres en utilisant l'algorithme HPS.

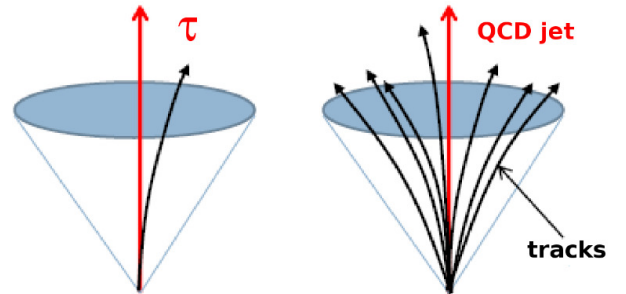


FIGURE 3: Différences entre un jet provenant d'un  $\tau_h$  et un jet purement chromodynamique quantique (QCD).

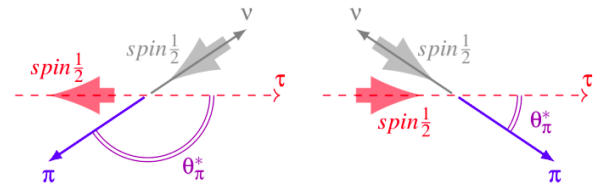


FIGURE 4: Différentes configurations de spins dans le canal  $\tau \rightarrow \pi\nu_\tau$ .

La valeur de  $\cos\theta_\pi^*$  permet donc de séparer les deux hélicités. Cependant ce canal ne représente qu'environ 11% des désintégrations. On a donc besoin d'autres canaux comme  $\tau \rightarrow \rho\nu_\tau$  ou  $\tau \rightarrow a_1\nu_\tau$ . Le canal avec un  $a_1$  possède 4 configurations différentes car ce hadron possède un spin entier égal à 1 et a donc deux orientations de spin possibles pour un même angle  $\theta_{a_1}^*$  (cf. Fig. 5). Cet angle ne suffit donc plus.

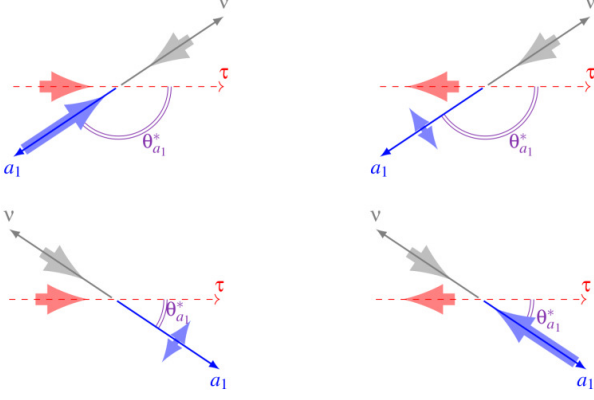


FIGURE 5: Différentes configurations de spins dans le canal  $\tau \rightarrow a_1\nu_\tau$ .

On a besoin de définir d'autres angles, plus compliqués, et de les réunir dans une variable dite optimale [4]. En théorie, les distributions des produits de désintégrations,  $W$ , dépendent linéairement de la polarisation :

$$W = \frac{1}{2}(1 + \vec{s} \cdot \vec{h}) = \frac{1}{2}(1 + |\vec{s}| \cdot |\vec{h}| \cos\theta_h)$$

Avec  $\vec{s}$  le spin du hadron,  $\vec{h}$  le vecteur polarimétrique qui est un vecteur unitaire dans la direction la plus probable du spin du  $\tau$  au repos et  $\theta_h$  étant l'angle entre la direction du  $\tau$  au repos et le vecteur polarimétrique. Mais dans les faits, du fait de la présence de neutrinos indétectables, nous ne connaissons pas la cinématique complète du système. C'est pourquoi nous avons besoin de plusieurs angles, qui seront utilisés pour calculer plus précisément  $\vec{s}$  et  $\vec{h}$ , afin de s'approcher de la formule théorique. Pour la suite on définit  $\omega = \cos\theta_h$  qui sera notre variable optimale séparant les différentes hélicités (cf. Fig. 6).

Une application de cette méthode sur les données à 8 TeV pour le processus  $Z \rightarrow \tau\tau$  [6] fut effectuée (cf. Fig. 7) ce qui a permis de valider cette approche.

Mais ce  $\omega$  ne décrit qu'un seul  $\tau$  se désintégrant. Afin d'obtenir une meilleure séparation des hélicités, nous pouvons combiner les informations des deux  $\tau$  :

$$\Omega = \frac{\omega_1 + \omega_2}{1 + \omega_1\omega_2}$$

Cela permet d'augmenter le pouvoir de séparation des hélicités de la nouvelle variable optimale  $\Omega$  par rapport à  $\omega$  (cf. Fig. 8).

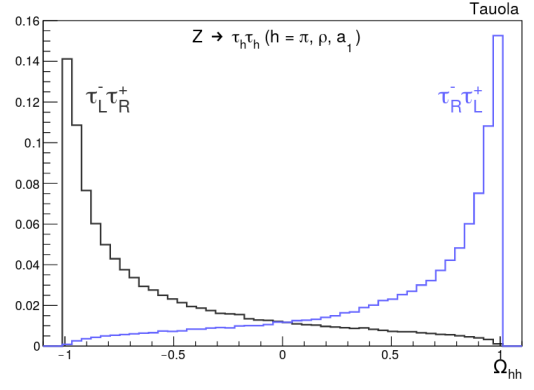


FIGURE 6: Distributions simulées des hélicités gauches (-) et droites (+) en fonction de  $\cos\theta_h$ . La séparation représentée est pour  $h = \pi, \rho$  et  $a_1$  [5].

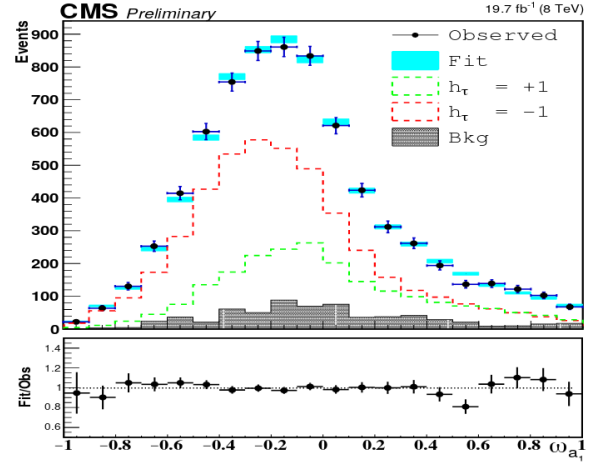


FIGURE 7: Distribution de la variable optimale  $\omega_{a_1}$  dans le canal  $a_1$  pour une énergie de collision de 8 TeV pour des événements  $Z \rightarrow \tau\tau$ . Un ajustement est appliqué avec les fractions relatives des deux hélicités comme paramètres libres [6].

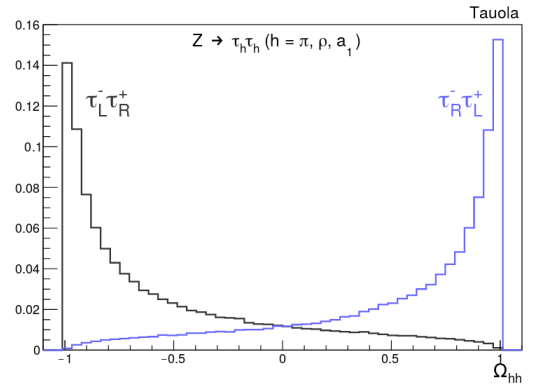


FIGURE 8: Distributions simulées pour les différentes combinaisons d'hélicités d'une paire de  $\tau$  en fonction de la variable optimale  $\Omega$  pour  $h = \pi, \rho$  et  $a_1$  [5].

## 4 Higgs CP

On étudie maintenant les corrélations transverses du boson de Higgs. Le couplage de Yukawa du  $\tau$  est donné par :

$$L_Y = g_\tau (\cos \alpha_\tau \bar{\tau} \tau + \sin \alpha_\tau \bar{\tau} \gamma_5 \tau)$$

Le paramètre  $\alpha_\tau$  est nul dans le modèle standard car d'après ce dernier, le boson de Higgs ne viole pas la symétrie charge-parité (CP). Or de supplémentaires violations de symétrie CP pourraient expliquer l'asymétrie matière-antimatière observée dans notre Univers. Afin de vérifier si le boson de Higgs est bien le boson prédit par le modèle standard, on peut extraire la composante CP de ce dernier à partir des corrélations entre les produits de désintégration des  $\tau$  dans le plan transverse à l'axe  $\tau^+ \tau^-$  en utilisant l'angle acoplaire. Ce dernier est défini par l'angle entre les deux plans formés par la direction des  $\tau_h$  dans le référentiel au repos du boson de Higgs et les vecteurs polarimétriques (cf. Fig. 9 et 10).

Les corrélations transverses pourront également être étudiées pour le boson Z et cette méthode d'analyse sera appliquée sur des données à une énergie dans le centre de masse de 13 TeV.

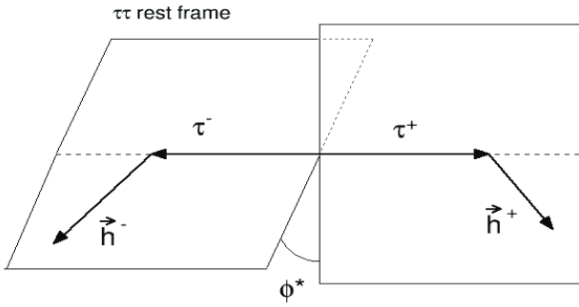


FIGURE 9: Représentation de l'angle acoplaire [7].

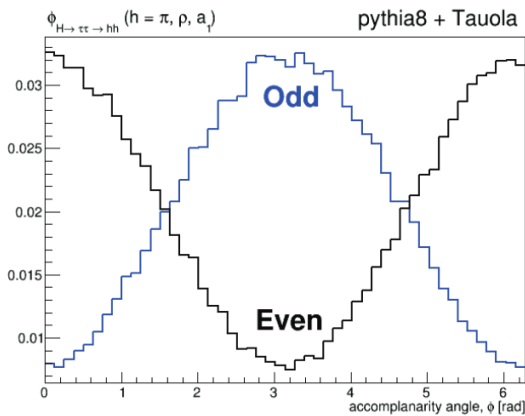


FIGURE 10: Distributions simulées montrant la séparation des composantes CP paire et impaire du boson de Higgs suivant l'angle acoplaire avec une reconstruction complète de la cinématique du système pour  $h = \pi, \rho$  et  $a_1$  [7].

## 5 Remerciements

Je remercie les organisateurs pour ce superbe séjour et la bonne ambiance qui y régnait. Merci au village vacances de nous avoir accueillis et merci aux participants d'avoir présenté leurs travaux. Je remercie également Reina Camacho pour ses corrections.

## Références

- [1] F. Sánchez Nieto, Measurement of the transverse spin correlation in the decay  $Z^0 \rightarrow \tau^+ \tau^-$ , <http://cds.cern.ch/record/389153/files/thesis-99-030.pdf?version=1>
- [2] CMS Collaboration, Measurement of  $\tau$  polarisation in  $Z/\gamma^* \rightarrow \tau\tau$  decays in proton–proton collisions at  $\sqrt{s} = 8$  TeV with the ATLAS detector, <https://arxiv.org/abs/1709.03490>
- [3] CMS Collaboration, Performance of reconstruction and identification of  $\tau$  leptons decaying to hadrons and  $\nu_\tau$  in pp collisions at  $\sqrt{s} = 13$  TeV, <https://arxiv.org/abs/1809.02816>
- [4] M. Davier, L. Duflot, F. LeDiberder and A. Rougé, The optimal method for the measurement of tau polarization, <https://www.sciencedirect.com/science/article/abs/pii/S037026939390101M>
- [5] V. Cherepanov, W. Lohmann, Methods for a measurement of  $\tau$  polarization asymmetry in the decay  $Z \rightarrow \tau\tau$  at LHC and determination of the effective weak mixing angle, <https://arxiv.org/pdf/1805.10552.pdf>
- [6] V. Cherepanov, Perspectives for a measurement of  $\tau$  polarization in  $Z \rightarrow \tau\tau$  with CMS, <https://indico.ihep.ac.cn/event/5221/session/10/contribution/44/material/slides/0.pdf>
- [7] Z. Was, V. Cherepanov, B. Le, E. Richter-Was, Monte Carlo, fitting, Machine Learning for Tau leptons, <https://indico.cern.ch/event/632562/contributions/3117827/attachments/1721691/2779846/Amst18.pdf>
- [8] V. Cherepanov, Measurement of the polarization of  $\tau$  leptons produced in  $Z^0$  decays at CMS and determination of the effective weak mixing angle  $\sin^2 \theta_{eff}$ , [https://cds.cern.ch/record/2206964/files/TS2016\\_014\\_2.pdf](https://cds.cern.ch/record/2206964/files/TS2016_014_2.pdf)

Cinquième partie

# Instrumentation

session dirigée par Sabrina SACERDOTI



# A High-Granularity Timing Detector for the Phase-II upgrade of the ATLAS Detector System

Agapopoulou Christina

*Universite Paris Sud - Laboratoire de l'Accelérateur Lineaire*

## Résumé

The expected increase of the particle flux at the high luminosity phase of the LHC with instantaneous luminosities up to  $L=7.5 \times 10^{34} \text{ cm}^{-2}\text{s}^{-1}$  will have a severe impact on pile-up. The pile-up is expected to increase on average to 200 interactions per bunch crossing. The reconstruction performance for especially jets and transverse missing energy will be severely degraded in the end-cap and forward region of the ATLAS detector. A High Granularity Timing Detector (HGTD) is proposed in front of the liquid Argon end-cap calorimeters of ATLAS for pile-up mitigation in the off-line reconstruction. An additional use of the detector as a luminometer is proposed. This device covers the pseudo-rapidity range of 2.4 to about 4. Silicon sensors are foreseen to provide precision timing information with a time resolution of the order of 30 picoseconds per minimum ionizing particle in order to help assign tracks to different proton-proton collision vertices. Each readout sensor pad has a transverse size of only a few mm, leading to a highly granular detector with several million readout channels. The expected improvements in performance are relevant for physics processes, i.e, vector-boson fusion and vector-boson scattering processes. The chosen silicon sensor technology is Low Gain Avalanche Detectors (LGAD). In this document, starting from the physics motivations of the High Granularity Timing Detector, the proposed detector layout and sensor technology, laboratory and beam test characterization of the prototype front-end electronics will be discussed.

## 1 Introduction

In 2026, LHC will enter its High Luminosity phase, where the instantaneous luminosity will increase from  $2\text{-}3 \times 10^{34} \text{ cm}^{-2}\text{s}^{-1}$  to  $7.5 \times 10^{34} \text{ cm}^{-2}\text{s}^{-1}$  [1]. One of the main challenges of HL-LHC will be the management of pile-up interactions, which are all the interactions happening around the interaction of interest. With the increased luminosity, an average of 200 pile-up interactions per event are expected, while the beam average spread is expected to be 50 mm along the beam axis. Fig. 1 shows the expected resolution of the  $z_0$  impact parameter used for track-to-vertex association as a function of the track pseudorapidity for tracks with different  $p_T$ . The impact parameter resolution grows rapidly as a function of the track  $|\eta|$  and, in the forward region, beyond  $|\eta| = 2.5$ , it reaches very large values

of several millimeters. The resolution also worsens at low  $p_T$  due to multiple scattering effect. In HL-LHC conditions, the local average vertex density is expected to be approximately 1.6 vertices/mm reaching up to 3 vertices/mm in certain occasions. Under such a high density of interactions, distinguishing the individual vertices, finding the primary vertex and matching the tracks to the vertices only using the spacial resolution of the Inner Tracker (ITk) of ATLAS becomes a challenge. As a consequence the accuracy of the reconstruction of all physics objects is expected to be degraded. This effect is especially pronounced in the forward region, where the particle density is the largest. The forward region contains physics signatures of great interest, such as Vector Boson Fusion (VBF) Higgs production, where forward jets provide the key handle for the process's trigger.

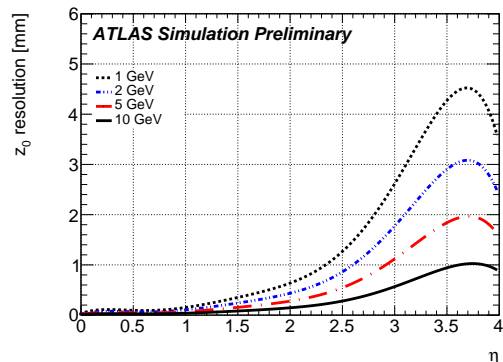


FIGURE 1: Impact parameter resolution of the ITk as a function of the  $|\eta|$  for tracks with different momentum.

The HGTD [2] gives a solution to this problem, since the additional time information it provides can be used to distinguish "merged" pile-up vertices that are in a distance below the spatial sensitivity of the Inner detector. In the HL-LHC, the collisions are expected to follow a Gaussian distribution in time with  $\sigma = 180 \text{ ps}$ . Given the current estimate for the time resolution of the HGTD of 30 ps, the detector can greatly help in the mitigation of pile-up. In addition, the HGTD can be used as a precise luminometer. Due to its high granularity, it is expected to provide good linearity between the number of hits and the number of interactions, while adjustable time windows can be used to study afterglow effects.

## 2 Detector Overview

The limited available space in ATLAS and the harsh radiation environment of the forward region in the HL-LHC are defining parameters for the design of the HGTD. The total envelope of the HGTD, including peripheral electronics and support structures, will occupy a space between  $R=110-1000$  mm in radius, while a volume that ranges from 2.4 to 4 in  $|\eta|$  or equivalently 120-640 mm in radius is currently considered free for the active area of the detector. To satisfy the space limitations in ATLAS, the HGTD is proposed to be a very thin, disk-shaped planar detector, occupying the forward region on both sides at  $|z| = (3435, 3485)$  mm, as illustrated in Fig. 2. HGTD will be placed between the ITK and 50 mm of moderator (used to protect the ITk and HGTD from radiated neutrons coming from the calorimeters). The lack of space is a limiting factor also for the number of layers of the detector and the design of the services, such as electronic readout and cooling. The current design includes 2 cooling plate layers per endcap with LGAD silicon sensors equipped on both the front and the back side to improve the time resolution. A maximum sensor overlap of 80% between the front and back side of each cooling plate is foreseen for the inner radius, where the radiation damage and particle density are the highest, while for the outer radius, the sensors are more sparsely placed with a 20% overlap. In order to be able to reconstruct individually most of the particles hitting the detector, a low occupancy is also necessary. An upper limit of 10% for the occupancy can be achieved by making the detector very granular. The current choice is to have  $1.3 \times 1.3$  mm<sup>2</sup> sensor pads. The signal from the sensors will be readout by  $2 \times 2$  cm<sup>2</sup> 225-channel Application-Specific Integrated Circuits (ASICs). The connection will be established by directly bump-bonding the sensors to the ASICs. The ASIC-sensor units will be organized in  $2 \times 4$  cm<sup>2</sup> modules containing 2 ASICs each. Kapton flexes will transfer the data from the ASICs to the peripheral on-detector electronics.

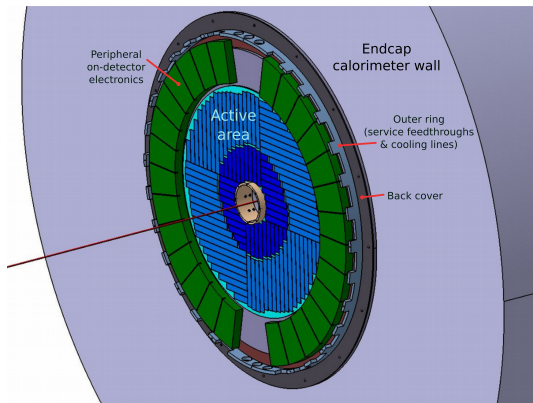


FIGURE 2: Illustration of the HGTD, showing the peripheral on-detector electronics in green and the layout of the readout rows, containing modules mounted on the inner half-disk support plates at  $R < 320$  mm (dark blue), and on staves at larger radii (light blue)

Due to the high particle rate in the forward region, it is also crucial for the HGTD to be radiation-hard to be able to function without the need for repair for a large period of time. With radiation levels reaching up to  $9 \times 10^{15}$  n<sub>eq</sub>/cm<sup>2</sup> and a Total Ionizing Dose (TID) of 9 MGy after 4000 fb<sup>-1</sup> (integrated luminosity at the end of HL-LHC) including safety factors, a replacement of the inner-radius ( $R < 320$  mm) modules is planned at the half-time of the HL-LHC. Consequently the HGTD will need to withstand radiation level that are half of the values mentioned above. The detector will be operated at a temperature of  $-30^\circ\text{C}$ , in order to limit the leakage current of the sensors due to irradiation.

## 3 Sensors

Following the constraints and requirements previously described, silicon has been chosen as the sensor material for the detector, since it can provide sufficient time resolution, high granularity and compactness. The sensor technology and design are driven by the desired timing performance of the detector.

### 3.1 Time resolution in the HGTD

The time resolution of the detector needs to be as good as possible, to allow for precise timing information. For the HGTD, the main contributions to the time resolution are given by the following equation :

$$\sigma_{\text{det}}^2 = \sigma_{\text{Landau}}^2 + \sigma_{\text{electronics}}^2$$

- the Landau fluctuations of the sensor, that are due to the non-uniformity of the particle energy deposit. Simulation results show that this contribution can be limited by choosing a thin sensor with medium doping. A sensor of about  $50 \mu\text{m}$  corresponds to a Landau fluctuation of about 25 ps, which makes the goal of a 30 ps time resolution achievable.
- the electronics contribution, which can be traced back to three main factors :
  - (1) The jitter, that is the noise contribution to the signal, is given by the expression :

$$\sigma_{\text{jitter}} = \frac{N}{dV/dt}$$

where  $N$  is the noise and  $dV/dt$  the slope of the signal. For a given signal amplitude, thin sensors have a faster rising time and therefore are optimal for the jitter suppression. Additionally, the jitter is minimized for small detector capacitance, which is achieved by making small-area sensors ( $C \propto A/d$ , where  $A$ =area and  $d$ =thickness of the sensor). On the other hand, the detector capacitance contribution to the noise is a limiting factor to the thinness of the sensor. A thickness of  $50 \mu\text{m}$  has been chosen as the default value for the HGTD, resulting in a detector capacitance of approximately 3.5 pF.

(2) The Time Walk which is the error due to the fact that, when measuring time with a constant threshold discriminator, high-amplitude signals cross the discriminator constant threshold faster than smaller ones. This effect produces a dependence of the digital signal on the amplitude of the analog one, but can be corrected by using a Time-over-Threshold (TOT) discriminator, which measures the width of the pulse that is proportional to the analog signal amplitude. After correction, the time walk is expected to give a negligible contribution, smaller than 10 ps RMS peak-to-peak.

(3) Digitization contribution, due to the finite binning of the Time to digital converter (TDC). This digitization method introduces a resolution equal to the cell delay value, which, for the HGTD, is around 20 ps. The final contribution of the TDC,  $\sigma_{\text{TDC}} = 20 \text{ ps}/\sqrt{12}$ , is negligible.

### 3.2 Sensor technology

Given the timing performance goals of the HGTD, the Low Gain Avalanche Detector (LGAD) [3, 4] sensor technology has been chosen. The LGAD is a n-p silicon detector with a highly doped p-layer below the n-p junction. As illustrated in figure 3, when a charged particle crosses the detector, it creates pairs of electrons and holes, which drift in opposite directions due to an externally applied voltage (bias voltage). When the electrons reach the doped layer, they produce more electrons and holes, inducing an avalanche which creates the amplified detected signal. For the HGTD, a moderate gain of 20 has been chosen in order to provide sufficient amplification, while minimizing the noise and the power consumption.

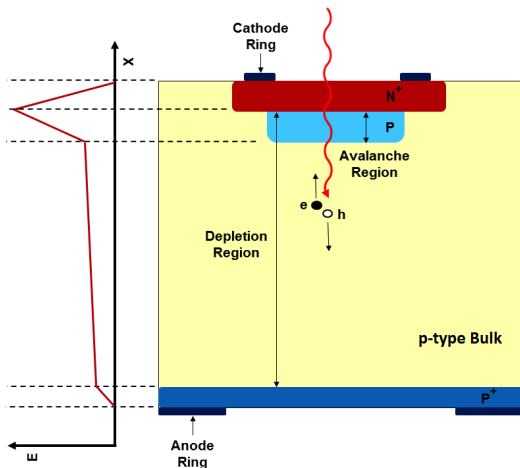


FIGURE 3: principle of an LGAD silicon sensor

## 4 Front-End Electronics

The LGAD signal will be read out and digitized by a 225 channels,  $2 \times 2 \text{ cm}^2$  ASIC on which the sensor will be bump-bonded. The design of the ASIC should be op-

timized to minimize the electronic noise contribution to the time resolution while withstanding the harsh radiation environment and trigger rates of the HL-LHC. In addition, the power dissipation should be minimized, to maintain the cooling budget. Each channel of the ASIC, will contain :

- a voltage preamplifier based on the 130 nm TSMC CMOS technology, followed by
- a discriminator that provides a Time-of-Arrival (TOA) and Time-Over-Threshold measurement
- two Time-to-Digital Converters (TDC) for the digitization of Time-of-Arrival and Time-Over-Threshold measurements
- buffers for storing the signal information until the trigger is received.

### 4.1 Prototype Measurements

A first prototype of this dedicated ASIC, named ALTIROC0 [5] was designed by Omega. This prototype is an 8-channel chip which integrates only the preamplifier and the discriminator parts of the readout chain. The digital part of the front end electronics has not been included, in order to test only the analog characteristics of the electronics. The prototype ASIC has been through two design iterations. In the later version, the speed of the voltage preamplifier was optimized for faster signals, while, in 4 out of the 8 channels, a different type of preamplifier, called trans-impedance, was used. The ALTIROC0 ASIC is readout by a custom-made board that provides a calibration input, direct discriminator outputs for all the channels as well as dedicated probes that monitor the output of the preamplifier.

#### Calibration results

Tests of the prototype were performed with a calibration setup. The setup contains a picosecond step generator which injects a step pulse of a well defined voltage to the board through a 100 fF capacitor, thus generating a very precise injected charge. The ALTIROC0 ASIC was either tested alone or with sensors bump-bonded. In the later case, the sensor was not involved in the signal production but was simply providing a realistic value of detector capacitance.

The performance of three preamplifier types, 2 voltage preamplifiers with different speeds and one trans-impedance, was tested, in order to choose the best design. For 10 fC, a value that corresponds to approximately 1 MIP, the best achieved jitter was found to be 8 ps for the voltage preamplifier of the highest speed (2nd version). It should be noted, that this result was obtained without the detector capacitance of the sensor that is expected to deteriorate the timing performance of the electronics. On the other hand, it was found that the total parasitic capacitance of the electronics was around 3 pF, of which, approximately 1 pF is attributed to the ASIC, while the rest is due to the test board contribution.

The accuracy of the time walk correction was also tested experimentally with calibration. The average resi-

dual after correction was found to be in a peak-to-peak range of 10 ps in both voltage and trans-impedance preamplifier types.

### Testbeam results

In September 2017 and June 2018, the prototype was also tested at the CERN testbeam line H6B of the SPS, using 120 GeV pions. The tested board included the ALTIROC0 prototype with a  $2 \times 2$  unirradiated bump-bonded sensor array of  $1 \times 1 \text{ mm}^2$  sensors. The time resolution in this case is defined as the convolution of the sensor and the electronics timing performances. During the testbeam campaign of June 2018, it was observed that, the time over threshold of the discriminator output is not scaling proportionally with the amplitude of the preamplifier probe in the case where there is a sensor bump bonded to the ASIC. Moreover, there is an oscillation on the discriminator falling edge. This effect is not present in measurements where the ASIC does not have a sensor, and while not fully understood, it is believed to be due to either an inductance caused by the length of the pad-sensor HV connection or a coupling of the direct discriminator output to the PCB. For this reason, the probe amplitude was used as an alternative method to perform the time walk correction. As shown in figure 4, after time walk correction, the best achieved time resolution was found to be around 40 ps.

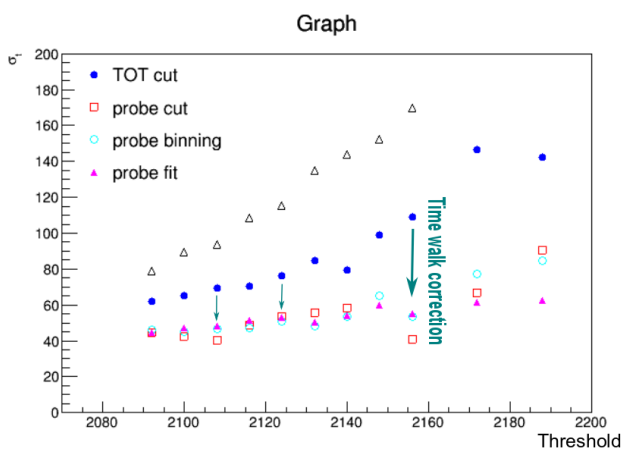


FIGURE 4: Time resolution in testbeam of an ALTIROC0 ASIC channel bump bonded to a  $2 \times 2$  unirradiated bump-bonded sensor array. To correct for the time walk, two alternative measurements have been used; the TOT of the discriminator and the probe amplitude. For the later, various methods (cut, binning, fitting) have been used, resulting in similar performance.

## 5 Conclusions

The HGTD is a detector proposed for the High-Luminosity Phase of the ATLAS experiment. The high granularity and precise time measurement will help mitigate the pile-up effects and improve the current reconstruction techniques by adding a new orthogonal

observable, the time. Its requirements to be radiation hard, compact and granular are satisfied by Si detectors, while the high quality time measurement can be provided by the LGAD technology. A first prototype of the front-end electronics ASIC, named ALTIROC0 has been fabricated. It includes 8 channels of only the analog parts of the design, the preamplifier and the discriminator. Preliminary tests attribute a 8 ps jitter when using a test pulse in testbench measurements without sensors bump bonded, while this performance is degraded to 40 ps at testbeam measurements with LGAD sensors bump-bonded to the ASIC. The results indicate that the best performance is achieved with a voltage type preamplifier. The next iteration of the ASIC, ALTIROC1 will integrate the analog and the digital parts of the front-end electronics.

## Références

- [1] *ATLAS Phase-II Upgrade Scoping Document*, CERN-LHCC-2015-020. LHCC-G-166, CERN, 2015, <https://cds.cern.ch/record/2055248>
- [2] *Technical Proposal : A High-Granularity Timing Detector for the ATLAS Phase-II Upgrade*, CERN-LHCC-2018-023. LHCC-P-012, CERN, 2018, <http://cds.cern.ch/record/2623663>
- [3] G. Pellegrini et al., *Technology developments and first measurements of Low Gain Avalanche Detectors (LGAD) for high energy physics applications*, Nucl. Instrum. Meth. A765 (2014) 12
- [4] H.-W. Sadrozinski, A. Seiden and N. Cartiglia, *4-Dimensional Tracking with Ultra-Fast Silicon Detectors*, arXiv:1704.08666
- [5] C. de la Taille, *ALTIROC0, a 20 Pico-Second Time Resolution ASIC for the ATLAS High Granularity Timing Detector (HGTD)*, 2017 Topical Workshop on Electronics for Particle Physics (TWEPP 2017) <https://indico.cern.ch/event/608587/contributions/2614083/>

# Cross-sections measurements for hadrontherapy : conception of a large acceptance mass spectrometer

Edgar Barlerin

*Laboratoire de Physique Corpusculaire de Caen,  
ENSICAEN, Université de Caen, CNRS/IN2P3*

## Résumé

In this work, a simulation systematic study of the FRACAS large acceptance mass spectrometer was made to find an optimal configuration of the detectors in terms of position and spatial resolution. Simulations of a  $^{12}\text{C}$  ion beam at 400 MeV/n on a PMMA target ( $\text{C}_5\text{H}_8\text{O}_2$ ) led to a fragment identification efficiency of 96.3%. In parallel, two detectors of FRACAS are being developed namely a multi-stage Parallel Plate Avalanche Counter (PPAC) for the beam monitor and Multi-Wire Proportionnal Chambers (MWPCs) for the downstream trackers. The beam monitor geometry was optimized using a home-made GPU based simulation code to achieve a theoretical spatial resolution around  $80\ \mu\text{m}$  FWHM, using read-out strips of  $500\ \mu\text{m}$  and a drift gap of 4.75 mm in 25 mbar of isobutane. Additionally, different tests were made with prototypes of the beam monitor and the downstream trackers to find their operating range. A simple image reconstruction of an  $\alpha$  particle source was also made with one stage of the beam monitor.

## 1 Introduction

Hadrontherapy consists in treating non-operable and radio-resistant tumors with a beam of heavy ion ( $^{12}\text{C}$  for exemple). Compared to conventionnal radio therapy the dose deposited in hadrontherapy is more localised and has a higher biological efficiency [1]. Yet heavy ions can fragment in the tissues causing a loss of primary beam ions and the creation of lighter elements resulting in a mixed radiation field. By knowing the fragmentation cross-sections of heavy ions in the human tissues the deposited dose can be more precisely controlled during the treatment planning phase. FRACAS as a large acceptance mass spectrometer, will be used to measure the fragmentation cross-sections of  $^{12}\text{C}$  on thin targets of medical interest. It will be composed of a beam monitor, a target, up- and downstream trackers surrounding a magnet and a time of flight (ToF) wall (Figure 1). The upstream trackers will be made of diamond or CMOS detectors providing the trajectory of the fragments before the magnet. The magnet with a magnetic field of 0.7 T in the center of its gap will provide mass separation of the fragments of the same charge. The downstream trackers will be made of Multi-Wire Proportionnal Chambers (MWPCs) with a large active area,  $\sim 50 \times 50\ \text{cm}^2$ , providing the trajectory of the fragments after the magnet. MWPCs allow

to build trackers with large active area at a reduced cost [2]. The ToF wall will be composed of 400 scintillating detectors of YAP :Ce crystals coupled to photomultiplier tubes, giving the energy and arrival time of the fragments to obtain their charge using a  $\Delta E$ -ToF method [3]. The beam monitor will be a multi-stage Parallel Plate Avalanche Counter (PPAC) as this type of gaseous detector is suitable for the detection of heavy ions and has a good time resolution [4]. One stage, with a small gap, will give the time reference for the time-of-flight measurement while two other stages, with bigger gaps and strips on the anode, will give the beam particle positions with a spatial resolution below  $100\ \mu\text{m}$  in both directions.

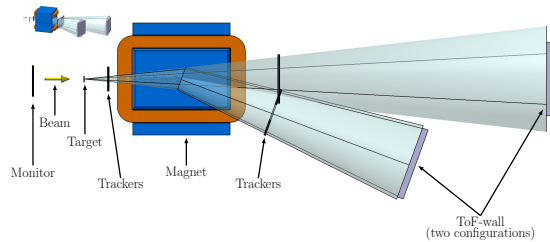


FIGURE 1: Representation of the FRACAS mass spectrometer.

Simulations of the whole system were made in order to find an optimal configuration of the position of the detectors and their spatial resolutions. To identify as precisely as possible the charge and the mass of most of the fragments. Simulations of FRACAS were made using Geant4 at two different  $^{12}\text{C}$  beam energies : 100 MeV/n and 400 MeV/n. Identifying a fragment can be decomposed in two parts : the charge reconstruction and the mass reconstruction.

### 1.1 Charge reconstruction

The charge reconstruction can be done with the  $\Delta E$  - ToF method based on the loss of energy of a charged particle in a material. Figure 2 shows that by representing the energy deposited by a fragment, converted in scintillation photons, in the ToF wall as a function of its reduced velocity, one can separate them by charge. The red lines represent the Bethe-Bloch function with varying  $Z$  from 1 to 6. A simple dichotomy algorithm was then used to calculate the distance between the data and each red lines. The charge attributed to a

fragment was the charge corresponding to the closest red line.

This method gave a reconstruction efficiency of 99% at 100 MeV/n and 400 MeV/n.

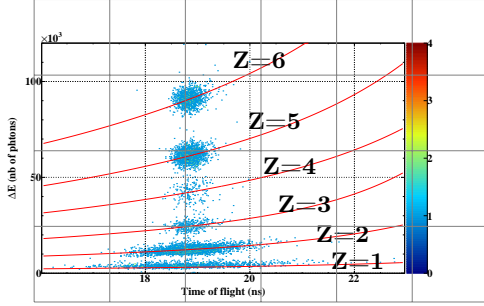


FIGURE 2: Energy loss of fragments in the ToF wall (nb of photons) as a function of their time of flight at 400 MeV/n. The red lines represent the Bethe-Bloch function with varying  $Z$  from 1 to 6.

## 1.2 Trajectory reconstruction

The mass reconstruction was based on the trajectory of a charged particle in a magnetic field  $\vec{B}$ . The trajectories are arcs of radius  $\rho$  given by :

$$B\rho \propto \frac{A\beta\gamma}{Z\sin(\theta)} \quad (1)$$

with  $\theta$  the angle between the magnetic field and the velocity of the fragment,  $B$  the magnetic field,  $A$  the number of mass of the fragment,  $Z$  the number of charge of the fragment and  $\beta$  and  $\gamma$  the Lorentz factors. Although  $Z$ ,  $\beta$  and  $\gamma$  are already known, the radius  $\rho$  must be obtained through the reconstruction of the trajectories.

The algorithm currently implemented tests all the combinations possible between the data of each detectors and select the ones that are most likely to be a trajectory of a fragment. Two parameters affect the reconstruction efficiency : the position of the trackers and their spatial resolution. Different MC simulations were made with different values of those parameters to determine an optimal configuration. Figure 3 represents the trajectory reconstruction efficiency (%) for different distances between the first downstream tracker and the magnet and distances between the two downstream trackers at 100 MeV/n.

The results obtained with this systematic study are presented in Table 1. The selected positions for the downstream trackers gave a trajectory reconstruction efficiency above 98% at 100 MeV/n and above 97% at 400 MeV/n.

## 1.3 Mass reconstruction

With the trajectory of the fragments reconstructed we can now reconstruct their mass. The method used was the same as for the charge reconstruction but by plotting the value  $\rho \cdot \sin(\theta) \cdot Z$  as a function of the reduced velocity  $\beta$  as shown in Figure 4.

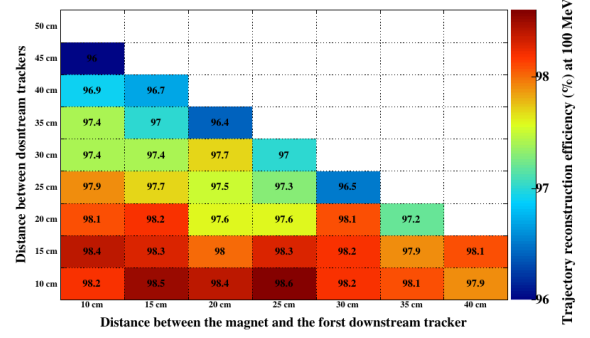


FIGURE 3: Trajectory reconstruction efficiency (%) for different distances between the first downstream tracker and the magnet and the distance between the two downstream trackers for 100 MeV/n.

Distance	100 MeV/n	400 MeV/n
magnet /trackers	10 cm to 15 cm	30 cm to 130 cm
between trackers	10 cm to 20 cm	15 cm to 50 cm
Reconstruction efficiency	> 98%	> 97%

TABLE 1: Selected positions for the downstream trackers at 100 MeV/n and 400 MeV/n

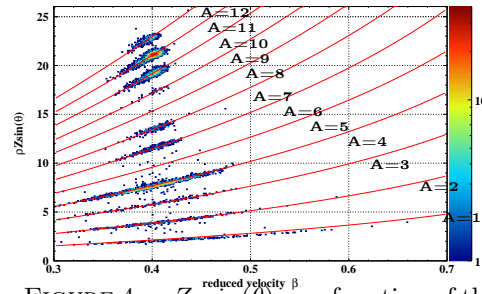


FIGURE 4:  $\rho \cdot Z \cdot \sin(\theta)$  as a function of the reduced velocity  $\beta$  at 100 MeV/n. The red lines represent equation (1) for  $A$  ranging from 1 to 12.

Figure 5 shows the mass reconstruction efficiency for different spatial resolution of the up- and downstream trackers. The spatial resolution of the upstream trackers seemed to be more critical than that of the downstream trackers. Raising the spatial resolution of the upstream trackers from 100  $\mu\text{m}$  to 500  $\mu\text{m}$ , reduced the efficiency by nearly 20%. The spatial resolution of the upstream trackers will have to be close to 100  $\mu\text{m}$  to have a good mass reconstruction efficiency while the resolution of the downstream trackers will just have to be kept below 500  $\mu\text{m}$  to maintain good performances.

This systematic study allowed to find an optimal configuration for the tracker positions and their spatial resolutions leading to a fragment identification efficiency of 96.3% at 400 MeV/n with simulation data.

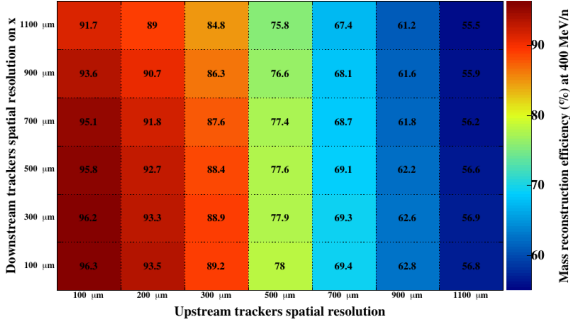


FIGURE 5: Mass reconstruction efficiency (%) as a function of the spatial resolution of the upstream trackers in both direction and the resolution of the downstream trackers in the x direction at 400 MeV/n.

## 2 Design and construction of FRACAS detectors

The other part of this work consisted in the design and construction of two of the FRACAS detectors : the beam monitor and the downstream trackers.

### 2.1 Beam monitor

Firtsly, an optimal geometry was designed for the tracking stages (size of the strips and interstrips, pressure and gas type) in order to meet the spatial resolution requirement of 100  $\mu\text{m}$  FWHM. MC simulations using a GPU based code developed in-house were made to retrieve the response of the detector to primary tracks. The mean and standard deviation of the charge induced on each strip were then extracted for different track positions. Those parameters were then used in a simple MC code to simulate thousands of primary tracks distributed in a Derno like phantom [5], within circles of a diameter  $D$  spaced by  $2D$  (Figure 6). For each detector configuration, the spatial resolution was extracted as the smallest separated  $D$  value. Figure 7 shows an example of extracted  $D$  values as a function of  $D$  for a detector made with strips of 500  $\mu\text{m}$ , interstrips of 50  $\mu\text{m}$ , a gap of 4.75 mm and isobutane at 25 mbar where the spatial resolution was around 80  $\mu\text{m}$ .

The second part of the developpement of the beam monitor consisted in evaluating its characteristics with experimental systematic tests : finding the operating range and making a simple image reconstruction of an  $\alpha$  source. The operating range was evaluated by measuring the counting rate of the detector at different pressure and high voltage configurations. This was done for both time and position stage with a  $^{241}\text{Am}$  source emitting 5.5 MeV  $\alpha$  particles in front of the detector.

Figure 8 shows the normalised counting rate of both time stage (1.6 mm gap) and position stage (3.0 mm gap) as a function of the reduced electric field ( $\text{kV}/(\text{cm}\cdot\text{bar})$ ). An efficiency plateau seemed to be reached for each different pressure for both stages meaning we can operate the PPAC at pressures ranging from 10 mbar to 50 mbar without losing any counting rate.

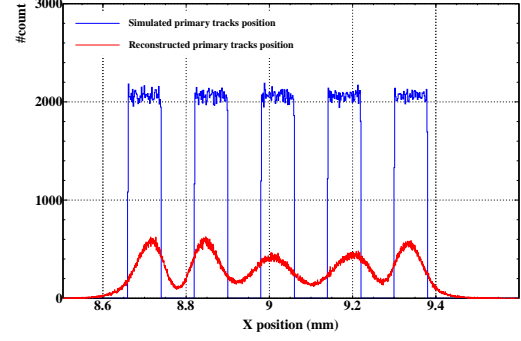


FIGURE 6: Reconstructed primary tracks position (red) compared to simulated primary tracks position (blue) in Derenzo like phantoms of 80  $\mu\text{m}$  diameter spaced by 160  $\mu\text{m}$  (blue). This has been done with parameters extracted from simulations of a detector made ofstrips of 500  $\mu\text{m}$ , interstrips of 50  $\mu\text{m}$ , a gap of 4.75 mm and isobutane at 25 mbar.

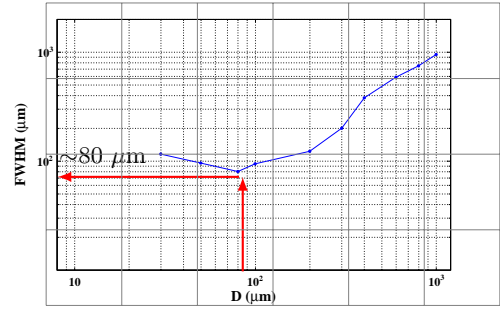


FIGURE 7: FWHM of the peaks ( $\mu\text{m}$ ) as a function of the diameter  $D$  ( $\mu\text{m}$ ) of the simulated segments.

For the position stage, the resistive read-out was made of aluminum strips to reduce the material budget and have less photoionisation. A simple image reconstruction of the  $^{241}\text{Am}$   $\alpha$  source was made with one of the position stage with isobutane at a pressure of 25 mbar (Figure 9).

### 2.2 Downstream trackers

While MC simulations are still in progress to find an optimal geometry meeting the requirements in terms of spatial resolution, different experimental tests were made to evaluate the operating range of the MWPC. Those tests were made with a prototype with the following characteristics : 20  $\mu\text{m}$  thick wires spaced by 2 mm, a gap of 8 mm and a Ar/ $\text{CO}_2$  mixture at 1 bar. In front of the detector was placed a  $^{55}\text{Fe}$  source emitting 5.9 keV photons.

Figure 10 shows the normalised counting rate of the MWPC as a function of the tension applied to the wires for different Ar/ $\text{CO}_2$  mixtures. The efficiency plateau seemed to be reached for all the different mixtures. However it seems the 75%-25% mixture seemed to show a longer stable operation range.

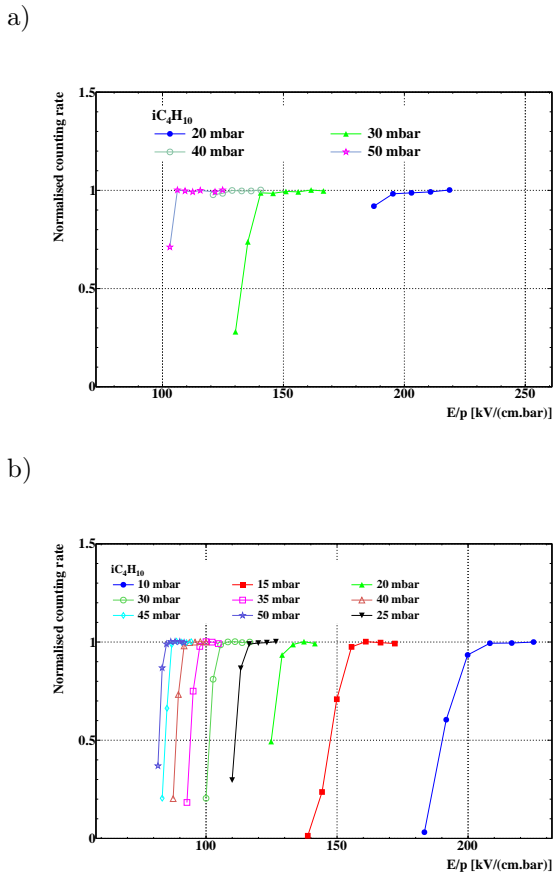


FIGURE 8: Normalised counting rate of the PPAC stages. a) Time stage (1.6 mm gap) b) Position stage (3.0 mm gap) as a function of the reduced electric field (kV/(cm.bar)).

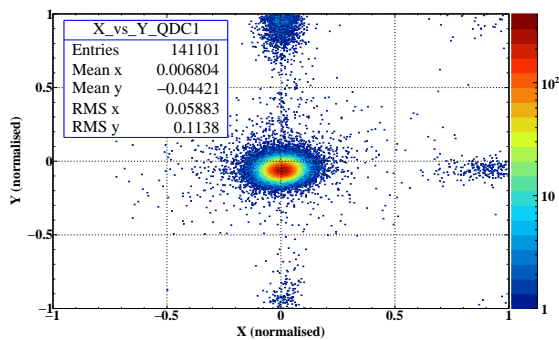


FIGURE 9: Simple image reconstruction of the  $^{241}\text{Am}$   $\alpha$  source done with one of the position stage of the beam monitor with isobutane at a pressure of 25 mbar.

### 3 Conclusion

Systematic MC studies have been performed in order to find an optimal configuration of different detectors of the FRACAS mass spectrometer. In this optimal configuration in terms of position and spatial resolution, the charge reconstruction based on the  $\Delta E$ -ToF method had an efficiency of 99% at 100 MeV/n and 400 MeV/n. The trajectory reconstruction efficiency was above 98%

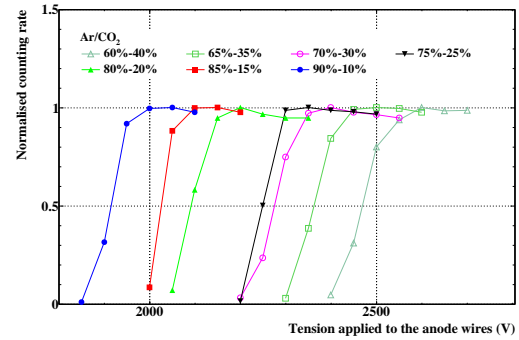


FIGURE 10: Normalised counting rate of the MWPC as a function of the tension applied to the wires for different Ar/CO<sub>2</sub> mixtures.

at 100 MeV/n and above 97% at 400 MeV/n. Finally the fragment identification efficiency was 96.3% at 400 MeV/n. The optimal configuration for the beam monitor found using GPU based simulations, consisted in 500  $\mu\text{m}$  strips with a gap of 4.75 mm and isobutane at 25 mbar, to obtain a theoretical spatial resolution of approximately 80  $\mu\text{m}$  FWHM. Experimental tests made with prototypes for the time stage and the tracking stages showed that it was possible to operate them for an isobutane pressure from 10 mbar to 50 mbar. A simple image reconstruction of an  $\alpha$  particle source was made with a tracking stage of the beam monitor. The next steps will be to do a calibration of the tracking stages for spatial distortions and to evaluate their spatial resolution. Concerning the downstream trackers, experimental tests made with a prototype with 20  $\mu\text{m}$  thick wires spaced 2 mm, a gap of 8 mm showed that the optimal Ar/CO<sub>2</sub> mixture seemed to be 75% – 25% at 1 bar.

### Références

- [1] U. Amaldi1 and S. Braccini, Eur.Phys.J.Plus 126, 2011, 70
- [2] A. Breskin *et al.*, High-accuracy, bidimensional read-out of proportionnal chambers with short resolution times, Nucl.Instrum.Meth. 143, 1977, 29
- [3] E. Nappi, Charged particle identification via ionization energy loss and Time-of-Flight measurements, AIP Conference Proceedings 674, 2003, 18
- [4] A. Breskin and N. Zwang, Timing properties of parallel plate avalanche counters with light particles
- [5] Q. Wang *et al.*, A dedicated high resolution PET imager for plant sciences, Phys.Med.Biol. 59, 2014

# Hadron selection using Boosted Decision Trees in the semi-digital hadronic calorimeter

Bing Liu

*Institut de physique nucléaire de Lyon, Lyon*

## 1 Introduction

The CALICE Semi-digital Hadronic CALorimeter (SDHCAL) prototype using Glass Resistive Plate Chambers as a sensitive medium is the first technological prototype in a family of high-granularity calorimeters developed by the CALICE Collaboration to equip the experiments of future leptonic colliders. It was exposed to beams of hadrons, electrons and muons several times on the CERN PS and SPS beamlines in 2012, 2015 and 2016. We present here a new method of particle identification within the SDHCAL using the Boosted Decision Tree (BDT) [4, 5] method applied to the data collected in 2015. The performance of the method is tested first with GEANT4-based simulated events and then on the data collected in the SDHCAL in the energy range between 10 and 80GeV with 10GeV energy step. The BDT method is then used to reject the electrons and muons that contaminate the SPS hadron beams

## 2 Particle identification using Boosted Decision Trees

To study the performance of the BDT method, we used the Geant4.9.6 Toolkit package [8] associated to the FTF-BIC physics list to generate pion, electron and muon events in the same conditions as in the beam test at CERN-SPS beamline. For the training of the BDT, 10000 events for each energy point from 10GeV to 80GeV with a step of 10GeV for pions, muons and electrons were produced. The same amount of events of each specie were produced and then used to test the BDT method.

In order to render the particle identification independent as much as possible on the energy, the pion samples of different energies are mixed before using the BDT technique. The same procedure is applied for muon and electron samples.

### 2.1 BDT input variables

The six variables we used as input are first layer of the shower, number of tracks segments in the shower, ratio of shower layers over total fired layers, shower density, shower radius and maximum shower position.

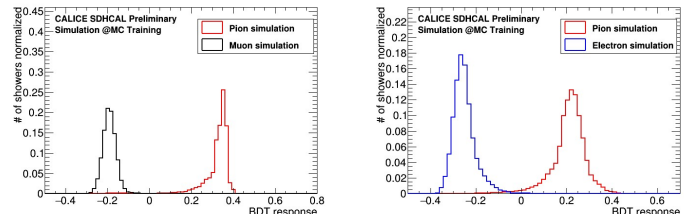


FIGURE 1: BDT output of the pions-muons sample(left) and of the pions-electrons one(right).

### 2.2 The methods to build the classifier of BDT

In order to make full a study and cross check for particle identification using BDTs, we adopt two different methods to build the classifier. The first method, referred to as MC Training, uses simulation samples of pions, electrons and muons to train. The second, referred to as Data Training, uses simulation samples of pions but the electron and muon samples are taken from data to train. For these two approaches, events are chosen in alternating turns for the training and test samples as they occur in the source trees until the desired numbers of training and test events have been selected. The training and test samples should contain the same number of events for each event class. The ratio between number of events of signal and background is 1 for both training and testing samples.

#### MC Training Approach

The six variables of the simulated pion, muon and electron events described in section 2.1 are used to train the classifier. After the training, the BDT provides the relative weight of each variable which represents its capability to distinguish the signal (pion events) from the background (electron and muon events). The procedure is applied first considering the muons as the background and then repeated with the electrons as the background. The output of the BDT applied to each of the test sample events is a variable belonging to the  $[-1,1]$  interval with the positive value representing more signal-like events and the negative to be more background-like events.

The left plot of Fig. 1 shows the output of the BDT for a test sample made of pions and muons while the right plot of the same figure shows the output for a test sample made of pions and electrons. It is clear that the

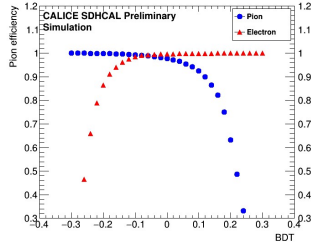
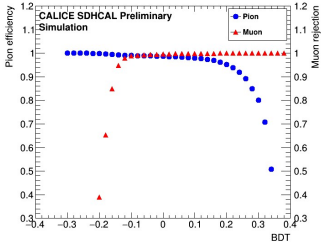


FIGURE 2: Pion efficiency and muon rejection (left) and pion efficiency and electron rejection(right) as a function of the BDT output.

separation power of the BDT method is very high. The pion selection efficiency and the muon(electron) rejection rates as a function of the BDT output of the test sample is shown in the left (right) plot of Fig. 2. The pion selection efficiency versus the muon(electron) rejection of the test sample is shown in the left(right) plot of Fig. 3. Seen from this figure, a pion selection efficiency exceeding 99% with a muon and electron rejection of the same level ( $> 99\%$ ) can be achieved. In order to check the validity of these two classifiers, we use the purified beam samples of muons and electrons. Fig. 4(left) shows the BDT output of pion-muon classifier and Fig. 4(right) shows the pion-electron one. The response of beam muons shows good agreement with respect to the simulated events. A slight shift of the beam electron shape is observed with respect to the one obtained from the simulated events. This difference could be due to the fact that the distribution of some variables in data and in the simulation are not identical. Next, as a first step of purifying the collected hadronic data events we apply the pion-muon classifier. Fig. 4 (left) shows the BDT response applied to the collected hadron events in the SDHCAL. We can clearly see there are two peaks. One peak in the muon range corresponds to the muon contamination of pion data and another one in the pion range. So, to ensure the rejection of the muons in the sample, the BDT variable is required to be  $> 0.1$  corresponding to the maximum value separating the signal side from the background side with negligible loss of pion events. The second step is to apply the pion-electron classifier to the remaining of the pion sample. Fig. 4 (right) shows the new BDT output. In order to eliminate as much as possible the contamination by electrons we apply to the pion samples a BDT cut of 0.05 to get almost a pure pion sample without losing so many pion events( $< 2\%$ ).

### DATA Training Approach

We also use the same variables of the MC Training approach on the data samples of muons and electrons but still on the simulated pion samples to build two classifiers. Then we apply the same procedure for the MC Training approach.

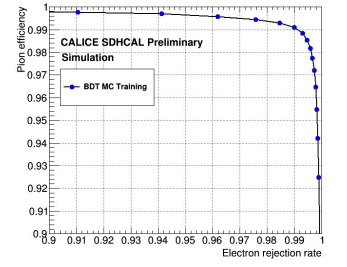
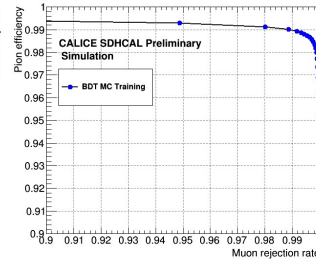


FIGURE 3: Pion efficiency versus muon rejection (left) and pion efficiency versus electron rejection(right).

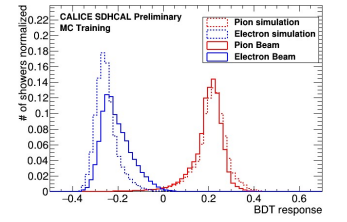
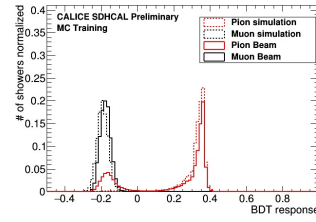


FIGURE 4: The BDT output using the pion-muon classifier on the data hadron sample (left) and the BDT output using the pion-electron classifier on the same sample(right).

## 3 Hadron events selection and hadronic energy reconstruction

The rejection of muons and electrons present in the hadron data sample using the BDT allows us to have more statistics and a rather pure hadron sample as explained in the previous section. As can be seen in Table. 1, using BDT we can get more statistics than standard selection in pion beam data

The selected sample is then compared to the one obtained applying the standard selection of ref. [3]. In order to check the validity of the new method, the same energy reconstruction technique presented in ref. [3] is applied to the pion samples selected with the MVA method as well as to the one selected following the requirements of ref. [3]. The same parametrization is used to estimate the pion energy of the three samples selected

TABLE 1: List of remaining number of data events after applying corresponding method(BDT and standard selection).

Energy(GeV)	Before cut	BDT	Standard selection
10	28091	16756	10995
20	18277	12321	9776
30	11417	8381	7356
40	47182	34206	31519
50	21512	16022	15170
60	19805	15338	14761
70	17977	13047	12645
80	39309	22357	21886

by the three methods. As in ref. [3], the reconstructed energy and associated energy resolution are obtained by fitting the energy distribution using Crystal Ball function that takes into account the tail due to shower leakage. Fig.5 shows the energy reconstructed as well as the deviation with respect to the beam energy using the BDT method as well as the standard selection. Fig.6 shows the comparison of energy resolution between standard selection and BDT method. Similar results are obtained with the three methods but using BDT we can get results with smaller statistical uncertainties than standard selection of ref. [3].

## 4 Uncertainties estimation

The linearity and energy resolution results presented previously include statistical and systematic uncertainties. We present here after the main contributions to the systematic uncertainties :

- The difference of the estimated energy before and after applying the selection criteria (BDT or standard selection) is evaluated using simulation samples of pions from 10GeV to 80GeV with 10GeV energy step. The difference is used as one source of the systematic uncertainties.
- To account for the difference in shape of the hadronic showers that are found to be sparser in the data than in the simulation [10], the difference of reconstructed energy estimated using data samples on the one hand and the simulation samples on the other hand is considered as another source of systematic uncertainties. It is worth mentioning here that this uncertainty contribution is the main contribution to the large uncertainty observed at 10GeV.
- For the standard selection, using all energy points data samples, each of the different selection criteria is varied by an arbitrary 5% in both directions with respect to the nominal values when this is possible. The maximum deviation with respect to the nominal value is used as the third source of systematic uncertainties in the case of the standard selection. For the BDT using MC training method, the BDT cut value is changed from 0.10 to 0.0 in pion-muon separation step and from 0.05 to 0.0 in pion-electron separation. The difference in energy of these two steps is added quadratically and taken as the third source of systematic uncertainties. For the BDT using data training, the same procedure is applied.

## 5 Conclusion

A new particle identification method based on the BDT MVA technique is used to purify the hadron events collected at the SPS H2 beamline in 2015 by the SDHCAL prototype. The new method uses the topological shape of events associated to muons, electrons and hadrons in the SDHCAL to reject the two first species. A significant statistical gain is obtained with respect to

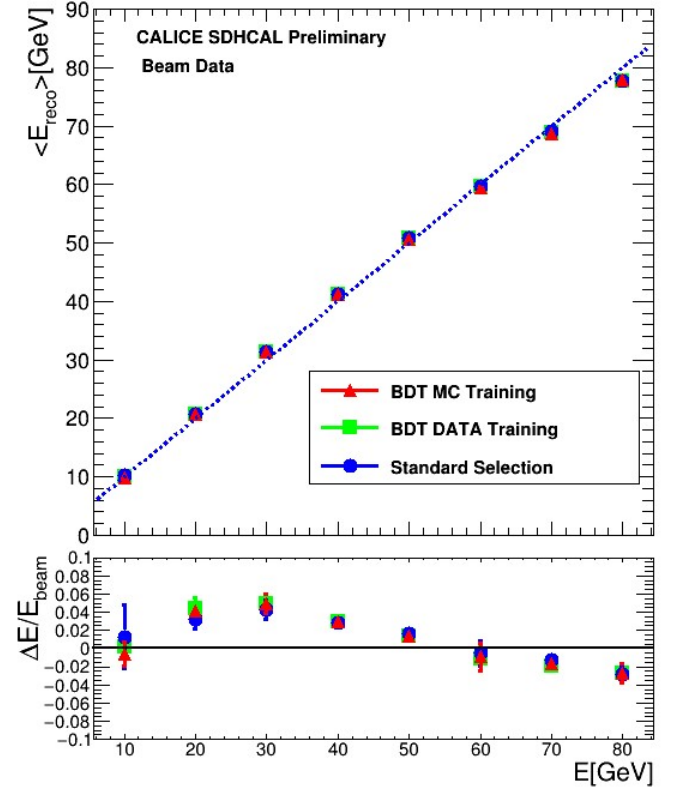


FIGURE 5: Mean reconstructed energy for pion showers as a function of the beam energy as well as relative deviation of the pion mean reconstructed energy with respect to the beam energy. Statistical and systematic uncertainties are included in the error bars.

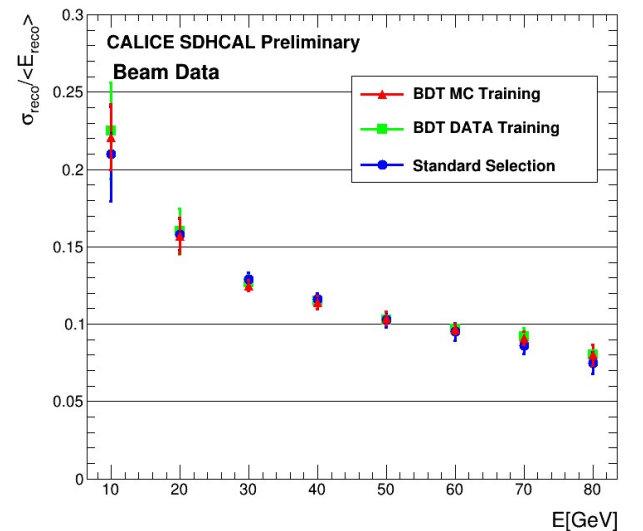


FIGURE 6: Resolution of the reconstructed hadron energy as a function of the beam energy. Statistical and systematic uncertainties are included in the error bars.

the method used in the work presented in ref [3]. This statistical gain is obvious at energies up to 40GeV and can be explained by the absence in the new method of the requirement on the start of the showers to be in the fifth layer and further as far as the number of fired layers is less than 30.

The reconstructed energy of the events selected in the new method shows similar distribution to the one obtained with events selected by the previous method. However the uncertainties in the low energy part especially at 10GeV are significantly reduced.

The particle identification using Boosted Decision Tree is a robust and a reliable method. The gain in statistics is an important result of this method with respect to the one used in ref. [3]. The results shown here confirm that the results obtained in the previous paper are not biased by the selection made in absence of appropriate discrimination detectors.

## Références

- [1] Baulieu, G., et al. "Construction and commissioning of a technological prototype of a high-granularity semi-digital hadronic calorimeter." *Journal of Instrumentation* 10.10 (2015) : P10039.
- [2] Dulucq, F., de La Taille, C., Martin-Chassard, G., Seguin-Moreau, N. (2010, October). HARDROC : Readout chip for CALICE/EUDET digital hadronic calorimeter. In *Nuclear Science Symposium Conference Record (NSS/MIC)*, 2010 IEEE (pp. 1678-1683). IEEE.
- [3] CALICE collaboration. "First results of the CALICE SDHCAL technological prototype." *Journal of Instrumentation* 11.04 (2016) : P04001.
- [4] Roe, Byron P., et al. "Boosted decision trees as an alternative to artificial neural networks for particle identification." *Nuclear Instruments and Methods in Physics Research Section A : Accelerators, Spectrometers, Detectors and Associated Equipment* 543.2 (2005) : 577-584.
- [5] Yang, Hai-Jun, Byron P. Roe, and Ji Zhu. "Studies of boosted decision trees for MiniBooNE particle identification." *Nuclear Instruments and Methods in Physics Research Section A : Accelerators, Spectrometers, Detectors and Associated Equipment* 555.1 (2005) : 370-385.
- [6] A. Hoecker et.al, "TMVA - Toolkit for Multivariate Data Analysis", arXiv :physics/0703039.
- [7] Mannai, Sameh, et al. "Energy reconstruction in a highly granularity semi-digital hadronic calorimeter." *Journal of Physics : Conference Series*. Vol. 664. No. 7. IOP Publishing, 2015.
- [8] Geant4 Collaboration., "Geant4 user's guide for application developers. Version Geant4 9.6. 0." Publication date 30th November (2012).
- [9] CALICE collaboration. "Tracking within Hadronic Showers in the CALICE SDHCAL prototype using a Hough Transform Technique." arXiv preprint arXiv :1702.08082 (2017).
- [10] CALICE Collaboration, *Resistive Plate Chamber Digitization in a Hadronic Shower Environment*, JINST (2016) 11 P06014, arXiv :1604.04550.

# Studies on Gas Mixture and Gas Recirculation Effects on GEM Detectors Operation

Mara Corbetta

*CERN & IPNL, Université C. B. Lyon I*

## Résumé

Several upgrades will affect LHC experiments Muon Systems, including measures to lower operational costs and gas emissions, as the operation of gas systems in recirculation mode. The purpose of this work is to illustrate a detailed study of the performance of Gas Electron Multiplier detectors (GEM), operated in various conditions and under gas recirculation. Indeed GEMs could be operated with gas mixtures based on  $\text{CF}_4$ , which is a greenhouse gas. A characterization of Triple-GEM detectors was performed in different gas mixture conditions (gas flow, mixture composition, mixture pollutants). Moreover, studies on GEMs performance were realized at the CERN Gamma Irradiation Facility (GIF++), that provides intense gamma irradiation from a  $^{137}\text{Cs}$  source. The aim of the measurement campaign at GIF++ is to study GEMs operation under gas recirculation in a high-rate radiation environment, similar to the one in HL-LHC experiments. The results of long-term performance monitoring and Muon test beam will be illustrated.

## 1 Introduction

The Large Hadron Collider (LHC) will reach around 2026 its High-Luminosity phase and the future high particle rate imposes consolidation and upgrades for all LHC Experiments. This work specifically focuses on Muon Systems upgrades, among which the ones of Detector Gas Systems [1]. Gas mixture is indeed the primary element influencing Gaseous Detectors performance, as its quality and stability are fundamental for good and safe long-term operation. Nonetheless, some of the gases used in LHC Experiments have a high Global Warming Potential (GWP) and their emission favours Greenhouse effect. For this reason, CERN is taking steps to reduce Greenhouse gases (GHG) emission to limit the cost of the use of these gases [2]. While R&D is ongoing to find efficient ways to recuperate Greenhouse gases, or use eco-friendly gas mixtures, gas systems can be operated with gas recirculation. Among other detectors, the issue of GHG emission also concerns Gas Electron Multiplier (GEM) Detectors, which gas mixture can contain  $\text{CF}_4$ , a Greenhouse Gas with GWP equal to 7390. For example, LHCb GEM moved to gas recirculation during LS1, reducing the GHG emission by 90% in Run 2 with respect to Run 1. Operating gas systems with recirculating gas has its drawbacks, as it favours

impurities accumulation. These impurities can be difficult to remove, and their presence could affect detectors performance.

The aim of this work is to study GEM detectors operation in gas recirculating systems. Studies of the effects on GEMs performances of specific variations in the gas mixture will be presented, as well as the long-term test on GEMs operation with a small replica of LHC gas recirculation system [3], in irradiation conditions as similar as possible to the ones in HL-LHC. GEMs detectors have indeed been successfully operated in the LHCb experiment during Run 1 and Run 2, and they will be installed in the CMS experiment during LHC LS2, to face the future High Luminosity phase. The high background rate could indeed compromise the CMS trigger system, and the new GEMs station in the experiment end-caps will help to reduce the trigger rate in the forward regions.

## 2 Gas-Related Studies

This paragraph illustrates the studies realized on specific variations in the GEMs gas mixture at laboratory level. The detector under test is a  $10 \times 10 \text{ cm}^2$  GEM prototype, with gap configuration 3-1-2-1 mm. The setup is composed by a gas mixer, to operate changes in the standard mixture, and the data acquisition system (Figure 1). Detector performance is studied collecting detector current and signal from  $^{55}\text{Fe}$  irradiation, with a PicoAmmeter and Desktop Digitizer respectively. Gas and environmental parameters are also collected with an ADC Data Logger. GEM efficiency is tested with High Voltage scans, in which the counting rate is used to reconstruct the efficiency curve : GEM is considered to be efficient when the plateau of maximum rate capability is reached.

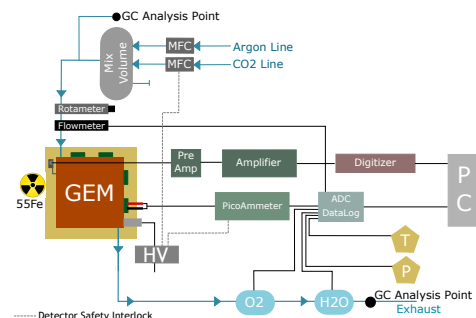


FIGURE 1: Scheme of the experimental setup.

## 2.1 Ar/CO<sub>2</sub> Mixture Ratio

As the gas mixture stability is a key element in determining detectors performance, the influence of the ratio of Ar and CO<sub>2</sub> in the standard mixture was studied. As CO<sub>2</sub> is a quencher gas, it absorbs gamma from excitation, and the more it is present in the mixture the more the electron avalanche development is limited.

The test showed how increasing the CO<sub>2</sub> concentration leads to a higher Working Point, with +25 V for 1% of CO<sub>2</sub> increase. It was also seen how the rate capability becomes lower with more CO<sub>2</sub> in the gas mixture, as well as detector gain.

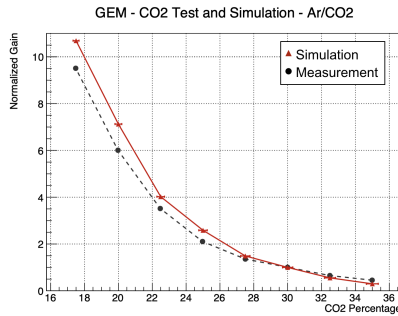


FIGURE 2: Trend of GEM gain (normalized to Ar/CO<sub>2</sub> 70/30) as a function of CO<sub>2</sub> percentage in the mixture.

The results for gain measurements are reported in Figure 2, together with the same data obtained with a GARFIELD [5] simulation of the Triple-GEM detector. Good accordance is found between results from experimental setup and simulation, confirming the importance of stable gas mixture composition for GEMs operation.

## 2.2 Presence of O<sub>2</sub> as pollutant

As O<sub>2</sub> is a common impurity in LHC Detector Systems, it is fundamental to understand what is its impact on GEMs performance. O<sub>2</sub> has a high electron attachment coefficient, so it has the tendency to attract electrons.

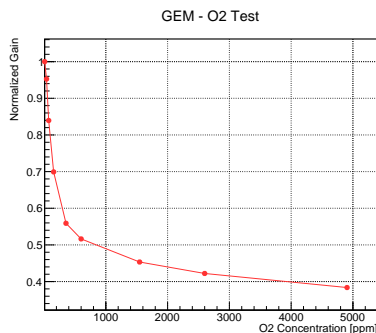


FIGURE 3: Trend of GEM normalized gain as a function of the O<sub>2</sub> concentration in standard gas mixture.

The O<sub>2</sub> concentration was varied in the range 10-5000 ppm, and its effect was seen on both detector rate and

gain measurements. Rate capability showed a decrease of 20% with high O<sub>2</sub> concentration (more than 1000 ppm). The gain drop reaches instead the 60%, with most of variation in the range 0-500 ppm (Figure 3). It is then deduced that O<sub>2</sub> presence limits both primary ionization and avalanche development. Nonetheless, working at O<sub>2</sub> concentrations higher than 500 ppm could help stabilizing detector response despite O<sub>2</sub> oscillations.

## 2.3 Detector Gas Flow

Another parameter that can influence detector performance is the input gas flow rate. The operation flow of gaseous detectors is normally around 0.5-1 volume/hour. In this study flows were tested up to 20 vol/h, to determine what is the flow suitable for GEMs.

The most significant result is that GEM gain considerably increases with higher gas flows, up to 20% (Figure 4). It was found that, in this specific case, the loss in performance for low flows is caused by the impurities absorption (O<sub>2</sub>, H<sub>2</sub>O), that decreases exponentially with the gas flow. It is thus concluded that high flows (from 10 volumes/hour) could allow to reduce the impurity intake of the prototype chamber, improving detector gain.

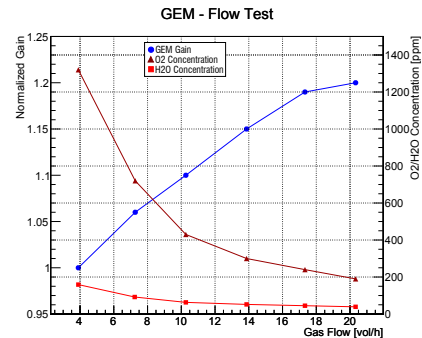


FIGURE 4: Trend of GEM normalized gain and concentration of gas mixture impurities (H<sub>2</sub>O and O<sub>2</sub>), with respect to the increase of input gas flow.

## 3 Irradiation Campaign at GIF++

In this section the Triple-GEM irradiation campaign at the CERN Gamma Irradiation Facility (GIF++) is described. The GIF++ facility is a dedicated test zone for large-area Muon chambers, for performance characterization and aging tests, currently hosting more than 15 setups. The facility provides irradiation with a source of <sup>137</sup>Cs (662 keV photons), with the possibility to vary the source intensity through the integrated filter-system. The source activity is 14 TBq, which makes it capable of delivering a dose rate that mimics the high radiation rate that will be present in the HL-LHC phase. Moreover, during some periods

of the year, the facility has the possibility to have delivered a Muon beam from the SPS accelerator.

The GEM Gas recirculation R&D setup is composed of two Triple-GEM detectors operated in gas recirculation, irradiated with  $^{137}\text{Cs}$  (Figure 5). The dedicated Gas System is a Closed Loop rack, that can be operated with standard Ar/ $\text{CO}_2$  and  $\text{CF}_4$ -based mixtures. The system is a small replica of LHC Gas Systems [3], including the purifier module for  $\text{H}_2\text{O}$  and  $\text{O}_2$ . Gas quality is monitored with two Single Wire Proportional Chambers, as well as with standard gas analysis techniques. The Data Acquisition System is analogue to the one already described for the laboratory setup.

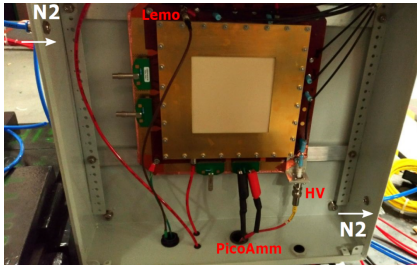


FIGURE 5: Triple-GEM prototype installed at GIF++.

GEMs performance is monitored with the continuous acquisition of detector current from  $^{137}\text{Cs}$  irradiation. As detector current is proportional to the gain, its trend in time can give indication on performance stability. Moreover, weekly scans in  $^{55}\text{Fe}$  are realized when the source is OFF for bunker access.

### 3.1 Gas System Results

The purifier system installed in the GEM GIF++ Gas System is equivalent to the ones installed in LHC Gas Systems. Two different types of materials are used : Molecular Sieve, that traps  $\text{H}_2\text{O}$  molecules, and  $\text{NiAl}_2\text{O}_3$ , that reacts with  $\text{O}_2$  retaining the molecule. Their action was tested along the irradiation campaign with the Gas System in gas recirculating mode. Operating gas systems with gas recirculation indeed favours the accumulation of impurities, which concentration increases when the recirculating fraction is higher, as the freshly injected mixture is decreased.

The module was tested with different gas recirculation fractions, and it was seen that  $\text{O}_2$  can be reduced by four times, down to 50 ppm with 90% recirculation, while  $\text{H}_2\text{O}$  concentration could be lowered to less than 10 ppm. Lowering the concentration of  $\text{H}_2\text{O}$  is fundamental when working with Freon gases ( $\text{CF}_4$ ), as they easily break when under heavy irradiation, the produced fluoride ions ( $\text{F}^-$ ) could indeed react with  $\text{H}_2\text{O}$  molecules creating HF, which is highly reactive and could damage GEM foils. The use of purifiers also allowed to maintain  $\text{H}_2\text{O}$  and  $\text{O}_2$  levels very stable (variations of 2/3%), avoiding oscillations in their concentration that, as showed in the previous

paragraph, could influence GEMs performance.

### 3.2 Irradiation Results

In a year-long campaign (2017-2018), the gas recirculating system was tested with the standard Ar/ $\text{CO}_2$  70/30 gas mixture. Different recirculating fractions were tested : 50%, 70% and 90%, that is the fraction normally used by LHC Gas Systems. Along the irradiation campaign a total charge of around 10  $\text{mC}/\text{cm}^2$  was accumulated for both chambers.

GEM current was constantly monitored during the irradiation period, as well as the gain from  $^{55}\text{Fe}$  irradiation. Both values were systematically corrected for the variations of Temperature and Atmospheric Pressure. As for other gaseous detectors, GEMs gain depends on the ratio T/P as  $\text{Gain} = A \cdot \exp[B \cdot (T/P)]$ . The gain value was found to be always consistent with progressive detector current measurement. Moreover, the use of the Purifier Module allowed to always have a sufficiently low and stable  $\text{O}_2$  concentration, so that the amplification gain was only weakly affected by its variations.

Both detectors showed a stable response over all the irradiation period. As an example, results are reported for one of the chambers (Figure 6). Detector amplification gain results to be stable along the progressive charge accumulation, regardless the recirculating fraction and the source attenuation, proving the good stability of operations with recirculating gas.

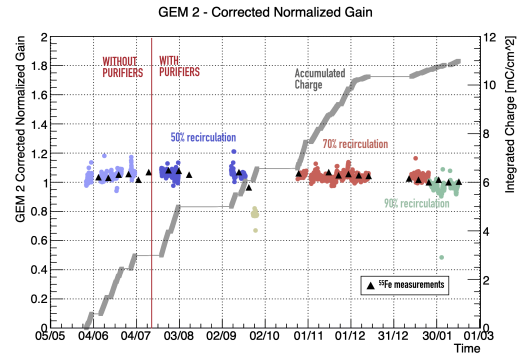


FIGURE 6: On left axis, in coloured markers, GEM normalized current for different periods (with/without purifiers, different recirculating fractions). In black markers, normalized gain weekly measured with  $^{55}\text{Fe}$ . On the right axis, in grey markers, the progressive accumulated charge.

### 3.3 Muon Test Beam

The GEM Gas R&D setup also participated to the Muon Test Beam, exploiting the beam line crossing GIF++. As GEMs are part of Muon Systems, it is interesting to study their performance for Muon detection in presence of HL-like gamma background and under gas recirculation.

The setup was placed along the Muon Beam, with a  $4 \times 4 \text{ cm}^2$  scintillator to provide trigger to DAQ electronics, in coincidence with the facility trigger system (Figure 7).

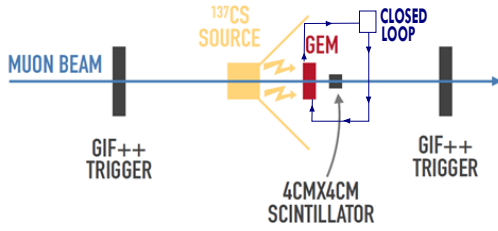


FIGURE 7: Schematic representation of the beam time setup configuration.

Differently from normal irradiation periods, during the Test Beam the SRS acquisition system from RD51 [7] was used. The SRS gives information on the X-Y position of the particle crossing the detector, as well as on the charge produced in the chamber.

GEM efficiency has been calculated as the ratio between detected events and total triggered events from scintillators coincidence, with negligible geometric losses. Efficiency curves were measured for Ar/CO<sub>2</sub> 70/30 and Ar/CO<sub>2</sub>/CF<sub>4</sub> 45/15/40 gas mixtures, in open loop and gas recirculation, and in different irradiation conditions, with a rate of gamma background of  $10^3 \text{ Hz/cm}^2$  and  $10^4 \text{ Hz/cm}^2$ . As it can be seen in Figure 8 (for Ar/CO<sub>2</sub>/CF<sub>4</sub> mixture), in all the cases efficiency could reach almost the 100%, following the typical sigmoid raise. An analogue result was obtained for the Ar/CO<sub>2</sub> mixture. It can then be concluded that GEM showed a good response with a gamma background up to  $10^4 \text{ Hz/cm}^2$ .

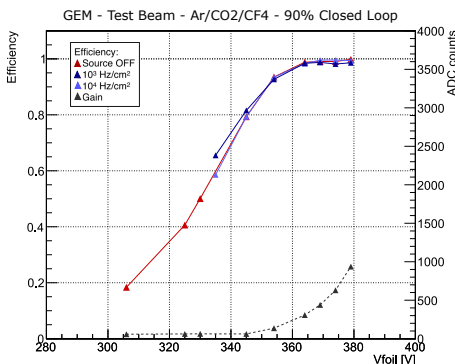


FIGURE 8: GEM efficiency curve (solid line) for different irradiation intensities, as a function of the average voltage on GEM foils. In dotted line, the corresponding value of GEM gain (right axis).

The cluster size was also estimated, counting the number of hit strip for each event. The mean value obtained is around 4 strips in Ar/CO<sub>2</sub> mixture and 3.2 strips for Ar/CO<sub>2</sub>/CF<sub>4</sub> mixture. The presence of less argon in the CF<sub>4</sub>-based mixture causes in fact

a decrease in the avalanche size. Nonetheless, data analysis is still ongoing to better understand the possible presence of double events, that could affect cluster size calculation.

## 4 Conclusion

Several studies were performed on the effects of gas mixture and gas system on GEMs performance. They showed how mixture composition instabilities can significantly influence detectors performance. Moreover, the presence of pollutants such as O<sub>2</sub> in the gas mixture contributes to decrease the amplification gain, and their accumulation is more severe when the detector is operated with low input gas flow rate.

Thanks to the irradiation campaign at the GIF++ facility, the operation of GEMs with Ar/CO<sub>2</sub> mixture was validated in gas recirculation, with a recirculating fraction up to the 90%, in presence of high-rate radiation (as in the future HL-LHC phase). Moreover, the Purifier module was found to be efficient in removing impurities that can accumulate in the Closed Loop systems (H<sub>2</sub>O, O<sub>2</sub>), and in keeping stable their concentration. Finally, with the participation to the Muon Test Beam, it was found that GEMs operated in gas recirculation are efficient in presence of high-rate gamma background up to  $10^4 \text{ Hz/cm}^2$ .

## Références

- [1] R. Guida, M. Capeans, F. Hahn, S. Haider, B. Mandelli, "The gas systems for the LHC experiments," 978-1-4799-0534-8/13/\$31.00 ©2013 IEEE, CERN, Geneva, Switzerland.
- [2] M. Capeans, R. Guida, B. Mandelli, "Strategies for reducing the environmental impact of gaseous detector operation at the CERN LHC experiments", Volume 845, p. 253-256, 0168-9002, 2016 Elsevier.
- [3] R. Guida, B. Mandelli, "A portable gas recirculation unit for gaseous detectors," 2017, CERN, Geneva, Switzerland, 2017 JINST 12 T10002.
- [4] Fabio Sauli, "The gas electron multiplier (GEM) : Operating principles and applications", Volume 805, 1 January 2016, p. 2-24, 0168-9002, 2015 CERN, Published by Elsevier B.V.
- [5] R. Veenhof, GARFIELD, Drift-Chamber Simulation Program, <http://garfield.web.cern.ch>
- [6] M.R. Jakel et al, "CERN GIF++ : A new irradiation facility to test large-area particle detectors for the high-luminosity LHC program", Technology and Instrumentation in Particle Physics 2014, 2-6 June, 2014 Amsterdam, the Netherlands.
- [7] S. Martoiu et al, "Development of the scalable readout system for micro-pattern gas detectors and other applications", Topical Workshop on Electronics for Particle Physics 2012, 2013 JINST 8 C03015.

# Caractérisation du système de lecture du CCD dans DAMIC

Khalil Latifa

LPNHE

## Résumé

Le projet DAMIC (Dark Matter in CCDs) est une expérience basée sur la détection directe de matière noire à l'aide d'un système de lecture CCD. Elle permet de sonder le domaine de masse des matières noires entre 1-20 GeV. Elle repose sur un système de détection pour lequel le LPNHE a une très grande expertise et il est le seul à avoir conçu une électronique de lecture et de contrôle totalement intégrée. Le but de ma thèse est la mise en route du CCD, à partir d'un banc de test électronique.

## 1 Introduction

Dans le but de lire un CCD, le groupe LPNHE a créé un système électronique de lecture basé sur l'ASPIC(Readout), ADC (conversion analogique numérique) et CABAC(horloges et biais).

## 2 Banc de test du DAMIC

Le système actuel comprend :

- CCD relié au FLEX qui est dans le Cryostat (Froid)
- Carte BEB3 qui contient un ADC 18 bits
- Carte CABAC (gestion des horloges, biais et tensions du CCD)
- FPGA qui est une interface entre l'électronique et le PC capable de contrôler le système entier

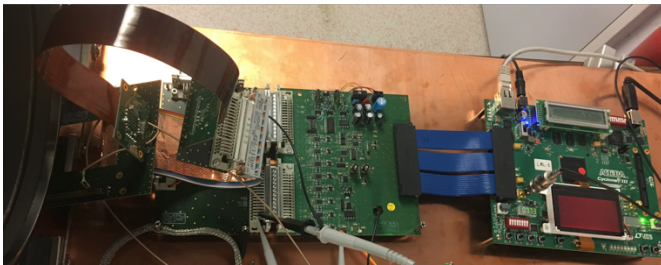


FIGURE 1: Banc de test.

### 2.1 ASPIC

C'est la carte support d'un circuit de lecture de CCD, l'ASPIC. Elle comporte deux trous métalliques mécaniques reliés à la terre afin d'amener le froid à l'Aspic à travers le plan de masse. L'ASPIC contient une sortie

différentielle, un amplificateur de tension pour déterminer le gain.

### Mesure du Gain

Pour mesurer le gain, j'ai mis sur l'entrée une pulse d'amplitude égale à 100 mV et on a obtenu le graphe suivant dans la figure 2. On remarque que le gain mesuré est égale au gain théorique.

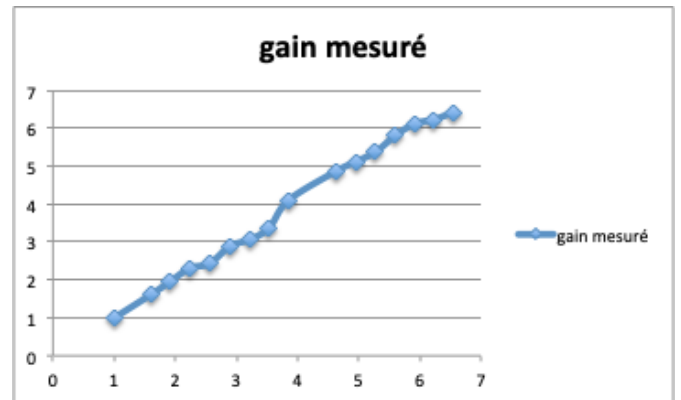


FIGURE 2: Mesure du gain

### Mesure de bruit

Pour mesurer de bruit, j'ai liée l'entré à la masse (GND) avec un gain maximale égale à 13. On remarque qu'au début de chaque signal, il y a une oscillation, cette oscillation est due de l'ADC. Quand on applique la transformée de Fourier, il y a un pic à  $F=10$  kHz avec le FLEX et un pic à  $f=5$  kHz avec l'ADC tout seul. La sortie de l'aspic et l'ADC est présentée dans la figure 3.

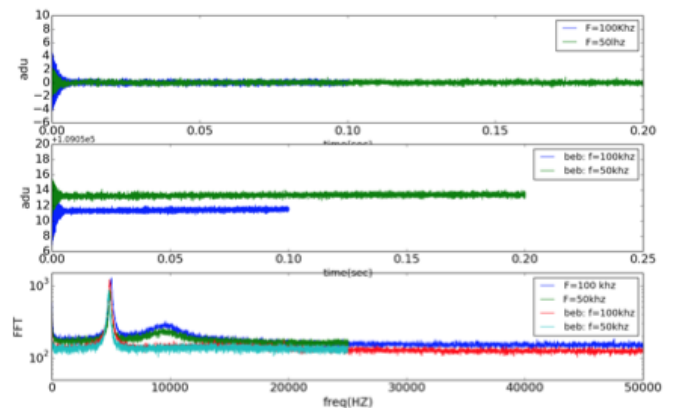


FIGURE 3: La sortie de l'ADC et l'ASPIC.

## 2.2 BEB3

C'est un circuit conçu pour l'ASPIC, il sert à numériser la sortie différentielle analogique de l'ASPIC et il transfère les données au FPGA. Il contient un convertisseur analogique numérique 18 bits à 4 canaux.

## 2.3 CABAC

Notre CCD actuel qui fait 1k x 500 a besoin au minimum de 14 horloges parallèles et séries. Puisque chaque CABAC fournit 5 horloges on a donc besoin de 3 CABAC. Cette carte permet de fournir les horloges parallèles et série, les biais et les tensions. On a beaucoup travaillé pour faire fonctionner cette carte parce qu'il était difficile de sortir les bons niveaux des rails des horloges et des biais. On a fait beaucoup de modification comme ajouter des sockets du CABAC, ajouter des diodes à la sortie de quelques biais, ajouter des filtres RC.. Les figure 4 par exemple montre les horloges horizontales

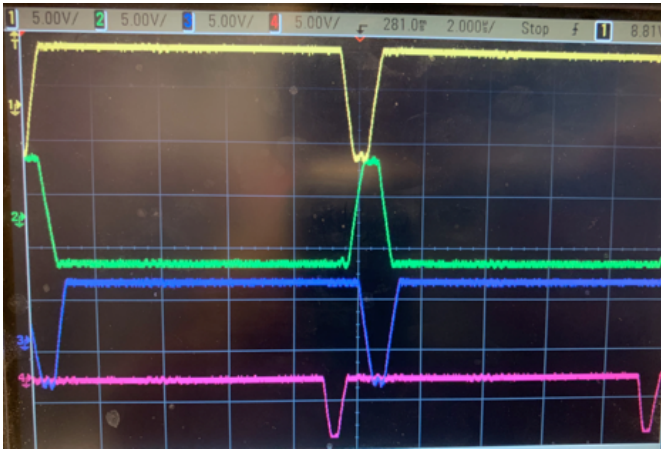


FIGURE 4: Les horloges horizontales.

## 3 L'ADC dans DAMIC M

DAMIC-M est une expérience dont le but est d'évaluer le potentiel de DAMIC. DAMIC-M utilise un skipper CCD, qui est un CCD permettant de lire chaque pixel N fois. Dans ce but il est prévu de changer l'ADC utilisé dans le système actuel. Après discussion, on a choisi un ADC 18 bits à 15 MSPS de référence LTC2387-18. Cet ADC a une vitesse rapide ce qui nous permet de faire du suréchantillonnage qui est une méthode prévue pour diminuer le bruit.

Après l'évaluation de la carte on a obtenu les résultats suivants :

**Mesure de bruit :** dans le but de mesurer le bruit de l'ADC, on a connecté l'entrée de l'ADC à la référence interne de l'ADC qui est égale à 2.048 V. On a obtenu un bruit constant égal à 1.4 LSB dans une bande de fréquences de 100 Hz à 8.5 Mhz.

**Mesure de la linéarité :** pour mesurer la linéarité, j'ai mis à l'entrée une tension continue contrôlée par un atténuateur. J'ai fait varier cette tension entre 100 mV et 3.2 V, et j'ai obtenu le graphe suivant. On remarque figure 5 une droite linéaire, et après ajustement de cette droite on a obtenu une erreur moyenne de 7 LSB.

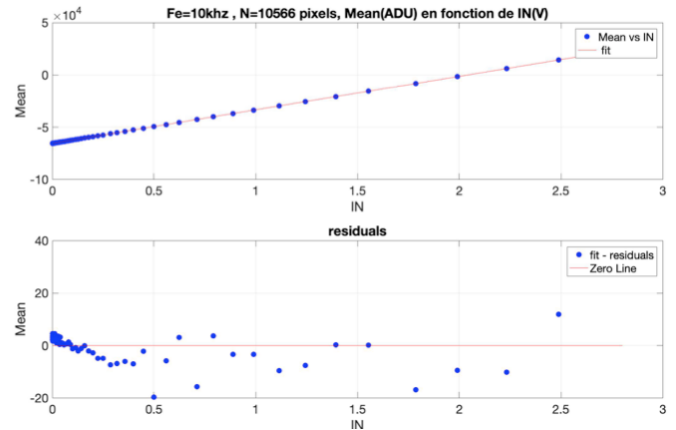


FIGURE 5: Linéarité et la résiduel de l'ADC.

## 4 Conclusion

Les étapes prévues dans le futur :

- Implémenter le système avec le CCD actuel et faire la mesure de bruit et acquisition des images
- Par rapport à DAMIC-M on veut :
  - Optimiser le rapport signal/bruit avec le nouvel ASIC (diviser par 20)
  - Une lecture sur échantillonnage à filtrage numérique avec un ADC rapide 15 MSPS
  - Implémenter le nouveau Système de Lecture avec un CCD Skipper

Sixième partie

# Flavour Physics

session dirigée par Joao COELHO



## Introduction to the Flavour Physics Session

João Coelho

*LAL, Université Paris-Sud, CNRS/IN2P3, Orsay, France*



The Standard Model of particle physics describes almost all the data we have collected so far, however we know it is incomplete. Gravity is not included in the model, we have very little understanding of the dark sector, neutrino mass is not explained, and a number of theoretical issues exist, including the fact that the model contains 19 free parameters with no explanation for their structure. Out of these 19 parameters, 15 are related to particle masses and at least an extra 7 would be needed to describe neutrino masses and mixing.

Mass generation in the Standard Model arises from spontaneous symmetry breaking due to the non-zero vacuum expectation value of the Higgs field [1]. The importance of the discovery of the Higgs boson in 2012 [2] cannot be overstated, as it confirmed this central aspect of the theory and deservedly resulted in the Nobel Prize in physics being awarded to Higgs and Englert in 2013. A very interesting aspect of this mass generation mechanism in the Standard Model is the relationship between the Yukawa couplings and the flavour structure of the model. Yukawa couplings are couplings between two fermions and a scalar field, which in the Standard Model is given by the Higgs field. These terms are responsible for the masses of all fermions. Because the Standard Model contains 3 copies (families) of each of the quark and lepton fields which share the same gauge charges, Yukawa interactions can couple fermions from different families without breaking gauge invariance. This breaks the flavour symmetry of the model and gives rise to flavour mixing.

From these considerations on the origin of mass we can contemplate the extent of our ignorance. Why are there different families of fermions? Where does the structure of the Yukawa couplings come from? In essence, what can we learn from these mass and flavour connections about the underlying high energy theory that gives rise to the Standard Model at low energies?

Answering these questions is among the goals of flavour physics. Heavy flavour experiments such as LHCb and Belle have explored these questions by studying b hadrons, looking in particular for decays that are rare in the Standard Model. These rare decays are often subject to what is known as the Glashow-Iliopoulos-Maiani (GIM) mechanism [3], where transitions between quarks of the same charge, i.e. Flavour-Changing Neutral-Currents (FCNC), are suppressed by a combination of the small mixing between quark families and the lack of tree-level FCNCs in the Standard Model. Because this suppression originates from a flavour symmetry of the Standard Model, one may expect

that possible new physics phenomena that may break these symmetries would avoid the suppression and their contribution to the decay amplitudes may become comparable to the Standard Model components even if their tree-level coupling is small. In this way, flavour physics can become sensitive to new physics at energy scales much larger than direct searches can currently reach.

Additionally, the existence of three families of quarks with mixing gives rise to CP violation, which is an essential condition to explain the baryon asymmetry in the universe. However, the current observed amount of CP violation in the Standard Model is at least 6 orders of magnitude smaller than what's required to explain the measured baryon/photon ratio in the universe [4]. New sources of CP violation must be present and flavour physics may be an important window into these new phenomena.

At present, no significant deviations from the Standard Model have been found either in CP violating measurements or in rare decays. However, some hints are currently on the horizon. In particular, some weak evidence ( $< 5\sigma$ ) now exists that B decays may violate the flavour universality principle of the Standard Model, in which all fermion families experience the same coupling to the weak force. Measurements from BaBar, Belle and LHCb [5] of the branching fractions of the semileptonic decay  $B \rightarrow D^{(*)}\tau\nu$  seem to be significantly larger than expected from the Standard Model when compared to similar decays such as  $B \rightarrow D^{(*)}\mu\nu$ . Similarly, an asymmetry between the rare decays  $B \rightarrow K^{(*)}\mu\mu$  and  $B \rightarrow K^{(*)}ee$  has been hinted at by LHCb [6], where none is expected from the Standard Model. These results are not yet conclusive, but new data from the LHCb and Belle II experiments should settle these questions in the near future.

At JRJC 2018, the heavy flavour session focused on on-going analyses of the LHCb experiment with two students :

Boris Quintana, from LPC, presented the current status of his analysis on B meson decays into two hadrons and a photon, which all occur through the transition  $b \rightarrow s\gamma$ . These decays are closely linked to the observed hints of lepton flavour universality in the so-called  $R(K^{(*)})$  anomalies involving  $B \rightarrow K^{(*)}ll$ , as they share the same b-quark transition. Being a FCNC, they are rare processes where the impact of new physics can be significant. A better understanding of the  $b \rightarrow s\gamma$  transition would be crucial to constraining possible new physics models and his research is doing just that.

Dawid Gerstel, from CPPM, presented his work on

the tests of lepton flavour universality  $B^0 \rightarrow D^{*-}l^+\nu$ , which currently contribute to a  $3.8\sigma$  discrepancy with respect to the Standard Model prediction when combined with other  $B \rightarrow D^{(*)}l\nu$  measurements. His contribution is focused on the update of the LHCb analysis of  $R(D^*)$  with new data from 2015 and 2016. This update faces serious challenges in reducing systematic uncertainties and will require, among other things, new techniques for the generation of huge Monte Carlo samples. He presented his contribution to validating new simulation tools and the prospects for analysis improvements with multivariate techniques.

The details of their exciting research are presented in the next few pages.

## Références

- [1] F. Englert and R. Brout, Phys. Rev. Lett. 13, 321 (1964); Peter W. Higgs, Phys. Rev. Lett. 13, 508 (1964).
- [2] ATLAS Collaboration, Phys.Lett. B716 (2012) 1-29; CMS Collaboration, Phys.Lett. B716 (2012) 30-61.
- [3] S.L. Glashow, J. Iliopoulos and L. Maiani, Phys.Rev. D2 (1970) 1285-1292.
- [4] Andrew G. Cohen, Proceedings of the 29th SLAC Summer Institute on Particle Physics (2001).
- [5] BaBar Collaboration, Phys. Rev. Lett. 109, 101802 (2012); Belle Collaboration, Phys. Rev. D 92, 072014 (2015); LHCb Collaboration, Phys. Rev. Lett. 115, 111803 (2015).
- [6] LHCb Collaboration, Phys. Rev. Lett. 113, 151601 (2014); LHCb Collaboration, JHEP 02 (2016) 104.

# Tests of Lepton Flavour Universality in semitauonic decays of b-hadrons at the LHCb experiment

Dawid Gerstel

Aix Marseille Univ, CNRS/IN2P3, CPPM, Marseille, France

## Résumé

Lepton Flavour Universality (LFU) states that the 3 generations of charged leptons in the Standard Model of particle physics have the same electro-weak couplings and the only difference between them is in their masses. In recent years, however, this principle has been challenged by several measurements of  $b$ -hadron decays involving the transition  $b \rightarrow c\ell\nu_\ell$  by BaBar, Belle and LHCb. In particular, the combined world averages of ratios of branching fractions,  $R(D^*) = \frac{\mathcal{B}(B^0 \rightarrow D^{*-}\tau^+\nu_\tau)}{\mathcal{B}(B^0 \rightarrow D^{*-}\mu^+\nu_\mu)}$  and  $R(D) = \frac{\mathcal{B}(B^0 \rightarrow D^-\tau^+\nu_\tau)}{\mathcal{B}(B^0 \rightarrow D^-\mu^+\nu_\mu)}$ , exhibit a  $3.8\sigma$  deviation from the LFU-conserving Standard Model prediction. The ongoing LFU tests at LHCb using semitauonic  $b$ -hadron decays will be discussed here.

## 1 Introduction

In the Standard Model of particle physics (SM), the three generations of fermions are assigned the same gauge charge, leading to the same electro-weak couplings. This property is called Lepton Flavour Universality (LFU). It is only the Yukawa interaction between the Higgs field and fermion fields that distinguishes the three generations.

It follows [1] that branching fractions of processes into lepton families differ only due to different masses of the leptons involved. Any further discrepancy would be a strong evidence of physics phenomena beyond the Standard Model.

One of the first hints of LFU violation was the LEP measurement of  $\frac{2\sigma(W \rightarrow \tau\nu_\tau)}{\sigma(W \rightarrow e\nu_e) + \sigma(W \rightarrow \mu\nu_\mu)} = 1.077 \pm 0.026$ , that was  $2.8\sigma$  above the SM prediction [2].

Nowadays there are two main channels hinting at LFU violation:  $b \rightarrow s\ell^+\ell^-$  (“loop-level”), as probed with *e.g.*  $R(K^{*0}) = \frac{\mathcal{B}(B^0 \rightarrow K^{*0}\mu^+\mu^-)}{\mathcal{B}(B^0 \rightarrow K^{*0}e^+e^-)}$  ratio and  $b \rightarrow c\tau^+\nu_\tau$  (“tree-level”) as measured by  $R(D^*) = \frac{\mathcal{B}(B^0 \rightarrow D^{*-}\tau^+\nu_\tau)}{\mathcal{B}(B^0 \rightarrow D^{*-}\mu^+\nu_\mu)}$ . The latter one is discussed in this article.

Figure 1 shows the SM Feynman diagram of the modes  $B^0 \rightarrow D^{*-}\tau^+\nu_\tau$  and  $B^0 \rightarrow D^{*-}\mu^+\nu_\mu$  used in the  $R(D^*)$  ratio, where the  $b \rightarrow c\tau^+\nu_\tau$  transition occurs via the  $W^+$  boson. The spectator  $d$ -quark might be replaced with one or two other spectator quarks, representing other transitions of the  $b \rightarrow c\tau^+\nu_\tau$  class that are probed with other ratios, *e.g.*  $R(D^0)$ ,  $R(J/\psi)$  and  $R(\Lambda_c)$ .

More recent results of the experiments BaBar, Belle

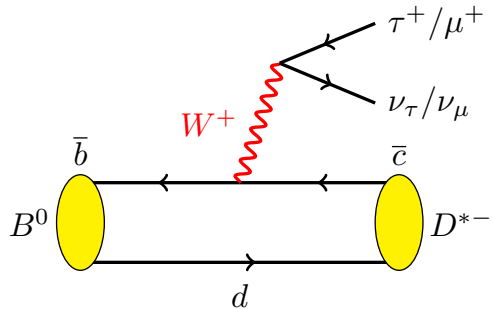


FIGURE 1: The SM Feynman diagram representing  $B^0 \rightarrow D^{*-}\tau^+\nu_\tau$  and  $B^0 \rightarrow D^{*-}\mu^+\nu_\mu$  transitions. Note it consists of the  $b \rightarrow c\tau^+\nu_\tau$  transition and a spectator  $d$ -quark.

and LHCb of  $R(D)$  and  $R(D^*)$ , once combined, exhibit a  $3.8\sigma$  tension with the SM estimate as shown in Figure 2.

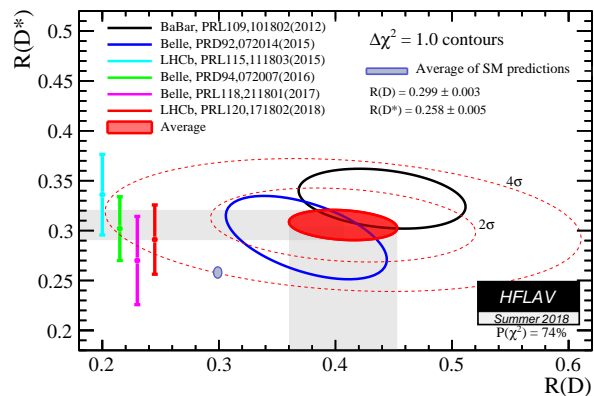


FIGURE 2: The  $R(D)$  and  $R(D^*)$  SM estimate (small blue ellipse) and experimental measurements as reported by BaBar, Belle and LHCb. The red ellipse shows the combined world average. The red vertical bar corresponds to the LHCb result discussed in section 2 [5].

The remainder of this article discusses the measurement of  $R(D^*)$  using 2011-2012 LHC data [3, 4] in Section 2, then describes an ongoing continuation and improvement of that analysis using 2015-2016 LHC data in Section 3 and concludes in Section 4.

## 2 $R(D^*)$ with $\tau \rightarrow 3\pi\nu_\tau$ at LHCb

The  $R(D^*)$  ratio can be expanded by multiplying and dividing by the branching fraction of the normalisation mode,  $B^0 \rightarrow D^{*-}\pi^+\pi^-\pi^+$ , as follows :

$$R(D^*) = \frac{\mathcal{B}(B^0 \rightarrow D^{*-}\tau^+\nu_\tau)}{\mathcal{B}(B^0 \rightarrow D^{*-}\pi^+\pi^-\pi^+)} \times \frac{\mathcal{B}(B^0 \rightarrow D^{*-}\pi^+\pi^-\pi^+)}{\mathcal{B}(B^0 \rightarrow D^{*-}\mu^+\nu_\mu)}.$$

Then, only the first fraction, *i.e.* relative branching fraction of the signal and normalisation mode is measured, whereas the ones present in the second fraction are taken from external measurements. The  $\tau^+$  is reconstructed from its decay into  $3\pi^\pm(\pi^0)\nu_\tau$ , as shown in Figure 3.

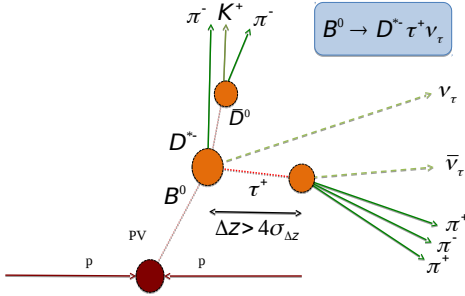


FIGURE 3: Signal mode topology with two non-reconstructed neutrinos. Also the  $3\pi$  vertex displacement w.r.t. the  $B^0$  cut is shown.

Since neutrinos are not reconstructed, the signal final-state particles are the same as in the normalisation mode whose topology is depicted in Figure 4. Thanks to that, some systematic effects cancel out in the ratio.

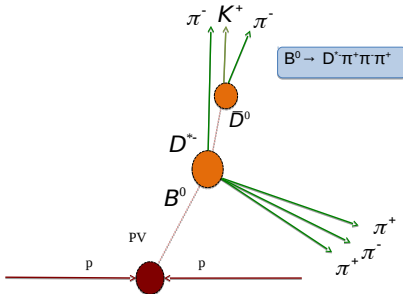


FIGURE 4: Normalisation mode topology. All final-state particles can be reconstructed.

Due to two neutrinos present in the signal, it can be reconstructed only partially, whereas full reconstruction of the normalisation mode is possible.

### 2.1 Selection and backgrounds

All the backgrounds belong to the  $b\bar{b} \rightarrow D^{*-}3\pi(X)$  inclusive mode, where the  $D^{*-}3\pi(X)$  system comes from one or more  $b$ -hadron(s). It is largely rejected by requiring a significant offset between the  $3\pi$  and  $D^{*-}$  vertices, as shown in Figure 5, due to abundance of events with  $3\pi$  coming directly from the  $B^0(D^{*-})$  vertex.

Other selection requirements include : particle identification (PID) constraints on the pions, sufficient flight distance of the  $\bar{D}^0$  and  $\pi$  from the  $3\pi$  system,  $\tau^+$  origin vertex matching the one of  $D^{*-}$ , and the mass window  $m(D^{*-}) - m(\bar{D}^0) \in [143, 148] \text{ MeV}/c^2$  considered.

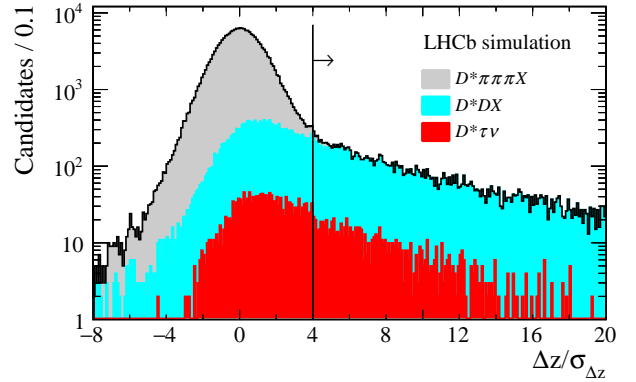


FIGURE 5: Distribution of the  $D^{*-}\tau^+\nu_\tau$  signal (red), and  $D^{*-}D(X)$  and  $D^{*-}3\pi(X)$  backgrounds (cyan and grey) as a function of the vertex displacement cut. Shown is applied cut at  $\Delta(z)/\sigma_{\Delta(z)} = 4$  that drastically decreases presence of the  $D^{*-}3\pi(X)$  mode.

The remaining background is mostly composed of the  $D^{*-}DX$  modes coming from a  $B$ -meson, *i.e.* with a  $D$  meson reconstructed as a  $\tau$  candidate. These are suppressed by : requiring no extra charged tracks forming a good vertex with the  $D$  meson (*charged isolation*), PID constraints, and a multivariate analysis, implemented as a Boosted Decision Tree (BDT). The latter incorporates, *e.g.* : differences between the  $\tau$  and  $D$  resonant states, kinematics, and quality of reconstruction under signal and background hypotheses. The BDT distribution for the signal and  $D^{*-}D(X)$  background is shown in Figure 6, where a cut applied in the selection is shown. The same BDT is used as one of the 3 variables in the fit aimed at extracting the signal yield, because of its discriminant power between the signal and  $D^{*-}D(X)$  backgrounds.

### 2.2 Signal and normalisation fits

From the simulation, templates for the signal-yield fit are constructed for the signal and remaining background modes (mostly  $D^{*-}D_s^+(X)$ ) which are then corrected with data control samples. In order to extract the signal yield

The signal yield is obtained from a three dimensional binned maximum likelihood fit based on : the  $\tau^+$  can-

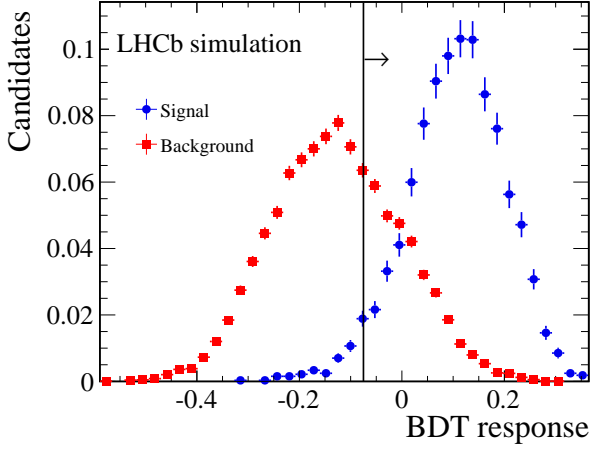


FIGURE 6: The Anti- $D^{*-}D(X)$  BDT distribution for signal (blue) and the  $D^{*-}D_s^+(X)$  background with a cut applied at -0.75.

candidate lifetime, the 4-momentum transfer to the lepton system ( $q^2$ ) and the aforementioned BDT. It is shown in Figure 7 in projections onto  $\tau^+$  lifetime and  $q^2$  in 4 bins of increasing BDT score. One can observe that the signal yield (red) increases and the  $D^{*-}D_s^+$  background (orange) decreases as a function of the BDT.

Regarding the normalisation mode, due to full reconstruction a fit can be applied to the mass of the  $D^{*-}3\pi$  system as shown in Figure 8.

The final result is :  $R(D^{*-}) = 0.291 \pm 0.019(\text{stat}) \pm 0.026(\text{syst}) \pm 0.013(\text{ext})$ , where the last uncertainty stems from external measurements. The result is  $\approx 0.94$  standard deviations above the SM estimate.

### 3 Updating $R(D^*)$ with $\tau \rightarrow 3\pi\nu_\tau$ using 2015-2016 data at LHCb

The analysis is continued with the 2015-2016 dataset from LHCb. The statistical uncertainty, due to the collected data sample size, will be reduced by a factor of 1.2, whereas the systematic uncertainty is targeted not to exceed the resulting statistical one. The largest sources of systematic uncertainty are simulated sample size, modelling of the double charm backgrounds and the uncertainty on efficiency. These are expected to be reduced with increased data and simulation sample sizes as well as more precise external inputs. To this end, simulated sample size has to be increased by a factor of 4. This necessitates employing fast simulation in order to generate the requested sample within a few months.

The chosen fast simulation algorithm is ReDecay [6]. It is used for all the modes (*i.e.* signal, normalisation and backgrounds) considered and works as follows.

Once a generated proton-proton ( $pp$ ) collision has produced a  $B^0$  meson besides all underlying (*i.e.* non-signal) tracks, such an event is saved. Subsequently the  $B^0$  is decayed into the signal mode 100 times. The final-state signal event for each decay is then merged with

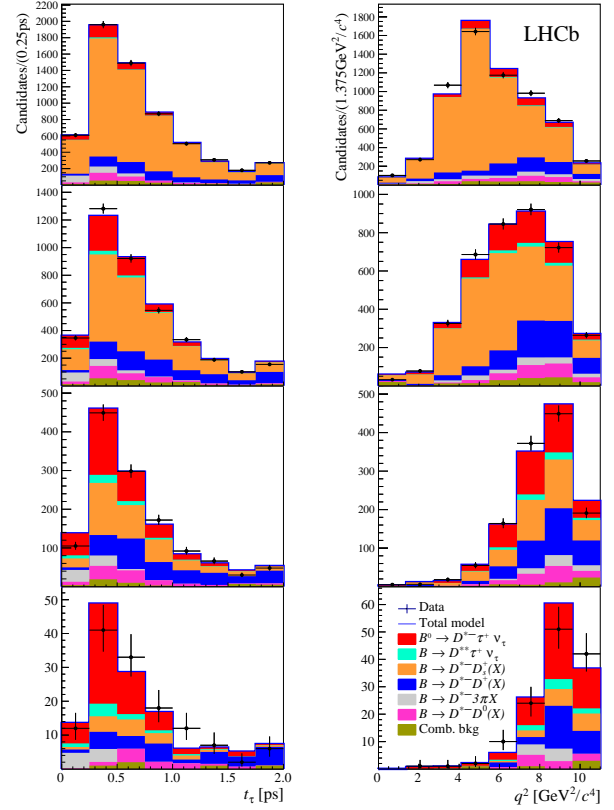


FIGURE 7: Projections of the final fit onto lifetime of the  $\tau^+$  candidate,  $t_\tau$  (left), and 4-momentum transfer to the lepton system,  $q^2$  (right), in 4 BDT bins of increasing score from top to bottom.

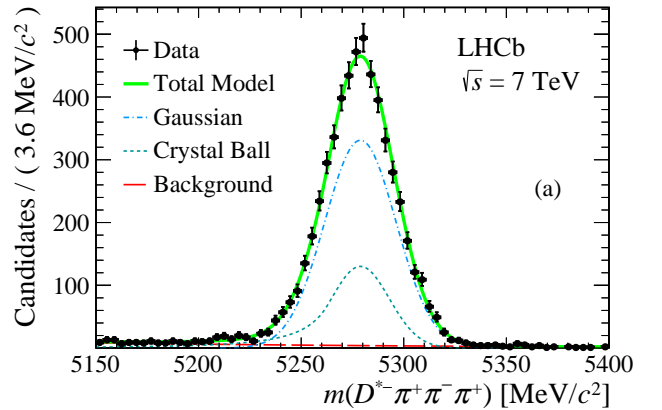


FIGURE 8:  $D^{*-}3\pi(X)$  distribution and fit for the normalisation mode. The fit consist of a gaussian added to a Crystal Ball for the normalisation mode plus an exponential for background.

the same underlying event. Then another  $pp$  collision occurs and the procedure repeats. Due to the abundance of the underlying tracks, generated only once per 100 signal events, this algorithm speeds up simulation by a factor of 10-100 depending on the specific decay mode.

Since ReDecay is a novel technique, it is crucial to show that it is fully acceptable for the analysis and all the potential problems should be pinpointed and controlled. To this end, for most of the simulated modes, small test samples have to be produced using both, the full simulation and ReDecay. Figure 9 confirms compatibility between the full simulation and ReDecay for the transverse momentum distribution of  $B^0$  in the signal mode at the generator level, as one example of many checks.

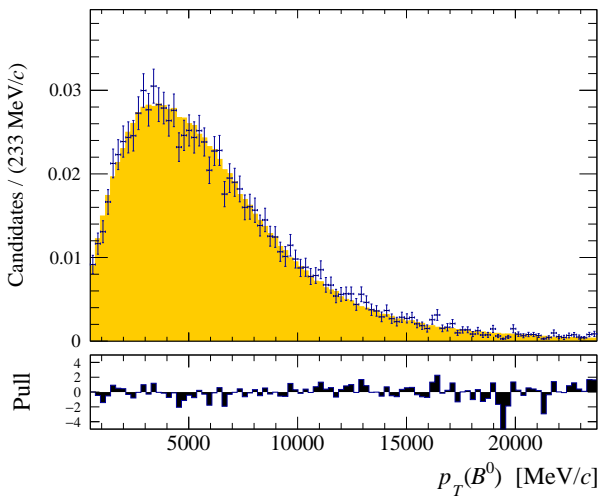


FIGURE 9: Transverse momentum ( $p_T$ ) of  $B^0$  of a generated signal mode full simulation (filled-in yellow bins) and ReDecay (black points).

A major challenge of using ReDecay stems from correlation of events in one ReDecay block (*i.e.* from the same original event). Consequently the per-bin uncertainties of certain distributions do not follow the Poisson distribution. Instead, the uncertainties can be computed bootstrapping event blocks (with 100 decays each) from a data sample.

Currently, the major work-in-progress tasks of the analysis involve using a BDT for the charged isolation and improving performance of the BDT discussed in Section 2 in order to further reduce the systematic uncertainties.

## 4 Conclusions and prospects

Lepton Flavour Universality is undergoing scrutiny in two main channels :  $b \rightarrow c\tau^+\nu_\tau$  and  $b \rightarrow sl^+\ell^-$ . Several tensions with the SM have been observed by  $B$ -factories and LHCb and need further investigation. If the discrepancies with respect to the SM model reach the size of 5 standard deviations, the SM will have to

be extended or replaced to account for LFU. Several NP models propose Leptoquarks as contributions to the  $b \rightarrow c\tau^+\nu_\tau$  transition.

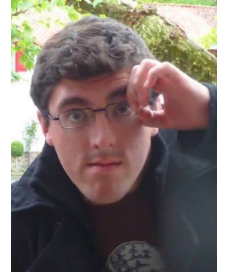
The 2015-16 LHCb dataset will improve precision of the already published analysis based on the 2011-2012 dataset and shed light on the  $R(D^*)$  anomaly.

## Références

- [1] S. Fajfer, J. F. Kamenik, and I. Nišandžić,
- [2] LEP Collaborations : ALEPH Collaboration, DELPHI Collaboration, L3 Collaboration, OPAL Collaboration, the LEP Electroweak Working Group, *A Combination of Preliminary Electroweak Measurements and Constraints on the Standard Model* arXiv:hep-ex/0511027, Nov 2005  $B \rightarrow D^*\tau\bar{\nu}_\tau$  sensitivity to new physics, Phys. Rev. D 85, 094025, 23 May 2012
- [3] R. Aaij et al. (LHCb Collaboration) *Measurement of the Ratio of the  $B^0 \rightarrow D^{*-}\tau^+\nu_\tau$  and  $B^0 \rightarrow D^{*-}\mu^+\nu_\mu$  Branching Fractions Using Three-Prong  $\tau$ -Lepton Decays*, Phys. Rev. Lett. 120, 171802, 25 April 2018
- [4] R. Aaij et al. (LHCb Collaboration) *Test of lepton flavor universality by the measurement of the  $B^0 \rightarrow D^{*-}\tau^+\nu_\tau$  branching fraction using three-prong  $\tau$  decays*, Phys. Rev. D 97, 072013, 25 April 2018
- [5] Heavy Flavour Averaging Group (HFLAV), *Average of  $R(D)$  and  $R(D^*)$  for Summer 2018*, <https://hflav-eos.web.cern.ch/hflav-eos/semi/summer18/RDRDs.html>
- [6] D. Muller, M. Gersabeck and C. Parkes, *Measurements of production cross-sections and mixing of charm mesons at LHCb*, Nov 2017, <https://cds.cern.ch/record/2297069>

# Study of $B \rightarrow hh\gamma$ decays with the LHCb experiment

**Boris Quintana**  
*LPC, Clermont-Ferrand*



## Résumé

One of the topics of interest of the LHCb experiment at CERN is the study of Flavor-Changing Neutral Currents, occurring for example in radiative decays of B hadrons. Such loop processes are highly sensitive to the presence of New Physics.

We present here the analysis of LHCb data for the search for  $B_s^0 \rightarrow f_2(1525)\gamma$  and  $B_d^0 \rightarrow K_1(1410)\gamma$  decays.

## 1 Introduction

Flavor-changing neutral-currents are forbidden at tree level in the Standard Model, which makes  $b \rightarrow (s/d)\gamma$  quark transitions sensitive to new physics effects that could arise from the exchange of new heavy particles in electroweak penguin diagrams (Figure 1).

Therefore, studying radiative decays of B hadrons is a good way of probing New Physics, given that they offer many physical observables to measure : branching ratios, asymmetries, angular distributions and photon polarisation([1],[2]).

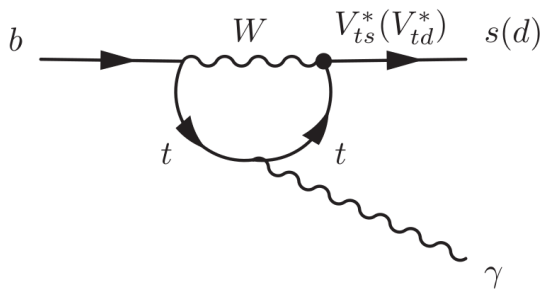


FIGURE 1:  $b \rightarrow s(d)\gamma$  quark transition in the SM

The aim of the presented analysis is to study simultaneously the  $B_d^0 \rightarrow (K\pi)\gamma$ ,  $B_s^0 \rightarrow (KK)\gamma$  and  $\Lambda_b^0 \rightarrow (pK)\gamma$  decay events selected by the LHCb detector, and do an amplitude analysis of the  $(K\pi)$  and  $(K^+K^-)$  resonances in order to look for orbitally excited mesons such as in non measured  $B_s^0 \rightarrow f_2'(1525)\gamma$  and  $B_d^0 \rightarrow K_1(1410)\gamma$  decays.

The study depicted here has two main motivations :  
- improve the mass models for  $B_d \rightarrow K^*\gamma$  and  $B_s \rightarrow \phi\gamma$  studies with a better understanding of the non-resonant states and high mass contamination.

- measure branching ratios of exclusive radiative modes to improve the inclusive  $B_{(s)} \rightarrow X_s\gamma$  in terms of sum over exclusives.

## 2 Data selection

### 2.1 LHCb Data

This analysis is performed using the data collected by the LHCb experiment [3] at a center-of-mass energy of  $\sqrt{s} = 7$  TeV for the 2011 campaign,  $\sqrt{s} = 8$  TeV for the 2012 campaign, and  $\sqrt{s} = 13$  TeV for the 2015 and 2016 campaign (Run II). These samples correspond respectively to integrated luminosities ( $\int \mathcal{L} dt$ ) of  $1 \text{ fb}^{-1}$ ,  $2 \text{ fb}^{-1}$ ,  $0.33 \text{ fb}^{-1}$  and  $1.67 \text{ fb}^{-1}$ .

After passing trigger requirements, decay events comprising two charged hadron tracks and a high momentum ( $> 3 \text{ GeV}/c$ ) photon are reconstructed and stored. In order to minimise the size of the analysed sample, and increase its purity, a set of preselection cuts is applied.

It ensures most non b-decay events are rejected. The same reconstruction and selection process is applied to both data and Monte Carlo (MC) simulated samples which are needed for the analysis.

### 2.2 PID studies

After the preselection process, the data has to be split into three samples, corresponding to the three final states we are willing to study, namely  $K\pi\gamma$ ,  $KK\gamma$  and  $pK\gamma$ . To achieve this we apply a selection based on Particle IDentification (PID) variables, which uses information on the nature of the charged hadron provided by LHCb subsystems, such as the Ring Imaging Cherenkov detectors (RICH), and combines them with a multivariate algorithm. This selection provides highly pure samples of exclusive decays.

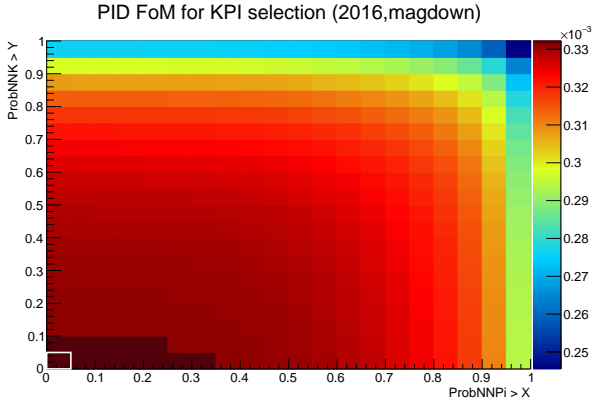


FIGURE 2: Scan of the purity of the sample for each cut on the PID variables of the tracks.

These cuts are tuned after PID studies based on calibration data samples and MC simulated signal events, in order to maximise the purity of the samples (Figure 2). From these studies we deduce the misidentification probability for each possible cross-feed.

### 2.3 MVA selection

Combinatorial background consists of events composed of tracks and photons that do not come from the decay of the same particle but have still been reconstructed as a radiative  $B$  decay and selected. This particular contribution can be strongly suppressed by applying a cut to the output of a multivariate algorithm, a Boosted Decision Tree (BDT, Figure 3), trained on MC signal and the data in the Right Handed Side Band of the  $hh\gamma$  invariant mass distribution, where only combinatorial events are found.

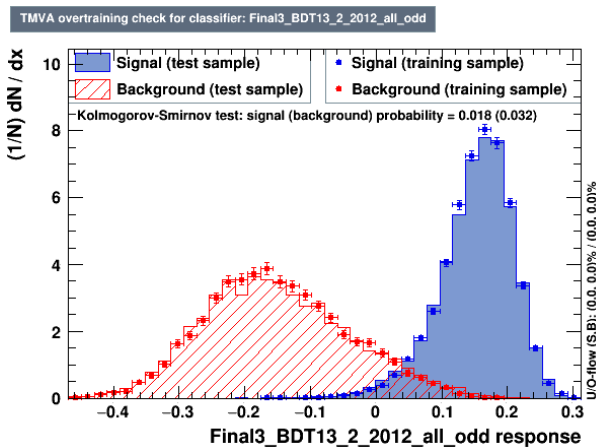


FIGURE 3: BDT output distribution for signal (blue) and combinatorial background (red).

## 3 $B_{(s)}$ mass fit

After the whole selection process, a simultaneous fit to the three  $hh\gamma$  invariant masses is developed, taking into account all the possible backgrounds contributions. Fitting them simultaneously allows cross-feed contributions to be fixed without any assumption on the  $hh\gamma$  modes branching ratio.

### Signal and peaking background description

The signal invariant mass distribution is extracted fitting the simulated events using a double tail Crystal-Ball (CB) PDF.

The left tail of the CB describes the low mass region and accounts for Bremsstrahlung and other possible losses in the photon energy due to the fiducial volume of the calorimeter. The tail at high masses models the imperfections of the track reconstruction. However, in the case of radiative decays, large pile-up deposits in the electromagnetic calorimeter (ECAL) cluster forming the photon candidate are also likely to contribute. The invariant mass resolution of the  $B$  candidate depends on the ECAL resolution as it is dominated by the photon contribution. The mean value of the gaussian can be a bit shifted from the  $B_{(s)}$  mass value depending on the quality of the calibration of the ECAL.

An example ( $K^+K^-\gamma$ , 2012) of the fit to the simulated signal is shown on Figure 4. In the fit to the data, the tail parameters are fixed to the values extracted in the simulation while the mean ( $\mu$ ) and mass resolution ( $\sigma$ ) are left free to float.

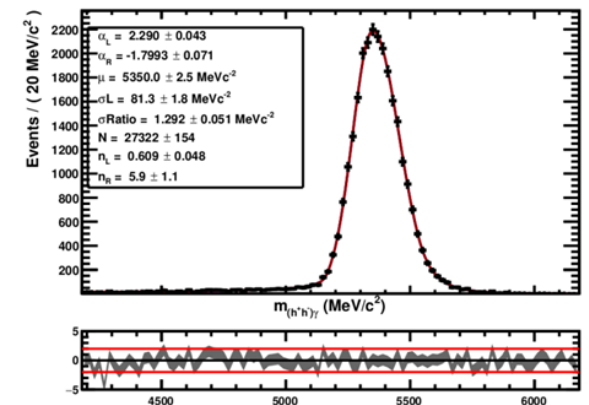


FIGURE 4: Fit of the simulated signal ( $KK\gamma$ ) invariant mass

All the  $hh'\gamma$  and  $hh'\pi^0$  peaking backgrounds are fitted using a symmetric double tail Crystal-Ball PDF. The various cross-feed contamination are used to constrain the respective yields in the final mass fit.

## Partially reconstructed and combinatorial background

Partially reconstructed backgrounds to the signal channels could be any B decays leading to  $h^+h^-\gamma X$  or  $h^+h^-\pi^0 X$  final states where  $X$  could be one or more not reconstructed charged or neutral particle. Simulated samples of partially reconstructed decays are fitted using an ARGUS function convoluted with a Gaussian PDF to model the detector resolution. The different parameters are then reported and fixed in the fit of the data and only the normalisation of the contribution is left free. An example for the simulated sample fit of partially reconstructed  $B_s \rightarrow \phi\pi^0\gamma$  decay is shown on Figure 5.

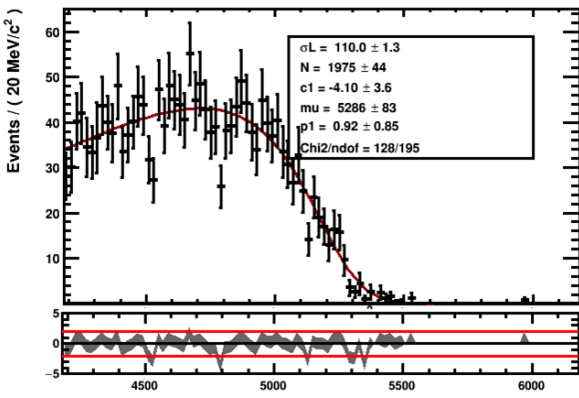


FIGURE 5: Fit of the simulated  $B_s \rightarrow \phi\pi^0\gamma$  (part. reconstructed) invariant mass

The combinatorial background is described with a first order polynomial, the yield and shape parameter for this contribution are left free. The fit to the  $B_s$  mass distribution of the  $KK\gamma$  selected data events corresponding to the year 2012 data taking is shown on Figure 6.

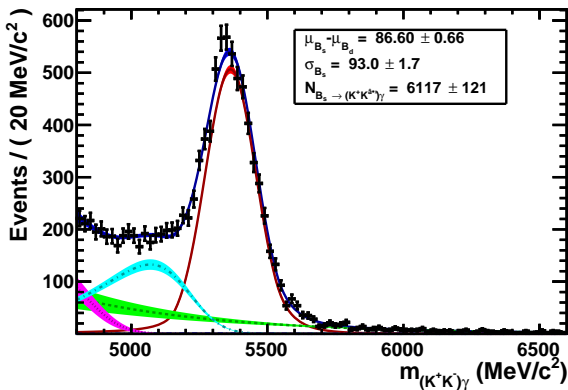


FIGURE 6: Fit of the  $(KK\gamma)$  invariant mass

## 4 Study of the $h^+h^-$ resonances

Using the sPlot method [4], one can unfold background and signal distributions. The  $hh$  invariant mass of the purified signal samples can then be studied. In order to disentangle between remaining backgrounds and possible contributions from high mass meson's decay, the aim of the analysis is to fit the  $hh$  invariant mass versus the helicity angle  $\theta_h$  of the resonance, which is defined as the angle between the momentum of any of the daughters of the meson and the momentum of the B candidate in the rest frame of the meson. It is expected to follow a  $\sin^2(\theta_h)$  function for vector decays,  $\sin^2(\theta_h) * \cos^2(\theta_h)$  for tensor decays and  $\cos^2(\theta_h)$  for  $hh\pi^0$  background.

The resulting sWeighted distribution of the  $K^+K^-$  signal in the  $m(hh)$  vs  $\theta_h$  plane is shown in Figure 7. One can clearly see a tensor contribution at approximately 1520  $\text{MeV}/c^2$ , corresponding to the  $f_2'(1525)$  decay.

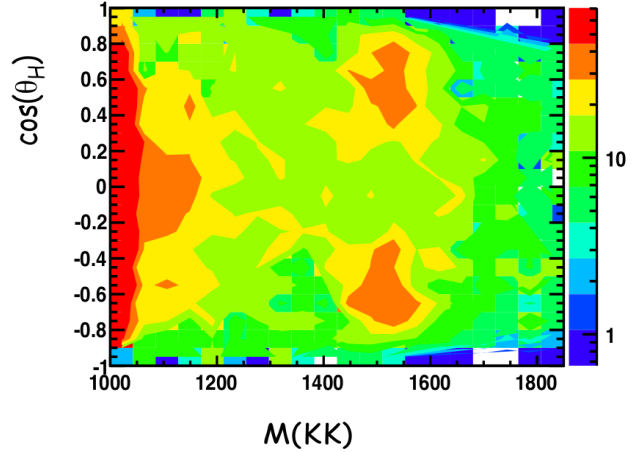


FIGURE 7: Signal distribution in the  $m(KK)$  vs  $\theta_h$  plane

## 5 Conclusion and prospects

In conclusion, we have developed a simultaneous selection of several  $B_{(s)} \rightarrow h^+h^-\gamma$  decay modes, as well as invariant mass fits that allow to unfold data and background distributions. The first look at the data is promising for a branching ratio measurement of  $B_s \rightarrow f_2'(1525)\gamma$  decay, and possible evidence of  $B_d \rightarrow K_1(1410)\gamma$ . Nevertheless, fits of the  $m(hh)$  vs  $\theta_h$  planes are still to be developed. In the case of the  $B_d \rightarrow K\pi\gamma$  decays the CP asymmetries will also be measured.

In addition to the amplitude analysis of the  $K\pi\gamma$  and  $KK\gamma$  modes, this work is a first step towards the analysis of  $\Lambda_b \rightarrow pK\gamma$  and  $B_d \rightarrow \pi\pi\gamma$ , for which exclusive modes are not measured yet at LHCb, such as  $\Lambda_b \rightarrow \Lambda^*(1520)\gamma$  and  $B_d \rightarrow \rho\gamma$ .

## Références

- [1] LHCb collaboration, *Observation of photon polarization in the  $b \rightarrow s\gamma$  transition*, *Phys. Rev. Lett.*, **112**, 161801, 2014.
- [2] LHCb collaboration, *Measurement of the ratio of branching fractions  $BR(B^0 \rightarrow K^{*0}\gamma)/BR(B_s^0 \rightarrow \phi\gamma)$  and the direct CP asymmetry in  $B^0 \rightarrow K^{*0}\gamma$* , *Nucl. Phys. B.*, **867**, 2013.
- [3] LHCb collaboration, *The LHCb detector at the LHC*, JINST **3** S08005 (2008)
- [4] M. Pivk and F. R. Le Diberder, *sPlot : a statistical tool to unfold data distributions* *Nucl. instr. Methods.*, **A555**, 356, 2005.

Septième partie

# Cosmology

session dirigée par Mickael RIGAULT



# Étude des biais cosmologiques induits par les variabilités nouvelles détectées sur les supernovas de type Ia

Florian Mondon

Laboratoire de Physique de Clermont, Clermont-Ferrand



## Introduction

L'utilisation des supernovas de types Ia (SNe Ia) comme chandelle quasi-standard a permis la découverte de l'accélération de l'univers par ajustement d'un diagramme de Hubble [1, 2]. La luminosité de ces supernovas possède cependant une variabilité venant de mécanisme interne et des effets environnementaux. La première source de variabilité, communément appelé le *stretch*, a avoir été identifiée vient du fait que le maximum de luminosité d'une SNe Ia dépend du temps de décroissance de sa courbe de lumière [3]. La deuxième source de variabilité vient de la dépendance entre le maximum de luminosité d'une SNe Ia et de sa couleur [4]. Cette dépendance serait due à la quantité de poussière entre la SNe Ia et l'observateur. Plusieurs standardisations ont été établies en tenant compte de ces deux effets connus sous le nom de relation de Tripp [5]. Le modèle temporel de distribution spectral en énergie pour les SNe Ia SALT2 [6] utilise une standardisation de type relation de Tripp et est devenu une référence pour les analyses cosmologiques avec les SNe Ia. Cependant, il a été démontré que malgré la paramétrisation en stretch couleur il reste une dépendance entre les résidus au diagramme de Hubble et les propriétés des galaxies hôtes (Mass, LsSFR) [8, 11, 10, 9]. Un autre problème majeur avec une standardisation SALT2 est l'existence d'une dispersion des résidus au diagramme de Hubble [1, 12, 7]. Ces deux problèmes sont une motivation suffisante pour aller au-delà d'une standardisation stretch couleur.

Un nouveau modèle de distribution spectrale en énergie *The Supernova Generator And Reconstructor* (SUGAR) [13] a été établi à partir d'une PCA<sup>1</sup> sur des indicateurs spectraux que nous verrons plus en détails dans la première section. Ce modèle a déjà permis une réduction de 0.02 de la dispersion au diagramme de Hubble à partir de données spectroscopiques par rapport à une standardisation SALT2 [13]. Cependant avec l'arrivée de la prochaine génération d'expérience telle que *Large Synoptic Survey Telescope* (LSST) [14] et leurs données purement photométrique, il est important de vérifier que les résultats obtenus avec des données spectroscopiques soient toujours valables avec des données photométriques.

## 1 Le modèle *The Supernova Generator And Reconstructor*

Le modèle SUGAR [13] a été entraîné avec 113 spectres de la collaboration SNfactory. Ces spectres ont été obtenus avec le spectrographe à champ intégral *The Supernova Integral Field Spectrograph* (SNIFS) entre 2004 et 2010 installé sur le télescope de 2,2 m de l'Université d'Hawaii. La spectroscopie est effectuée sur une voie bleue qui couvre les longueurs d'onde de 3200 à 5200 Å et une voie rouge de 5100 à 10000 Å.

La première étape pour la construction du modèle SUGAR est la mesure des indicateurs spectraux. Les indicateurs spectraux utilisés sont des pseudo-largeurs équivalents de raie et la position des minimums de profil p-cygni. Ces deux grandeurs sont reliées au mécanisme interne des SNe Ia et sont donc reliées à la partie intrinsèque de la variabilité des SNe Ia. L'utilisation des indicateurs spectraux comme méthode de standardisation a déjà fait l'objet de nombreuses études [16, 17, 18, 19, 20, 21] mais aucune d'entre elles ne va jusqu'à en faire un modèle de distribution spectrale en énergie (SED).

Le modèle SUGAR est construit à partir de 13 de ces

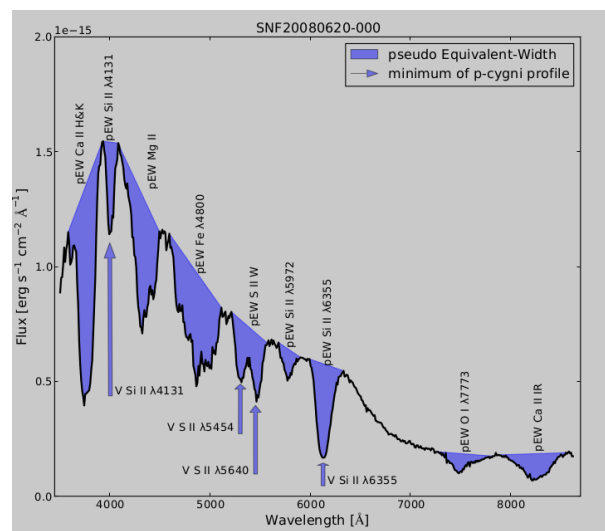


FIGURE 1: Les 9 pseudo-largeurs équivalents de raie et 4 minimums de profil p-cygni qui ont servi à la construction de SUGAR [13]

indicateurs spectraux dont 9 pseudo-largeurs équivalents de raie et 4 minimums de profil p-cygni listés sur la Figure 1. Une PCA sur ces indicateurs spectraux

1. Principal component analysis [15]

permet de réduire le nombre de dimension et de passer à un espace où les variables sont décorréelées. Les trois premiers vecteurs propres de cette PCA modéliseront pour SUGAR la partie intrinsèque de la variabilité. La partie extrinsèque quant à elle est modélisée par une loi d'extinction de type Cardelli et al. [22] par la même méthode que celle proposée dans l'analyse de Chotard et al. [21], estimée au maximum de luminosité. La dernière étape avant la construction du modèle SUGAR est l'interpolation en temps des données de l'entraînement car celle-ci sont toutes prises à des époques différentes ce qui est géré ici par des processus gaussiens. Nous pouvons donc à partir de tout cela écrire les équations du modèle SUGAR de la façon suivante :

$$M_{t,\lambda} = M_{t,\lambda,0} + \sum_{i=1}^3 q_i \alpha_{t,\lambda,i} + A_V \left( \alpha_\lambda + \frac{1}{R_V} \beta_\lambda \right) + \Delta M_{grey} \quad (1)$$

où  $M_{t,\lambda,0}$  est la magnitude du spectre moyen,  $q_i$  sont les vecteurs propres de la PCA venant de l'analyse des indicateurs spectraux,  $\alpha_{t,\lambda,i}$  sont les coefficients directeurs liés à la variation des  $q_i$ ,  $A_V$  est l'absorption dans la bande V provoquée par la loi d'extinction déterminée au maximum de luminosité avec  $R_V = 2,6$ .  $\Delta M_{grey}$  est un terme gris (qui ne dépend pas de la longueur d'onde) permettant de travailler indépendamment de la distance. La loi d'extinction étant déterminée au maximum de luminosité, les seules inconnues restantes sont la magnitude du spectre moyen et les coefficients  $\alpha_{t,\lambda,i}$  qui sont déterminés par la méthode de régression orthogonale des distances donnant ainsi un modèle complet de SED.

## 2 Résultats obtenus après ajustement de données spectroscopiques par le modèle de SED SUGAR

Une fois le modèle de SED établi nous pouvons directement l'utiliser pour ajuster des données spectroscopiques par la méthode de minimisation de  $\chi^2$  afin d'obtenir les paramètres SUGAR ( $q_1, q_2, q_3, A_V$ ) que l'on utilisera pour la standardisation tel que le jeu de paramètres ( $x_1, c$ ) pour SALT2. L'un des premiers résultats avec SUGAR et que l'ajout de deux nouveaux paramètres pour la partie intrinsèque permet une meilleure description des SED des SNe Ia tel que le montre la Figure 2. Par la suite nous avons réalisé un diagramme de Hubble avec une standardisation SUGAR c'est-à-dire en déterminant un module de distance analogue à celui de SALT2 mais corrigé des paramètres SUGAR comme décrit l'équation suivante :

$$\mu_{SUGAR} = m_B^* - M_B - \sum_{i=1}^3 \alpha_i q_i - \beta A_V \quad (2)$$

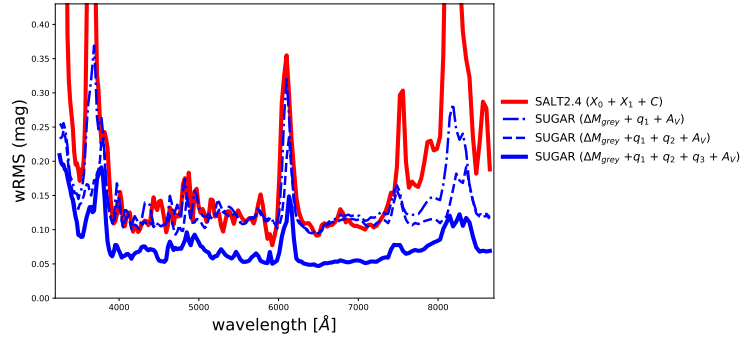


FIGURE 2: Écart-type des résidus en fonction de la longueur d'onde pour le modèle SUGAR (en bleu) avec l'ajout des différents paramètres et le modèle SALT2 (en rouge) [13].

où  $\mu$  est le module de distance pour une SNe Ia,  $m_B^*$  est la magnitude apparente au maximum de luminosité qui provient directement du modèle SUGAR.  $M_B$  est la magnitude absolue moyenne dans la bande B, et enfin les coefficients  $\alpha$  et  $\beta$  représentent les coefficients directeurs liés aux facteurs  $q_i$  et à l'absorption  $A_V$ . Nous faisons par la suite un ajustement par minimisation du  $\chi^2$  en fixant la cosmologie afin d'obtenir notre diagramme de Hubble pour ainsi pouvoir le comparer avec un diagramme de Hubble fait avec une standardisation SALT2. Nous obtenons les résultats présentés à la Figure 3. SUGAR permet donc une réduction de 0.17 du wRMS sur ce jeu de données spectroscopiques mais reste assez similaire quant à la valeur de la dispersion intrinsèque.

	Salt2	SUGAR Spectro
$\sigma_{int}$	0.130	0.117
wRMS	0.142 ± 0.010	0.125 ± 0.009

FIGURE 3: Résultats obtenus après réalisation d'un diagramme de Hubble avec standardisation SALT2 et SUGAR où  $\sigma_{int}$  est la dispersion intrinsèque.

## 3 Ajustement des courbes de lumière à partir du modèle de SED SUGAR

Comme dit précédemment les prochaines expériences telles que le LSST auront des données purement photométriques. Il est donc important de vérifier que l'utilisation du modèle SUGAR soit toujours valable face au modèle SALT2 avec des données photométriques. Pour faire cette étude nous utilisons les mêmes spectres que ceux utilisés dans l'analyse précédente mais nous les intégrons cette fois dans des filtres synthétiques (BVR). Nous obtenons ainsi des courbes de lumière dans chaque bande. Nous avons par la suite intégré le modèle SU-

GAR à SNCOSMO qui est un programme permettant l'ajustement de courbes de lumière connaissant un modèle temporel de SED tel que SALT2 ou SUGAR. Ceci dans le but d'obtenir comme précédemment un jeu de paramètres SUGAR pour une SNe Ia à partir de ces courbes de lumière pour pouvoir par la suite les utiliser pour standardiser sa luminosité.

Nous allons dans un premier temps comparer les paramètres SUGAR obtenus avec données spectroscopiques et ceux obtenus avec des données photométriques. En effet, les données photométriques nous donnent moins d'information que des données spectroscopiques ce qui dégrade la qualité de reconstruction des paramètres SUGAR obtenus par photométrie. La Figure 4 présente les résultats obtenus. 2.

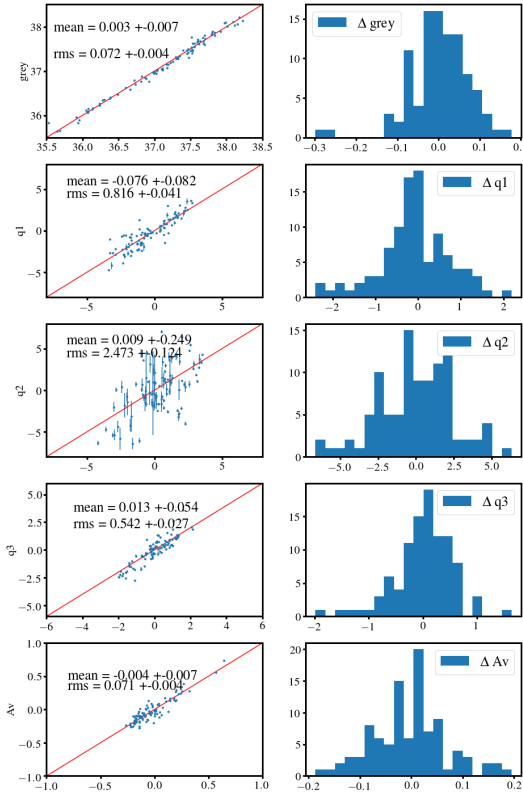


FIGURE 4: Comparaison des paramètres SUGAR obtenus avec des données spectroscopiques avec ceux obtenus avec des données photométriques (BVR) et distribution de la différences entre ces deux jeux de paramètres.

Nous pouvons remarquer que la plupart des paramètres sont bien reconstruit sauf les paramètres  $q_2$ . En effet, le RMS de la distribution de la différence  $\Delta q_2$  entre photométrie et spectroscopie est de  $2.473 \pm 0.124$  alors que le RMS de la distribution du  $q_2$  en spectroscopie est de  $1,70 \pm 0,086$ . Nous nous sommes demandés par la suite si l'ajout de la bande U et I pouvait améliorer la reconstruction de  $q_2$  (Figure 5). L'ajout de ces bandes fait passer le RMS du  $\Delta q_2$  à  $1,374 \pm 0,069$ , ce qui montre que la qualité du  $q_2$  est acceptable seulement avec 5 bandes.

Nous avons par la suite utilisé ces paramètres dé-

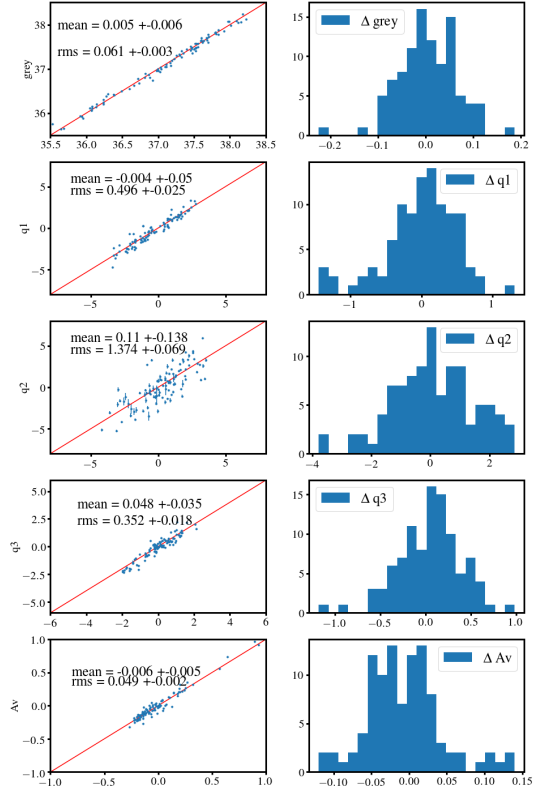


FIGURE 5: Comparaison des paramètres SUGAR obtenus avec des données spectroscopiques avec ceux obtenus avec des données photométriques (UBVRI) et distribution de la différences entre ces deux jeux de paramètres.

	BVR	UBVRI	Spectro
$\sigma_{int}$ SUGAR	0,125	0,123	0,117
wRMS SUGAR	$0,135 \pm 0,010$	$0,132 \pm 0,010$	$0,125 \pm 0,010$
$\sigma_{int}$ SALT2	0,130	0,125	
wRMS SALT2	$0,142 \pm 0,010$	$0,136 \pm 0,010$	

FIGURE 6: Performances comparées de SUGAR et SALT2 sur les valeurs du wRMS et de  $\sigma_{int}$  du diagramme de Hubble

terminé avec des données photométriques pour reproduire un diagramme de Hubble avec une standardisation SUGAR tel que décrite par l'équation (2). Nous obtenons les résultats présentés dans la table 6. Nous obtenons toujours avec des données photométriques de meilleurs résultats avec SUGAR qu'avec SALT2 mais l'écart entre les wRMS SUGAR et SALT2 n'est plus que de 0.04 en UBVRI. La dispersion intrinsèque quant à elle, reste assez similaire entre les deux standardisations.

## Conclusion

Le modèle SUGAR permet d'aller au-delà d'une standardisation *stretch* couleur à partir d'une PCA sur des indicateurs spectraux et d'une loi d'extinction de type Cardelli et al. [22] déterminé au maximum de luminosité. Dans cette analyse nous présentons les premiers résultats sur l'utilisation de SUGAR pour standardiser la luminosité des SNe Ia. La différence sur le wRMS du diagramme de Hubble est de 0.17 avec des données spectroscopiques et passe à 0.04 avec des données photométriques UBVRI.

Nous devons à présent nous assurer que cette analyse est reproductible sur des données externes à la SNfactory. Par la suite, nous voulons appliquer une standardisation SUGAR à un plus large échantillon de SNe Ia avec une plus grande distribution en redshift pour pouvoir étudier l'impact d'une standardisation SUGAR sur une analyse cosmologique complète.

## Références

- [1] Perlmutter, S., Aldering, G., della Valle, M., et al. 1998, *Nature*, 391, 51
- [2] Riess, A. G., Filippenko, A. V., Challis, P., et al. 1998, *AJ*, 116, 1009
- [3] Rust, B. W. 1974, PhD thesis, Oak Ridge National Lab., TN
- [4] Riess, A., Press, W., & Kirshner, R. 1996, *AJ*, 473, 88
- [5] Tripp, R. 1998, *A&A*, 331, 815
- [6] Guy, J., Astier, P., Baumont, S., et al. 2007, *A&A*, 466, 11
- [7] Betoule, M., Kessler, R., Guy, J., et al. 2014, *A&A*, 568, 32
- [8] Kelly, P. L., Hicken, M., Burke, D. L., Mandel, K. S., & Kirshner, R. P. 2010, *ApJ*, 743
- [9] Rigault, M., Brinnel, V., Aldering, G., et al. 2018, *A&A* submitted
- [10] Roman, M., Hardin, D., Betoule, M., et al. 2018, *A&A*, 615, A68
- [11] Sullivan, M., Conley, A., Howell, D. A., et al. 2010
- [12] Astier, P., Guy, J., Regnault, N., et al. 2006, *A&A*, 447, 31
- [13] Léget, P.-F. 2016, Phd theses, Université Blaise Pascal
- [14] LSST Dark Energy Science Collaboration. 2012, ArXiv e-prints
- [15] Pearson, K. 1901, *Philosophical Magazine*, 2, 559
- [16] Nugent, P., Phillips, M., Baron, E., Branch, D., & Hauschildt, P. 1995, *ApJ*, 455, L147+
- [17] Arsenijevic, V., Fabbro, S., Mourão, A. M., & Rica da Silva, A. J. 2008, *A&A*, 492, 535
- [18] Bailey, S., Aldering, G., Antilogus, P., et al. 2009, *A&A*, 500, L17
- [19] Wang, X., Filippenko, A. V., Ganeshalingam, M., et al. 2009, *ApJ*, 699, L139
- [20] Foley, R. J. & Kasen, D. 2011, *ApJ*, 729, 55
- [21] Chotard, N., Gangler, E., Aldering, G., et al. 2011, *A&A*, 529, L4+
- [22] Cardelli, J. A., Clayton, G. C., & Mathis, J. S. 1989, *ApJ*, 345, 245

# Host galaxies environment influence study on Type Ia Supernovae



**Martin BRIDAY**

*Institut de Physique Nucleaire de Lyon (IPNL)*

## Résumé

Type Ia Supernovae (SNeIa) are standard candles which allow us to measure cosmic distances. Using them, we discovered the accelerated expansion of the Universe, which led to the 2011 Nobel prize. As the number of observed SNeIa is still increasing, we are now limited by systematic errors, partly due to astrophysical effects. Last decades studies have shown several relations between SNeIa properties and those of their host galaxy. Yet, the way to correct the astrophysical effects remains uncertain. In this paper, we propose to compare the environmental analysis methods previously used, trying to understand the similarities and the differences between all these studies, using a Markov Chain Monte Carlo simulator. Using the age of the stars surrounding the supernovae as a SNeIa progenitor age tracer, we show that this latter is a central parameter in the environment analysis. We also highlight that the observations made in these studies are most likely related to the same effect : SNeIa progenitor ages has an impact on SNeIa magnitudes.

## 1 Introduction

### 1.1 Type Ia Supernovae

Type Ia Supernovae (SNeIa) are thought to be the thermonuclear explosion of a white dwarf star located in a star binary system [1]. However, we don't exactly know the production mechanism of these events. We only can empirically observe that the SNeIa luminosity is almost the same each time, so we can consider them as standard candles. Their luminosity is often as intense as their whole host galaxy, visible over very long distances. We can consequently use them to precisely measure distances at the cosmological scale (several Gpc).

We define the distance modulus  $\mu$  of an object by :

$$\mu \equiv m - M = 5 \log \left( \frac{d_L}{d_0} \right) \quad (1)$$

where  $m$  is the object magnitude, corresponding to an inversed luminosity at a logarithm scale,  $M$  is the absolute magnitude, which represents the source magnitude if it were located at  $d_0 = 10 \text{ pc} \approx 32.6 \text{ light-years}$  (for example, for the sun  $M = 4.74 \text{ mag}$  and for SNeIa,  $M \approx -19 \text{ mag}$ ), and  $d_L$  is the luminosity distance.

The luminosity distance is cosmology dependent. We

express it with the cosmological parameters  $\{\Omega\}$  from the  $\Lambda$ CDM model (Cold Dark Matter, where  $\Lambda$  represents the dark energy parameter) by :

$$d_L = \frac{c(1+z)}{H_0} \times \int_0^z [\Omega_R(1+z')^4 + \Omega_M(1+z')^3 + \Omega_k(1+z')^2 + \Omega_\Lambda]^{-1/2} dz' \quad (2)$$

where  $c$  is the speed of light,  $z$  is the redshift,  $H_0$  is the Hubble-Lemaître constant,  $\Omega_R$  is the radiation parameter,  $\Omega_M$  is the matter parameter,  $\Omega_k$  is the curvature parameter,  $\Omega_\Lambda$  is the cosmological constant of the dark energy. These constants are defined today ( $z = 0$ ) and have the following closing relation :  $\Omega_R + \Omega_M - \Omega_k + \Omega_\Lambda = 1$ .

Perfect standard candles don't exist, but some object are standardizable, i.e. it exists relations between their observed brightness and other observables that able us to derived their (relative) absolute magnitude. For SNeIa, the pick magnitude in B band ( $m_B^{\text{max}}$ ) is correlated to the stretch ( $x_1$ ) of their lightcurve (evolution of their brightness as a function of time) and their lightcurve color ( $c$ ). Those three parameters are extracted from their SNeIa light curves, corresponding to the temporal evolution of the supernovae flux, using fitting models (for example SALT2 : Spectral Adaptive Light-Curve Template [2]). Thanks to these three parameters, we can correct the SNeIa magnitude by :

$$\mu_{\text{corr}} = m_B^{\text{max}} - M_B^0 + (\alpha x_1 - \beta c) \quad (3)$$

where  $M_B^0$  is the SNeIa average magnitude, and  $\alpha$  and  $\beta$  are the correcting parameters, respectively, for the stretch and color. The SNeIa dispersion, while naturally small with 0.4 mag, can further be reduced down to 0.15 mag thanks to these empirical standardisation relations. This corresponds to  $\sim 8\%$  precision for distance measurements.

Using the SNeIa, we plot the Hubble diagram, for example in Figure 1, adapted from *Betoule et al.* [3]. This figure highlights the accelerated expansion of the Universe [4][5], which led to the 2011 Nobel prize, here represented by the gap at high redshift between the  $\Lambda$ CDM fit (black line) and what we expected from a constant speed expansion (blue surface). Since then, this acceleration, supposedly caused by dark energy, has been confirmed by independent observations, notably that of the CMB [7], and with a high precision using SNeIa [3][6].

As the number of observed SNeIa is still increasing,

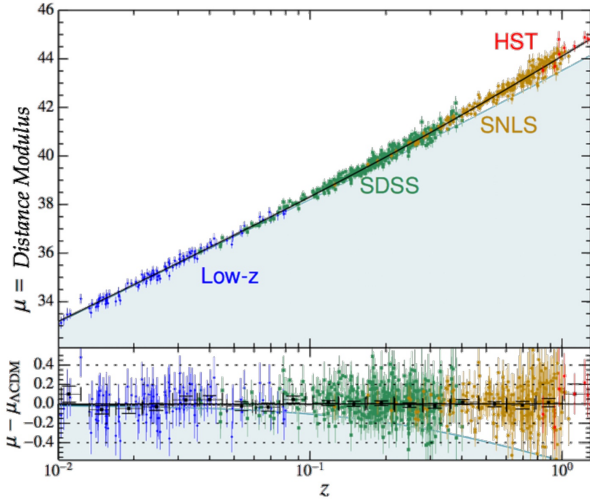


FIGURE 1: Hubble diagram, adapted from [3]. SNeIa distance modulus (**Top**) and Hubble residuals (**Bottom**) versus their redshift. Blue points come from low redshift catalogs, green ones from SDSS (Sloan Digital Sky Survey) catalog, yellow ones from SNLS (SuperNova Legacy Survey) catalog and red ones from the HST (Hubble Space Telescope) catalog. The blue surfaces correspond to a constant speed expansion of the Universe. The black line is the  $\Lambda$ CDM fit.

they are now limited by systematic errors, mainly due to two sources : instrumental calibration and astrophysic biases, due to the unknown production mechanism. This study will focus on the latter error source.

## 1.2 Host galaxy influence

As we don't fully understand the explosion mechanism of SNeIa, one could ask the question about how standard this object is. Recent studies have shown out a correlation between the host galaxy host environment and the Hubble residual (HR here after) from SNeIa.

This dependency has first been observed as a correlation between the HR and the host galaxy global mass [8][9][10][11][12]. This correlation has been presented as a step function, called the *mass step*. As a result, *Chidress et al.* (2013)[13] show that SNeIa are, on average, brighter in heavy galaxy than those in light galaxies. However, the galaxy mass can be considered as global parameter, including several factors, for example the star metallicities or star ages. Focusing on more local influencing parameters, an objective was to study on possible SNeIa intrinsic bias.

New studies highlight a correlation between the HR and the Local specific Star Formation Rate (LsSFR), which represents the SFR normalized by the stellar mass in 1 kpc around SNeIa (cf. Part 2.1). This correlation shows that SNeIa located in a young star environment are, in average, fainter than those in older star environment. Consequently called the *age step*, its most recent measurement is  $0.163 \pm 0.029$  mag ( $5.6\sigma$ )[14], plotted in Figure 2.

Nonetheless, several methods exist to measure the

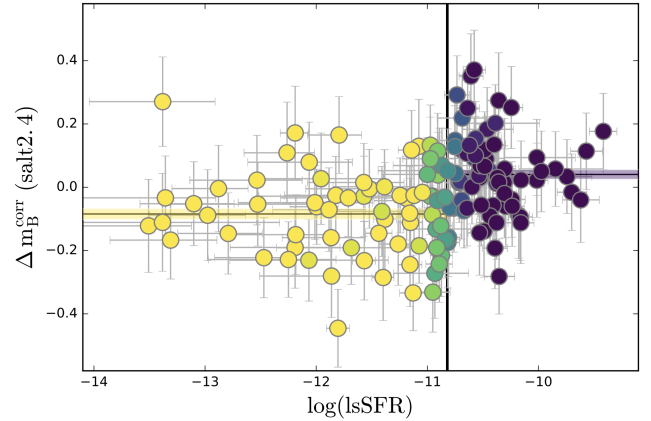


FIGURE 2: Hubble residuals (HR, here corresponding to  $\Delta m_B^{corr}$ ) as a function of  $\log$  LsSFR for 141 SNeIa from the Nearby Supernova Factory (SNf) [14]. The color bar represents the probability for each SN to have a young progenitor, based on LsSFR. The black vertical line is the step function cut, located here at  $\log$  LsSFR =  $-10.82$ . The histogram counts SN on each side of the cut. The horizontal lines are the mean on each step with their corresponding colored error surrounding.

supernovae stellar age environment, for example the use of the environment color. Recent similar studies noticed that, using either these different measurement methods, or different samples, we find in general lower values of the *age step*, sometimes compatible with zero [15][16][17].

Questioning the significance of the age-correlation, in this project, we will compare every method from the litterature to test their differences and similarities and verify the existance of the age step. In the next section, we will briefly describe all these methods, then we will present the results, finishing with the conclusion.

## 2 Star age measurement methods

### 2.1 Local specific Star Formation Rate

The specific Star Formation Rate (sSFR [ $\text{year}^{-1}$ ] =  $\frac{\text{SFR}}{M_\odot}$ ) is a common tool used to trace star ages. SFR ( $[M_\odot \cdot \text{year}^{-1}]$ ) is derived from  $H\alpha$  luminosity using the *Calzetti* (2013) relation :

$$\text{SFR}(H\alpha) = 5.45 \times 10^{-42} L(H\alpha) [\text{text} \cdot \text{s}^{-1}] \quad (4)$$

This SFR is then normalized to sSFR by the stellar mass in the studied zone. The stellar mass is derived using optical photometric relation using *Taylor et al.* relation (cf. 2.3 Equation 5).

For the host analysis, we focus on the 1 kpc location around the SN explosion site to probe the fraction of young stars in the supernova vicinity. We call this parameter the LsSFR for supernova local sSFR ; usually given in  $\log_{10}$  scale. We define as young environment

those with LsSFR greater than the median LsSFR, i.e.  $\text{LsSFR} > -10.82$  dex (for more details, look at [14]).

In this project, we will consider this tool as the reference, and we will compare every other age tracer to this one. Further study could consider testing this assumption.

## 2.2 Environment colors

Strong correlations exist between the LsSFR and some color of the environment [19]. We limited our study to  $u-r$  and  $g-r$  colors, but in the future, we will extend our result with  $\text{NUV}-r$  and  $\text{FUV}-r$  data. We have chosen to study these two colors within three radii around SNeIa :

- 1 kpc, to correspond with measurements in [14],
- 3 kpc, to produce similar measurements as in [16] and [15],
- global (the whole host galaxy), to study the influence of local vs. global measurements.

The magnitudes obtained from each wavelength band filter and each studied radius are K-corrected to remove the redshift effect. There isn't any cleared defined step cut in the litterature, so the convention is to take the median, corresponding to the assumption that there are 50/50% young and old progenitors.

## 2.3 Stellar mass

Stellar mass measurement is made using photometric data with  $g$  and  $i$  wavelength band filters. Stellar mass is extracted using the relation (cf. [20]) :

$$\log M_*/M_\odot = 1.15 + 0.70(g - i) - 0.4M_i \quad (5)$$

where  $g$  and  $i$  are magnitudes measured for the studied object (galaxies, star clusters, etc.) in  $g$  and  $i$  bands, and  $M_i$  is the AB absolute magnitude in the  $i$  band. The step cut is defined in the litterature by  $\log M_*/M_\odot = 10$  dex when using the global stellar mass. About local stellar mass, as nothing is precisely defined in the litterature, the convention is to use the median. We can see the correlation between this tracer and the LsSFR on Figure 3.

## 2.4 Morphology

It has been observed that elliptic galaxies present a much lower SFR than spiral galaxies, meaning that elliptic galaxies should contain, on average, older stars than those in spiral galaxies. Thus, we can use the galaxy morphology as a global age tracer. It exists several methods to classify galaxy morphologies, more or less precise on the result. The most commonly used is the inversed concentration index [21][22].

The galaxy surface luminosity evolution is correlated with the morphology. In spiral galaxies, we generally notice a bright bulb at the center of the galaxy, gathering the big majority of light in the center, whereas in elliptic galaxies, the luminosity is more distributed all over the galaxy.

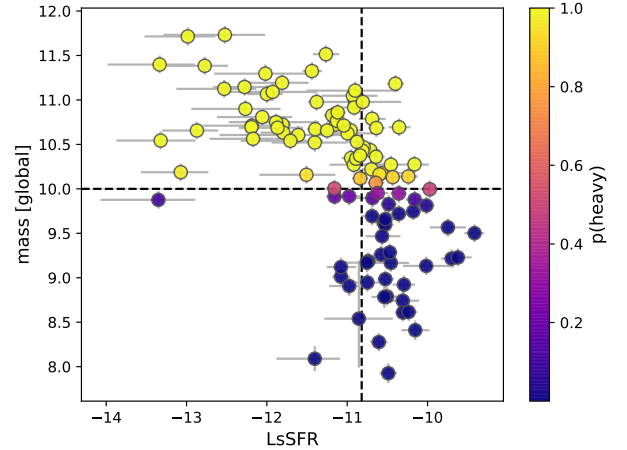


FIGURE 3: Host galaxy global stellar mass versus LsSFR. The color bar defines the probability for a SNeIa host galaxy to be considered as heavy one, The more yellow, the heavier. The LsSFR cut is located at  $\text{LsSFR} = -10.82$  dex, while the global stellar mass is  $\log M_*/M_\odot = 10$  dex, both of them represented by the dashed lines.

The inversed concentration index measures the ratio between the two radii containing 50% and 90% of the Petrosian flux, conventionnaly measured in  $r$  band. Early made galaxies (E and S0) get an index around 0.43, whereas late galaxies (Sab and Scd) get an index around 0.3. Based on litterature, we define the step cut by  $0.40 \pm 0.02$ .

## 3 Results

The correlation between the HR and the SNeIa progenitor ages is presented as a step function. Thus, we can distinguish two kinds of population : young and old progenitors. Considering the LsSFR as the best SNeIa progenitor age tracer, the goal is to quantify how bad are the other tracers in comparison with this one. A way to reach this objective is to measure the false positive and false negative rates, which means that the LsSFR is telling that the SN has a young progenitor whereas an other tracer tells it is old, and conversely. The sum of these two rates will then be called age tracer contamination.

To measure these contaminations, we use a Markov Chain Monte Carlo (MCMC) simulation. Designed with a forward modeling method, the MCMC will look for the best correlation between the LsSFR and every other age tracer, based on what we expect from the litterature. Using the step cuts defined in the previous part (cf. 2), the contamination is the sum of the two off-diagonal data proportions on a plot age tracer versus LsSFR. Then we measure the age step obtained with each age tracer to clearly see the contamination influence.

In Figure 4, we can see the MCMC result using 9

age tracers in comparison with the LsSFR. Our sample contains 110 SNeIa from the Nearby Supernova Factory (SNf) catalog, which provide spectroscopic data leading to the LsSFR. The host galaxy photometric data, used for colors measurements, morphology classification and stellar mass, are extracted from the Sloan Digital Sky Survey (SDSS, DR12) catalog.

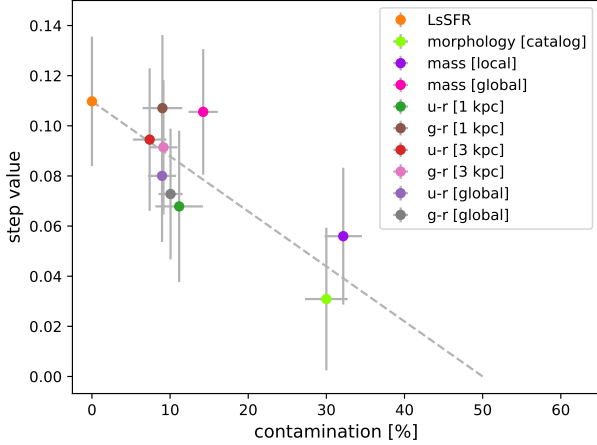


FIGURE 4: Age step values versus age tracer contaminations in comparison with the LsSFR. Each colored point correspond to an age tracer, described in the legend. Color and stellar mass tracers are studied with some radii : 1 kpc around SNeIa, 3 kpc, or globally for the whole host galaxy. The dashed grey line links the LsSFR point to 50% contamination at a zero age step value.

## 4 Conclusion

Simulating an increased contamination from LsSFR data, we observed a linear decreasing of the age step value until 50% contamination, for which the value reach zero. In Figure 4, we mainly observe the same effect. We already can conclude from this result that some age tracers are worse to trace the SNeIa progenitors than the LsSFR. It brings an explanation on why some age tracers are measuring age steps lower than LsSFR.

We can notice an outlier : the global mass. We discussed about this tool in Part 1.2, the global mass depend on many factors, including star ages. We expect from this tracer to be influenced by other parameters. Dust on the line of sight could be one of these other parameters, and will be studied during this PhD, thanks to Hubble Space Telescope (HST) pictures for  $\sim 70$  galaxies.

Using GALEX catalog, we will extend our age tracer list with colors  $NUV - r$  and  $FUV - r$ . Moreover, thanks to the Zwicky Transient Facility (ZTF) collaboration, we will have data provided for  $\sim 3000$  SNeIa ( $\sim 200$  nowadays).

The next step for this project is to go beyond the LsSFR reference assumption, considering it as an age

tracer like the others. The goal is to model the true SNeIa progenitor age using all the tracers by a MCMC simulation with the objective of finding the true age step. This final result could conclude on the correction to bring to the SNeIa standardization (cf. 3).

## Références

- [1] Whelan & Iben, 1973
- [2] Guy et al., 2007
- [3] M. Betoule, R. Kessler, J. Guy, et al., 2014, arXiv : 1401.4064
- [4] A. G. Riess, A. V. Filippenko, P. Challis, et al. , 1998, arXiv : astro-ph/9805201
- [5] S. Perlmutter, M. S. Turner, and M. White, 1999, arXiv : astro-ph/9901052
- [6] D. M. Scolnic, D. O. Jones, A. Rest, et al., 2018, arXiv : 1710.00845
- [7] P. Collaboration, P. A. R. Ade, N. Aghanim, et al., 2016, arXiv : 1502.01589
- [8] J. D. Neill, M. Sullivan, D. A. Howell, et al., 2009, arXiv : 0911.0690
- [9] P. L. Kelly, M. Hicken, D. L. Burke, et al., 2010, arXiv : 0912.0929
- [10] H. Lampeitl, M. Smith, R. C. Nichol, et al., 2010, arXiv : 1005.4687
- [11] M. Sullivan, A. Conley, D. A. Howell, et al., 2010, arXiv : 1003.5119
- [12] R. R. Gupta, C. B. D’Andrea, M. Sako, et al., 2011, arXiv : 1107.6003
- [13] M. J. Childress, G. Aldering, P. Antilogus, et al., 2013, arXiv : 1304.4720
- [14] M. Rigault, V. Brinnel, G. Aldering, et al., 2018, arXiv : 1806.03849
- [15] D. O. Jones, A. G. Riess, and D. M. Scolnic, 2015, arXiv : 1506.02637
- [16] M. Roman, D. Hardin, M. Betoule, et al., 2018, arXiv : 1706.07697
- [17] Y.-L. Kim, M. Smith, M. Sullivan, and Y.-W. Lee, 2018, arXiv : 1801.01192
- [18] D. O. Jones, A. G. Riess, D. M. Scolnic, et al., 2018, arXiv : 1805.05911
- [19] S. Salim, 2014, arXiv : 1501.01963
- [20] E. N. Taylor, A. M. Hopkins, I. K. Baldry, et al., 2011, arXiv : 1108.0635
- [21] K. Shimasaku, M. Fukugita, M. Doi, et al., 2001, arXiv : astro-ph/0105401
- [22] I. Strateva, Z. Ivezić, G. R. Knapp, et al., 2001, arXiv : astro-ph/0107201

# Backreaction of the infrared modes of scalar fields on de Sitter geometry

Gabriel Moreau  
*Université Paris Diderot*



## Résumé

We study the back-reaction of the infrared modes of an  $O(N)$  scalar theory in a classical de Sitter background. We use the nonperturbative renormalization group (NPRG) method to extract the flow of the Hubble constant as we integrate the gravitationally enhanced long wavelength modes. The scalar theory flows towards an effective zero dimensional theory for the super-horizon modes, which allows to perform analytical computations. For a massless theory, the interactions tend to renormalize negatively the Hubble constant, thus drawing energy from the classical gravitational field. This phenomenon saturates however, due to the generation of a mass.

## 1 Introduction

Studying quantum field in curved spacetime is a semi-classical approach motivated by the absence of a complete theory of quantum gravity [1]. Putting together general relativity and quantum fields is expected to be a good approximation for energies way below the Planck scale. Still, it allows to grasp some non-trivial gravitational effects when one consider more complicated geometries.

Among these effects is the production of particles in the presence of a strong gravitational field. It is similar to the Schwinger effect for charged particles in the presence of an electric field. The picture goes as follows. As the particle content is of quantum nature, its fluctuations produce virtual pairs which are driven apart when submitted to an external force and become real pairs. The particles are then expected to have a non trivial backreaction. For example, for charged particles, the electric field produced by the pair tends to oppose the external field. This backreaction is the effect that we want to compute in a particular gravitational setup.

The spacetime we are interested in is de Sitter spacetime in  $D = 4$  dimensions, defined as the Lorentzian sphere of radius  $1/H$  in  $D + 1 = 5$  dimensions, see Fig. 1. The reason for this choice is related to inflation, which is a postulated epoch in the history of the universe when it was in a phase of accelerated expansion. The inflationary universe is approximately described by de Sitter spacetime (more precisely a sub part called the expanding Poincaré patch). Studying the behavior of matter fields and their quantum corrections in such a universe is of primordial importance. The metric we will use is that of the expanding Poincaré patch, rele-

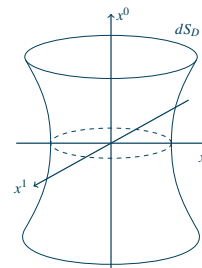


FIGURE 1: Representation of de Sitter spacetime for  $D = 2$ .

vant for our case, which reads in conformal coordinates  $ds^2 = a(\eta)^2(-d\eta^2 + d\vec{X}^2)$  with  $a(\eta) = -\frac{1}{\eta H}$ .  $H$  is the expansion rate and characterizes the speed at which two points are driven apart while the universe expands.

Large gravitational effects are expected to occur in the infrared or large wavelength regime (compared to  $H$ ), as opposed to the ultraviolet or small wavelength, which do not feel the curvature. As we will illustrate in section 2, it is the infrared modes of a scalar field that are gravitationally amplified as a signature of this particle production phenomenon.

It is also a known fact that the interaction of these amplified modes cannot be treated perturbatively [2, 3, 4, 5]. For example, take a scalar field with a  $\lambda\varphi^4$  term in its lagrangian. One could try to expand every physical quantity in the coupling constant  $\lambda$ , which is related to the strength of the interaction. However, such attempt is made difficult in de Sitter because one encounter infrared divergences which cannot be treated with the usual perturbative renormalization. We will need more sophisticated tools to deal with the interaction, and there exist already a number of possibilities [2, 5]. The one we use is the non perturbative renormalization group (NPRG) first used in a cosmological context in [6, 7, 8] and presented briefly in section 3.1.

Using this tool to study the interacting scalar field, we want to address the question of the backreaction due to the interaction of these amplified infrared modes and whether it can modify the curvature enough to relax de Sitter space to flat space. This is one aspect of a widely studied subject, namely de Sitter stability against quantum fluctuations, which has been studied in quite different contexts [9, 10, 11, 12]. A more detailed version of the computations presented in what follows can be found in [14].

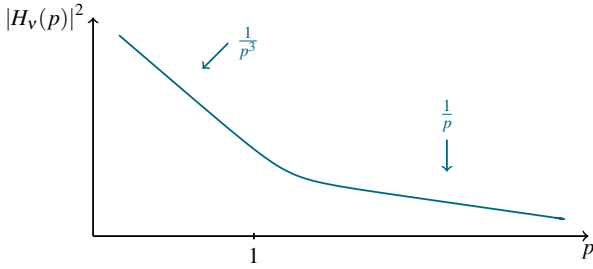


FIGURE 2: Mode occupation number for a free massive scalar field as a function of the physical momentum  $p = k/a$ . We took  $\nu = \frac{3}{2}$ .

## 2 Free scalar field in de Sitter spacetime and particle production

Let us first discuss how particle production actually occur in a simple computation for a free massive scalar field in a de Sitter geometry.

The theory is defined through the following action.

$$S = \int d^4x \sqrt{-g} \left( \frac{1}{2} \hat{\varphi} \square \hat{\varphi} - \frac{m^2}{2} \hat{\varphi}^2 \right) \quad (1)$$

The next steps to quantize such a theory is to decompose the field into modes by going to spatial Fourier space and impose the usual commutation relations to the  $a_k$  and  $a_k^\dagger$  operators. Here, as stated before, we use the conformal coordinates, which means that we work with the comoving momentum  $\vec{k}$ . The mode function, the time dependent coefficient in front of the creation and annihilation operators, can be computed by solving the Klein-Gordon equation  $(-\square + m^2)\hat{\varphi} = 0$ , with a modified box operator

$$\square = \frac{1}{a(\eta)} \left( -\partial_\eta^2 + \frac{2}{\eta} \partial_\eta + \partial_X^2 \right). \quad (2)$$

We get the following decomposition for the scalar field

$$\hat{\varphi}(\eta, \vec{X}) \sim \int \frac{d^3k}{(2\pi)^3} \left( e^{i\vec{k} \cdot \vec{X}} H_\nu \left( \frac{k}{a(\eta)} \right) a_k + \text{h.c.} \right) \quad (3)$$

with  $\nu = \sqrt{\frac{9}{4} - \frac{m^2}{H^2}} \approx \frac{3}{2}^1$  and  $H_\nu(p)$  the Hankel function of the first kind. This mode function coincide with the flat space result for high energies (i.e. high values of the physical momentum  $p = k/a$  in units of  $H$ ). However it has a higher modulus in the infrared regime  $p < 1$ , meaning that the mode occupation number for the infrared modes is amplified, see Fig. 2. In a more general field theory, these enhanced modes will possibly interact. What we want to compute is the backreaction due to such modes interaction.

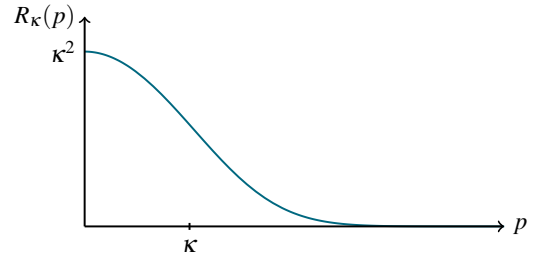


FIGURE 3: Typical regulator function as a function of the physical momentum.

## 3 Getting to the modified Friedman equation

### 3.1 Non perturbative renormalization group

To do this we need some more sophisticated tools than the usual perturbative approach and we will use the NPRG. Let us define the functionals  $\mathcal{W}[j, g]$  and  $\Gamma[j, g]$  for an arbitrary scalar theory

$$e^{i\mathcal{W}[j, g]} = \int \mathcal{D}\hat{\varphi} e^{iS[\hat{\varphi}, g] + i \int j \hat{\varphi}} \quad (4)$$

and  $\Gamma[\varphi, g] = \mathcal{W}[j, g] - j \cdot \varphi$ . Derivatives of  $\mathcal{W}[j, g]$  with respect to  $j$  generate the correlation functions of the theory.  $\Gamma[\varphi, g]$  is called the effective action, it depends on the classical field  $\varphi = \langle \hat{\varphi} \rangle$  and contains all the information of the theory (its derivatives generate the so-called vertex functions which form an equivalent set to the correlation functions).

The NPRG consists in defining a continuum of theories by adding a regulator to the action  $S$  which depends on a mass scale  $\kappa$  that we will vary

$$i\Delta S_\kappa[\hat{\varphi}, g] = i \int_{x, y} R_\kappa(x, y) \hat{\varphi}(x) \hat{\varphi}(y). \quad (5)$$

This regulator is a mass term which effectively freezes the quantum fluctuations of the modes below this scale  $\kappa$ . Indeed, the  $R$  function is chosen so that it gives a mass of order  $\kappa^2$  to the modes of energy below  $\kappa$ , see Fig. 3.

Again we define the effective action for each value of the regulating scale  $\Gamma_\kappa[\varphi, g] = \mathcal{W}_\kappa[j, g] - j \cdot \varphi - \Delta S_\kappa[\varphi, g]$ . The functional  $\Gamma_\kappa$  interpolates between the microscopic action  $\Gamma_{\kappa \rightarrow \infty} = S$  and the full effective action  $\Gamma_{\kappa \rightarrow 0} = \Gamma$  as we take into account more and more quantum fluctuations.

The variation of the effective action is described by the so called Wetterich equation [13]

$$\partial_\kappa \Gamma_\kappa = \frac{i}{2} \text{tr} \left\{ \partial_\kappa R_\kappa (\Gamma_\kappa^{(2)} + R_\kappa)^{-1} \right\} \quad (6)$$

where  $\Gamma^{(2)}$  is the second derivative of the effective action with respect to the scalar field.

So far, the metric  $g$  has been left unspecified. The idea is now to compute it at each scale to see how it

1. We consider small masses compared to  $H$  in the following

varies as we integrate more and more quantum fluctuations. The physical value of the scalar field and the metric are specified as the minima of the effective action

$$\frac{\delta\Gamma_\kappa}{\delta\varphi} = 0, \quad \frac{\delta\Gamma_\kappa}{\delta g^{\mu\nu}} = 0. \quad (7)$$

Notice that the second equation can be written as the semi-classical Einstein equation

$$G_{\mu\nu}^\kappa = \langle T_{\mu\nu}^\kappa \rangle \quad (8)$$

As an additional assumption, we project all this on a de Sitter metric, with a de Sitter invariant quantum state and constant  $\varphi$ . This leaves only one degree of freedom  $H$ , and we are able to compute how it is renormalized (i.e. modified by the backreaction of the scalar field fluctuations). This is a strong assumption as it forbids us to capture more general metric fluctuations, but it allows us to compute analytically and non-pertubatively part of the effect as it preserves the de Sitter symmetries.

### 3.2 Dimensional reduction

In order to solve the Wetterich equation (6), we can make some additional assumptions. As illustrated in the case of the free scalar field, the enhanced modes are the infrared modes, so we will restrict ourselves to the infrared regime  $\kappa \ll H_\kappa$ . We also want these modes to fluctuate so they should have a small mass, i.e. the potential has to have a small curvature, compared to  $H_\kappa$ . The last hypothesis we make is to take an ansatz for the effective action. Instead of taking a general functional we discard all derivative interactions, which are expected to be subdominant in the infrared, and restrict our computation to the effective potential<sup>2</sup>. This is the so called local potential approximation.

In the end, the solution of the flow is a zero-dimensional theory, which means that we can compute physical quantities from a simple integral [8]. In the case of  $N$  scalar fields with an  $O(N)$  symmetry one gets the following generating function for the expectation values

$$e^{\mathcal{V}W_\kappa(j,h)} = \int d^N\hat{\varphi} e^{-\mathcal{V}(V_{in}(\hat{\varphi},h) + \frac{\kappa^2}{2}\hat{\varphi}^2 - j\cdot\hat{\varphi})} \quad (9)$$

with  $\mathcal{V} = \frac{8}{3}\pi^2 H^{-4}$  a volume factor. This should be seen as an effective theory for the scalar field averaged over a Hubble patch (i.e. a spacial region of extension  $1/H$ ), and coincides with the equilibrium probability distribution obtained in the stochastic formalism [2]. The information from the high energy theory is encoded in the potential  $V_{in}$ , which is an initial condition for the flow equation ( $V_{in}$  is the effective potential at the scale  $H$ ).

We choose for  $V_{in}$  the following form

$$V_{in}(\hat{\varphi}, h) = N \left( \alpha - \frac{\beta}{2} H^2 \right) + \frac{\lambda}{8N} (\hat{\varphi}_a^2)^2. \quad (10)$$

<sup>2</sup> the effective potential  $V(\varphi, g)$  is defined as the effective action for constant values of the field up to a volume factor  $\Omega$ ,  $\Gamma[\varphi, g]|_{\varphi=cst.} = \Omega V(\varphi, g)$

corresponding to  $N$  massless interacting scalar fields. The parameters  $\alpha$  and  $\beta$  are related to the usual gravitational quantities through  $\alpha = \Lambda M_P^2$  (cosmological constant term) and  $\beta = 12M_P^2$  (scalar curvature term) with  $M_P$  the Planck mass. The factors of  $N$  are here to ensure the good scaling of the different coupling at large  $N$  (see below section 4).

The equations (7) become

$$\begin{cases} \varphi_{a,\kappa} = \langle \hat{\varphi}_a \rangle \\ H_\kappa^2 = \frac{4\alpha}{\beta} + \frac{2\kappa^2}{N\beta} (\langle \hat{\varphi}^2 \rangle - \varphi_\kappa^2) + \frac{\lambda}{2\beta N^2} \langle (\hat{\varphi}^2)^2 \rangle \end{cases} \quad (11)$$

where the expectation values are to be computed with the generating function (9) at  $j = 0$  and contain implicit dependence on both  $\varphi_\kappa$  and  $H_\kappa$ . Notice that the second equation is the Friedman equation with  $4\alpha/\beta$  the classical solution to which one adds quantum corrections.

## 4 Analytic results for large $N$

Solving Eqs. (11) can be easily done by numerical computation of the expectation values. However we can gain some insight by considering the regime when  $N$  the number of scalar fields becomes large, as in this case everything can be computed analytically. In the massless case that we took for the initial condition (10), the  $O(N)$  symmetry is not broken, the minimum for  $\varphi_{a,\kappa}$  sits at zero. The second equation of (11) can now be written as

$$H_\kappa^2 = \frac{4\alpha}{\beta} + \frac{H_\kappa^4}{\beta\Omega} \left( 1 + \frac{\kappa^2}{m_{t,\kappa}^2 + \kappa^2} \right) \quad (12)$$

where the mass  $m_{t,\kappa}$  can be expressed as

$$m_{t,\kappa}^2 = -\frac{\kappa^2}{2} + \sqrt{\frac{\kappa^4}{4} + \frac{\lambda H^4}{2\Omega}}. \quad (13)$$

This equation has no implicit dependence on  $H$  anymore, and we can solve for the ultraviolet ( $\kappa \rightarrow \infty$ ) and infrared ( $\kappa \rightarrow 0$ ) asymptotic values

$$H_\infty^2 = \frac{\beta\Omega}{4} \left( 1 - \sqrt{1 - \frac{32\alpha}{\beta^2\Omega}} \right) \approx \frac{4\alpha}{\beta} + \frac{2}{\beta\Omega} \left( \frac{4\alpha}{\beta} \right)^2 + \dots \quad (14)$$

$$H_0^2 = \frac{\beta\Omega}{2} \left( 1 - \sqrt{1 - \frac{16\alpha}{\beta^2\Omega}} \right) \approx \frac{4\alpha}{\beta} + \frac{1}{\beta\Omega} \left( \frac{4\alpha}{\beta} \right)^2 + \dots \quad (15)$$

The full flow is represented on Fig. 4 along with some finite values of  $N$  and one sees that the general features are well captured by the large  $N$  computation.

Several comments can be made. First,  $H_\kappa$  decreases along the flow. This means that the enhanced interacting modes tend to draw energy from the gravitational field, as anticipated.

Also, the flow saturates at a finite value. This says that de Sitter geometry is stable against the type of quantum perturbation that we are considering here, as it does not blow up or tend to zero. In fact, the high

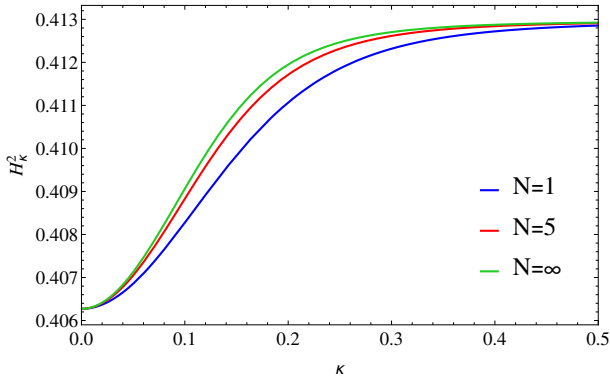


FIGURE 4: Flow of  $H_\kappa^2$  as  $\kappa$  goes to 0. The parameters are chosen are set to  $\lambda = 0.1$ ,  $\alpha = 0.1$   $\beta = 1$ . The flow is computed for three values of  $N$  and one sees that it keeps similar features. It always saturates at a finite value.

energy value is renormalized by a quantity of order  $\frac{\alpha}{\beta^2}$  which is small by assumption in our semi-classical framework.

Looking at the Friedman equation (12) one understands the role played by the mass  $m_{t,\kappa}$ . Indeed, this quantity is the effective mass of the scalar field at a given scale  $\kappa$ . Starting from a zero value for high  $\kappa$ , one sees that a mass is generated by the interaction, as when  $\kappa$  goes to zero it becomes proportional to  $\sqrt{\lambda}$ . This screens the renormalization in the infrared as it freezes the fluctuations as soon as  $\kappa$  becomes lower than the generated mass.

One last comment we can make is that, having regulated the theory with a mass term, one can make a perturbative computation for a finite scale  $\kappa$  and compute a flow at some finite loop order. As expected, such a flow diverges when  $\kappa$  goes to zero see Fig. 5. A one loop computation appears to be misleading as it seems to indicate the relaxation of de Sitter spacetime towards flat space. However the phenomenon at hand is deeply non perturbative : the expansion parameter is non simply  $\lambda$  the coupling constant but  $\frac{\lambda H_\kappa^4}{\kappa^4}$ , which shows that the expansion breaks down at small  $\kappa$ .

## 5 Conclusion

In conclusion, the we studied the backreaction of the gravitationally amplified infrared modes for massless interacting scalar fields. We used the NPRG to circumvent problems encountered in usual perturbative computations. The relaxation of de Sitter that one could expect from one loop computation appears to saturate due to the dynamical mass generation, which is an intrinsically non perturbative phenomenon.

So far, however, this does not solve entirely the question of de Sitter stability. Indeed, we made some assumptions to preserve de Sitter symmetries, such as imposing a de Sitter invariant state, and constraining the geometry. It could be interesting to repeat this study in a more general spacetime such as Friedman-Lemaitre-Robertson-Walker spacetime, as this has not yet been

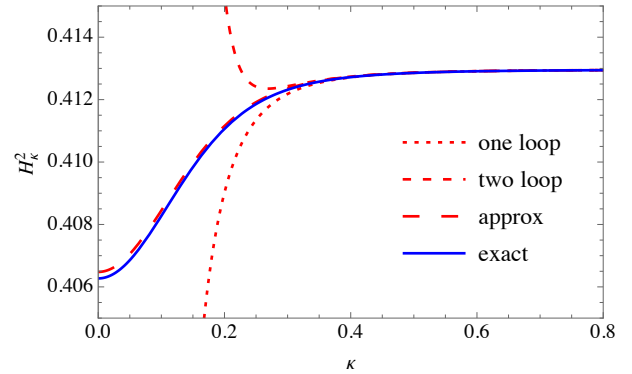


FIGURE 5: Flow of  $H_\kappa^2$  as computed with the NPRG or with perturbative computations. The parameters are set to  $\lambda = 0.1$ ,  $\alpha = 0.1$  and  $\beta = 1$ . The perturbative computation breaks down quickly and that one needs to take all loops into account to see the saturation. The “approx” curve refers to a first order development in the semi-classical regime controlled by  $\frac{\alpha}{\beta^2}$ .

studied.

## 6 Acknowledgments

This work was realized under the supervision of my PhD advisor Julien Serreau.

## Références

- [1] N. D. Birrell and P. C. W. Davies, doi :10.1017/CBO9780511622632
- [2] A. A. Starobinsky, J. Yokoyama, Phys. Rev. D **50** (1994) 6357.
- [3] N. C. Tsamis and R. P. Woodard, Nucl. Phys. B **724** (2005) 295.
- [4] S. Weinberg, Phys. Rev. D **72** (2005) 043514; Phys. Rev. D **74** (2006) 023508.
- [5] C. P. Burgess, R. Holman, L. Leblond and S. Shandera, JCAP **1010** (2010) 017
- [6] J. Serreau, Phys. Lett. B **730** (2014) 271.
- [7] A. Kaya, Phys. Rev. D **87** (2013) 123501
- [8] M. Guilleux and J. Serreau, Phys. Rev. D **92** (2015) 084010. Phys. Rev. D **95** (2017) 045003.
- [9] A. M. Polyakov, Nucl. Phys. B **797** (2008) 199; Nucl. Phys. B **834** (2010) 316; arXiv :1209.4135 [hep-th].
- [10] E. Mottola, Phys. Rev. D **31** (1985) 754.
- [11] I. Antoniadis, J. Iliopoulos and T. N. Tomaras, Phys. Rev. Lett. **56** (1986) 1319.
- [12] V. F. Mukhanov, L. R. W. Abramo and R. H. Brandenberger, Phys. Rev. Lett. **78** (1997) 1624
- [13] C. Wetterich, Phys. Lett. B **301** (1993) 90.
- [14] G. Moreau and J. Serreau, Phys. Rev. Lett. **122** (2019) no.1, 011302, Phys. Rev. D **99** (2019) 025011

Huitième partie

Astrophysics

session dirigée par Julien MASBOU



# Étude des sources gamma HESS J1640.6-4633 et HESS J1641.0-4619

Arnaud Mares

Centre d'Etude Nucléaire de Bordeaux-Gradignan, Gradignan

## 1 Introduction

C'est au début du  $XX^{eme}$  siècle que l'on découvre qu'un flux constant de particules chargées pouvant atteindre des énergies phénoménales bombarde l'atmosphère terrestre. Ces particules, appelées rayons cosmiques, sont issues des événements les plus violents de l'univers. En effet, ces particules sont accélérées au sein d'onde de choc non collisionnel telle que les vestiges de supernova, ou encore dans les champs magnétiques des nébuleuses à vents de pulsar. Ces particules, accélérées jusqu'à des vitesses relativistes, interagissent de multiples façons dans le milieu interstellaire, interactions se traduisant par un rayonnement de hautes énergies. Ainsi, un électrons relativiste va rayonner par effet synchrotron le long des lignes de champ magnétique ou par interactions inverse Compton sur les champs de photons environnant. Un proton va lui interagir sur les nuages de gaz interstellaire en produisant des pions qui se désintègrent en photon. L'astronomie gamma est un outil puissant permettant d'étudier ces événements et les mécanismes d'accélération de ces particules.

## 2 Présentation de l'instrument et des sources

### 2.1 Le LAT

Le nouveau et ultime format des données du LAT du satellite Fermi, appelé *pass8* [W.atwood & all, 2012], fournit de nombreuses améliorations par rapport au format précédent. Cette nouvelle base de données est considérée comme la meilleure pour tous types d'analyses, notamment grâce à une augmentation de l'intervalle en énergie jusqu'à 3 TeV permettant l'observation de sources de très haute énergie de façon plus efficace grâce une mesure plus précise de l'énergie des photons. Les différentes sources gamma sont observées avec davantage de statistiques, notamment grâce à l'augmentation de la surface efficace de détection du LAT de 5 à 10% au-dessus de 1 GeV.

Le LAT enregistre le passage de photons gamma et en déduit leur énergie ainsi que leur provenance probable à l'aide de différents algorithmes. Ces informations sont ensuite envoyées sur terre pour être analysées. Un ensemble d'outils permettant l'analyse de ces données a été développé par la NASA en même temps que les détecteurs et optimisé au cours de la mission. Ces outils forment une chaîne permettant un traitement



FIGURE 1: Le satellite Fermi avec le LAT (partie blanche)

complet des données, de la sélection des événements qui nous intéressent à la génération de cartes, jusqu'à la fabrication d'un modèle contenant les sources gamma d'une région donnée du ciel. Ce modèle permet de mettre en évidence de nouvelles sources et, par la suite, permet de remonter aux mécanismes ayant produit le rayonnement gamma observé en utilisant une méthode de maximum de vraisemblance.

### 2.2 Présentation des sources

HESS J1640-465 est une source gamma de haute énergie découverte par *H.E.S.S.*<sup>1</sup> en 2006 et détectée peu après par le LAT du satellite Fermi [Slane et al. 2010].

HESS 1641-463 est une source gamma de très haute énergie et située à  $0.25^\circ$  de J1640. Cette source n'a tout d'abord pas été détectée, car sa luminosité est noyée dans celle de J1640 pour une large bande en énergie [H.E.S.S. Collaboration, 2014]. Ce n'est qu'à très haute énergie qu'elle se démarque comme une source à part entière. En effet pour des énergies de l'ordre du TeV, elle émet bien plus de photons que J1640 (son spectre pour des énergies supérieures au TeV est plus dur que celui de J1640).

Quelle soit observée par H.E.S.S ou par Fermi, J1641 ne semble pas avoir d'extension spatiale. Elle est considérée comme ponctuelle car la prise en compte

1. H.E.S.S (High Energy Stereoscopic System) [Aharonian et al. 2006b] est un réseau de télescopes à imagerie Tcherenkov situé en Namibie permettant l'observation de sources de rayonnements gamma de très hautes énergies.

d'une extension spatiale dans les analyses n'améliore pas le modèle de façon significative.

L'analyse du milieu environnant ces deux sources et les caractéristiques de l'absorption du HI (hydrogène neutre) ont permis de contraindre la distance des deux sources à (8-13) kpc [Lemiere et al. 2009].

## 2) Origines du rayonnement gamma/scenarii

Le rayonnement gamma de haute énergie et le rayonnement X de J1640 ont d'abord été interprétés comme l'émission Compton inverse (sur des photons du fond diffus cosmologique<sup>2</sup> ou d'étoile proche) et l'émission synchrotron d'électrons relativistes accélérés dans le champ magnétique d'une PWN associée à la SNR G338.3-0.0 [Funk et al. 2007; Lemiere et al. 2009; Slane et al. 2010] corrélé à J1640. Le scénario hadronique, qui consiste quant à lui à la production de photons gamma par la désintégration de pions neutres créés par l'interaction proton-proton, a été jugé improbable à l'époque de la première publication car il nécessite une densité très élevée du milieu interstellaire [H.E.S.S. collaboration, 2014].

En supposant une corrélation (spatiale) entre J1640 et J1641, le rayonnement gamma de très haute énergie de J1641 peut être expliqué en considérant que les protons d'énergie la plus élevée s'échappent de la zone d'accélération et interagissent avec le nuage moléculaire situé à la même position que J1641, d'où un spectre plus dur que J1640 à haute énergie. Cependant, seule une jeune supernova est capable d'accélérer les protons au-delà de la dizaine de TeV. Cela pourrait indiquer que ce sont les jeunes supernovæ qui sont responsables d'une partie du flux de rayons cosmiques dans la galaxie puisque J1641 est l'une des sources HESS la plus brillante au dessus de 1 TeV.

## 3) Discussion

Aucun des deux scénarios ne semble s'imposer de lui-même, les modélisations actuelles des spectres des deux sources ne permettant pas de contraindre le mécanisme de production du rayonnement gamma, hadronique ou leptonique. De plus, la séparation angulaire de ces deux sources est assez faible, et leur causalité est une simple hypothèse, sans autre argument physique que la mise en évidence d'une faible contrepartie observée en radio et semblant les relier.

L'analyse de ces deux sources est difficile car elles sont situées dans le plan galactique et dans une région possédant un grand nombre de sources gamma. Ainsi, même si les sources environnantes sont bien reproduites/approximées dans le modèle servant à l'analyse, limitant ainsi la contamination des signaux provenant de J1640 et J1641, la présence du diffus galactique détériore énormément les statistiques de ces sources à

basse énergie. En effet, la galaxie est baignée dans un rayonnement gamma intense de basse énergie compris entre 100MeV et 1GeV, provenant de l'interaction des rayons cosmiques avec les photons et les noyaux du milieu interstellaire pendant leur propagation à travers la galaxie. A ce jour, le diffus galactique n'est pas parfaitement modélisé. En effet, le modèle de rayonnements diffus utilisé dans *pass8* consiste en une analyse en maximum de vraisemblance du ciel dans lequel on a retiré toutes les sources gamma. Cependant, en plus d'être rétroactif<sup>3</sup>, l'ajustement des différents paramètres des différents processus de rayonnement<sup>4</sup> ne convergent pas, surtout à basse énergie. Ainsi, le modèle de diffus actuelle possède des structures artificielles qui peuvent détériorer les sources.

L'étude de ses sources est très importante car si la preuve est faite que c'est une région d'accélération de protons efficace, alors ce sont peut-être des sources contribuant significativement au flux de rayons cosmiques que l'on observe. Au vu de son spectre sans cassure à haute énergie, J1641 pourrait même être un des rares PeVatron de la galaxie [H.E.S.S. Collaboration, 2014] et ainsi contribuer au « genou »<sup>5</sup> du digramme du spectre du rayonnement cosmique.

## 3 Résultat

Pour la première fois, l'extension spatiale de J1640 a été vue et mesurée de manière significative en utilisant les données du LAT. Une extension  $0.05^\circ \pm 0.015^\circ$  est mesurée au dessus 1GeV avec un  $TS_{ext}=17$ . Ce n'est pas meilleur que l'extension vue par HESS, donc nous utilisons l'extension et la position de HESS ( $0.07^\circ$ ) pour notre analyse.

Dans notre modèle, nous avons pris en compte toutes les sources gamma dans une zone de  $20^\circ * 20^\circ$  autour de nos sources. L'algorithme de *gtlike* ne peut travailler au maximum de vraisemblance que pour un maximum de 100 degrés de liberté. Notre région est très peuplée en sources gamma donc à sa localisation, il nous est donc impossible d'ajuster toutes les sources présentes à l'intérieur des  $20^\circ * 20^\circ$ . Ainsi, nous avons laissé libre le préfacteur et l'indice spectral (ou indice et la courbure) des sources dans une zone de  $4^\circ$  autour du centre de notre région d'intérêt.

3. la connaissance du diffus permet de trouver des nouvelles sources qui permettent de modifier le diffus ect

4. synchrotron, inverse Compton, bremsstrahlung

5. changement dans l'indice du spectre à  $5 * 10^{15}$  eV, une particule par an par  $m^2$

2. CMB pour Cosmic Microwave Background

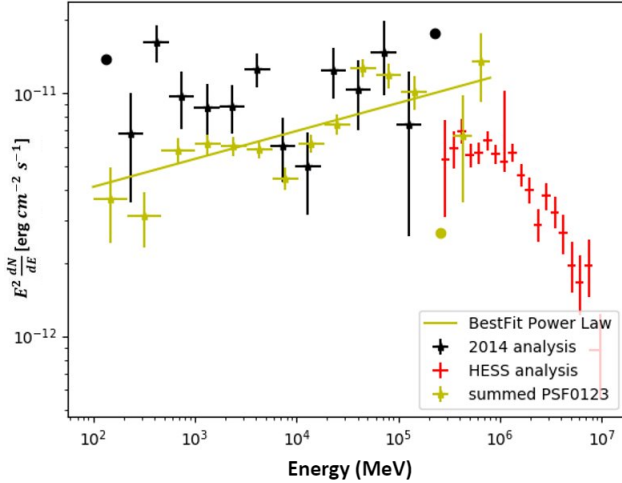


FIGURE 2: *Figure 5 : Distribution spectrale en énergie de la source J1640. Les points et les triangles correspondent respectivement aux données Fermi et H.E.S.S. Le meilleur ajustement des données Fermi est représenté par la ligne jaune.*

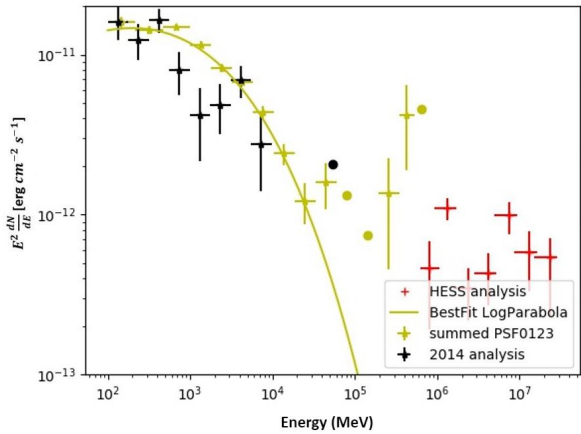


FIGURE 3: Distribution spectral en énergie de la source J1641

La source J1641 est vue avec une courbure significative qui n'était pas détecté dans les analyses précédente. Un tel spectre ressemble beaucoup à un spectre de pulsar.

Le raccord entre les points Fermi et HESS est très étrange. Il est possible qu'il soit nécessaire d'ajouter une deuxième composante pour interpréter les points HESS de très haute énergie. Il est également possible que Fermi et HESS ne détecte pas la même source, ce qui expliquerait le mauvais raccord entre leurs points.

Une sed multi- $\lambda$  de J1641 n'est pas envisageable car aucune contrepartie dans le domaines X ou radio n'a été observée à ce jour. De plus, il est difficile d'expliquer le spectre des points Fermi et celui des points HESS. Il semble y avoir deux composantes distinctes. De plus, si le scénario leptonique est l'explication du rayonnement de J1640, alors J1641 est à ce jour une source non identifiée mais

toujours candidate comme un Pévatron dans la galaxie.

## 4 Conclusion

L'astronomie gamma permet une étude indirecte des processus d'accélération des particules à l'origine des rayons cosmiques. Les sources gamma J1640 et J1641, situées dans le plan galactique, sont candidates comme accélérateurs de protons de hautes énergies. Les résultats obtenus pendant ce stage ont cependant montré que le scénario hadronique par échappement de proton, permettant d'expliquer le rayonnement de ces deux sources, ne semble pas reproduire les données multi-longueur d'onde observées. Dans ce scénario, des protons sont accélérés dans le résidu de supernova SNR G338.3-0.0 puis interagissent avec un nuage moléculaire situé dans la partie nord de la SNR et par désintégration du pion, serait à l'origine du rayonnement gamma de J1640. Les protons les plus énergétiques quant à eux s'échappent de la zone d'accélération et interagissent avec un autre nuage moléculaire situé à la position de J1641, ce qui expliquerait son spectre extrêmement dur dans les très hautes énergies.

Les résultats présentés ci-dessus remettent en question les précédentes analyses et les conclusions effectuées par la communauté Fermi qui favorisait un scénario hadronique. Le rayonnement de J1640 serait de source leptonique, par accélération d'électrons à l'intérieur d'une PWN âgée possédant un faible champ magnétique plutôt que par l'accélération de protons au niveau de l'onde de choc de la SNR.

Les analyses effectuées pendant ce début de thèse ont été réalisées dans un intervalle en énergie allant de 100MeV à 1TeV et en utilisant le catalogue de source préliminaire des 8ans du LAT. Nous sommes en train de réaliser une nouvelle analyse en utilisant le catalogue de sources définitive de la collaboration (le 4FGL), ainsi que tout les changements et améliorations effectuées sur le rayonnement diffus de la galaxie.

## Références

- [1] Atwood, Albert et al : Pass 8 : Toward the Full Realization of the Fermi-LAT Scientific Potential. the Fermi Symposium : Monterey, CA : 28 Oct-2 Nov 2012
- [2] Condon : Observations de vestiges de supernovae en coquille avec le Fermi Large Area Telescope. Thèse au CENBG, 2017
- [3] S. Funk <sup>1,2</sup>, J. A. Hinton <sup>3</sup>, G. Pöhler et al. : XMM-Newton Observations Reveal the X-Ray Counterpart of the Very High Energy Gamma-Ray Source HESS J1640-465. *The Astrophysical Journal*, 662 :517-524 (2007)
- [4] Gotthelf, J.A Tomsick et al. : NuSTAR discovery of a young, energetic pulsar associated with the luminous gamma-ray source HESS J1640-465. *The Astrophysical Journal*, 788 :155(8pp) (2014)
- [5] H.E.S.S. Collaboration, A. Abramowski, F.Aharonian et al : HESS J1640-465-an exceptionally luminous TeV  $\gamma$ -ray supernova remnant. H.E.S.S. Collaboration (2014)
- [6] H.E.S.S. Collaboration, A. Abramowski, F.Aharonian et al. : Discovery of the hard spectrum VHE  $\gamma$ -ray source HESS J1641-463. H.E.S.S. Collaboration (2014)
- [7] Lau, Rowell, Burton et al : Interstellar gas towards the TeV gamma-ray sources HESS J1640-465 and HESS J1641-463. arXiv :1610.05444 [astro-ph.HE] (2016)
- [8] Lemiére, Slane et al : High-resolution X-ray Observations of the Pulsar Wind Nebula Associated with the Gamma-ray Source HESS J1640-465. *The Astrophysical Journal*, Volume 706, Issue 2, pp. 1269-1276 (2009)
- [9] M.Lemoine-Goumard, M.-H. Grondin et al : HESS J1640-465 and HESS J1641-463 : two intriguing TeV sources in the light of new Fermi LAT observation. *Not to appear in NonLearned J.*, 45. 2014)
- [10] Mattana, Falanga, Götz et al : The Evolution of the  $\gamma$ - and X-Ray Luminosities of Pulsar Wind Nebulae. *The Astrophysical Journal*, Volume 694, Issue 1, pp. 12-17 (2009)
- [11] Slane, Castro, Funk et al : Fermi Detection of the Pulsar Wind Nebula HESS J1640-465. *The Astrophysical Journal*, Volume 720, Issue 1, pp. 266-271 (2010)
- [12] Patrick Slane : Pulsar Wind Nebulae. Author version of chapter for 'Handbook of Supernovae, edited by A. Alsabti and P. Murdin, Springer (2017)
- [13] Rochester et al : Upgrades to the Event Simulation and Reconstruction for the Fermi Large Area Telescope. Fermi Symposium, Washington, D.C., Nov 2-5 (2009)
- [14] <http://www.slac.stanford.edu/exp/glast/groups/canda/lat-Performance.html>
- [15] Whiteoak & Green : The Most supernova remnant catalogue *Astrin. Astrophys. Suppl. Ser.* 118, 329-380 (1996)
- [16] Xin, Liao, Guo et al : HESS J1640-465 - A gamma-ray emitting pulsar wind nebula ? arXiv :1802.03520 [astro-ph.HE] (2018)

# Variability of Active Galactic Nuclei at Very High Energy with H.E.S.S.

Gabriel Emery

*Sorbonne Université, Université Paris Diderot, Sorbonne Paris Cité, CNRS/IN2P3,  
Laboratoire de Physique Nucléaire et de Hautes Energies, LPNHE, 4 Place Jussieu,  
F-75252 Paris, France*

## Résumé

Active Galactic Nuclei (AGN) are powerful photon and particle emitters located at the center of some galaxies. It is currently commonly accepted that such sources are made of a central super massive black hole, around which accretion processes take place and in some cases relativistic jets are present. Photons emitted by the jets reach very high energies, with both emission processes and acceleration processes of the emitting particles being largely unknown. A better understanding can come from the study of variability of the jet emissions and would affect multiple domains : very high energy physic, neutrinos, (ultra high energy) cosmic rays, ...

The presented work was made in the H.E.S.S. experiment, an array of Cherenkov telescopes located in Namibia. It present the studies of flaring state of multiple AGN in a multi-wavelength program of “Target of Opportunity”.

## 1 Introduction

Astrophysical studies are important in better understanding our Universe. Phenomenon can be observed without equivalent on Earth : particles at energies impossible to produce in man-made accelerators, extreme densities, long range interactions, ... All of this happens in giant engines and laboratories such as stars, galaxies and compact objects. Thank to the finite speed of all particles, observing far in the Universe is also observing in the past of the Universe. Hence, it is possible to study the evolution of the content of the Universe as well as the evolution of the law of physics.

Astrophysics faces multiple limitations. First we have no control over the input parameters of what we observe. An unknown source, inside an unknown environment, exists and sends us continuous or punctual signal from which we have to deduce as much as possible. Then comes the non-repeatability of the experiments. If we missed an event, we may never be able to observe something equivalent ever, and we also can not repeat observations, limiting the reach of statistical studies. Finally there are also heavy observational constraints. From each event we can only observe the part of signal that reaches us : directional emissions need to point toward us, the signal needs to neither be absorbed nor deviated and must live long enough. At last, the detection of the particles can be challenging, as well as the reconstruction of their interesting properties.

In the following, the subject will be focused on AGNs which are powerful extragalactic sources, and their observation with photons at very high energies with H.E.S.S.

## 2 Very High Energy Astronomy

### 2.1 Detection of high energy signal

Powerful sources in the Universe are expected to be observed through three specific outputs at high energy : cosmic rays (proton, electron,...), photons and neutrinos. Deviation of charged particles over cosmic distance by magnetic fields makes it impossible to point back to the source of those particles. Neutrinos and photons are not deviated this way but the low interaction of neutrinos make them difficult to detect while the photons are more likely to be stopped (Figure 2).

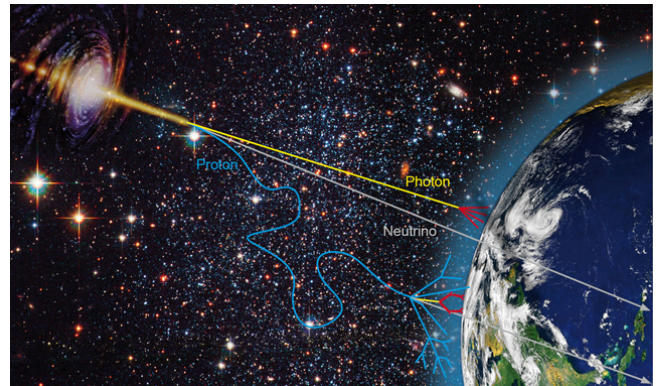


FIGURE 1: Particles travels depending on their nature

Depending on the photon energy, Earth atmosphere is more or less transparent to light (Figure 3). At high energy (HE, 100 MeV to 100 GeV) and very high energy (VHE, >100 GeV), photon interactions make direct detection on the ground impossible. In case of high energy photons, a solution is to send satellites outside of the atmosphere. One such detector is Fermi-LAT which offers a full sky coverage as seen on Figure 4. At very high energy, the fluxes are too low for such detectors [1] and other techniques must be used.

### 2.2 High Energy Stereoscopic System

An IACT (Imaging Atmospheric Cherenkov Telescope) is a detector using the interaction of the VHE photons in the atmosphere to indirectly detect them.

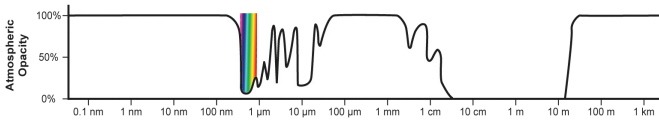


FIGURE 2: Opacity of the atmosphere depending on wavelength, Credit : NASA

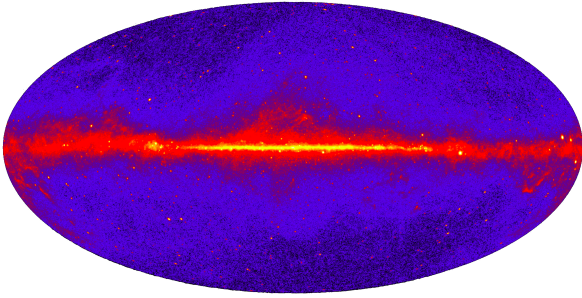


FIGURE 3: Sky map obtained with 9 years of observations with Fermi-LAT at High Energy, Credit : NASA/DOE/Fermi LAT Collaboration

One VHE photon reaching the atmosphere will interact, creating an electron/positron pair. These electron and positron will then emit Bremsstrahlung photons still energetic enough to create new pairs. This process will repeat, creating an electromagnetic shower in the atmosphere. The energy of the original photon is so important that a large part of the electromagnetic shower will contain electrons and positrons whose speed is higher than the speed of light in the air, leading to the emission of Cherenkov light. It is this Cherenkov light that is detected by the IACT and used to reconstruct the original photon (Figure 5). Charged cosmic rays entering the atmosphere will also produce Cherenkov light acting as an overwhelming background for IACTs observation. Most of the background associated with hadrons can be rejected using discrimination on the morphological differences of electromagnetic and hadronic air showers.

The High Energy Stereoscopic System (H.E.S.S.) is an array of 5 telescopes located in Namibia. It is the only IACT of the current generation (including MAGIC and VERITAS) located in the southern hemisphere. The location has been chosen to minimize light pollution, and at an altitude of 1800m, which leaves enough atmosphere above the telescope for the shower to develop, while limiting the additional height where it would be attenuated. H.E.S.S. was built in two steps, first four telescopes installed between 2002 and 2004 with 12 meters diameter mirrors and then a 28 meters diameter mirror telescope in 2012. Multiple telescopes are necessary for the use of stereoscopic reconstruction, allowing for a better shower reconstruction and discrimination between electromagnetic and hadronic showers than with a single telescope (Figure 5). The addition

of a bigger telescope allowed for a lower energy threshold, reaching the high energy limit of HE detectors like Fermi-LAT.

H.E.S.S. has a field of view of  $3^\circ$  diameter for the large telescope and  $5^\circ$  diameter for the smaller ones, and was built to point anywhere in around 50 seconds to minimize the lost observation time when changing the area of the sky observed. High resolution cameras are used to discriminate between photons and protons using the differences in morphology of the associated shower and Cherenkov light, and to obtain more precise images of the electromagnetic showers. In the end, H.E.S.S. energy resolution is 15-20% and the angular resolution of  $0.1^\circ$ . An important limitation of IACTs is their sensitivity to light, observations are thus possible only during cloudless, moonless nights leaving for H.E.S.S. a 10% duty cycle.

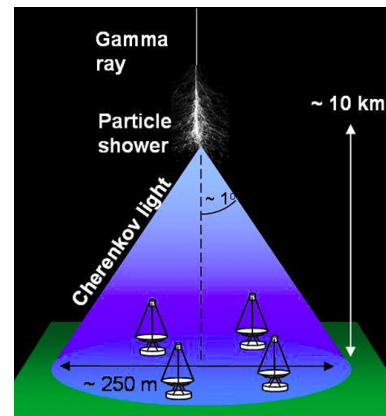


FIGURE 4: The Cherenkov light emitted will be detected as ellipses over an extended area [2]

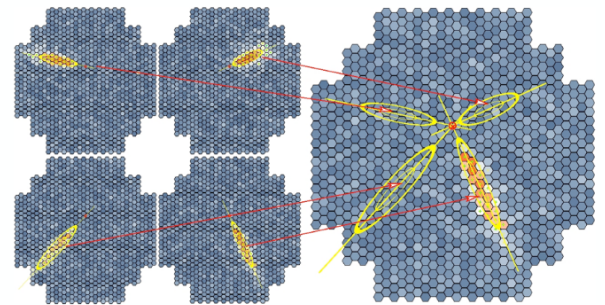


FIGURE 5: For the same event, images obtained with multiple telescopes are combined to obtain the incident photon direction [2]

### 3 Active Galactic Nuclei

Active Galactic Nuclei are powerful sources located at the center of some galaxies. They display strong emission from radio to VHE with the detailed emission depending on the source. It is commonly accepted that AGN are powered by accretion of matter on a

super-massive black hole of the order of  $10^6$  to  $10^9$  solar masses. The black hole is surrounded by an accretion disk which emits light through black body processes. Some of this light is then reprocessed by gas and emitted as X-rays. Farther from the black hole, dust form an obscuring torus limiting the visibility of the accretion disk on its plane. Then, AGNs can be divided in two categories depending on the presence of a relativistic jet. When a jet is present, the AGN is called radio-loud as jets are responsible for radio emissions in all direction. What is interesting for high energy physics, is the sub-category of radio-loud AGN called blazars for which the jet is directed along our line of sight. All of this is resumed in figure 6 (See also [3] for more details on AGN properties and classification).

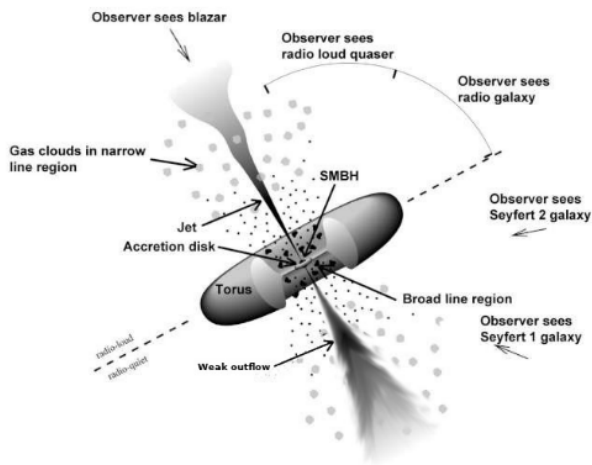


FIGURE 6: General picture of an AGN, with detail on the AGN category depending on the presence of a jet and the viewing angle. SMBH stands for Super Massive Black Hole. Adapted from [4]

With blazars it is possible to observe the relativistically boosted and focused emission from the jet. Their spectral energy distribution (SED) usually displays 2 main components. One at low energy range roughly from radio to X-rays, while the higher energy one goes from HE to VHE. This is a simplified vision as both component can be centered at higher or lower energy depending on the source (Figure 7).

The low energy bump is known to be synchrotron emission from relativistic electrons while it is unknown whether the high energy component is from inverse Compton by electrons or due to hadronic processes from protons and nuclei. Hadronic processes add a lot of complexity with new particles and interactions, but the added emissions could explain part of the observed cosmic rays and neutrinos.

## 4 Target of Opportunity program and analysis

AGNs are variable sources, with variations on time scale ranging from minutes to years. The Target of Op-

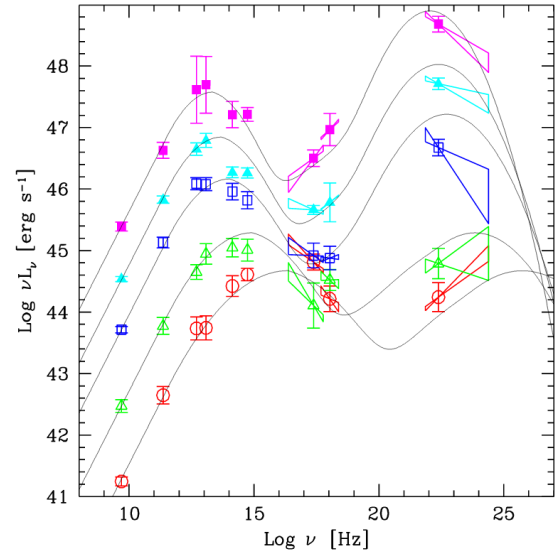


FIGURE 7: Blazar sequence SED, showing blazar with peak emission from lower to higher energies.[5]

portunity (ToO) program searches for sources in high emission state seen by other experiments at all energies (optical, X-rays, HE, VHE) and trigger observations. This allows for the detection of sources which would otherwise be too weak to be seen, and to observe short time variability.

I am working on two analysis using data collected during ToO observations. The first is on 3C 279, a well known source for which the study of the variability can give interesting results as it was really active in the past few years. The second one is on PKS 2022-077. In this case the goal would be a detection as it is a high redshift source ( $z=1.388$ ), farther than any source detected at VHE. The main factor limiting the observable flux at VHE is the absorption by the extragalactic background light, an ambient light created during galaxy formation and evolution which interacts with TeV photons through electron-positron pair creation [7].

## 5 Other activities

Apart from analysis, I perform other work for the collaboration.

### 5.1 Software development

Two additions to the analysis software were developed. The first one is an adaptive light curve algorithm which automatically adapts the time binning to the significance of the signal. It allows for a finer precision in the light curve when the signal is brighter, which is useful to reveal fast variability (Figure 8).

The second one removes part of observations with a bad quality (due to cloud, hardware failures,...). The goal is to recover observation runs which would be lost due to a few problematic minutes while most of the observation was of good quality. This work is still in

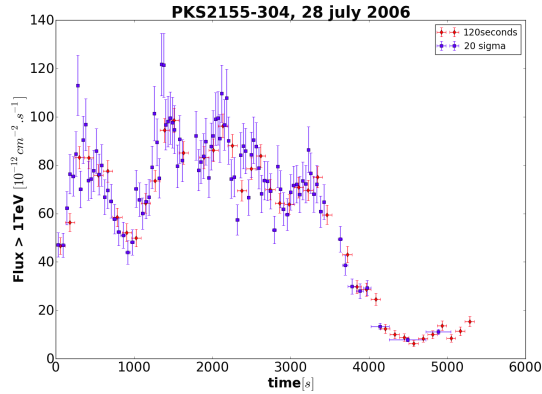


FIGURE 8: Light curve of a historically strong flare of PKS 2155-304, produced with fixed 2 minutes binning (red) and with the adaptive algorithm with a minimum significance of 20 sigma per point. A binning of a few seconds at the flux maximum and minutes at the flux minimum are visible, showing the usefulness of the method. 20 sigma was chosen for visibility and is over-constraining for scientific studies.

testing phase but results are promising. This is particularly interesting for time sensitive observations like transient or variable sources. For example, during a promising observation on 3C 279, 4 runs of 28 minutes each were taken. One of the run is problematic for 3 minutes and this new tool can be used to recover the 25 good minutes instead of losing one fourth of the overall observation time.

## 5.2 Continuous monitoring

A monthly analysis, called the extragalactic round up, is performed over all the extragalactic data. The goal is to check if sources were active or variable during the observation period, and to search for serendipitous transients in the field of view.

H.E.S.S. performs a real time analysis (RTA) over all the observations done on site. This allows for a quick estimation of the source signal but before the results can be used for communication their reliability needs to be studied. Indeed, the RTA relies on a preliminary calibration to avoid any computation time intensive steps, but produces less robust results. Two studies are performed. The significance given by the RTA is compared to the significance obtained during the offline analysis. This is mainly useful for internal use. The other study, is the correlation between RTA results and the flux of the source obtained in offline analysis (Figure 9). This is important for external communication, especially to initiate multi-wavelength observations with external partners.

## 6 Conclusion

Variability studies will be critical in understanding sources at VHE. Such programs will be an increasingly

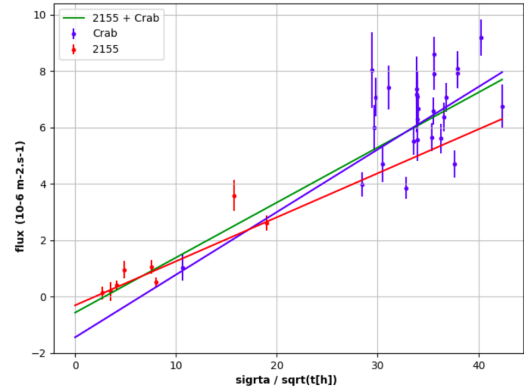


FIGURE 9: Comparison between offline flux and associated significance in the RTA divided by the square root of the observation time (points). At constant flux, the significance should increase linearly with the square root of the observation time. The best linear fit for each source used is displayed. The best linear fit is also plotted in green for both sources fit together.

important part of current IACTs observation in the future, before the start of CTA (Figure 10). CTA is the future IACT observatory which will cover both hemispheres with better performances than current instruments [6].



FIGURE 10: The newly installed telescope for CTA , Credit : Iván Jiménez (IAC)

Another big evolution in VHE astrophysics is the multi-messenger aspects rapidly developing after the recent observation of a neutrino associated at a 3 sigma confidence level with the blazar TXS 0506+056 [8] and observations of gravitational waves with LIGO/VIRGO associated with a multi-wavelength counterpart from the neutron star merger GW170817 [9].

## Références

- [1] Frank M. Rieger et al. TeV astronomy. *Frontiers of Physics*, 8 :714–747, December 2013.
- [2] David Sanchez. *Étude et modélisation des noyaux actifs de galaxie les plus énergétiques avec le sa-*

- tellite Fermi. Cosmologie et astrophysique extragalactique.* PhD thesis, Ecole Polytechnique X, 2010.
- [3] P. Padovani et al. Active galactic nuclei : what's in a name? *Astronomy and Astrophysics Review*, 25 :2, August 2017.
  - [4] C. M. Urry and P. Padovani. Unified Schemes for Radio-Loud Active Galactic Nuclei. *Publications of the ASP*, 107 :803, September 1995.
  - [5] D. Donato et al. Hard X-ray properties of blazars. *Astronomy and Astrophysics*, 375 :739–751, September 2001.
  - [6] B. S. Acharya et al. Introducing the CTA concept. *Astroparticle Physics*, 43 :3–18, March 2013.
  - [7] Alberto Franceschini and Giulia Rodighiero. The extragalactic background light revisited and the cosmic photon-photon opacity. *Astronomy and Astrophysics*, 603 :A34, July 2017.
  - [8] IceCube Collaboration et al. Multimessenger observations of a flaring blazar coincident with high-energy neutrino IceCube-170922A. *Science*, 361 :eaat1378, July 2018.
  - [9] Abbott B. P. et al. Multi-messenger Observations of a Binary Neutron Star Merger. *Astrophysical Journal*, 848 :L12, October 2017.



# Gamma-Ray Burst detection at very high energy

Quentin Piel

Laboratoire d'Annecy Le Vieux de Physique des Particules

## Résumé

Resume

## 1 Gamma Ray Bursts

### 1.1 History

Gamma Ray Burst (GRB) were discovered in 1962 by the VELA satellites. The purpose of these network of satellites was to monitor the U.R.S.S. nuclear bomb tests. Nuclear explosions were the only known source of  $\gamma$ -ray. A first signal was detected in 1967 (see Fig. 1), however due to the bad localisation accuracy, instruments were not able to identify the direction of  $\gamma$ . The energy and the high frequency of the detection excluded a human origin.

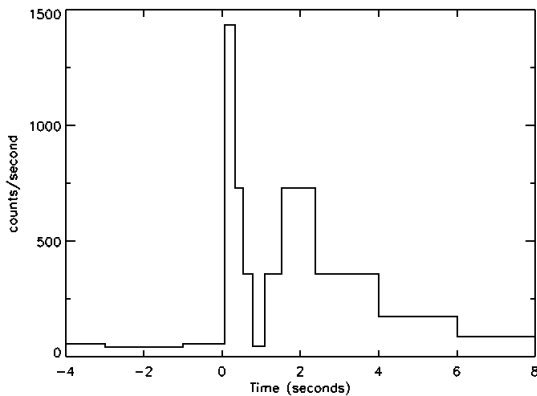


FIGURE 1: First Gamma-Ray Burst detection by VELA.

This discovery was classified until 1973 by the U.S. After the release, numerous facilities such as CGRO, Fermi and Swift were built to study this kind of source.

### 1.2 Gamma Ray Burst characteristics

After several decades of study, the origin of GRB emissions are still not fully understood. But some general characteristics can be highlighted.

- Extragalactic progenitors (from low to high redshifts) ??
- Two classes of GRBs : short GRBs (duration below 2s) and long ones (duration above 2s)
- Two phases of emission : Prompt (between 0.1s and 1000s depending on the GRB kind) and afterglow (until weeks or months)

- Huge released energy ( $\approx 10^{51} - 10^{54} \text{erg}$ )
- Not thermal spectra
- Linked between long GRBs and Supernovae by collapsing scenario (but in only 0.4% to 3% the SN Ibc in linked to a GRB)
- Merging scenario as origin of short GRBs (see GW170817 event)
- Most of energy released in X and low energy  $\gamma$  domains (10-100 keV)

GRBs have been detected in all the electromagnetic domain except the very high  $\gamma$  energies above 100 GeV (until the GRB 190114C ATEL 12390). Figure 2 shows several instruments used to study GRBs and the energy boundary before the MAGIC detection.

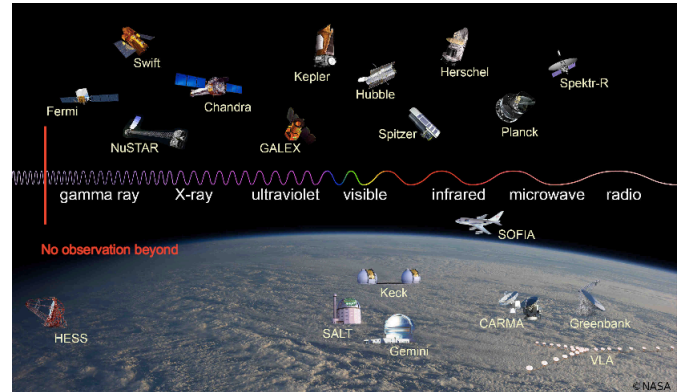


FIGURE 2: Schematic of the position of several instruments on energetic range. Credit : NASA.

## 2 The H.E.S.S. telescope array

### 2.1 Cherenkov light

Čerenkov light is created when a particle moves faster than light in the medium. An electromagnetic ray focused in a cone of light is emitted as shown in Figure ???. Secondary particles produced in atmospheric showers are ultra-relativist and move faster than the speed of light in the atmosphere. Considering usual parameters for showers, a Lorentz factor  $\beta \approx 1$  and an index  $n \approx 1$ ,  $\theta_c \approx 0.6^\circ$ . With a first interaction about 10 km, a circle of radius  $\approx 100$  m will be created on the ground.

The flash of Čerenkov emission is very short (about 3 ns). The typical wave length is between 300 nm and 600 nm (blue color). So sensors to observe this specific light has to be fast and sensitive to blue.

## 2.2 Array description

The H.E.S.S. experiment is located at the coordinate ( $23^{\circ}16'18''\text{S}$ ,  $16^{\circ}30'00''\text{E}$ ) on the Khomas Highland in Namibia at an altitude of 1800 m. Its localization on the highland was chosen for several reasons.

- The site has to be far from city to avoid human activities and light pollution.
- Desert highlands such as Khomas have a semi-desertic climate. It means that a small amount of time is lost because of clouds or rain.
- There is a geomagnetic anomaly called the South Atlantic. The geomagnetic field is lower (0.2 G) than at other places. This lower magnetic field implies a lower deviation of charged particles in showers. So showers are more collimated and easily identifiable.

The H.E.S.S. array is actually composed of five telescopes of two kinds made in two step. First in 2004, four telescopes of 12 m diameter at the corner of a 120 m side square have been built. The distance of the telescopes was chosen as a compromise between two effects. Further the telescopes are better the stereoscopic vision is. But the probability of a shower to be detected in several telescopes decreases. So according to typical shower parameters explained in the previous part the best distance between the telescopes is around 100 m.

These four telescopes implied a breakthrough in  $\gamma$  astronomy. More than 80 new  $\gamma$  sources were discovered. However there were a gap in energy between the  $\gamma$  satellites such as *Fermi-LAT* and H.E.S.S. energy ranges. This energy domain is crucial to effectively constraint models of emission.

This four telescopes array called H.E.S.S.-I worked until 2013 and the commissioning of a 28 m diameter telescope called CT5. This new array composed of five telescopes is still used to observe  $\gamma$  sources. The picture 3 shows the five telescopes in the Namibian desert. CT5 is in the center of this square. The aim of this new configuration was to increase sensitivity at low energy ( $\approx 100$  GeV). Thanks to this new telescope, a continuous energy range from 100 MeV to 100 TeV was obtained by using Fermi and H.E.S.S.-II.



FIGURE 3: Picture of the H.E.S.S. array

## 2.3 Gamma Ray Burst detections

The H.E.S.S. experiment does not have a large field of view such as Fermi or Swift satellites to observe happening GRBs. So H.E.S.S. is connected to an international network grouping (called GCN) several tens of facilities operating at different wave lengths. Once an alert is sent through the GCN, H.E.S.S. try to observe this position as soon as possible.

However, most of the alert can not be followed instantaneously. As H.E.S.S. does not work during day or cloud conditions, all the observations are delayed. Figure 4 shows the H.E.S.S. delay of observation during the last years follow-ups. The lowest delays are around 20s. It corresponds to the average time of alert sending.

After data taking, GRBs are analyzed using standard procedure including calibration and analysis cuts ??.

None GRBs have been detected by H.E.S.S. Only empty maps have been observed as shown in figure 5.

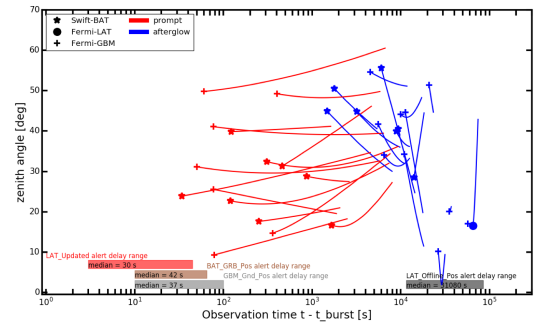


FIGURE 4: Delay of H.E.S.S. follow-ups.

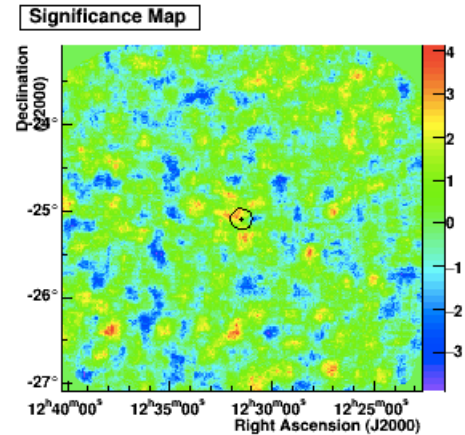


FIGURE 5: H.E.S.S. observation of GRB150227. Significance map of detection. Li&Ma formula has been applied.

## 3 Cherenkov Telescope Array

### 3.1 Array description

Cherenkov Telescope Array (CTA) will be the future main facility of  $\gamma$ -ray astronomy. The hardware and software improvements will make CTA a major advance in grounded  $\gamma$  detectors.

Characteristics	Energy range	Value
Diff. sensitivity ( $\text{erg cm}^{-2} \text{s}^{-1}$ )	at 50 GeV	$8 \times 10^{-12}$
	at 1 TeV	$2.10^{-13}$
	at 50 TeV	$\approx 10^{-12}$
Collection Area	at 1 TeV	$> 10^4$
	at 10 TeV	$\approx 10^6$
Angular resolution	at 0.1 TeV	$0.1^\circ$
	$> 1$ TeV	$0.05^\circ$
Energy resolution	at 50 GeV	$< 25\%$
	$> 1$ TeV	$< 10\%$
Field of view	at 0.1 TeV	$5^\circ$
	at 1 TeV	$8^\circ$
	$> 10$ TeV	$10^\circ$
Repointing time	$< 0.1$ TeV	20 s
	0.1-10 TeV	60s

FIGURE 6: Performances to reach for the CTA observatory.

The CTA array is currently under construction on two sites. The northern one in La Palma on the Canaries islands and the southern one in Paranal, Chile. These two sites were chosen in order to maximize scientific possibilities of discovery. Indeed, observable sources are different between the northern and the southern hemispheres. The Chile site will be mainly used to study galactic sources whereas the La Palma site observation time which will be mostly dedicated to study extra-galactic sources.

In order to improve the sensitivity over a large energy range, CTA will be composed of 3 kinds of telescopes.

- The Small Size Telescope (SST) (4m high) to observe at the highest energies ( $>1$  TeV).
- The Middle Size Telescope (MST) (12m) to cover the middle part of the energy range (between 100 GeV and a few TeV).
- The Large Size Telescope (LST) (24m) to increase the sensitivity to low energy (around 100 GeV).

The table 6 shows some of the characteristics to be reached by CTA.

The most important characteristics for the GRB detection are the high sensitivity at low energy around 100 GeV and the fast repositioning.

### 3.2 Gamma Ray Burst detections

Estimating the possibilities of GRB detection with CTA is one of the major key science projects. In order to estimate the chance of GRB detection with CTA, a preliminary study using a theoretical model has been performed.

The GRB modeling during afterglow and prompt emissions have been done by applying some equations coming from the literature for prompt and afterglow modelings. The processes taken into account are :

- Synchrotron
- Synchrotron Self-Compton (SSC)
- $\gamma - \gamma$  absorption
- Geometrical correction

COSMOLOGICAL PARAMETERS		
$H_0$	Hubble constant ( $\text{km/s Mpc}^{-1}$ )	71
$\Omega_m$	matter density ( $\rho_m/\rho_c$ )	0.27
$\Omega_\Lambda$	vacuum energy density ( $\rho_\Lambda/\rho_c$ )	0.73
VARIABLES (PROMPT)		
$L_{iso}$	GRB luminosity	[ $\text{erg/s}$ ]
$T_{90}$	GRB duration	[s]
$t_v$	GRB variability time-scale	[s]
$p$	particle population slope	
$\Gamma$	Boost Lorentz factor	
$\epsilon_e \epsilon_B$	energy equipartition parameters	
$z$	GRB redshift	
VARIABLES (AFTERGLOW)		
$En$	GRB energy per solid angle	[ $\text{erg}$ ]
$t_h$	Observer time from $T_0$	[h]
$n$	ambient density	[ $\text{cm}^{-3}$ ]
$p$	particle population slope	
$\zeta$	fraction of accelerated particles	
$\epsilon_e \epsilon_B$	energy equipartition parameters	
$z$	GRB redshift	

TABLE 1: Parameters and variables used in the source code to model GRBs during both prompt and afterglow phases.

— EBL attenuation (Dominguez ??)

An example of spectrum obtained is given in Figure 7. Parameters taken into account for the modeling are shown in Table 1.

However the GRB modeling is still largely unknown. So several assumptions were taken concerning emission processes. Moreover taking into account all the variety light curves of GRBs is not possible. So three kinds of light curves taken into account the shape of light curves shown in Figure 8 were assumed.

After defining spectra and light curves, simulations were ran using ctools, one of the software developed by the CTA collaboration. This software takes as inputs ; spectrum, light curve and instrument response functions. Spectra and light curves are described by the model. Instrument Response Functions describing the characteristics of telescopes are provided by the CTA collaboration.

1 000 000 simulations were ran by changing the different physical parameters (such as  $\epsilon_e, \epsilon_B$  and  $\Gamma$ , light curve and delay of observation. Then the number of detection above  $5\sigma$  is reported in the table ??.

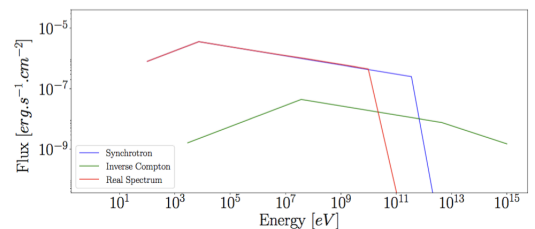


FIGURE 7: Spectra obtained from the GRB modeling.

Array configuration	$\epsilon_e, \epsilon_B$	$t_{start}[s]$	Mean number of detection
South	0.4, 0.4	0, 20	$5.3 \pm 1.7, 3.9 \pm 1.6$
North	0.4, 0.4	0, 20	$4.2 \pm 1.7, 2.2 \pm 1.3$
South	0.01, 0.79	0, 20	$1.2 \pm 1.0, 0.5 \pm 0.7$
North	0.01, 0.79	0, 20	$1.8 \pm 1.3, 0.7 \pm 0.8$
South	0.1, 0.01	$T_{90}, 600$	$8.8 \pm 1.7, 7.1 \pm 1.8$
		3600, 7200	$7.1 \pm 1.8, 6.8 \pm 1.8$
North	0.1, 0.01	$T_{90}, 600$	$8.5 \pm 1.7, 6.5 \pm 1.8$
		3600, 7200	$6.5 \pm 1.8, 6.1 \pm 1.8$
South	0.01, 0.79	$T_{90}, 600$	$0.5 \pm 0.7, 0.1 \pm 0.3$
		3600, 7200	0, 0
North	0.01, 0.79	$T_{90}, 600$	$0.6 \pm 0.7, 0.1 \pm 0.3$
		3600, 7200	0, 0

TABLE 2: GRBs detections with different array configurations and different set of parameters  $\epsilon_e$  and  $\epsilon_B$ .

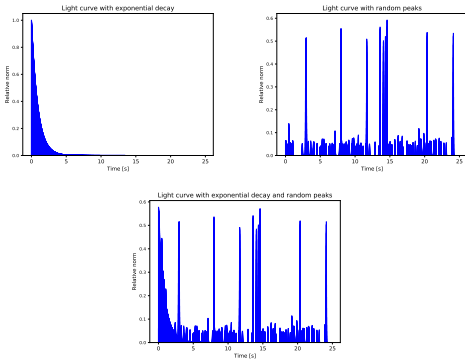


FIGURE 8: Kind of light curves used for the GRB simulations.

For the both cases, two set of values for  $\epsilon_e$  and  $\epsilon_B$  were chosen. As expected, the number of detection is lower for relatively high  $\epsilon_e/\epsilon_B$  cases (low SSC component). A further reduction is expected when a delay in observation time is introduced (a factor  $\sim 2$ ) in the two considered scenarios without delay in the follow up and with a delay of 20 s. For optimistic cases, several GRBs should be detected with CTA during the first years of operation. But for the pessimistic case, detecting GRBs at very high energy for the first time a GRB is very unlikely.

## 4 Conclusion

Gamma Ray Burst have been largely detected at different wave lengths since their discovery in 1962.

H.E.S.S. is the current generation of Cherenkov Telescope. H.E.S.S. have observed several tens of GRBS since 2007. Moreover, non detection occurred. Very high energy upper limits put by H.E.S.S. observations are very useful for modeling.

CTA is the next step of Cherenkov astronomy. The improved sensitivity at low energy and its fast repositioning capacities will increase the GRB detection possibilities. According to the first estimations, CTA should be able to detect GRBs during the first years of operation.

## Pulsars at very high energies

Marion Spir-Jacob

APC laboratory, Paris



### Résumé

Pulsars are strongly magnetized, fast-spinning neutron stars. Their emission consists of pulses separated by regular and short intervals with a great stability. They have been discovered in 1967 in radio. Since then, more than 2600 radio pulsars and more than 240 gamma-ray pulsars have been discovered, as well as some pulsars in X-ray (with  $\sim 100$  specimen) and a few others.

This proceeding focuses on gamma-ray emitting pulsars, and among them, the ones that emit at particularly high energies. All gamma-ray pulsars are observed by Fermi, a space telescope sensitive between 100 MeV and 100 GeV. Ground-based VHE (very high energy) telescopes (sensitive between 20 GeV and 100 TeV) are starting to detect their first VHE pulsed signal. And these observations around the TeV bring exciting new challenges for pulsar theory, especially because such detections were not expected at all.

### 1 Compact objets, final stages of stellar evolution

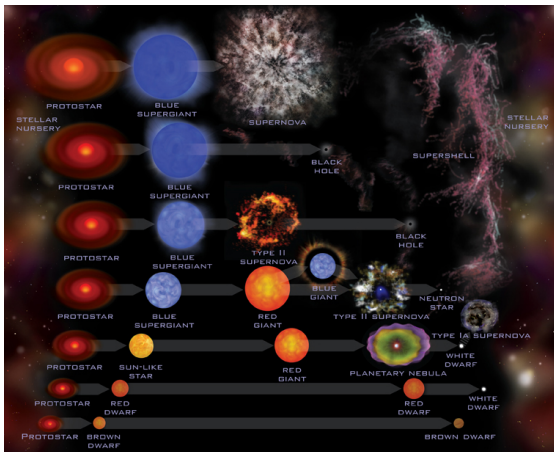


FIGURE 1: Stellar evolution (mass goes upwards)

A star is a hydrostatic equilibrium between the gravitational pressure and the radiation pressure generated by the nuclear fusion reactions taking place in its core.

When the nuclear reaction rate starts to diminish, the gravitational pressure compresses the core of the star. The final evolution depends mainly on the mass of the star – even if other factors can have some influence,

like the rotation speed, the metallicity, the presence of a companion, etc. What is left of the core of the star is a compact object, and there exist three different types of them : white dwarfs (for stellar masses  $\lesssim 8M_{\odot}$ ), neutron stars (for stellar masses between 8 and  $30M_{\odot}$ ) and black holes (for stellar masses  $\gtrsim 30M_{\odot}$ ).

In the case of white dwarfs, they are about the size of the Earth and the mass of the Sun, and the main pressure term is the electron degeneracy one. Neutron stars are intermediate stages, much denser and more compact than white dwarfs, but not massive enough to collapse into black holes. Their mass is also of the order of  $1M_{\odot}$  but their radius is approximately 10 kilometers, leading to densities similar to the nuclear liquid density, and even higher in the core. The electrons are then so degenerate that the Fermi energy level is extremely high. As a result, it costs much more energy to create an electron than only its rest mass energy. The usual equilibrium between the neutron decay and the electronic capture (shown below) changes : there is a global neutronization of matter, hence the name of neutron star.

$$n \rightarrow p^{+} + e^{-} + \bar{\nu}_{e}$$

$$p^{+} + e^{-} \rightarrow n + \nu_{e}$$

The strong interaction between neutrons is the main term balancing gravity.

All pulsars are neutron stars, but the name of pulsar (**pulsating radio star**) refers to the phenomenon taking place around the neutron star. To understand it, a parallel with a light-house is often proposed. A light house emits a spinning beam of light. An observer sees a peak of light at regular intervals, when the beam points towards him. In a pulsar, the emission is strongly anisotropic because of the very intense magnetic field and that results in a periodicity of its luminosity with a period equal to the rotation period as for a light-house.

In the following sections, I will present an overview of pulsar emission models, and particularly the VHE (very high energy) pulsar observations and phenomenology, which are the topics of my PhD.

There are different categories of pulsars, and the focus here will be only for one type : the rotation-powered pulsars. They are less than a few  $10^5$  years, and their period is of the order of 0.1-1s. Their main energy source is their rotational kinetic energy, as opposed to magnetars, powered by their magnetic field, or millisecond pulsars, powered by the accretion of a companion.

## 2 Gamma-ray emitting pulsar models

### 2.1 Rotating dipole in the vacuum

The simplest model to describe a pulsar is the rotating dipole in the vacuum. Despite being unrealistic (for reasons we will develop later), it is still used to estimate the magnetic field and the age of a pulsar.

A rotating dipole emits electromagnetic waves, which makes it lose some energy, under the form of rotational kinetic energy  $E_K$ . The core relation of the model is simply  $\dot{E}_{em} + \dot{E}_K = 0$  : the dipole slows down with time because of all the energy it emits.

Thanks to this relation, and with the measure of the period of a pulsar and its derivative, it is possible to have an idea of its time evolution and hence its age. The strength of the magnetic field is related to  $\dot{E}_{em}$ , so it is possible to estimate it as well.

A major flaw of the model is the idea of a pulsar in the vacuum. As we will discuss now, a pulsar is in reality surrounded by a conducting magnetosphere. And even if a pulsar was initially in the vacuum, it would charge its magnetosphere extremely quickly.

Moreover, no particle around the star means no particle emission mechanisms. Yet we observe a pulsed high-energy emission, which means that somewhere around the pulsar, there should be high energy particles emitting these photons in one way or another.

### 2.2 Magnetosphere models

#### The Golreich and Julian model

The reason why a pulsar should be surrounded by a magnetosphere can be understood by analogy with the Faraday disk experiment. A Faraday disk is a rotating, conductor disk put in a magnetic field. This generates an electric potential difference between two different points at its surface. Computing the electric potential difference between two points on the star's surface yields a force much stronger than the gravitational's attraction. Consequently, no pulsar could really be in the vacuum. This work was shown by Golreich and Julian in 1969 [2].

#### Presence of cavities

However, the Golreich and Julian model is also not realistic. Pulsar magnetospheres are actually not fully filled but contain vacuum gaps [3].

They form in regions where there is a flow of particles outwards that are not replaced by an equally important input of particles.

These gaps are essential to account for the acceleration of particles, because without them, there would be no strong electric fields. Indeed, within the conducting plasma of the magnetosphere, charged particles can move and prevent strong potential difference from occurring. On the contrary, a cavity isolates different parts of the plasma and is a favorable location for

strong electric fields and particle acceleration up to very high energies.

This can happen near the poles, where the particles follow the magnetic field lines and can eventually escape in the wind. This idea is developed in the polar caps model [4].

Another location for a vacuum gap is near the light cylinder.

The light cylinder is the limit beyond which particles cannot follow a solid corotation with the neutron star because they would have to go faster than  $c$ . Particles within a closed field region will stay in it ; particles just outside of it will escape in the wind and this can create a cavity called the outer gap [5].

Some models develop the idea that the emission takes place along the last closed magnetic field line, all the way from the star's surface to the light cylinder : this is the slot gap [6].

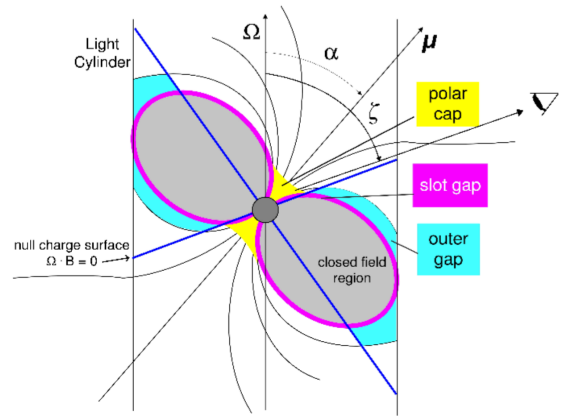


FIGURE 2: Very schematic view of the different gaps, where the acceleration and emission would take place. The neutron star is the grey disk in the middle,  $\Omega$  represent the angular rotation vector, and  $\alpha$  is the angle between the magnetic dipole and the rotation axis. The light cylinder is parallel to the rotation axis. The observer has an angle of view inclined of  $\zeta$  with respect to  $\Omega$ . The polar cap is in yellow, the slot gap in purple and the outer gap in blue. The magnetosphere goes until the light cylinder and is not colored in this scheme. Outside the light cylinder starts the pulsar wind, fed by escaping particles.

The polar cap is the closest to the neutron star and the gap in which the magnetic field is the strongest. Any photon above a certain energy threshold interacts with the field and creates an electromagnetic shower. The stronger the field, the lower the energy threshold. In the case of polar caps, it means  $e^+/e^-$  pair creations and showers are expected. This is a nice framework to work in for radio pulsar theorists, but not for gamma-ray emission, since there is a strong attenuation of gamma-rays through pair production.

Modeling gamma-ray pulsar emission requires to take some more distance with the neutron star and its ma-

gnetic field. The models favor synchrotron emission and Inverse Compton effect in the outer gap, in the slot gap or in the pulsar wind, which we will describe now.

### 2.3 Striped wind models

At the light cylinder, the particles can't have a rigid corotation with the pulsar : it would mean going faster than  $c$ .

Magnetic field lines open and charged particles escape along them. They feed the pulsar wind, which represents the major part (about 90 %) of the energy losses of the pulsar.

Outside the light cylinder, the magnetic field can be described as a double-half-monopole. The lines converge towards the magnetic South pole in a half-space while they diverge away from the magnetic North pole in the other half-space. On one side the magnetic field polarization is positive, on the other side negative. At the interface, the polarizations cancel exactly and it creates a current sheet of hot particles with very little magnetization. This current sheet has a striped shape because of the angle between the rotation axis and the dipole's axis.

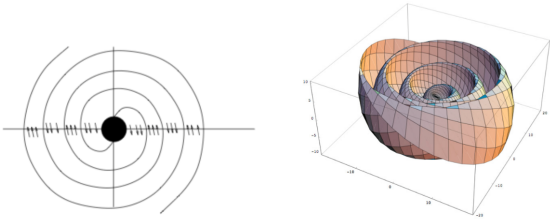


FIGURE 3: Shape of the current sheet in the striped wind model, where magnetic reconnection could accelerate particles. The figure on the left is from [12] and the figure on the right from [11].

It is thought that magnetic reconnection takes place in the current sheet. Magnetic reconnection happens when two plasmas of opposite magnetic polarization collide (or get closer together) and the magnetic field lines rearrange themselves. The magnetic energy generated by the rearrangement is converted into kinetic energy of particles in the wind.

The idea that particles in the current sheet could generate pulses spaced from one to the next has all to do with special relativity. The wind is relativistic and moves towards the observer, causing its emission to be focused in the direction of the observer. The extension of the region emitting towards the observer is of the size of the beaming angle (outside this region, the emission will be focused in another direction). There can only be pulses if the duration of one pulse is smaller than the duration of the total emission, otherwise all pulses would add up and smooth the pulsations. [7]

## 3 PIC simulations

The advance of numerical simulations gives a precious tool to understand objects like pulsars, too complex to be fully treated analytically. The PIC (Particle-In-Cell) method is used to describe the behavior and emission of particles around a pulsar, with the least hypotheses possible. A grid divides space in cells, with a value for the charge density, the charge current, the electromagnetic field, in each cell. The simulation is performed step by step. To go from one step to the other, equations of motion and Maxwell's equation for the fields are solved.

The main emission mechanisms are encoded in the code and the result (the intensity of the emission and its location) are the outputs of the simulations.

As a result, the gamma-ray emission seems to come from the transition between the magnetosphere and the pulsar wind, close to the light cylinder.

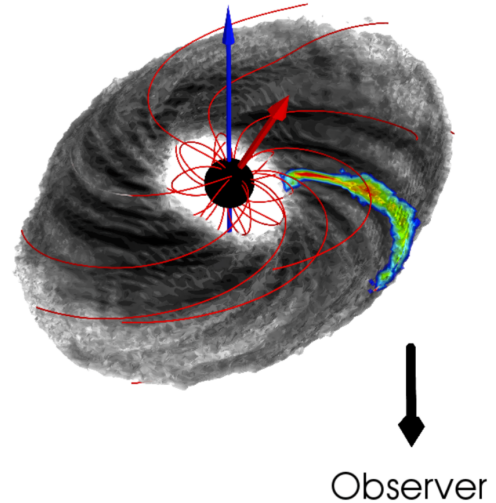


FIGURE 4: In grey : emission from the wind to different directions than the observer's. In color : emission in the direction of the observer, contributing to the pulse from different locations in the wind. From Cerutti, 2016 [8]

## 4 Pulsars in the VHE domain

The Crab pulsar and the Vela pulsars were among the first pulsars to be discovered in radio, and a few years later in the gamma-ray domain. They remained the only two gamma-ray emitting pulsars for almost two decades, and then EGRET (Energetic Gamma Ray Experiment Telescope) found them five new companions. In 2008, just before the launch of Fermi (a gamma-ray space telescope), seven gamma-ray pulsars were known. Fermi operated a revolution in the field, discovering more than 200 such objects. This opened the way to population studies.

In particular, the spectra of all Fermi pulsars seemed to behave in a similar way. Around the GeV, there would be a strong cutoff in the spectrum (an  $\sim$  exponential cutoff).

Consequently, no signal was expected at very high energy, and none of the models predicted a signal like the ones that were recently detected.

After a first detection in 2011 by the VERITAS collaboration of the Crab pulsar up to 400 GeV [9], in 2015, the MAGIC collaboration announced the detection of the Crab pulsar up to 1 TeV [10]. The spectrum (figure 5) shows that it is possible to fit with a single component the high energy and very high energy emission for the two pulses of the pulsar (P1 and P2).

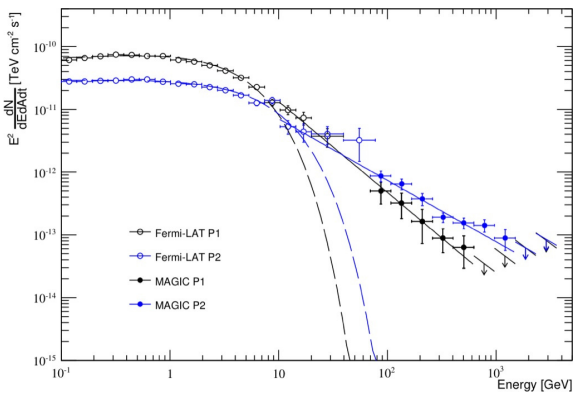


FIGURE 5: Fermi and MAGIC spectrum of the Crab pulsar. The peak P1 is in black, the peak P2 in blue. For both peaks, a power law is used to fit the spectrum from the GeV up to the TeV. The dashed line is the exponential cutoff that was expected from the fit on Fermi data alone.

In 2017, the H.E.S.S. collaboration announced the detection of the Vela pulsar above 3 TeV. In contrast to the Crab, this component is not in continuation of the GeV emission. This is a distinct spectral component, which has even more unexpected consequences for the pulsar models.

This discovery will help discriminate between the magnetospheric models and the pulsar wind models, if one or the other is not capable of explaining the TeV emission while conserving reasonable values for all other physical quantities. To this day, this remains an open question.

My PhD is focused on the analysis of this very high energy component, with an observation part and a phenomenology part, focused on the wind model near the light cylinder. This is in continuation of the thesis of Thomas Tavernier in 2015 [11].

## 5 Perspectives for the future

This new spectral component at the TeV is a challenge for the models, none of which predicted such a strong signal at such high energies. This will help discriminate between magnetospheric and wind models. Further observations on the Vela pulsar to probe the

highest energy reached by this component will provide some major constraints for the phenomenology of pulsars.

The Crab pulsar and the Vela pulsar seem to have different behavior at very high energy but a common explanation is not excluded either. Studying other pulsars and finding whether they have a Crab-like or a Vela-like component (or neither!) is on the road map for understanding pulsars at very high energies.

## Références

- [1] How Pulsars Really (perhaps) Work (maybe), Curtis Michel, 1994
- [2] Pulsar electrodynamics, P. Golreich and W. H. Julian, 1969
- [3] Holloway, Nature Physical Science 246, 1973
- [4] Theory of pulsars : polar caps, sparks, and coherent microwave radiation, M. A. Ruderman and P. G. Sutherland, 1974
- [5] Energetic radiation from rapidly spinning pulsars. I. Outer magnetosphere gaps II. Vela and Crab, K. S. Cheng, C. Ho and M. Ruderman, 1985
- [6] The slot gap model of pulsars, J. Arons, 1981
- [7] Very high energy emission as a probe of relativistic magnetic reconnection in pulsar winds, Iwona Mochol and Jérôme Pétri, 2015
- [8] Modeling high-energy pulsar lightcurves from first principles, B. Cerutti, A. A. Philippov and A. Spitkovsky, 2016
- [9] Detection of the Crab Pulsar with VERITAS above 100 GeV, Andrew McCann and for the VERITAS Collaboration, 2011
- [10] TeV pulsed emission from the Crab pulsar detected by MAGIC, MAGIC collaboration, 2015
- [11] Une quête de l'émission du pulsar de Vela aux hautes et très hautes énergies : observation, détection et étude, du GeV au TeV avec le satellite Fermi et les télescopes à imagerie Tchénkov H.E.S.S., Thomas Tavernier, 2015
- [12] On the physics of cold MHD winds from oblique rotators, Bogovalov, 1999

# Calibration of XENON1T for the search of new physics

Chloé Therreau

*Subatech, CNRS, IMT-Atlantique, Université de Nantes*



## Résumé

XENON1T is the third and largest dark matter (DM) direct detection experiment of the XENON collaboration. It consists of a dual-phase (liquid-gas) Time Projection Chamber (TPC) filled with xenon (Xe). With its total mass of 3.2 tonnes of xenon, XENON1T is at present the largest TPC ever built for DM searches. It proved to be capable to reach the lowest background level ever achieved in liquid xenon (LXe) detectors and set the world best limit for Spin-Independent WIMP-nucleon cross section for WIMP masses above  $6 \text{ GeV}/c^2$  [1].

Thanks to the ultra-low background environment, the same detector allows to study other rare processes, among which, the search for neutrinoless double  $\beta$  decay is of particular interest because it allows to probe the majorana nature of neutrinos. This search is possible thanks to the presence of the  $^{136}\text{Xe}$  double  $\beta$  emitter in the natural xenon used as a target.

Both DM and neutrinoless double  $\beta$  decay searches require a very good understanding and characterization of the detector response at different energies over time. In this proceeding, a quick summary of the XENON1T experiment will be reviewed, then calibration and detector monitoring using an internal radioactive source of  $^{83m}\text{Kr}$  will be discussed. Finally, a preliminary investigation of the neutrinoless double beta decay sensitivity in XENON1T will be presented.

## 1 Introduction

The concept of DM was introduced to explain several astrophysics observations which indicate the presence of a missing mass in the universe. Particle physics theories beyond the Standard Model suggest Weakly Interactive Massive Particle (WIMP) as one of the best candidate for DM. One of the possible approaches to search for them is the direct detection, whose working principle is based on the proposal of M. Goodman and E. Witten [2]. In 1985, they extended the neutral current neutrino detection to DM : WIMPs are expected to elastically scatter off nuclei in the target. The energy transferred during such interactions induces low energy nuclear recoils whose measurable signal has a typical energy of a few keV to 100 keV.

The current most stringent limit on the Spin-Independent WIMP-nucleon cross-section was reached by XENON1T in September 2018 after a total exposure of  $1 \text{ ton} \times \text{year}$ , and corresponds to  $4.1 \times 10^{-47} \text{ cm}^2$  for

a WIMP mass of  $30 \text{ GeV}/c^2$  at 90% confidence level [1]. To reach such good sensitivity, XENON1T showed the lowest background noise ever achieved in such experiments (see section 2.2) and stable experimental conditions over more than one calendar year.

These reaches are of fundamental importance also for other rare event searches, like the search for neutrinoless double  $\beta$  decay of  $^{136}\text{Xe}$  that will be presented in section 4.

## 2 XENON1T experiment

### 2.1 Detector principle

XENON1T is located at the Laboratori Nazionali del Gran Sasso (LNGS) in Italy. It consists of a dual-phase TPC of 1 m high per 1 m diameter filled with 2 tons of Xe, designed to detect rare events particles scatterings. The TPC and its two arrays of PhotoMultiplier Tubes (PMTs)<sup>1</sup> allow the detection of the light and charge signals produced by a particle interaction with Xe atoms.

In LXe, it is possible to distinguish two types of interactions depending on the incoming particle. In case of WIMPs or neutrons, elastic scatterings with target nuclei will lead to Nuclear Recoils (NR). If the incoming particle is a photon (with a typical energy of [0.1, 10] MeV, since it will come from the ambient radioactivity), a photoelectric effect, a Compton effect or an electron-positron pair production will lead to Electronic Recoils (ER). In the same way, ER can be induced by  $\beta$  particles (i.e. electrons) which interact with atomic electrons through elastic scattering.

In both (NR and ER) cases, Xe atoms are ionized and excited. Excited Xe atoms decay to the ground state emitting a light signal, called S1. Electrons generated by the ionization follow the lines of the applied electric field, as they drift towards the gas phase, where an other stronger field extracts them from the liquid phase to the gas phase. During the extraction, the proportional scintillation charge signal, S2, is generated.

Because the S2 signal is produced in the gaseous phase, close to the top PMT array, the  $x - y$  position of the interaction is extracted from the top PMTs : its resolution is of the order of a few cm. The  $Z$  coordinate is determined with a resolution of the order of  $100 \mu\text{m}$  through the measurement of the drift time of the electrons inside the TPC.

1. 248 PMTs in total.

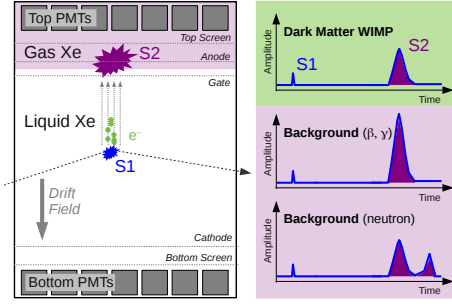


FIGURE 1: Working principle of the XENON1T TPC, showing the S1 and S2 signals production. The black arrow indicates an incoming particle [1].

Electronic Recoils (induced by gamma or beta particles) can be distinguished from Nuclear Recoils (induced by WIMPs or neutrons) thanks to the relative intensity of S1 and S2 signals. The S2/S1 ratio is lower for a NR than for an ER. This discrimination between NR and ER is one of the techniques used to reduce the background noise for DM searches, presented in section 2.2

## 2.2 Backgrounds

WIMPs are predicted to have a low interaction probability with standard matter (with a cross-section lower than the weak scale) which leads to expect few detectable events in our detector. In order to extract this tiny signal, it is crucial to operate at the lowest possible background level. Several techniques are used to reduce the background noise in XENON1T.

First, XENON1T is placed under the Gran Sasso mountain, at 3 600 m water equivalent, reducing the background noise from **cosmic ray** by a factor  $\sim 10^6$  [3]<sup>2</sup>. NR produced by remaining muon-induced neutrons are suppressed thanks to the active Cherenkov muon veto detector, instrumented with 84 PMTs of 8 inches.

Secondly, the **ambient radioactivity** is reduced thanks to shielding : an external shielding is provided by the water Cherenkov detector, and an internal one is given by the LXe itself. Indeed, thanks to the high stopping power of the LXe, most of the ambient radioactivity events are confined at the edge of the detector. Therefore, knowing the 3D position of the interaction, a fiducial volume can be defined to select events at the center of the TPC in order to reduce this background contribution.

Thirdly, LXe does not contain **Xe radioactive isotope**. Two radioactive isotopes are dissolved<sup>3</sup> in the LXe and represent the majority of the ER background :  $^{85}\text{Kr}$  and  $^{222}\text{Rn}$ .  $^{222}\text{Rn}$  and its daughters decay emitting  $\beta$  and  $\alpha$  particles.  $^{222}\text{Rn}$  is produced inside detec-

tor materials by the decay of  $^{226}\text{Ra}$  and can emanate inside the LXe through diffusion or recoil from prior  $\alpha$ -decay. Its half-life is of 3.8 days and it is uniformly distributed inside the TPC [1]. A careful selection of low  $^{222}\text{Rn}$  emanation materials was performed in order to reduce this background contribution prior to the construction of the experiment [3].  $^{85}\text{Kr}$  is present in the atmosphere and thus in the natural xenon<sup>4</sup> used as target. The different boiling points of Xe and  $^{85}\text{Kr}$  allow for the removal of  $^{85}\text{Kr}$  contaminants down to a negligible level via a cryogenic distillation procedure [5].

Finally, since WIMPs are expected to generate NRs, **all ER background sources** can be reduced during data analysis, making use of the S2/S1 ratio (see section 2.1).

**NR backgrounds** are more significant for DM searches. Given their low interaction probability, WIMPs are more likely to generate single-scatter (SS) NR, while neutrons induce multiple scatters (MS) (see figure 1). Dedicated analysis algorithms allow to distinguish SS from MS events, reducing the MS neutrons backgrounds. On the other hand, a SS NR induced by a neutron or a neutrino represents an irreducible background for WIMP searches.

XENON1T showed the lowest Electronic Recoil background ever achieved in such kind of experiments, corresponding to  $(82^{+5}_{-3} \text{ syst} \pm 3 \text{ stats}) \text{ events}/(\text{t. yr. keV}_{ee})$ , in the DM search region of interest [1].

## 3 Calibration using a $^{83m}\text{Kr}$ source

### 3.1 Introduction

Calibration is essential to study and understand the detector response to a wide range of energies as well as its stability. Indeed, XENON1T recorded data during several years in order to maximize the probability of detecting a WIMP-nucleon scattering or other rare events (such as the neutrinoless double  $\beta$  decay) : its response needs to be well-known and as stable as possible over time. Therefore, regular calibrations were made by the XENON collaboration during all the data taking periods. One of the source used bi- or tri-weekly is the  $^{83m}\text{Kr}$  (whose advantages will be described in more details in section 3.2). These regular calibrations allow for correction and monitoring of S1 and S2 signals, as it will be discussed in section 3.3.

### 3.2 $^{83m}\text{Kr}$ characteristics

$^{83m}\text{Kr}$  source has several advantages : first of all, it is an internal source that can be directly injected in the xenon recirculation system, providing a homogeneous calibration of the detector, allowing for the corrections of S1 and S2 signals<sup>5</sup>. Secondly, it has a half-life of

2. The muon flux at sea level is of the order of  $1 \text{ cm}^{-2} \text{ min}^{-1}$  [4], while it is of the order of  $3 \times 10^{-8} \text{ cm}^{-2} \text{ s}^{-1}$  under the Gran Sasso mountain.

3. They are uniformly distributed in the TPC : fiducialisation can not reduced them.

4. Xe is extracted from the atmosphere.

5. Indeed, because of several effects (like light or electron absorption by impurities, solid angle effect, reflection on the TPC's

1.83h, short enough to have all radioactive components disappearing in few hours after the source is closed. Finally, it has the advantage of decaying through two subsequent emissions of  $\gamma$  rays at 32.2 keV and 9.4 keV (i.e. in the region for DM searches), spaced in time by an average of **156.94 ns**, that allows a good identification, and thus a clean selection, of the  $^{83m}\text{Kr}$  decay.

### 3.3 Electron lifetime

The  $^{83m}\text{Kr}$  source is used to correct for the attenuation of the S2 signal. Because of electronegative impurities into the LXe, some of the electrons coming from the ionization are trapped during their drift. As a consequence, the observed S2 signal decreases exponentially with the drift time<sup>6</sup>. The evolution of the S2 signal as a function of the drift time can be written as in equation 1 [3]

$$S2 = S2_0 \times \exp\left(\frac{-\Delta t}{\tau}\right) \quad (1)$$

where S2 is the charge signal that is measured after the electrons drift, while  $S2_0$  is the charge signal that should have been measured if no impurities were present in the LXe (which also corresponds to the amplitude of an S2 signal generated on the top of the TPC).  $\tau$  is the electron lifetime, i.e. the average survival time of free electrons before being captured by impurities. Therefore, the determination of the electron lifetime allows to estimate the number of impurities inside the LXe and provide a way to correct S2 signals.

The electron lifetime is regularly monitored during data taking using the  $^{83m}\text{Kr}$  source, as shown in figure 2. An increase from February 2017 to February 2018 (which corresponds to a decrease of the impurity concentration) can be attributed to the continuous purification of the LXe during the data taking period.

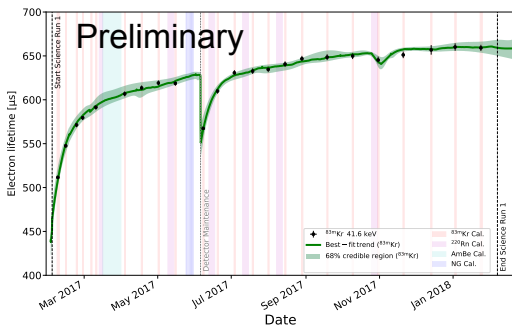


FIGURE 2: Monitoring of the electron lifetime. The electron lifetime increases over time thanks to the LXe purification system. The drop in June corresponds to the meshes cleaning that introduced impurities in LXe.

wall...), the collection of the light (S1) and charge (S2) depends on where the interaction occurs in the TPC.

6. The deeper the interaction is, the more likely the electrons are trapped while drifting toward the gaseous phase.

## 4 Search for neutrinoless double $\beta$ decay with XENON1T

### 4.1 Introduction

Neutrinos, detected for the first time 63 years ago [6], are mysterious particles : their absolute mass is unknown as well as their nature : are they Majorana<sup>7</sup> or Dirac<sup>8</sup> particles? Or, in other words, are neutrinos their own antiparticles? The detection of a double  $\beta$  decay without neutrino emission could answer this question.

Double  $\beta^-$  decay ( $2\nu\beta\beta$ ) is an isobaric nuclear decay, consisting of two neutrons transformed into two protons, with the emission of two electrons and two anti-neutrinos (see figure 3). Double  $\beta$  decay without neutrino emission ( $0\nu\beta\beta$ ) is possible only if neutrino is its own anti-particle (i.e. if neutrinos are Majorana particles).

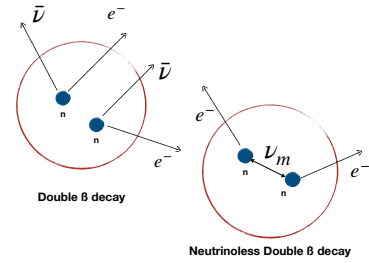
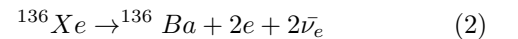


FIGURE 3: Double  $\beta$  and neutrinoless double  $\beta$  decay processes. The neutrinoless double  $\beta$  decay implies that neutrino and anti-neutrino are the same particle (i.e. Majorana particle).

$^{136}\text{Xe}$  is a double  $\beta$  decay emitter (see equation 2).



Its natural isotopic abundance in XENON1T (measured to be of 8.49%), gives the possibility to study the  $0\nu\beta\beta$  decay by measuring the total energy deposited by the two electrons (i.e. ERs).

While experimental signature of the  $2\nu\beta\beta$  decay is a continuous energy spectrum, the  $0\nu\beta\beta$  decay should lead to a discrete peak at the energy of the Q-value of the  $^{136}\text{Xe}$  decay<sup>9</sup>, i.e.  $2457.83 \pm 0.37 \text{ keV}$  [7]. To be able to detect this peak, XENON1T needs to prove a good energy resolution to ERs in this region. In section 4.2, the energy reconstruction method, as well as the preliminary energy resolution in the region of interest for the  $0\nu\beta\beta$  search is presented. In section 4.3, the current sensitivity of XENON1T, compared to other dedicated experiments and future projections, is shown.

7. Majorana particle : particle coincides with its anti-particle (like  $\gamma$ )

8. Dirac particle : particle and anti-particle are distinct (for example, positron is the anti-particle of electron : they differ by their charges).

9. In  $2\nu\beta\beta$  decay, the total energy emitted is split between the two neutrinos and the two electrons, while in  $0\nu\beta\beta$  decay, all the energy is carried by the two electrons.

## 4.2 Energy reconstruction

The combination of the S1 and S2 signals, shown in equation 3, is used to determine the energy of each interaction

$$E = W \cdot \left( \frac{S1}{g_1} + \frac{S2}{g_2} \right) \quad (3)$$

where  $W$  is the average energy needed to generate one photon or electron in LXe,  $g_1$  and  $g_2$  are parameters that depend only on the detector's characteristics. They are determined using calibration sources at different energies (such as the  $^{83m}\text{Kr}$  source) as well as  $\gamma$ -lines from materials decays. The light and charge yields (i.e. S1 and S2 signals per unit of deposit energy) of each identified energy line are determined. These quantities are anti-correlated<sup>10</sup>, therefore, a linear fit of the charge yield as a function of the light yields allows the extraction of  $g_1$  and  $g_2$  [8].

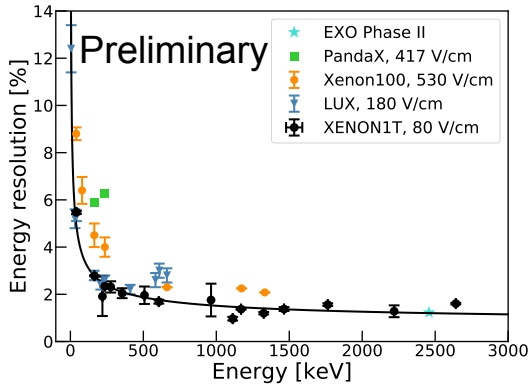


FIGURE 4: XENON1T energy resolution as a function of the energy.

The energy resolution is determined by fitting calibration-peaks by a Gaussian function. The current energy resolution of  $\sim 2\%$  at the  $^{136}\text{Xe}$  Q-value (shown in figure 4) could reach less than 1% by improving the reconstruction of events at high energy. A study in this direction is undergoing.

## 4.3 Sensitivity

The sensitivity to  $0\nu\beta\beta$  decay depends on the number of events and the number of background events in the region of interest, as shown in equation 4

$$S(T_{1/2}^{0\nu\beta\beta}) = \epsilon \frac{a}{A} \sqrt{\frac{m \times t}{\Delta E \times b}} \quad (4)$$

with :  $a$  the isotopic abundance of  $^{136}\text{Xe}$ ,  $A$  the atomic number of  $^{136}\text{Xe}$ ,  $m \times t$  the total exposure,  $\epsilon$  the detection efficiency,  $\Delta E$  the energy resolution and  $b$  the number of background events.

<sup>10</sup>. S1 and S2 are anti-correlated since electrons coming from the ionization of Xe atoms can recombine with other Xe atoms and form an excited state that decays emitting scintillation light (i.e. S1). Ionization of Xe atoms is thus involved in both S1 and S2 signals.

For XENON1T, the major background contribution for the  $0\nu\beta\beta$  search is coming from the material radioactivity of the detector ( $^{222}\text{Rn}$  emanation and decay from detector components, see section 2.2). As shown in figure 5, XENON1T expected sensitivity is lower than the current limits from dedicated experiments such as KamLAND-ZEN [9] or EXO-200 [10]. However, the first  $0\nu\beta\beta$  search with XENON1T could indicate the understanding of the detector at high energies, and will be a first proof of principle that future LXe experiments (XENONnT ( $\sim 8$  tons of LXe) and DARWIN ( $\sim 50$  tons of LXe)) could reach the so-called "Inverted neutrino's mass hierarchy" zone<sup>11</sup>. Indeed, while neutrino oscillation had proven the massive nature of neutrinos, only the difference between the masses of the three neutrinos is known, the mass hierarchy (i.e. which neutrino is the lighter/heavier<sup>12</sup>) is still unknown. As shown in figure 5, DARWIN could start constraining the neutrino mass hierarchy.

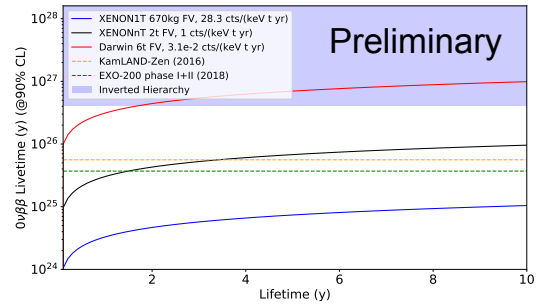


FIGURE 5: Average sensitivity to neutrinoless double beta decay of  $^{136}\text{Xe}$  at 90% CL for XENON1T and other present (KamLAND-Zen and EXO-200) and the future experiments (XENONnT and DARWIN). These sensitivities have been determined using equation 4, and assuming the background contaminations reported in the legend.

## 5 Conclusion

In this proceeding, the calibration of the XENON1T experiment was discussed. With stable operations over more than one calendar year, and with the lowest background noise ever achieved in such experiment, XENON1T reached the world best limit on the Spin-Independent WIMP-nucleon cross-section. The low background level and detector stability allow the search of other rare physics processes, among which of particular interest is the neutrinoless double  $\beta$  decay search, presented in this proceeding. This new analysis is a proof of concept for future dual phase LXe based DM experiments that could become competitive also in the search for neutrinoless double  $\beta$  decay.

<sup>11</sup>. In figure 5, the lower background levels indicated for future experiments assume a improvement of the  $^{222}\text{Rn}$  emanation reduction.

<sup>12</sup>. In the inverted mass hierarchy, the second mass eigenstate of neutrinos is heavier than the two other ones.

## Références

- [1] XENON collaboration, Dark matter search results from a One Tonne x Year exposure of XENON1T. *Phys. Rev. Lett.* 121, 111302
- [2] M. Goodman and E. Witten. Detectability of certain dark-matter candidates. *Physical Review D*, Volume 31, Number 12, 1985.
- [3] XENON collaboration, The XENON1T Dark Matter Experiment, arXiv :1708.07051
- [4] M. Tanabashi et al. (Particle Data Group), *Phys. Rev. D* 98, 030001 (2018).
- [5] XENON collaboration, Removing krypton from xenon by cryogenic distillation to the ppq level *Eur. Phys. J. C* 77 (2017) no.5, 275
- [6] C. L. Cowan, Jr., F. Reines, F. B. Harrison, H. W. Kruse et A. D. McGuire, Detection of the Free Neutrino : A Confirmation, *Science* 124, 103 (1956).
- [7] M. Redshaw, E. Wingfield, J. McDaniel, and E. G. Myers, Mass and double-beta-decay  $q$  value of Xe-136, *Phys. Rev. Lett.* 98 (Feb, 2007) 053003.
- [8] E. Aprile, K. L. Giboni, P. Majewski, K. Ni, and M. Yamashita, Observation of anticorrelation between scintillation and ionization for MeV gamma rays in liquid xenon, *Phys. Rev. B* 76, 014115 (2007)
- [9] KamLAND-Zen Collaboration, Search for Majorana Neutrinos near the Inverted Mass Hierarchy Region with KamLAND-Zen, *Phys.Rev.Lett.* 117 (2016)
- [10] EXO-200 Collaboration, Search for Neutrinoless Double-Beta Decay with the Upgraded EXO-200 Detector, *Phys. Rev. Lett.* 120, 072701 (2018)



Neuvième partie

# Neutrino Physics

session dirigée par Laura ZAMBELLI



# Introduction à la physique des neutrinos

Laura ZAMBELLI

LAPP, Annecy



## 1 Du postulat aux découvertes

La “solution désespérée” de Pauli en 1930 pour expliquer le spectre continu des émissions  $\beta$  nécessite l’existence d’une nouvelle particule sans charge, de spin  $1/2$  et de masse très faible : le neutrino. Sa mise en évidence est compliquée expérimentalement : étant un lepton neutre, il n’interagit que par interaction faible. En 1956, Reines et Cowan découvrent un premier type de neutrino ( $\bar{\nu}_e$ ) grâce à un détecteur placé près du cœur du réacteur de la centrale nucléaire de Savannah River. En 1962, Lederman, Schwartz et Steinberger construisent le premier faisceau de neutrino grâce à un accélérateur et découvrent un nouveau type de neutrino : le  $\nu_\mu$  à Brookhaven. Enfin, en 2000, l’expérience DONUT découvrent un troisième type de neutrino : le  $\nu_\tau$ . Ces mesures sont confirmées par le LEP en 1989 : la largeur invisible du boson  $Z^0$  n’est compatible qu’avec l’existence de 3 saveurs de neutrinos associés aux 3 leptons chargés ( $e$ ,  $\mu$ ,  $\tau$ ). En parallèle, Wu démontre expérimentalement que les neutrinos ne sont que d’hélicité gauche : il ne peuvent se coupler au champ de Higgs et ne possèdent donc pas de masse.

## 2 Les anomalies et les oscillations

Sans charge, sans masse, interagissant que par interaction faible : les neutrinos apparaissent donc parfaitement adaptés pour être utilisés comme messagers d’astrophysique. L’explosion d’une supernova dans l’univers proche peut être annoncé et étudié par le spectre des neutrinos qu’elle émet, comme ce fut le cas en 1987. Les processus de fusion nucléaire intervenant au cœur du soleil peuvent être étudiés par le spectre en énergie des  $\nu_e$  émis. L’origine, l’énergie et la nature des rayons cosmiques arrivant sur terre et interagissant dans l’atmosphère peut être déterminés par l’étude des produits de désintégrations comme les  $\nu_e$  et  $\nu_\mu$ .

Pour ces deux derniers projets, de nombreuses expériences ont été conçues dès les années 70. Cependant, les résultats ont montrés des anomalies dans le flux des neutrinos observés :  $2/3$  des neutrinos solaires manquent tout comme près de la moitié des neutrinos muoniques atmosphériques. De nombreuses hypothèses voient alors le jour pour expliquer ce phénomène. L’idée d’un mécanisme d’oscillation suggéré par Pontecorvo en 1957 ( $\nu \rightarrow \bar{\nu}$ ) est reprise par Maki, Nakagawa et Sakata modifiée en oscillation entre saveurs. Cela repose sur le postulat que les états propres de masse et les états propres de saveurs ne se superposent pas,

mais sont liés par une matrice de mélange unitaire. En conséquence, un neutrino créé avec une certaine saveur a une probabilité non nulle d’être détecté avec une saveur différente. En considérant trois familles de neutrinos, cette probabilité dépend de l’énergie du neutrino, de la distance source-détecteur, de trois angles de mélange, deux différences de masses entre les états propres ainsi qu’une phase de violation de  $CP$ . En 2002, l’expérience SNO mesure le flux total des neutrinos solaires par courant neutre : il est compatible avec les prédictions et seuls  $1/3$  des neutrinos arrivant terre ont une saveur électronique. Le reste a oscillé soit en  $\nu_\mu$  soit en  $\nu_\tau$ , leurs énergies est trop faible pour interagir par courant chargé. En 1998, Super-Kamiokande mesure le flux de neutrino atmosphérique en fonction de leur direction et de leur énergie. Le spectre est compatible avec les dépendances attendues par le mécanisme d’oscillation. Le phénomène d’oscillation des neutrinos est alors mis en évidence, et introduit un nouveau problème : contrairement aux prédictions du Modèle Standard, les neutrinos sont massifs.

## 3 Les questions actuelles

De nombreuses expériences reprenant les techniques qui permis la découverte des  $\bar{\nu}_e$  et des  $\nu_\mu$  ont été créés ou sont en projet afin de caractériser pleinement le phénomène des oscillations de neutrinos. C’est le cas des expériences comme Daya-Bay ou JUNO auprès d’une centrale nucléaire et T2K ou DUNE auprès d’un accélérateur. Aujourd’hui les 3 angles de mélange ainsi que les différences de masses sont relativement bien contraints. Le signe d’une des 2 différences de masse ainsi que la phase de violation de  $CP$  reste encore inconnus et devraient être résolus dans la prochaine décennie.

La mesure du flux de  $\bar{\nu}_e$  émis par les centrales nucléaires a montré un déficit de près de 6 % par rapport aux prédictions pour des distances inférieures au km. Cette nouvelle anomalie peut être expliquée par la présence d’un quatrième neutrino qui, selon la mesure du LEP, ne pourrait être détecté : ce serait un neutrino stérile. De nombreuses expériences d’oscillographie situées au plus près de cœur de réacteurs nucléaires essayent de mettre en évidence son existence, c’est le cas de STEREO ou encore SOLID.

La masse des neutrinos peut être contrainte de deux façons. Les expériences comme KATRIN ou TROITSK tentent de mesurer directement la masse des neutrinos en regardant la queue du spectre des désintégrations  $\beta$ . Des observations cosmologiques permettent des

contraintes indirectes.

Le mécanisme d'acquisition de la masse aux neutrinos reste encore un mystère et deux méthodes sont considérées actuellement. Par le mécanisme de Dirac, via un couplage au Higgs, il est alors nécessaire d'avoir un neutrino stérile d'hélicité droite. Le mécanisme de Majorana impose qu'il n'y aurait pas de distinction entre  $\nu$  et  $\bar{\nu}$ . Il est possible de démontrer expérimentalement cette dernière hypothèse par l'observation d'une double désintégration  $\beta$  sans émission de neutrino ( $\beta\beta 0\nu$ ). Cette catégorie de processus de désintégration (avec ou sans neutrino) est extrêmement rare, et les conditions expérimentales doivent être les plus propres possible, sans rayons cosmiques ni pollution radioactive interne ou externe. À ce jour, il n'y a pas eu d'observation d'un signal  $\beta\beta 0\nu$ . Les expériences actuelles comme SuperNEMO, CUORE ou encore SNO+ utilisent des approches expérimentales très différentes : tracker-calorimètre, bolomètre, liquide scintillant. Cependant, ces techniques ne permettront pas de complètement sonder/exclure l'espace de phase permettant le mécanisme de Majorana, de nouvelles techniques de détection ont besoin d'être pensés.

# Study of the nature of neutrinos with the SuperNEMO experiment and the LiquidO project

Axel PIN

Centre d'Etudes Nucléaires de Bordeaux-Gradignan



## Résumé

An important research topic about neutrinos is to determine their nature by studying the neutrinoless double beta decay. The discovery of this very rare decay ( $T_{1/2} > 10^{26}$  years) could prove the Majorana nature ( $\nu = \bar{\nu}$ ) of neutrinos. There stands the SuperNEMO experiment. The detector is composed of a tracker to reconstruct the trajectory of particles and a calorimeter to measure their energy. This unique technology, known as tracko-calor, allows to reject a lot of background events and to maximise the identification of the two electrons coming from the searched decay (2 tracks &  $E_1 + E_2 = Q_{\beta\beta} = \text{maximal energy available}$ ). However, such a precise measurement requires a good control of every systematics, especially on the non-linearity of light production (Birks, Cherenkov) and on the non-uniformity on photon collection (geometry). I will present the study made in order to optimise the demonstrator performances, more precisely by taking into account those effects in the calorimeter and how it is possible to correct them. I will also present the R&D work made on LiquidO, an original project using a new technology which might prove effective for the study of double-beta decay.

## 1 Introduction

The neutrino is the most common matter particle in the Universe, but the less known of all particles described in the Standard Model (SM). The only known properties of the neutrino are :

- it is a lepton which comes in three flavours associated to the known lepton flavours ( $e, \mu, \tau$ )
- it is a neutral charged fermion ( $spin = 1/2$ )
- it has a mass, despite this mass not having been predicted by the SM
- the neutrino flux on Earth is about  $70 \bar{M}/cm^2/s$

In order to learn more about this particle, there are several experiments in the world which are studying its unknown properties, such as its absolute mass, the mass hierarchy between the three neutrino flavours, its nature, the search of sterile neutrinos, etc. The SuperNEMO experiment and the LiquidO project aim at studying the neutrino nature, in other words to settle if the neutrino is a Dirac ( $\nu \neq \bar{\nu}$ ) or a Majorana ( $\nu = \bar{\nu}$ ) particle. The only known method to determine the nature of the neutrino is to study the double beta decays and to discover the neutrinoless one.

## 2 Double beta decays with SuperNEMO and LiquidO

### 2.1 Double beta decays

A double beta decay is the simultaneous disintegration of two neutrons of a nucleus, followed by the emission of two electrons [1]. In the case of the two neutrino double beta decay ( $2\nu\beta\beta$ ), the two electrons are accompanied by two anti-neutrinos (Figure 1a). This decay had already been observed with a half-life of  $[10^{18} - 10^{20}]$  years depending on the emitting isotope. The neutrinoless double beta decay ( $0\nu\beta\beta$ ) is characterised by the emission of only two electrons (Figure 1b). This decay is possible only if the neutrino is a Majorana particle. It is not allowed by the SM, because of a violation on the conservation of the leptonic number of two units. It has not been observed yet and the limit on its half-life is higher than  $10^{26}$  years. Because of the absence of neutrinos in the output, the expected signal is a peak at the maximal energy available  $Q_{\beta\beta}$ . However, if we want to study such a rare decay, we need a very precise control on the background, i.e on the energy.

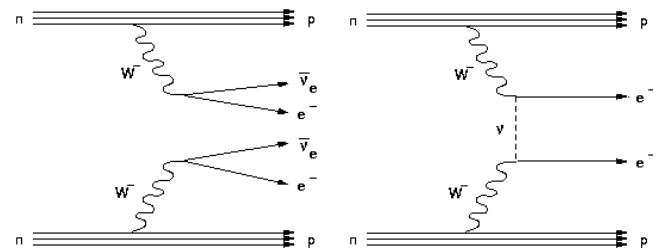


FIGURE 1: Feynmann diagrams for the 2 neutrinos double beta decay (left, a) and the neutrinoless double beta decay (right, b).

### 2.2 The SuperNEMO experiment

#### The SuperNEMO demonstrator

The SuperNEMO detector is placed underground to be protected against cosmic muons. Besides, its unique technology allows a very good background rejection and a precise measurement of the energy of particles. The detector is composed of a source foil of 7kg of  $^{82}\text{Se}$ , a tracker to reconstruct the particle path and to identify them, and a calorimeter to measure their energy and their time of flight, as shown in Figure 2.

In order to perform a very precise measurement of

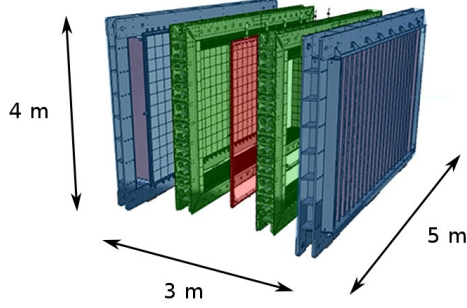


FIGURE 2: Scheme of the SuperNEMO demonstrator with the source foils in red, the tracker in green and the calorimeter in blue.

the energy, one needs to know every effect which can affect this measurement.

The calorimeter is composed of more than 700 optical modules (OM), an assembly of a plastic scintillator and a photomultiplier tube (PMT). When a particle interacts in the scintillator, its energy is converted into scintillation photons. The scintillator is wrapped with aluminised Mylar and Teflon to contain the light in the medium, as presented in Figure 3. The photons are then collected on the photocathode of a PMT, which converts them in photoelectrons. The amplification system delivers an electric signal proportional to the deposited energy [2]. But in order to control the systematics below one percent, one becomes sensitive to tiny effects like the calibration precision, the non-linearity of light production and the non-uniformity of the scintillator and the PMT.



FIGURE 3: SuperNEMO optical modules with the 8-inch photomultiplier tubes on the top and the wrapped scintillators ( $256 \times 256 \times 194$  mm) below.

### Optical effects

There are three main types of optical effects which can affect the measured energy [3].

The geometrical effect depends on the interaction point of the particle as we can see in the Figure 9. It is mainly caused by the non uniformity of the photocathode (which affects the light collection efficiency) of the PMT and the geometry of the scintillator (huge volume + step).

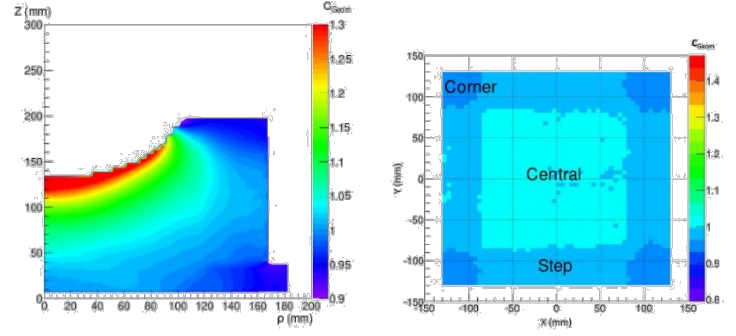


FIGURE 4: Geometrical correction factor for the full volume (left, a) and the front face (right, b) of a scintillator normalised to 1 in the center of the entrance face.

The Birks effect [4] is caused by the local saturation of the scintillation. Even if the particle is still losing its energy in the scintillator, the medium doesn't produce more light. As a consequence, the measured energy is lower than the deposited one and this effect is stronger for low energy particles (higher stopping power). Moreover, this effect doesn't follow a linear law with the energy (Figure 5) but :

$$LY(\mathbf{E}_0) = S \int_0^{\mathbf{E}_0} \frac{1}{1 + k_B \frac{dE}{dx}} dE. \quad (1)$$

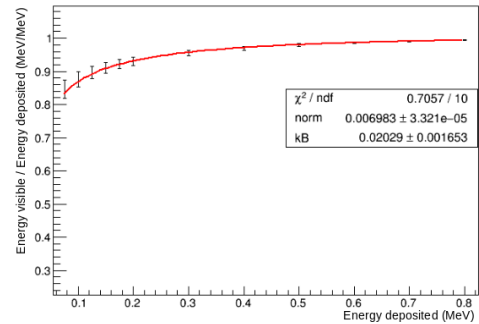


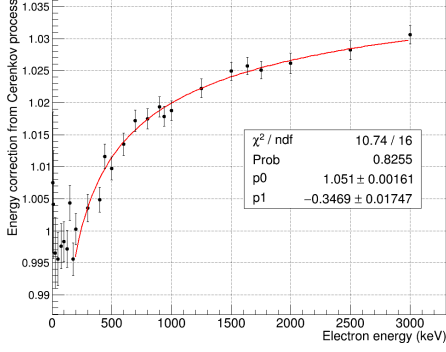
FIGURE 5: Birks correction factor *vs* energy.

The Cherenkov effect appears for particles travelling faster than light in the scintillator ( $>150$  keV in our case). Thus, the measured energy is higher than expected. This effect, as it is the case for the Birks one, is not linear with the energy deposited (Figure 6).

Because of these optical effects, the measured energy is different from the deposited one. Thus, it is necessary to take them into account to recover the true energy deposited by the particles in the detector and to improve the energy resolution.

### 2.3 The LiquidO project

The rarity of the neutrinoless double beta decay can be compensated by increasing the amount of mass

FIGURE 6: Cherenkov correction factor *vs* energy.

of emitting isotopes. However, in the case of experiments using transparent liquid scintillator, increasing the mass means reducing the transparency of the liquid, increasing the background (more mass = more contaminations) and the cost of the experiment (enrichment).

The idea of LiquidO is to use opaque scintillator : it is possible to load it without problems of transparency and to use natural abundances of isotopes. With opaque scintillator, the light is confined in it. Then, we collect the trapped photons using optical fibers. The topology of the expected signal depends on the particle. As a consequence, it is possible to have a particle identification in order to reduce the background, as shown in Fig 7.

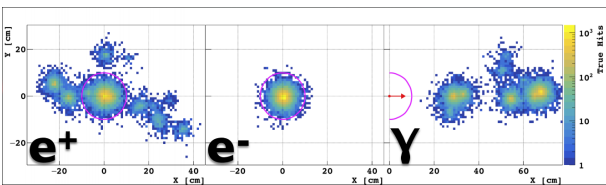


FIGURE 7: Simulation of different particles in LiquidO : expected signals for 1 MeV particles with opaque scintillator. Each point is a hit on a fiber.

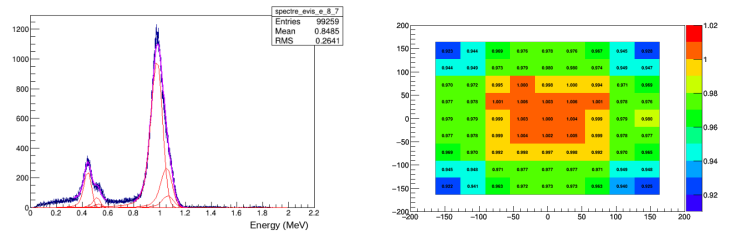
The  $\mu$ LiquidO setup aims at proving that we are able to confine the light in the opaque scintillator and to collect it on a detector. It is composed of a vessel filled with liquid scintillator, a PMT on the top, at the opposite side of the entrance face where particles will interact, and 3 optical fibers coupled to a mirror on one side and a Silicon PM (SiPM) on the other side. The three fibers are separated by 1.5 cm from each other, in order to see if the light will be confined close to the entrance face where photons will be created.

FIGURE 8:  $\mu$ LiquidO experimental setup.

### 3 Results

#### 3.1 Optical corrections for the SuperNEMO calorimeter

As the demonstrator is currently being built, the following results were obtained using the simulation software of the SuperNEMO experiment.  $^{207}\text{Bi}$  events were simulated in the detector. This isotope emits two conversion electrons of 482 keV and 976 keV and gamma rays. Keeping electrons only and using the knowledge of the interaction point thanks to the tracker, it is possible to measure the local geometrical correction for the entrance face of an OM. This local correction is given by :  $C_{geom} = \frac{E_{fit}}{E_{deposited}}$  where  $E_{fit}$  is the measured energy obtain with a Langaus fit, a convolution of a Landau and a Gaussian fit on the spectrum, as presented in Fig.6a where  $E_{deposited} = 976$  keV is the real electron energy deposited in the scintillator.

FIGURE 9:  $^{207}\text{Bi}$  electron spectrum (left, a) and the reconstructed geometrical corrections (right, b).

Then, it is possible to compare this reconstructed mapping of geometrical correction to the true one given in Figure 9b. As shown in Figure 10 the difference is lower than 0.5%. It means that we will be able to correct the geometrical effect *in situ*.

The use of these corrections is presented in Figure 11. A Gaussian fit on the two spectra for the 976 keV electron peak allows us to access the width of each peak. We obtained  $\sigma_{black} = 5.0 \pm 0.1\%$  and  $\sigma_{red} = 4.4 \pm 0.1\%$ , i.e an improvement on the energy resolution of about 12%.

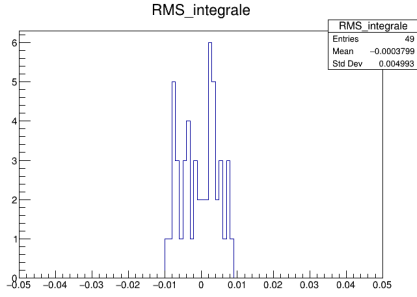


FIGURE 10: Difference between the true and the measured correction mapping.

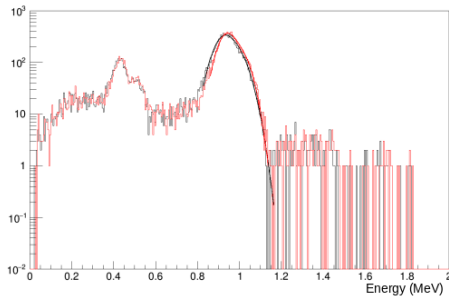


FIGURE 11: Non corrected (black) and corrected  $^{207}\text{Bi}$  electron spectra.

### 3.2 First results with $\mu\text{LiquidO}$

Using the  $\mu\text{LiquidO}$  setup, we were able to test some samples of opaque scintillators and to compare them with transparent liquid scintillator. The goal is to check if photons are confined in the medium. In Figure 12, we compare the amount of light we obtained for both opaque and transparent liquid scintillators on the three SiPM and on the PMT.

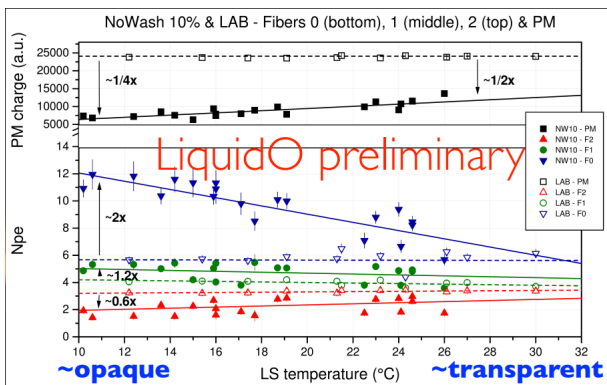


FIGURE 12: Light collected *vs* temperature of the liquid scintillator for the PMT (black) and on the 3 SiPM (bottom, closer to the entrance face in blue, middle in green, top, farther to the entrance face in red) with transparent (empty points and dashed lines) and opaque (full points and straight lines) scintillators.

According to the simulations shown in Figure 7, the size of the light ball is almost 20 cm, but the size of the

$\mu\text{LiquidO}$  setup ( $\simeq 10$  cm) doesn't allow us to measure this light ball.

However, as expected, more photons were collected on the bottom SiPM, the one closer to the entrance face where electrons interact, with the opaque liquid scintillator than with the transparent one. Besides, the farther we are from the entrance face, the less we observe light. We also observe that the opacity is stronger with a cold liquid.

## 4 Conclusions

Despite being the most common matter particle in the Universe, the neutrino remains the less known one. In order to study its nature, the SuperNEMO experiment and the LiquidO project aim at discovering the neutrinoless double beta decay.

The SuperNEMO detector is using an unique technology to detect this decay and to study the involved mechanisms. However, to perform such a precise measurement, we need to control all systematics on the measurement of the energy of particles. Thanks to the SuperNEMO technology, we will be able to measure and to correct these systematics. As a consequence, it will be possible to improve the energy resolution of the detector.

The LiquidO project, thanks to its new and innovative technology, has the potential to become a double beta multi-ton experiment. It is still in R& D. However, the first results we obtained with the  $\mu\text{LiquidO}$  prototype setup are very promising for the future of the experiment.

## Références

- [1] M. Goeppert-Mayer, "Double beta-disintegration", Phys. Rev. 48(6) : 512-516, 1935.
- [2] E. Chauveau, "Développement de compteurs à scintillation hautes performances et de très basse radioactivité pour le calorimètre du projet SuperNEMO" (2010).
- [3] A. Huber, "Recherche de la nature du neutrino : mise en route, simulation et analyse des données du démonstrateur de SuperNEMO" (2017)
- [4] J.B. Birks, "The Theory and Practice of Scintillation Counting" (1964).